
Matrix product state calculations for one-dimensional quantum chains and quantum impurity models

Wolfgang Munder

Dissertation
an der Fakultat fur Physik
der Ludwig-Maximilians-Universitat
Munchen

vorgelegt von
Wolfgang Munder
aus Munchen

Munchen, den 30.08.2011

Erstgutachter: Prof. Dr. Jan von Delft

Zweitgutachter: Prof. Dr. Ulrich Schollwöck

Tag der mündlichen Prüfung: 28.09.2011

Contents

Abstract	v
I General Introduction	1
1 Introduction	3
2 Strongly correlated electron systems	7
2.1 Fermi liquid theory	8
2.2 Luttinger liquid theory	8
2.3 Renormalization group approaches	9
3 Quantum impurity problems	13
3.1 Kondo effect and Kondo temperature	13
3.2 Quantum dots	15
3.3 Single-impurity Anderson model	15
3.4 Fermi sea	16
3.5 Anderson orthogonality	17
3.5.1 Static quantities	17
3.5.2 Dynamical quantities after a quantum quench	19
3.6 Population switching in quantum dots	21
4 Numerical renormalization group (NRG)	25
4.1 Hamiltonian	25
4.2 From the electronic band to the Wilson chain	27
4.2.1 Logarithmic discretization	27
4.2.2 Mapping to the Wilson chain	29
4.2.3 Wilson chain in the original form	30
4.2.4 Improved discretization scheme	30
4.3 Key points of the Wilson chain mapping	32
4.4 NRG solution of the Wilson chain	34
4.4.1 Description of the iteration procedure	36
4.4.2 Renormalization group flow	37

4.4.3	Matrix product state structure of the basis states	38
4.5	Anders-Schiller basis	42
4.5.1	Definition	42
4.5.2	Local operators	44
4.6	Density matrix	47
4.7	Spectral functions	49
4.8	Expectation values	53
4.9	Overlap calculations in the context of Anderson Orthogonality	54
4.10	Scattering phase shifts from the energy flow diagram	55
II	Results	59
5	The correlation density matrix	61
6	Anderson orthogonality	113
6.1	Anderson Orthogonality and the Numerical Renormalization Group	113
6.2	Anderson Orthogonality in the Dynamics After a Local Quantum Quench	123
III	Miscellaneous	145
	Bibliography	147
	List of Publications	153
	Deutsche Zusammenfassung	155
	Acknowledgements	157

Abstract

This thesis contributes to the field of strongly correlated electron systems with studies in two distinct fields thereof: the specific nature of correlations between electrons in one dimension and quantum quenches in quantum impurity problems. In general, strongly correlated systems are characterized in that their physical behaviour needs to be described in terms of a many-body description, i.e. interactions correlate all particles in a complex way. The challenge is that the Hilbert space in a many-body theory is exponentially large in the number of particles. Thus, when no analytic solution is available - which is typically the case - it is necessary to find a way to somehow circumvent the problem of such huge Hilbert spaces. Therefore, the connection between the two studies comes from our numerical treatment: they are tackled by the density matrix renormalization group (DMRG) [1] and the numerical renormalization group (NRG) [2], respectively, both based on matrix product states.

The first project presented in this thesis addresses the problem of numerically finding the dominant correlations in quantum lattice models in an unbiased way, i.e. without using prior knowledge of the model at hand. A useful concept for this task is the correlation density matrix (CDM) [3] which contains all correlations between two clusters of lattice sites. We show how to extract from the CDM, a survey of the relative strengths of the system's correlations in different symmetry sectors as well as detailed information on the operators carrying long-range correlations and the spatial dependence of their correlation functions. We demonstrate this by a DMRG study of a one-dimensional spinless extended Hubbard model [4], while emphasizing that the proposed analysis of the CDM is not restricted to one dimension.

The second project presented in this thesis is motivated by two phenomena under ongoing experimental and theoretical investigation in the context of quantum impurity models: optical absorption involving a Kondo exciton [5, 6, 7] and population switching in quantum dots [8, 9, 10, 11, 12, 13, 14, 15]. It turns out that both phenomena rely on the various manifestations of Anderson orthogonality (AO) [16], which describes the fact that the response of the Fermi sea to a quantum quench (i.e. an abrupt change of some property of the impurity or quantum dot) is a change of the scattering phase shifts of all the single-particle wave functions, therefore drastically changing the system. In this context, we demonstrate that NRG, a highly accurate method for quantum impurity models, allows for the calculation of all static and dynamic quantities related to AO and present an extensive NRG study for population switching in quantum dots.

Part I

General Introduction

Chapter 1

Introduction

The field of strongly correlated electronic systems has emerged from the awareness that for the correct description of many phenomena interactions play the key role, thereby correlating all particles in the system in a complex way. Prominent examples are Mott insulators [17], which cannot be explained within the conventional band theories, and the Kondo effect [18]. The latter was observed already in the 1930's by de Haas *et al.* [19] as a resistivity anomaly at low temperatures: instead of a decrease of the resistivity with decreasing temperature it increases again when the temperature is lowered below what is nowadays called the Kondo temperature T_K . The reason for this behaviour is that the local moment of magnetic impurities in some metals (the first observation was about iron impurities in gold and silver) is screened by the conduction electrons, forming a strongly correlated state. This explanation has been found by Jun Kondo in the 1960's [18]. Nevertheless, the question which specific realization of his model yields a realistic description of the observations of de Haas *et al.* could be answered only recently [20].

The necessity to include (electron-electron) interactions into models describing solid state systems caused an enormous challenge: the description of these systems in terms of single particles is not appropriate any longer and instead many-body theories had to be established. Evidently, the complexity of these systems increases with the number of particles, manifesting in the scaling of the dimension of the Hilbert space: it grows exponentially with the number of particles. The problem is now that for most systems no analytic solution is available and exact diagonalization requires huge computational effort even for small systems. Thus, several numerical methods have been established, which somehow circumvent the treatment of the full, high-dimensional Hilbert space.

The two studies presented in this work are tackled by two of these methods, namely the density matrix renormalization group (DMRG) [1, 21] and the numerical renormalization group (NRG) [2, 22, 23]. Both methods take advantage, albeit each in somewhat different form, of the concept of the renormalization group (RG) [2] which earned Kenneth G. Wilson the Nobel prize in 1982. In general, RG proposes a way to iteratively consider all degrees of freedom of a problem by systematically thinning out irrelevant degrees of freedom at each step.

The first project presented in this thesis generally addresses correlations in quantum

lattice systems. When investigating correlations the problem arises that a priori the form of the dominant correlations is unknown. One needs to guess in advance - based on experience or prior knowledge - which operators could carry long range correlations and check whether this is really the case. The concept of the correlation density matrix (CDM) [3] is intended as an *unbiased* way to numerically find the operators carrying the dominant correlations.

For two disjoint, separated clusters the CDM is defined by the density matrix of their union minus the direct product of their respective density matrices (to get rid of trivial correlations). Varying the position of the two clusters yields a distance-dependent CDM to obtain information about the spatial dependence of the correlations. So far the concept is quite simple, but it is a highly non-trivial challenge to extract useful, easily digestible information from the mass of data that constitutes the CDM. To this end we propose the *dominant operator basis* method which systematically extracts from the CDM a small number of operators that carry the dominant correlations over large distances, thereby truncating all correlations of negligible weight.

We propose this method with no limitations to the system's dimension, but choose to restrict ourselves to one dimension for a demonstration of the method in practice. The reason is (i) that for our model of choice, a spinless extended Hubbard model that features a competition between charge density correlations and pairing correlations, an extensive study of the dominant correlations has already been performed [4], so that we can compare our results to those, and (ii) that with DMRG we possess a tool to numerically obtain the relevant quantities with high accuracy, where comparable methods for higher dimensions are not available.

The second project presented in this thesis covers Anderson orthogonality (AO) [16], which arises in the context of (electronic) quantum impurity models. These consist of an essentially zero-dimensional structure (the impurity; usually also called dot, following the advances in the field) with only a few degrees of freedom coupled to one or more electronic reservoirs. For example, in the context of the Kondo problem, J. Kondo introduced the Kondo model, where the magnetic impurities are described via a localized spin which acts as a spin-flip scatterer for the conduction band electrons of the underlying metal. The electronic reservoirs are usually described as Fermi liquids and we will henceforth refer to them as Fermi seas.

Even though AO was originally introduced as a ground state property, it also affects dynamic quantities like absorption spectra. The original notion of AO states that for a given quantum impurity model the ground states of two realizations thereof which differ only in some quantity of the impurity (for example the level energy of the degrees of freedom of the impurity) are orthogonal in the thermodynamic limit. For finite systems the overlap between the two ground states decays exponentially with system size, where the exponent is proportional to the square of the difference in scattering phase shifts at the Fermi energy. In turn, this difference in scattering phase shifts is related by the Friedel sum rule [24, 25, 26] to the difference in electron number within a large but finite volume around the impurity. In the first part of our investigations about AO, we show how to extract from NRG calculations the AO exponent as well as the difference in electron number and demonstrate our techniques for various elementary models where the statements above

hold with remarkable accuracy.

The second part of our investigations is motivated by recent studies of two phenomena in which AO turned out to be crucial in the explanation of the observed physics. The first is the creation of a Kondo exciton in quantum dots via optical absorption [5, 6, 7], where an electron is excited from a deep lying valence-band level to a conduction-band level in a quantum impurity. The absorption spectrum can be effectively derived from a model which is subject to a quantum quench: the creation of the Kondo exciton is considered only in that the arising exciton binding energy abruptly changes the level energy of the impurity which is exactly the kind of situation to render AO as introduced above.

Further, we address the intriguing problem of population switching (PS) in quantum dots [8, 9, 10, 11, 12, 13, 14, 15]. For a two-level quantum dot with asymmetric coupling to the two attached Fermi seas an adiabatic sweep of the level position causes a level inversion where the initially occupied level is emptied in favour of the other level. In recent work it has been argued that AO is relevant in this situation, especially regarding the question whether the PS takes place continuously or abruptly [14, 15]. Even though the influence of AO in this context can not be seen as directly as for the Kondo exciton, the complete physical behaviour in this context can be explained in terms of AO.

The key point for these two phenomena is that AO does not only appear as a property between ground states, but also influences optical absorption spectra as was already known at the time of its introduction by Anderson (in particular also in the context of exciton creation) [27, 28, 29, 30]. In general, when a quantum quench is applied to the Hamiltonian at hand, more specifically to the impurity part of the Hamiltonian, AO affects the subsequent dynamics. This can be understood in that the initially equilibrated system reacts to the quantum quench in completely rearranging itself, thereby evolving to the ground state of the new Hamiltonian. The stronger the orthogonality between the initial ground state and the (desired) final ground state, the stronger the imprint of AO on the dynamics subsequent to the quantum quench. We apply a comprehensive NRG study to cover all aspects of AO in quantum quench dynamics, thereby establishing a formalism for the general case of a switch between an initial and a final Hamiltonian, and finally apply this formalism to clarify the role of AO for population switching.

The following paragraphs give an outline of the contents of this thesis, divided into three parts: Part I gives a general introduction to the methods and topics presented in this thesis, in Part II we show our results, published in three papers, and Part III contains the bibliography, a list of the publications presented in this thesis, the “Deutsche Zusammenfassung” and the author’s acknowledgements.

Part I introduces the major topics of this thesis, beginning with the field of strongly correlated electron systems (Chap. 2). After a short general introduction we present the parts of the field relevant to this thesis: Fermi liquid theory (Sec. 2.1), Luttinger liquid theory (Sec. 2.2), and renormalization group approaches (Sec. 2.3). In Chap. 3 we turn to quantum impurity problems which we shortly introduce also from the experimental side (Sec. 3.1 and Sec. 3.2). We depict two models common in this context, the Kondo model (Sec. 3.1) and the single impurity Anderson model (Sec. 3.3), and how we usually model the Fermi sea (Sec. 3.4). Most important, we elucidate the Anderson orthogonality (Sec. 3.5)

and its far reaching consequences to static (Sec. 3.5.1) and dynamic (Sec. 3.5.2) properties of quantum impurity systems. Finally, we describe the phenomenon of population switching (Sec. 3.6) and how it is influenced by Anderson orthogonality. The last chapter of this part, Chap. 4, gives a detailed introduction to the numerical renormalization group.

Part II contains our results, published in three papers: *Correlation density matrices for one-dimensional quantum chains based on the density matrix renormalization group* (Chap. 5), *Anderson Orthogonality and the Numerical Renormalization Group* (Sec. 6.1), and *Anderson Orthogonality in the Dynamics After a Local Quantum Quench* (Sec. 6.2).

Chapter 2

Strongly correlated electron systems

The field of strongly correlated electron systems is built upon the realization that many phenomena could not be explained without taking correlations into account. In condensed matter physics metal-insulator transitions, Mott insulators, high-temperature superconductivity, electrons in one dimension, and quantum impurity problems are only a few examples. Of course, there are also other strongly correlated systems apart from electrons, e.g. quantum spin chains and ultracold gases to name only two. The latter are particularly interesting for condensed matter physics as they can be used to model solid state systems in a highly controlled fashion [31].

Generally, strongly correlated systems are characterized in that the relevant physics in these systems is given within a many-body description including interactions, i.e. particles influence each other in a complex way via correlations. However, the consideration of interactions drastically increases the complexity of the underlying models. An example is the nearly-free electron model of electrons in a lattice of positively charged ions (an extension to the ideal Fermi gas). It establishes the band theory of solids, which includes the conventional classification of solids into metals, insulators and semiconductors depending on the filling of the bands. Although this concept can be used to explain many basic experimental observations, it fails for others where interactions play a dominant role. For example Mott insulators [17] are classified as metals within band theory but experimentally turned out to be insulators. Here the Coulomb repulsion between the electrons outweighs the energy gain due to delocalization, therefore creating an energy gap above the ground state in which the electrons are localized at the lattice sites.

Unfortunately, analytic solutions or exact methods are seldom to be found for strongly correlated systems, and exact diagonalization (as a numerical tool) is only realistically applicable for small finite systems. Thus, more sophisticated methods had to be established, of which we present those relevant to this thesis. In the following, we assume that we have to deal with a problem consisting of interacting electrons only.

2.1 Fermi liquid theory

In the late 1950's Lev Davidovich Landau introduced the Fermi liquid theory [32, 33] which has been further developed since, especially using quantum field theory, see e.g. [34, 35]. The basic conclusion is that weak excitations of the system can be represented by quasi-particles which show Fermi statistics and resemble the excitation spectrum of the Fermi gas. This resemblance constitutes the surprising success of the nearly-free electron model in the description of many solid state phenomena. The quasi-particles have the same spin, charge and momentum as the original fermions, but other properties take the interactions into account and are replaced by effective values, e.g. the effective mass m^* . Physically speaking, a quasi-particle consists of a fermion, e.g. an electron, together with its screening cloud of surrounding fermions which are disturbed by the motion of the fermion and vice versa, which justifies the one-to-one correspondence of quasi-particles and fermions of the non-interacting Fermi gas.

However, the quasi-particles are still weakly interacting, but with a lifetime that goes to infinity for energies close to the Fermi energy ε_F , which means that the quasi-particle picture is well-defined for small excitation energies. The reason lies in the Pauli exclusion principle: in a low-energy many-body state of the system nearly all single-particle states with energy less than ε_F will be occupied. A quasi-particle with energy slightly above ε_F can scatter with another one also with energy above ε_F . After the scattering, both particles will still have energy larger than ε_F due to the Pauli exclusion principle and thus the phase space volume of the possible states after scattering is considerably reduced. Using Fermi's golden rule to calculate the scattering cross section, we find that it goes to zero for excitation energies close to ε_F . Due to the fact that the quasi-particle states are still well-described in terms of their momentum, we will refer to a Fermi liquid system as Fermi sea.

The properties of Fermi liquids and the influence of the quasi-particles will be of particular interest for quantum impurity problems in Chap. 3. The electronic reservoirs in these systems are usually described as Fermi liquids and we will refer to them as Fermi seas, henceforth. The presence of the impurity typically features strong correlation effects between the impurity and the electrons in the Fermi seas and often gives rise to quite unexpected physics. For example, in the symmetric two-channel Kondo model where two electronic reservoirs are coupled to a magnetic impurity and hence compete in the screening process, the final combined system even cannot be described as a Fermi liquid any more [36]!

2.2 Luttinger liquid theory

Although the Fermi liquid theory is very successful in two and three dimensions, it turned out that it fails in one dimension where it is replaced by the Tomonaga-Luttinger liquid theory (often simply referred to as Luttinger liquid theory). The foundations thereof were laid by S. Tomonaga [37] and further developed by J. M. Luttinger [38] and D. C. Mattis

and E. H. Lieb [39]. They were the first to identify the excitations of one-dimensional interacting fermions as collective modes showing *boson*-like behaviour. This development eventually led to the complete picture of the bosonization formalism introduced by Haldane [40], see the tutorial by J. von Delft and H. Schoeller for an introduction [41]. The insights of this theory were the starting point of our treatment of the correlation density matrix (CDM).

The key point of the Luttinger liquid theory is that the low-lying excitations of the one-dimensional interacting fermions are spin- and particle-density waves which can be expressed in terms of Boson fields. The original Hamiltonian can be transformed into a bosonic Hamiltonian characterized by the sound velocity of the collective excitations u and a dimensionless parameter K , both depending on the strength of the interactions. For non-interacting fermions u will be equal to the Fermi velocity. The two parameters u and K allow for the calculation of any correlation function of interest and fully characterize the low-energy properties of the system. Thus, this description is the 1D-analogue of the Fermi liquid description in higher dimensions.

We want to stress two features of this theory: one is the phenomenon of spin-charge separation, i.e. spin and charge excitations propagate individually, which is a formal consequence of the theory. More important for our purposes is that correlation functions which exhibit long-range behaviour are non-universal power-law functions in space and time, oscillating in space with the Fermi momentum. This result has direct impact on our analysis of the CDM as it gives some intuition on the expected form of the CDM, cf. the section on the [Goals of the DOB method](#) of our publication about the CDM in Chap. 5.

2.3 Renormalization group approaches

One of the most important approaches in the field of strongly correlated electron systems is the renormalization group [2] (RG) from which several numerical methods have emerged, including DMRG and NRG that are used in this thesis. Even though renormalization was successfully applied already in the 1950's, eliminating the divergences of quantum electrodynamics, for example, it was the work of Kenneth G. Wilson that was the major physical advance for which he was awarded the 1982 Nobel Prize in Physics. Apart from his solution of the Kondo problem being the first one where renormalization group transformations were numerically solved, his insight that the RG is more than just a mathematical tool but also has a significant physical interpretation was his major contribution.

The basic physical idea in the RG approach is that for strongly correlated systems all length or energy scales are of importance, not only those initially inherent to the system like the atomic wavelength. Moreover, the fluctuations at all these length scales are locally coupled, i.e. they are affected by fluctuations at nearby length scales. This is ultimately the reason why perturbation theory fails in these systems. There are two conclusions following from this picture of coupled scales: (i) scaling and (ii) amplification and deamplification, respectively. The first states that for scales which are well away from any inherent scales the behaviour of the system tends to be identical apart from changing the scale, precisely

because there are no characteristic scales in that regime. The second conclusion is that microscopic changes may be amplified to macroscopic changes (this is particularly important in the context of AO in Sec. 3.5) or that they may be smeared out until they are negligible for macroscopic properties. In particular, the latter supports the observation of universality in critical phenomena.

Wilson's application of the RG method makes use of these insights by a sequential treatment of the different scales. Starting from an initial scale, e.g. the atomic wavelength, described by an initial Hamiltonian, a renormalization group transformation is defined which transforms the Hamiltonian of one scale to the one of the next scale, thereby taking into account the coupling between the scales. This introduces a renormalization flow which converges when all characteristic scales of the system are left behind. This scheme can be used in various forms like diagrammatic formulations for critical phenomena or the original treatment of Feynman diagram expansions within quantum field theory. Here we are more interested in the form where the transformation is constructed such that it can be solved numerically.

A characteristic - and in fact essential - ingredient of the numerical RG procedure is the thinning out of degrees of freedom after each iterative step. The iterative treatment of the problem allows to access all energy scales but only when the number of considered degrees of freedom per iteration step stays constant because otherwise its number sooner or later becomes too large to be handled numerically. Thus, each numerical implementation of the RG needs to establish a criterion to decide which degrees of freedom are considered relevant and will thus be kept for the next step.

Another characteristic of RG is the parameter flow even though not always accessible in numerical implementations. The renormalization flow is described by a sequence of Hamiltonians, each acting on a different renormalized set of degrees of freedom. Each Hamiltonian is of the same form \hat{H} , albeit with a different set of (interaction) parameters \mathbf{K} which change under the RG flow. This is expressed formally by

$$R(\hat{H}(\mathbf{K})) = \hat{H}(\mathbf{K}') , \quad (2.1)$$

or equivalently

$$R(\mathbf{K}) = \mathbf{K}' , \quad (2.2)$$

where R represents the RG transformation. The RG transformation is expected (but not guaranteed) to have one or more fixed points \mathbf{K}^* which are invariant under the RG transformation

$$R(\mathbf{K}^*) = \mathbf{K}^* . \quad (2.3)$$

These fixed points are called stable and unstable depending on whether the RG flow in their vicinity tends to flow towards to or away from the fixed point, respectively. In particular, as a result of the abovementioned self-similarity of the RG flow, after exceeding all relevant energy scales of the system, one expects a stable fixed point in that regime.

In numerical implementations it is not always possible to construct this parameter flow out of the numerical data, but for example for the Kondo problem it is well known how the parameter flow looks like and which physical behaviour can be expected from its stable and unstable fixed points [22].

Numerical renormalization group

The NRG nicely adopts the RG concept from a numerical perspective. It has been developed to solve the Kondo problem, but generally applies to the class of quantum impurity problems, with a few localized degrees of freedom coupled to one or more Fermi seas. The first crucial step in this method is to map the part of the Hamiltonian describing the Fermi sea(s) onto a semi-infinite chain with exponentially decreasing couplings between nearest neighbours, the Wilson chain. The sites of this chain correspond to wave functions located in shells with exponentially increasing radius, centred around the impurity.

The numerical solution of this problem then follows closely the steps of the RG: starting with the smallest structure, the impurity, the size of the system is increased by one site at each iterative step, i.e. one iteratively considers contributions of larger and larger length scales. The resulting chain is solved numerically to yield energy eigenvalues and eigenstates, while the thinning out of degrees of freedom is achieved by keeping only the lowest-lying energy eigenstates after each iteration. In this way the ground state of the initial problem is determined to very good accuracy, but the method is capable to calculate much more properties of the system beyond the ground state as we show in more detail in Chap. 4.

Density matrix renormalization group

The second important renormalization group approach in this thesis is the density matrix renormalization group. The setting of this method is quite different from that of NRG and different opinions have been put forth about whether DMRG belongs to the renormalization group approaches in a rigorous meaning thereof [21]. DMRG was investigated for the ground state calculation of one-dimensional quantum chain systems and has widely evolved since then. We give a short overview over DMRG developments and an extensive introduction into our implementation of the DMRG method in the [appendix](#) of our publication about the CDM (see Chap. 5), so we will stick to general RG features of DMRG here.

DMRG follows the spirit of the renormalization group in that degrees of freedom are systematically thinned out. In each step of the DMRG iterative scheme a certain density matrix is constructed describing degrees of freedom in the current - imperfect - description of the state. Based on their weight in this density matrix a good part of the degrees of freedom is truncated, where details depend on the specific implementation (see the section on [Hilbert space truncation](#) in Chap. 5). However, there is no kind of cutoff in the degrees of freedom (like the infrared energy cutoff in NRG), which is often considered as an essential part of the original RG method. Thus, in this sense DMRG is no RG method. In any case, most implementations (including ours) nowadays treat DMRG as a variational

method within the space of matrix product states, with no reference to the RG apart from the name. For an introduction, see the section on the [Variational optimization scheme](#) in Chap. 5.

Chapter 3

Quantum impurity problems

In this chapter we give a short introduction to quantum impurity problems, which are a prime example for strongly correlated electron systems as here a tiny structure, the impurity, consisting of a few localized quantum degrees of freedom drastically influences the global properties of the full many-body system due to strong correlation effects. Such systems are theoretically investigated and experimentally realized for Bosons and Fermions as well. However, we will focus on fermionic problems, but the adaptation to bosonic problems is straightforward.

We show in this section how this field has risen from “real” impurity problems, e.g. iron impurities in gold and silver, and developed along with the increasing interest in nanotechnology towards artificial devices which are similar in the theoretical description but completely different in geometry. We show how in the context of NRG the Fermi sea of the electrons is described. Finally, we describe in more detail how the strong correlations in the system result in the far-reaching effect of Anderson orthogonality (AO), which is at the heart of several phenomena characteristic of quantum impurity models. In particular we will further investigate the connection between AO and population switching in quantum dots.

3.1 Kondo effect and Kondo temperature

One of the very first long standing puzzles which initiated the investigation of correlation effects is the Kondo effect [18]. In 1934 de Haas, de Boer and van den Berg found a resistivity anomaly at low temperatures in gold and silver. In stark contrast to the usual decrease of the resistivity with temperature due to potential scattering, electron-electron and electron-phonon interactions, the samples showed an *increasing* resistivity at some unknown low-temperature scale.

It lasted 30 years until J. Kondo [18] would explain this behaviour as correlation effect between the conduction electrons, induced by magnetic impurities (namely iron impurities in case of the above experiments). He introduced a model where the dominant physics at low temperature is governed by spin-flip scattering of the conduction electrons at the

magnetic impurity. The major physics are described by the Kondo model:

$$\hat{H} = J\mathbf{S} \cdot \mathbf{s} + \sum_{k\sigma} \varepsilon_k \hat{c}_{k\sigma}^\dagger \hat{c}_{k\sigma}. \quad (3.1)$$

It consists of a single electronic band (an electron in the conduction band with spin σ and momentum k is created and annihilated by $\hat{c}_{k\sigma}^\dagger$ and $\hat{c}_{k\sigma}$, respectively) and an impurity which interact via the coupling term $J\mathbf{S} \cdot \mathbf{s}$, where \mathbf{S} is the local moment of the impurity and \mathbf{s} the spin of the conduction electrons at the position of the impurity:

$$\mathbf{s}_i = \sum_{kk'\sigma\sigma'} \frac{1}{2} \hat{c}_{k\sigma}^\dagger \sigma_{\sigma\sigma'}^{(i)} \hat{c}_{k'\sigma'}, \quad (3.2)$$

with the usual Pauli matrices $\sigma^{(i)}$ ($i \in \{x, y, z\}$). The interaction is taken to be antiferromagnetic, $J > 0$, resulting in a ground state that is a spin singlet.

It turns out that an exponentially small *dynamical* energy scale arises, the Kondo temperature

$$k_B T_K \sim D |2\rho J|^{1/2} e^{-1/(2\rho J)}, \quad (3.3)$$

where D is the half-bandwidth and ρ the density of states in the conduction band [26]. Spin-flip scattering is the only relevant process in the system, hence the Kondo temperature the only relevant energy scale. For temperatures below the Kondo temperature, the system is able to form a strongly correlated state where the conduction electrons screen the magnetic moment of the impurity, the so-called Kondo screening cloud.

One should note, however, in the definition of the Kondo temperature that the most relevant part of Eq. (3.3) is the exponent with prefactor of order 1 depending on convention. Thus, in the context of NRG we additionally calculate T_K via the static spin susceptibility χ_s to obtain a result arising consistently within the NRG calculations. The connection to χ_s comes from a Fermi liquid relation, cf. Eq. (42) in [42], which reduces for $T = 0$ to

$$k_B T_K = \frac{(g\mu_B)^2}{4\chi_s}. \quad (3.4)$$

In turn, the $T = 0$ static spin susceptibility can be obtained from the real part of the $\omega \rightarrow 0$ spin-spin spectral function (cf. Sec. 4.7 with \hat{S}_z taken as operator for the spectral function).

The Kondo model is neither restricted to $S = 1/2$ impurities nor to a single electronic band. In fact the exact model for the results by de Haas *et al.* was found only recently to be a $S = 3/2$, three channel model [20] (i.e. the impurity is described by a spin 3/2 object interacting with three electronic bands). However, the role of T_K giving the energy scale at which spin-flip scattering transforms into a many-body singlet, remains also for more complex models as we are investigating in Sec. 6.2.

3.2 Quantum dots

The fast developments in nanotechnology offer the opportunity for completely new applications of quantum impurity physics. In 1998 Goldhaber-Gordon *et al.* [43] managed to measure the Kondo effect in an artificial device, namely a quantum dot. Quantum dots mimic the behaviour of impurities in a lattice in that a tiny structure which is spatially confined such that it has only a few degrees of freedom is still coupled to one or more electronic reservoirs.

This can be achieved, for example, by a thin layer of a semi-conductor on top of a thick layer of a differently doped semi-conductor. This geometry allows for the formation of a two-dimensional electron gas in the thin layer which can be manipulated by additional electrodes etched on the thin layer. By applying a voltage on the electrodes it is possible to deplete certain areas of the underlying electron gas, thereby producing the situation introduced above.

The great advantage of quantum dots is that their physical properties are highly controllable by varying the applied voltages or using different materials and geometries. Quantum dots can be used as single-electron transistors with applications for example in quantum information processing or measuring devices. Moreover, there are realizations of quantum dots where they absorb and emit light, making them highly interesting for optical and photovoltaic applications.

However, it is stressed that these devices can be treated on a theoretical level exactly like quantum impurity models. Their physics is determined by the same intricate interplay of the electrons in the reservoirs with the electrons on the tiny structure. Nowadays, most interest in quantum impurity problems comes from quantum dots and we will sometimes refer to the impurity as dot, but usually stick to the original term impurity.

3.3 Single-impurity Anderson model

A model closely related to the Kondo model is the single-impurity Anderson model (SIAM), introduced by P.W. Anderson [44] to explain the properties of magnetic impurities in metals:

$$\hat{H}_{\text{SIAM}} = \sum_{\sigma} \varepsilon_d \hat{d}_{\sigma}^{\dagger} \hat{d}_{\sigma} + U \hat{d}_{\uparrow}^{\dagger} \hat{d}_{\uparrow} \hat{d}_{\downarrow}^{\dagger} \hat{d}_{\downarrow} + \sum_{k\sigma} V_k \left(\hat{d}_{\sigma}^{\dagger} \hat{c}_{k\sigma} + \hat{c}_{k\sigma}^{\dagger} \hat{d}_{\sigma} \right) + \sum_{k\sigma} \varepsilon_k \hat{c}_{k\sigma}^{\dagger} \hat{c}_{k\sigma}. \quad (3.5)$$

It consists of a single spinful impurity tunnel-coupled to a Fermi sea of spinful electrons. The impurity is described by the operators $\hat{d}_{\sigma}^{\dagger}$ and \hat{d}_{σ} , creating and annihilating an electron on the impurity with spin σ , respectively. Similarly, the operators $\hat{c}_{k\sigma}^{\dagger}$ and $\hat{c}_{k\sigma}$ create or annihilate an electron with momentum k and spin σ in the Fermi sea. The tunnel-coupling is given by the matrix-elements V_k , usually assumed to be momentum-independent, $V_k \equiv V$, resulting in an effective level broadening $\Gamma \equiv \pi\rho|V|^2$, where ρ is the density of states within the energy window of interest in the Fermi sea.

The SIAM is an extension of the Kondo model in that it allows for the impurity to be unoccupied or doubly-occupied, apart from being singly-occupied, but can be exactly

mapped onto the Kondo model in the regime around the particle-hole symmetric point, $\varepsilon_d = -U/2$. This can be achieved by the Schrieffer-Wolff transformation [45], which was originally proposed for the SIAM, but can also be used for more complex Anderson-like models (which then result in more complex Kondo-like models).

Due to the direct correspondence between Kondo model and SIAM the Kondo temperature can be also expressed in terms of the parameters of the SIAM [42]:

$$T_K = \sqrt{\frac{\Gamma U}{2}} \exp\left(\frac{\pi \varepsilon_d (\varepsilon_d + U)}{2\Gamma U}\right), \quad (3.6)$$

defined only in the Kondo regime, $-U \ll \varepsilon_d \ll 0$ (remember that $\varepsilon_F \equiv 0$), with a predominantly singly occupied impurity. The prefactor depends on the exact definition, cf. [26], but these differences are irrelevant as the transition to the Kondo regime is not sharp but continuous and we are only interested in an estimate for the energy scale, cf. Sec. 3.1.

The SIAM is very successful in the description of quantum-impurity models, especially as it can be easily extended to more impurity degrees of freedom or several Fermi seas which can consist of different electronic bands in a metal or spatially separated electronic reservoirs. The latter is easily implemented in artificial quantum dot geometries where one is typically interested in transport properties through the dot from one reservoir to the other.

The extension of the SIAM to several Fermi seas makes it increasingly difficult to find a solution for the problem at hand, e.g. there exists an exact solution of the SIAM using Bethe ansatz [46, 47, 48] which is in general not the case for more complex Anderson-like models. However, methodically, the solution of a multi-lead problem using NRG is not more complicated as for a single lead, but of course the numerical costs increase considerably.

3.4 Fermi sea

In most realizations of quantum impurity problems, the electronic reservoirs consist of the conduction bands of metals (as in the original Kondo problem) or semi-conductors (c.f. the experimental realization of a two-dimensional electron-gas in [49]) at half-filling, with bandwidth $2W$ much larger than all inherent energy scales of the impurity Hamiltonian, typically of the order of several eV or meV for metals and semi-conductors, respectively. Besides, in the context of NRG one always considers only a single branch from the band. The coupling of the Fermi sea to the impurity is determined by the dispersion relation, the density of states ρ and, of course, the strength of the coupling terms in the Hamiltonian, as will be elucidated in Sec. 4.2. These quantities are characteristics of the experimental realization and must be treated as input of the model. However, in the context of NRG one typically makes the following assumptions, which simplify the numerical treatment a lot (see Sec. 4.2 for an explanation).

Generally, we assume that the most relevant contributions for the description of the physical phenomena come from states with energy close to the Fermi energy. This is

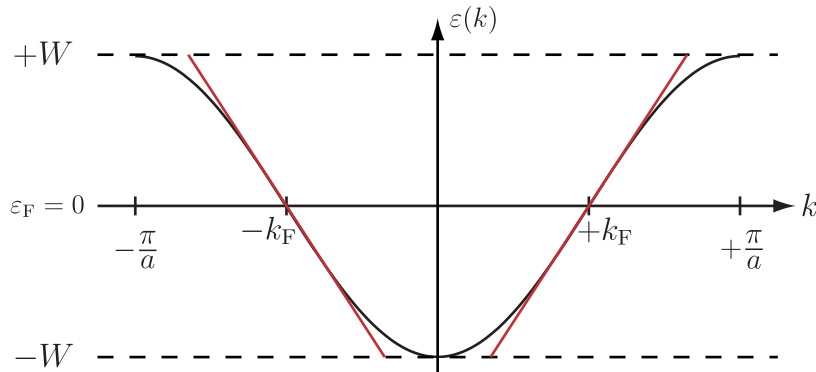


Figure 3.1: Approximations on the band structure of the Fermi sea: the black curve shows the dispersion relation $\varepsilon(k)$ against momentum k . We extrapolate the linearized dispersion relation around the Fermi energy over the full energy band (red lines) and assume a constant density of states.

supported by the fact that all inherent energy scales of the impurity Hamiltonian and its coupling to the Fermi sea are small compared to the bandwidth. Moreover, it turns out that emergent energy scales are also small, for example the Kondo temperature is exponentially small in the coupling of the impurity to the Hamiltonian.

Therefore, it is a reasonable assumption to fully describe the Fermi sea by its properties at the Fermi energy, while taking the wide-band limit, $\varepsilon_k \in [-W, W]$ with $W \gg \{\Gamma, U, T, T_K, B, \dots\}$ (whichever parameters appear in or emerge from the Hamiltonian), cf. Fig. 3.1. Moreover, far from the band-edges the periodicity of the lattice does not play an important role and we may approximate the Bloch states by simple plane waves.

In total, we assume for all our NRG calculations that the energy band consists of a constant density of states with energies between $-W$ and W and corresponding momenta $\pm k$, given by a linear, isotropic dispersion relation. The momentum eigenstates are given in terms of plane waves.

3.5 Anderson orthogonality

In a Fermi liquid, the influence of a local scattering potential on the system can be characterized in terms of the scattering phase shifts: the scattering potential induces a phase shift δ in all the single-particle wave functions dependent on the details and the strength of the scattering potential. This effect has far reaching consequences, in particular in the response of these systems to local perturbations.

3.5.1 Static quantities

Consider two Hamiltonians \hat{H}_i and \hat{H}_f (initial and final, for later convenience) which differ only in the scattering potential the Fermi sea is experiencing. This could be the spin-flip

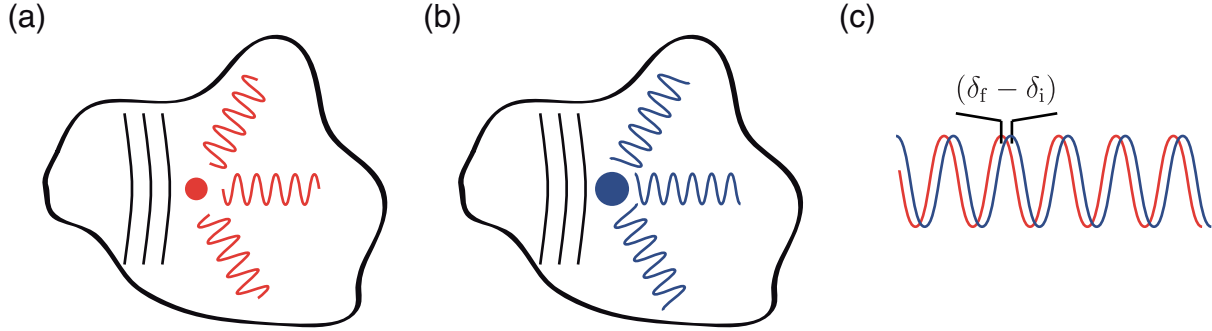


Figure 3.2: Sketch of the single-particle wave functions of the Hamiltonians (a) \hat{H}_i and (b) \hat{H}_f which differ in the strength of the local scattering potential. The different strength of the scattering potential leads to different scattering phase shifts, (c) i.e. the waves are shifted against each other by $(\delta_f - \delta_i)$ which can result in an overlap of scattering states that is decaying with system size.

interaction J in the Kondo model or the hybridization Γ in the SIAM. The ground states of the two Hamiltonians, $|G_i\rangle$ and $|G_f\rangle$, respectively, are orthogonal in the thermodynamic limit, leading to the Anderson orthogonality (AO) catastrophe [16]. However, for finite systems their overlap scales with the total particle number N (and hence with the system size) like [16, 28]

$$|\langle G_i | G_f \rangle| \sim N^{-\frac{1}{2} \Delta_{\text{AO}}^2}, \quad (3.7)$$

with the AO exponent Δ_{AO} characterizing the degree of orthogonality. Anderson showed that this exponent is equal to the change in scattering phase shifts at the Fermi surface in reaction to the change in the scattering potential:

$$\Delta_{\text{AO}} = \Delta_{\text{ph}} = [\delta_f(\varepsilon_{\text{F}}) - \delta_i(\varepsilon_{\text{F}})]/\pi. \quad (3.8)$$

This connection can be easily motivated in terms of elementary scattering theory, see Fig. 3.2: due to the different scattering phase shifts the single-particle wave functions of \hat{H}_i and \hat{H}_f with momentum k will have an overlap of smaller than 1 when integrated over the spatial interval $2\pi/k$. Thus, the overlap is exponentially decaying with the system size.

The actual sign of Δ_{AO} relative to Δ_{ph} (plus not minus) does not influence physical properties - cf. Eq. (3.7) where Δ_{AO} enters quadratically - and follows standard convention. (However, in later context it turns out to be necessary to have some convention, as will be elucidated in Sec. 6.2.)

In the following, we will call positive (negative) phase shifts attractive (repulsive), as motivated by the following connection: Exploiting Friedel's sum rule [24], we relate the difference in phase shifts to the so called *displaced charge* Δ_{ch} via $\Delta_{\text{ch}} = \Delta_{\text{ph}}$. Here the positive (negative) displaced charge Δ_{ch} is defined as the charge in units of e (i.e. the number of electrons) flowing inward from (outward to) infinity into a region of large but finite volume, say V_{large} , surrounding the dot, upon switching from \hat{H}_i to \hat{H}_f :

$$\Delta_{\text{ch}} \equiv \langle G_f | \hat{n}_{\text{tot}} | G_f \rangle - \langle G_i | \hat{n}_{\text{tot}} | G_i \rangle. \quad (3.9)$$

Here $\hat{n}_{\text{tot}} \equiv \hat{n}_{\text{sea}} + \hat{n}_{\text{dot}}$, where \hat{n}_{sea} is the total number of Fermi sea electrons within V_{large} , whereas \hat{n}_{dot} is the local charge of the dot. Hence a positive (negative) phase shift corresponds to a positive (negative) value of Δ_{ch} , i.e. charge is attracted from (repelled towards) ∞ .

Another important consequence of Eq. (3.7) is that it not only affects the ground state overlap, but also matrix elements of the form $|\langle G_f | \hat{O} | G_i \rangle|$, where \hat{O} is a local operator acting at the site of the localized potential. These matrix elements necessarily also vanish in the thermodynamic limit.

Although in the original formulation of Anderson local interactions (like the Coulomb repulsion U in the SIAM) were not included [16], his prediction Eq. (3.7) still applies, provided the ground states $|G_i\rangle$ and $|G_f\rangle$ describe Fermi liquids (as is the case for Anderson-like models but not, for example, for the symmetric two-channel Kondo model).

In our first publication concerning AO (see Sec. 6.1) we show how all these quantities can be calculated consistently within the NRG. Our focus there lies on the technical details for such calculations and that AO is present even in rather complicated models yet easily accessible within the NRG.

3.5.2 Dynamical quantities after a quantum quench

All quantities related to AO so far (Δ_{AO} , Δ_{ph} , Δ_{ch}) are *static* properties of the system, emerging from the ground states of the Hamiltonians \hat{H}_i to \hat{H}_f . However, AO also leaves its fingerprint in *dynamical* quantities as has already been observed at the time of Anderson's derivation: the Fermi edge singularity [27, 28, 29, 30], the Altshuler-Aronov zero bias anomaly [50] in disordered conductors, tunnelling into strongly interacting Luttinger liquids [51, 52, 53, 54], and optical absorption involving a Kondo exciton [5, 6, 7], where photon absorption induces a local quantum quench, to name but a few.

For all of these, the low-temperature dynamics is governed by the response of the Fermi sea to a sudden switch of a local scattering potential. A prime example for this effect is the creation of a Kondo exciton by optical absorption: a system consisting of an Anderson like model plus a fully occupied valence band level. The optical absorption process causes an electron of the valence band level to be excited onto the dot level, thereby together with its respective hole forming an exciton. The physical behaviour of this excited state can be effectively described under the assumption that (i) the deep hole and the electrons on the dot are essentially decoupled apart from the exciton binding energy $U_{\text{exc}} > 0$ and (ii) we may neglect the time-evolution of the hole. Moreover, by allowing the electron to hybridize with its adjacent Fermi sea, Kondo physics emerges. Then, the Hamiltonian can be written in block structure, depending on the presence or absence of a hole:

$$\begin{pmatrix} |0\rangle_{\text{vb}} & |1\rangle_{\text{vb}} \\ \hat{H}_i & 0 \\ 0 & \hat{H}_f \end{pmatrix}, \quad (3.10)$$

where $|0\rangle_{\text{vb}}$ and $|1\rangle_{\text{vb}}$ represent the presence of no hole or hole in the valence band level, respectively. We show no spin-dependence (while it is implicitly included) as there is no

magnetic field, and initially no hole in the valence band is assumed. The Hamiltonians \hat{H}_i and \hat{H}_f describing dot and Fermi sea differ only in that the dot level of the latter is reduced by the exciton binding energy U_{exc} [5]:

$$\hat{H}_i = \hat{H}_{\text{SIAM}}(\varepsilon_d) \quad (3.11a)$$

$$\hat{H}_f = \hat{H}_{\text{SIAM}}(\varepsilon_d - U_{\text{exc}}). \quad (3.11b)$$

Thus, optical absorption related to the creation of a Kondo exciton at zero temperature can be described as outlined below. For finite temperature, the system is initially not in the ground state, but described by the thermal density matrix given by the Boltzmann weights. However, for small temperatures the AO-related physics still survives with temperature serving as an infrared cutoff [6]. For $T = 0$ we find:

(1) Initially, the system is described by the Hamiltonian \hat{H}_i and is fully equilibrated, i.e. given by the ground state $|G_i\rangle$ of \hat{H}_i .

(2) At time $t = 0$ the absorption of the photon induces two effects: (i) an electron is excited onto the dot level of the SIAM (with spin σ depending on the polarization of the light) and the state at $t = 0$ is projected into

$$|\psi_i\rangle = \hat{d}_\sigma^\dagger |G_i\rangle. \quad (3.12)$$

Additionally, (ii) the Hamiltonian for the dot and Fermi sea is switched from \hat{H}_i to \hat{H}_f into a different sector in Hilbert space, causing an altered time-evolution.

(3) The dynamics after the sudden change in potential can be characterized by the correlator

$$\mathcal{G}(t) \equiv -i\theta(t)\langle G_i | \hat{d}_\sigma(t) \hat{d}_\sigma^\dagger | G_i \rangle, \quad (3.13)$$

with the *mixed* time-evolution

$$\hat{d}_\sigma(t) = e^{i\hat{H}_i t} \hat{d}_\sigma e^{-i\hat{H}_f t}, \quad (3.14)$$

reflecting the fact that \hat{d}_σ switches \hat{H}_f to \hat{H}_i when the electron settles back into the valence band level. This, however, can be easily also seen as a regular time-evolution for $\hat{d}_\sigma(t)$ with Hamiltonian

$$\hat{H} = |0\rangle_{\text{vb vb}} \langle 0| \otimes \hat{H}_i + |1\rangle_{\text{vb vb}} \langle 1| \otimes \hat{H}_f, \quad (3.15)$$

which in the expectation value of Eq. (3.13) consistently reduces to Eq. (3.14). In the context of optical absorption this results in the investigation of the corresponding spectral function:

$$\mathcal{A}(\omega) \equiv -\frac{1}{\pi} \Im \left(\int_0^\infty dt e^{i(\omega+i0^+)t} \mathcal{G}(t) \right). \quad (3.16)$$

(4) The point where AO shows up is in the long-time (low-frequency) limit: the time-evolution of the state $|\psi_i\rangle$, $|\psi(t)\rangle = \exp(-i\hat{H}_f t)|\psi_i\rangle$ will asymptotically approach the state

$|G_f\rangle$ or, more generally, the lowest-lying eigenstate $|\psi_f\rangle$ of \hat{H}_f with non-zero overlap to $|\psi_i\rangle$. Hence, with increasing time the Fermi sea feels ever more the changed scattering potential which leads to an increasing suppression of the matrix elements in Eq. (3.13) (by inserting a complete basis for \hat{H}_f), and thus [28, 29]:

$$\mathcal{G}(t) \sim t^{-\Delta_{\text{AO}}^2}, \quad (3.17)$$

for $t \rightarrow \infty$, while the corresponding spectral function behaves for $\omega \rightarrow 0$ like:

$$\mathcal{A}(\omega) \sim \omega^{-1+\Delta_{\text{AO}}^2}. \quad (3.18)$$

Thus, the presence of AO drastically changes the behaviour of spectral functions in the low-frequency regime, showing power-law behaviour with possible divergence instead of the usual smooth spectral dependence across $\omega = 0$ at zero temperature, cf. Sec. 3.1.

The details of the influence of AO on dynamical quantities are subject to our second publication on AO (see Sec. 6.2) where we clarify the relation between AO and spectral functions in more complex settings. In particular, we investigate the importance of AO for the phenomenon of population switching, see next section for an introduction.

3.6 Population switching in quantum dots

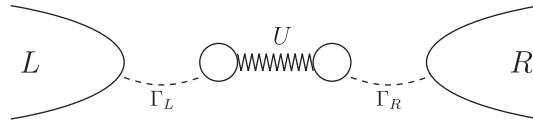


Figure 3.3: Cartoon of the Hamiltonian (3.19) for the asymmetric SIAM.

A further concrete motivation for our study of AO related quantities is to develop a convenient tool for calculating AO exponents for quantum dot models that display the phenomenon of population switching (PS) [8, 9, 10, 11, 12, 13, 14, 15]. In such models, a quantum dot tunnel-coupled to leads contains levels of different widths, and is capacitively coupled to a gate voltage that shifts the level energies relative to the Fermi level of the leads. Under suitable conditions, an (adiabatic) sweep of the gate voltage induces an inversion in the population of these levels (a so-called population switch), implying a change in the local potential seen by the Fermi seas in the leads.

This already indicates that AO plays an important role here, as the Fermi seas have to adjust to two different situations on the dot levels. To be more concrete we will use the *spinless* two-level model for which Goldstein, Berkovits and Gefen (GBG) have shown [14, 15] that PS will always be continuous as function of the level position:

$$\begin{aligned} \hat{H} &= \sum_{\alpha} \varepsilon_d \hat{d}_{\alpha}^{\dagger} \hat{d}_{\alpha} + U \hat{d}_L^{\dagger} \hat{d}_L \hat{d}_R^{\dagger} \hat{d}_R \\ &+ \sum_{k\alpha} \varepsilon_k \hat{c}_{k\alpha}^{\dagger} \hat{c}_{k\alpha} + \sum_{\alpha} \sqrt{\frac{2\Gamma_{\alpha}}{\pi}} \sum_k (\hat{d}_{\alpha}^{\dagger} \hat{c}_{k\alpha} + \hat{c}_{k\alpha}^{\dagger} \hat{d}_{\alpha}), \end{aligned} \quad (3.19)$$

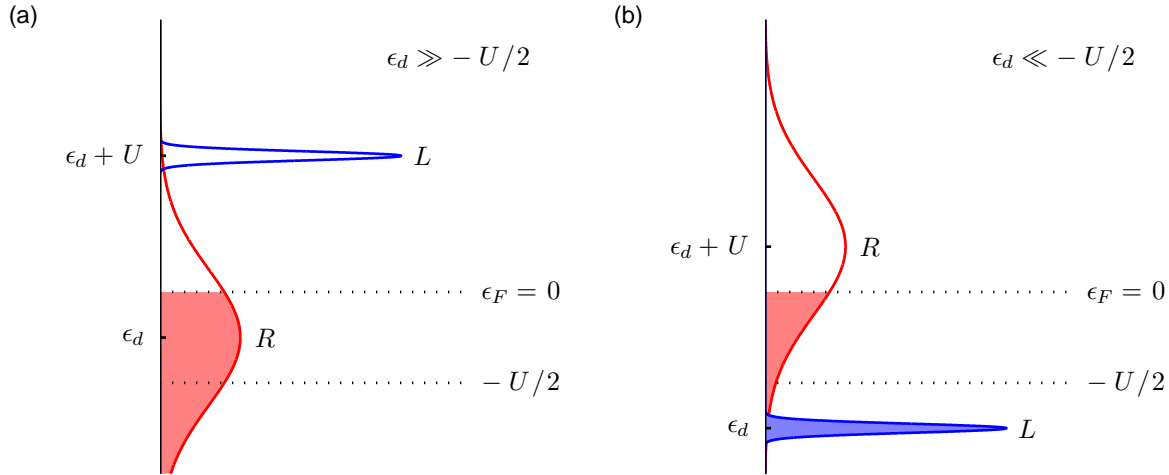


Figure 3.4: Sketch of the filling fraction of the two levels from the Hamiltonian 3.19 for (a) $\epsilon_d \gg -U/2$ and (b) $\epsilon_d \ll -U/2$. In the first case we see that left level is not filled as its level energy is pushed well above the Fermi energy by the right level. However, when ϵ_d is lowered below the particle-hole symmetric point the situation is reversed, the now completely filled left level pushing the right level upwards.

where α runs over the pseudo-spin index L and R for left and right system, respectively (i.e. we have a SIAM where physical spin is replaced by a pseudo-spin representing left and right). PS becomes visible if the coupling of the dot levels to their respective Fermi seas is (highly) asymmetric, i.e. we have $\Gamma_R \gg \Gamma_L$.

Based on this setup, PS is conceptually easily explained, see Fig. 3.4: for $\epsilon_d \gg -U/2$ (i.e. far above the particle-hole symmetric point) only the right level with the larger hybridization will be populated while the hybridization of the left level is too small that it could be populated. Thus, effectively, the left level is pushed upwards by the Coulomb repulsion U due to the right level being occupied (this situation is henceforth called 01 for left level unoccupied and right level occupied). However, as ϵ_d is lowered below the particle-hole symmetric point it becomes energetically more favourable for the system to populate the left level due to its lower kinetic energy. Therefore, the left level becomes (nearly) completely occupied while the right level is pushed upwards by U and its occupation drops down (henceforth called 10). This transition, however, is smooth and continuous in ϵ_d [14, 15].

It is natural that AO plays a role in this behaviour: as we have seen in the previous section, the occupation on the dot makes a clear difference for the Fermi seas as a different occupation comes along with a different scattering potential. Therefore, when we compare the occupations 01 and 10 we find two AO factors, one for each Fermi sea. Thus, it is reasonable to assume that the scale (with respect to ϵ_d) over which PS takes place will be connected to AO. A larger value of Δ_{AO} will decrease this scale because it will suppress transitions between the occupations 10 and 01 more strongly. However, as GBG have

shown there is no choice of parameters such that AO will be so strong that this scale is reduced to zero, i.e. such that PS will be abrupt at the particle-hole symmetric point.

In Sec. 6.2 we will investigate PS for this model in more detail and show how AO is related to the scale over which the PS takes place. Further, we will build on the idea of GBG to increase the AO factor between the occupations 10 and 01 by adding another Fermi sea which only couples to the left level and eventually increases the influence of AO such that the population switch becomes abrupt.

Chapter 4

Numerical renormalization group (NRG)

The numerical renormalization group is tailored to solve quantum impurity models as introduced in the previous section. Here we will give an introduction to the method and how it has evolved since its introduction for the solution of the Kondo problem in 1975 [2]. Thereby, we will focus on fermionic applications (or more precisely electronic applications), while generalizations to Bosons exist [55, 56]. Nowadays, it is possible to calculate dynamic quantities like spectral functions, absorption and emission spectra and transport properties with high accuracy. A good overview over basic NRG techniques can be found in Krishnamurthy *et al.* [22] and the review of Bulla *et al.* [23], which we will follow in the next sections as well as the dissertation by Theresa Hecht [57], where some of the figures have been adapted from.

If the reader is only interested in a general overview about the method as used in the later parts of this thesis, we advise to skip Sec. 4.2. However, for a deeper understanding of the method it is instructive to also read the details given there.

4.1 Hamiltonian

The general class of Hamiltonians solvable with NRG can be written in the following simple form:

$$\hat{H} = \hat{H}_{\text{imp}} + \hat{H}_{\text{imp-sea}} + \hat{H}_{\text{sea}} , \quad (4.1)$$

with

$$\hat{H}_{\text{sea}} = \sum_{\mu=1}^{n_c} \sum_k \varepsilon_{k\mu} \hat{c}_{k\mu}^\dagger \hat{c}_{k\mu} , \quad (4.2)$$

describing a free Fermi sea involving $\mu = 1, \dots, n_c$ species of electrons, generally representing different reservoirs but also different spin and other electron flavour (e.g. for one

spinful electronic reservoir $\mu = \uparrow, \downarrow$). An electron of species μ with energy $\varepsilon_{k\mu}$ is created and annihilated by $\hat{c}_{k\mu}^\dagger$ and $\hat{c}_{k\mu}$, respectively. As elucidated in Sec. 3.4, all energies lie in the interval $[-W, W]$, with a constant density of states and the Fermi energy in the middle of the band, $\varepsilon_F \equiv 0$, assuming the same band structure for all electronic species. Henceforth, we choose the half-bandwidth $W \equiv 1$ as the unit of energy.

The impurity degrees of freedom are described by \hat{H}_{imp} , which is not restricted in any way. The connection between impurity and the Fermi sea is contained in $\hat{H}_{\text{imp-sea}}$, restricted only in that for a band as in Sec. 3.4 it may only involve the local operators $\hat{f}_{0\mu} = \frac{1}{\mathcal{N}} \sum_k \hat{c}_{k\mu}$ (\mathcal{N} being a normalization constant) and $\hat{f}_{0\mu}^\dagger$ that annihilate or create a Fermi sea electron of species μ at the position of the impurity, i.e. at position $\vec{r} = 0$.¹ In particular, this means that any hybridization term needs to be momentum-independent. However, this is not a crucial simplification (cf. section D. Universality in [22]) and still allows for the treatment of a wide range of models.

We will see that the presence of a hybridization term is crucial in the following derivation. However, it is possible to calculate models where no particle transfer between the impurity and the Fermi sea takes place. This is achieved by a hybridization term whose amplitude goes to zero after the mapping.

Single-impurity Anderson model

For simplicity, we will show the mapping from the electronic band onto the Wilson chain for the single-impurity Anderson model (SIAM, see Sec. 3.3), where a single spinful impurity level is coupled to an electronic reservoir:

$$\hat{H}_{\text{imp}} = \sum_{\sigma} \varepsilon_d \hat{d}_{\sigma}^{\dagger} \hat{d}_{\sigma} + U \hat{d}_{\uparrow}^{\dagger} \hat{d}_{\uparrow} \hat{d}_{\downarrow}^{\dagger} \hat{d}_{\downarrow} \quad (4.3a)$$

$$\hat{H}_{\text{imp-sea}} = \sum_{k\sigma} V_k \left(\hat{d}_{\sigma}^{\dagger} \hat{c}_{k\sigma} + \hat{c}_{k\sigma}^{\dagger} \hat{d}_{\sigma} \right) \quad (4.3b)$$

$$\hat{H}_{\text{sea}} = \sum_{k\sigma} \varepsilon_k \hat{c}_{k\sigma}^{\dagger} \hat{c}_{k\sigma}, \quad (4.3c)$$

with $\sigma = \uparrow, \downarrow$ replacing μ . The impurity level is described by \hat{d}_{σ} and $\hat{d}_{\sigma}^{\dagger}$, annihilating and creating an electron with spin σ on the impurity, respectively. The Coulomb repulsion between the electrons on the impurity is given by U and the impurity is coupled to the Fermi sea via a k -dependent hybridization V_k . For pedagogical reasons, we will use a general dispersion relation, density of states and hybridization. The mapping of the electronic band for the SIAM is easily generalized to the Hamiltonian in Eq. (4.1) as will be apparent below.

¹The reason for $\hat{f}_{0\mu}^\dagger$ creating a Fermi sea electron at location $\vec{r} = 0$ is that the electrons in the Fermi sea are given in terms of plain waves and thus the sum over k in $\hat{f}_{0\mu}^\dagger$ is equivalent to a Fourier transform with argument $\vec{r} = 0$.

4.2 From the electronic band to the Wilson chain

The mapping from the electronic band to the Wilson chain in the SIAM is determined by the hybridization function $\Delta(\omega)$:

$$\Delta(\omega) = \pi \sum_k V_k^2 \delta(\omega - \varepsilon_k). \quad (4.4)$$

By definition, it completely determines the action of the Fermi sea onto the dot. In particular, for a constant density of states ρ and k -independent hybridization V , it takes the simple form:

$$\Delta_0 = \pi \rho V^2, \quad (4.5)$$

i.e. the influence of the Fermi sea onto the impurity is completely determined by the product ρV^2 , which is the only physical parameter in that case (apart from the impurity contributions).

Any reformulations of the Hamiltonian which leave $\Delta(\omega)$ invariant still represent the same physics. We choose to rewrite the Hamiltonian in a one-dimensional energy representation (which also resembles the derivation in Krishna-murthy *et al.* [22]):

$$\hat{H} = \hat{H}_{\text{imp}} + \sum_{\sigma} \int_{-1}^1 d\varepsilon g(\varepsilon) \hat{a}_{\varepsilon\sigma}^{\dagger} \hat{a}_{\varepsilon\sigma} + \sum_{\sigma} \int_{-1}^1 d\varepsilon h(\varepsilon) (\hat{d}_{\sigma}^{\dagger} \hat{a}_{\varepsilon\sigma} + \hat{a}_{\varepsilon\sigma}^{\dagger} \hat{d}_{\sigma}), \quad (4.6)$$

with dispersion $g(\varepsilon)$, hybridization $h(\varepsilon)$ and fermionic operators $\hat{a}_{\varepsilon\sigma}$ and $\hat{a}_{\varepsilon\sigma}^{\dagger}$. It has been shown [58] that using the inverse of the dispersion $\varepsilon(\omega)$, defined as $g(\varepsilon(\omega)) = \omega$,

$$\Delta(\omega) = \pi \frac{d\varepsilon(\omega)}{d\omega} h^2(\varepsilon(\omega)) \quad (4.7)$$

which is crucial in the following derivation because it means that one may choose either $g(\varepsilon)$ or $h(\varepsilon)$ without restrictions while still leaving $\Delta(\omega)$ invariant. The functions $g(\varepsilon)$ and $h(\varepsilon)$ are determined by the original dispersion relation ε_k , the density of states ρ and the hybridization V_k .

4.2.1 Logarithmic discretization

For a numerical treatment it is necessary to discretize the energy band to obtain a finite description. To this end Wilson [2] introduced a parameter $\Lambda > 1$ which defines the intervals

$$\pm [\Lambda^n, \Lambda^{n+1}) \quad n = 0, 1, 2, \dots, \quad (4.8)$$

with width $d_n = \Lambda^{-n}(1 - \Lambda^{-1})$. These divide the energy band with increasing resolution towards the Fermi energy. The Fourier expansion of the operators $\hat{a}_{\varepsilon\sigma}$ within these intervals reads as (see [23] for more details):

$$\hat{a}_{\varepsilon\sigma} = \sum_{np} (\hat{a}_{np\sigma} \psi_{np}^+(\varepsilon) + \hat{b}_{np\sigma} \psi_{np}^-(\varepsilon)), \quad (4.9)$$

where the operators $\hat{a}_{np\sigma}$ and $\hat{b}_{np\sigma}$ fulfil standard fermionic commutation relations. The Fourier modes

$$\psi_{np}^{\pm}(\varepsilon) = \begin{cases} \frac{1}{\sqrt{d_n}} e^{\pm i\omega_n p \varepsilon} & \varepsilon \in \pm [\Lambda^n, \Lambda^{n+1}] \\ 0 & \varepsilon \notin \pm [\Lambda^n, \Lambda^{n+1}] \end{cases}, \quad (4.10)$$

are defined via the fundamental frequencies $\omega_n = \frac{2\pi}{d_n}$, while p labels the harmonics. In particular, $p = 0$ represents a constant function within the respective interval.

Representing the Hamiltonian in Eq. (4.6) in this basis, we make the first essential simplification: if we choose $h(\varepsilon)$ to be constant within each interval, the impurity will couple to the $p = 0$ modes only. In particular, this is achieved by a constant hybridization function Δ_0 . However, this is also possible for a non-constant $\Delta(\omega)$ as all ω -dependence can be shifted into $g(\varepsilon)$, i.e. in deriving the Hamiltonian Eq. (4.6) for general $\Delta(\omega)$ one transforms the electronic basis such that it has a simpler form of the hybridization, shifting any complexities into $g(\varepsilon)$.²

Based on this choice, we make an approximation on the conduction electron term in Eq. (4.6): we drop the contributions of the $p \neq 0$ terms. This is supported by the fact that these states are only indirectly coupled to the impurity via their coupling to the $p = 0$ states and that this coupling is small compared to the coupling between the impurity and the $p = 0$ states. Consequently, one may treat this indirect coupling as a perturbation, neglected in 0th order [2]. Thus, we obtain the logarithmically discretized Hamiltonian

$$\begin{aligned} \hat{H} &= \hat{H}_{\text{imp}} + \sum_{n\sigma} (\xi_n^+ \hat{a}_{n\sigma}^\dagger \hat{a}_{n\sigma} + \xi_n^- \hat{b}_{n\sigma}^\dagger \hat{b}_{n\sigma}) \\ &+ \frac{1}{\sqrt{\pi}} \sum_{\sigma} \hat{d}_{\sigma}^\dagger \sum_n (\gamma_n^+ \hat{a}_{n\sigma} + \gamma_n^- \hat{b}_{n\sigma}) + \text{h.c.}, \end{aligned} \quad (4.11)$$

where we dropped the index $p = 0$ for convenience. The factors ξ_n^{\pm} and γ_n^{\pm} are derived from $\Delta(\omega)$ in the respective intervals.

For a constant hybridization function Δ_0 the couplings γ_n^{\pm} are equal to $\sqrt{d_n \Delta_0}$, i.e. they become exponentially small according to their supporting energy interval. Approximating the logarithmic discretization with the $p = 0$ states means that we obtain an increasing density of states towards the Fermi energy, while the couplings γ_n^{\pm} decrease accordingly. For a non-constant hybridization function the argument is similar in that the couplings have to allow for the changed density of states, but with more complex expressions for γ_n^{\pm} .

So far, the only approximation is that we neglect the $p \neq 0$ terms in Eq. (4.11) due to their indirect coupling to the impurity. However, in principle, this becomes exact in the limit $\Lambda \rightarrow 1$. Moreover, we still allow for a general dispersion relation, density of states and hybridization, which determine the functional form of $g(\varepsilon)$ such that $\Delta(\omega)$ is unchanged.

²This is not possible for a constant density of states and linear dispersion relation and we need to choose $V_k \equiv V$ to decouple the $p \neq 0$ terms. Therefore the restriction of $\hat{H}_{\text{imp-sea}}$ in Sec. 4.1.

4.2.2 Mapping to the Wilson chain

Investigating the Hamiltonian in Eq. (4.11) immediately shows how it can be mapped onto the semi-infinite Wilson chain. The first site is given by the impurity and it directly follows that the next site must be given by

$$\hat{f}_{0\sigma} = \frac{1}{\sqrt{\xi_0}} \sum_n (\gamma_n^+ \hat{a}_{n\sigma} + \gamma_n^- \hat{b}_{n\sigma}), \quad (4.12)$$

because it contains all terms of Eq. (4.11) which couple to the impurity. The normalization factor turns out to be

$$\xi_0 = \int_{-1}^1 d\varepsilon \Delta(\varepsilon). \quad (4.13)$$

For a constant hybridization function Δ_0 this operator is equal to the annihilation operator of an electron in the Fermi sea at $\vec{r} = 0$. This can be seen from $\gamma_n^\pm = \sqrt{d_n \Delta_0}$ and $\xi_0 = 2\Delta_0$, in this case, and inserting the inverse transformation to Eq. (4.9) into Eq. (4.12). Going back from energy to momentum space yields the desired result, cf. Sec. 4.1. If the hybridization function is not constant, the operator still annihilates an electron in a small shell around $\vec{r} = 0$, if not exactly at $\vec{r} = 0$.

Starting from the operator $\hat{f}_{0\sigma}^{(\dagger)}$, we need to find a new set of mutually orthogonal single-particle states described by the operators $\hat{f}_{n\sigma}^{(\dagger)}$ from $\hat{a}_{n\sigma}^{(\dagger)}$ and $\hat{b}_{n\sigma}^{(\dagger)}$, which is achieved by a standard tridiagonalization technique (e.g. the Lanczos algorithm). In this basis we obtain the chain Hamiltonian

$$\begin{aligned} \hat{H} &= \hat{H}_{\text{imp}} + \sqrt{\frac{\xi_0}{\pi}} \sum_{\sigma} (\hat{d}_{\sigma}^{\dagger} \hat{f}_{0\sigma} + \hat{f}_{0\sigma}^{\dagger} \hat{d}_{\sigma}) \\ &+ \sum_{\sigma n=0}^{\infty} (\varepsilon_n \hat{f}_{n\sigma}^{\dagger} \hat{f}_{n\sigma} + t_n (\hat{f}_{n\sigma}^{\dagger} \hat{f}_{n+1\sigma} + \hat{f}_{n+1\sigma}^{\dagger} \hat{f}_{n\sigma})). \end{aligned} \quad (4.14)$$

The new set of operators is given by an orthogonal transformation in terms of the operators $\hat{a}_{n\sigma}^{(\dagger)}$, $\hat{b}_{n\sigma}^{(\dagger)}$ and the parameters ε_n and t_n are given by a recursion relation with input parameters ξ_n^\pm and γ_n^\pm , see [23] for details. It is crucially important for the NRG that the t_n decrease exponentially for large n like $\Lambda^{-\frac{n}{2}}$. Moreover, it should be noted that $\varepsilon_n = 0$ for all n if $\Delta(\omega) = \Delta(-\omega)$.

The sites of the Wilson chain representing the electronic band possess an important and enlightening physical meaning in the original model. In particular, one should keep in mind that the one-dimensional structure of the Wilson chain is not related to the dimensionality of the original model. As already elucidated above, the operator $\hat{f}_{0\sigma}^{(\dagger)}$ is connected to wave functions with maximal amplitude at or close to the position of the impurity. Analogously, the operators $\hat{f}_{n\sigma}^{(\dagger)}$ can be seen as a series of spherical shells centered around the impurity with inner radius $\Lambda^{\frac{n-1}{2}}$ and outer radius $\Lambda^{\frac{n}{2}}$ (s-wave approximation). Apart from small tails the wave function of the states is non-zero only in their respective shell.

The derivation of the Hamiltonian Eq. (4.14) from Eq. (4.11) did not include any further approximations. However, for general dispersion relation, density of states and hybridization the transformation onto the operators $\hat{f}_{n\sigma}^{(\dagger)}$, ε_n and t_n must be carefully determined numerically.

4.2.3 Wilson chain in the original form

For a constant hybridization function $\Delta_0 \equiv \Gamma$ the mapping can be solved analytically and we obtain the Wilson chain as given by Wilson [2]:

$$\begin{aligned} \hat{H} = & \hat{H}_{\text{imp}} + \sum_{\sigma} \sqrt{\frac{2\Gamma}{\pi}} (\hat{d}_{\sigma}^{\dagger} \hat{f}_{0\sigma} + \hat{f}_{0\sigma}^{\dagger} \hat{d}_{\sigma}) \\ & + \frac{1}{2} (1 + \Lambda^{-1}) \sum_{\mu} \sum_{n=0}^{\infty} \xi_n \Lambda^{-\frac{n}{2}} (\hat{f}_{n\mu}^{\dagger} \hat{f}_{n+1\mu} + \hat{f}_{n+1\mu}^{\dagger} \hat{f}_{n\mu}), \end{aligned} \quad (4.15)$$

where

$$\xi_n \equiv \frac{1 - \Lambda^{-n-1}}{\sqrt{1 - \Lambda^{-2n-1}} \sqrt{1 - \Lambda^{-2n-3}}} \quad (4.16)$$

with $\lim_{n \rightarrow \infty} \xi_n = 1$. Thus,

$$\begin{aligned} t_n & \equiv \frac{1}{2} (1 + \Lambda^{-1}) \xi_n \Lambda^{-\frac{n}{2}} \\ & \sim \Lambda^{-\frac{n}{2}} \quad n \gg 0. \end{aligned} \quad (4.17)$$

One always needs the logarithmic discretization because it is the reason for the exponential decrease of the couplings t_n . While the exact values of the latter have changed, see Sec. 4.2.4, the form of the coupling in Eq. (4.15) is still a good guide to understand the details of the mapping.

4.2.4 Improved discretization scheme

The influence of the artificial discreteness in energy space can be reduced by using ‘‘z-averaging’’ [59]. One introduces a new parameter z in the interval $(0, 1]$ which shifts the discretization points to ε_n^z with

$$\begin{aligned} \varepsilon_1^z & = 1 \\ \varepsilon_n^z & = \Lambda^{2-n-z} \quad n = 2, \dots \end{aligned} \quad (4.18)$$

Averaging of the final results over a uniformly distributed choice of N_z z -values in $(0, 1]$ yields much smoother results in many ways. While for each choice of z a new calculation has to be made as all couplings are changed, in this way more data points are produced. This is particularly important in the calculation of spectral functions, see Sec. 4.8, where

it reduces certain oscillations with frequency Λ . It must be stressed that even for infinitely large N_z one does not reach the continuum limit.

It was observed early on that the hybridization function $\Delta(\omega)$ is systematically underestimated in the final form of the Wilson chain due the representation of logarithmically defined intervals, each represented by only a single state (cf. the A_Λ -factor in Eq. (5.20) in [22]). The problem is explained in detail in [60] where also a slightly altered logarithmic discretization is proposed. This idea has been further developed in [61] and we use this implementation in our numerical work.

However, the qualitative picture presented above remains the same: the interpretation of the first Wilson site is the same as well as the large n scaling. There are only minor yet important differences in the t_n of the first ~ 10 Wilson sites.

4.3 Key points of the Wilson chain mapping

In the following we give a summary of the most important points of the mapping to the Wilson chain as used throughout this thesis for the Hamiltonian as described in Sec. 4.1, see Fig. 4.1 for a pictorial view. We assume a linear dispersion relation, constant density of states ρ and, if present, constant hybridization. The Fermi sea of the original model is represented in terms of the semi-infinite Wilson chain:

$$\hat{H} = \hat{H}_{\text{imp}} + \hat{H}_{\text{imp-sea}} + \sum_{\mu=1}^{n_c} \sum_{n=0}^{\infty} t_n (f_{n\mu}^\dagger \hat{f}_{n+1\mu} + \hat{f}_{n+1\mu}^\dagger f_{n\mu}), \quad (4.19)$$

where

$$t_n \sim \Lambda^{-\frac{n+1}{2}} \quad n \gg 0, \quad (4.20)$$

i.e. the couplings fall off exponentially for large n . We reintroduced the general index μ and replaced the hybridization part by the general form $\hat{H}_{\text{imp-sea}}$, which may only contain terms including $\hat{f}_{0\mu}^{(\dagger)}$. For this form of the Hamiltonian it is important that all electron species are mapped in exactly the same way and the individual Wilson sites are constituted from all species at once, i.e. all electron species together form a single Wilson chain. Therefore, a single Wilson site n consists of n_c fermionic degrees of freedom, forming a site Hilbert space with dimension $d = 2^{n_c}$ and basis $|\sigma_n\rangle$.

For example, in the single-impurity Anderson model we have a dimension of 4 due to one spinful reservoir, hence $n_c = 2$. The basis states are $|\sigma_n\rangle = \{|0\rangle, |\uparrow\rangle, |\downarrow\rangle, |\uparrow\downarrow\rangle\}$, representing an unoccupied, singly (with spin up or down) or doubly occupied Wilson site.

For a model where each impurity degree of freedom couples to its own Fermi sea channel with constant hybridization function $\Gamma_\mu = \pi\rho V_\mu^2$ (as for the SIAM with $\mu = \sigma$) the hybridization term has the form

$$\sum_{\mu} \sqrt{\frac{2\Gamma_\mu}{\pi}} (\hat{d}_\mu^\dagger \hat{f}_{0\mu} + \hat{f}_{0\mu}^\dagger \hat{d}_\mu), \quad (4.21)$$

where the generalization to other couplings is easily implemented.

In the course of the mapping the energy band is logarithmically discretized with discretization parameter Λ , where the mapping is exact in the limit $\Lambda \rightarrow 1$. However, as we will show in the next section, Λ must not be too small for the numerical solution using NRG. In practice, Λ is varied between 1.5 and 3 as a compromise between methodical and numerical error.

The first site of the Wilson chain represents electronic wave functions in the direct vicinity of the impurity and is the only one directly coupled to it. The remainder of the Wilson chain consists of a nearest-neighbour hopping chain with exponentially decreasing hopping elements. Because of this separation of energy scales, the Hamiltonian can be

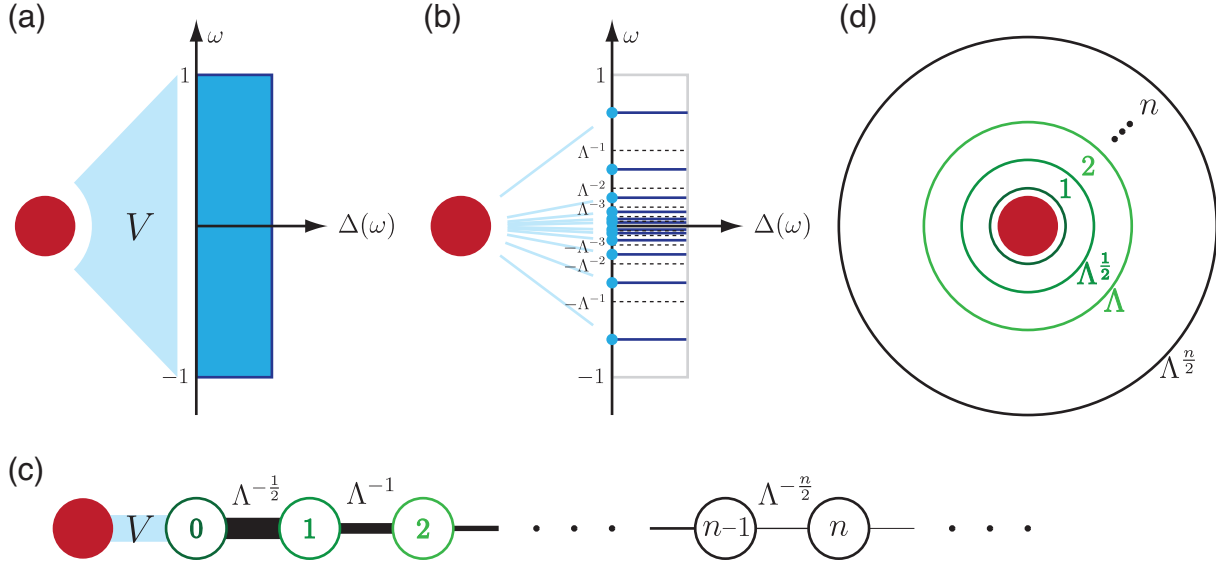


Figure 4.1: Sketch of the key points of the mapping to the Wilson chain for constant hybridization V and, thus, constant hybridization function $\Delta(\omega)$. Panel (a) shows the initial model where the impurity (red) is coupled by V (light blue) to the Fermi sea (dark blue) with constant hybridization function. In panel (b) the energy band has been logarithmically discretized with $\Lambda = 2$ and each interval is represented by a single state (dark blue circles) which give rise to the same hybridization function due to the altered couplings. The final Wilson chain is depicted in panel (c) where the coupling between the impurity and the first Wilson site is again given by V . The thinning bonds between the sites depict the exponentially decreasing couplings of order $\Lambda^{-\frac{n}{2}}$. In panel (d) we depict the shell structure of the wave functions corresponding to the Wilson sites. For increasing Wilson site index n the respective wave functions have support only within a spherical shell with exponentially growing size.

solved iteratively as will be explained in the next section. For a Wilson site with index n the typical energy resolution introduced through this site is given by ³

$$\delta_n \simeq t_{n-1} = \frac{1}{2}(1 + \Lambda^{-1})\Lambda^{-\frac{n-1}{2}} \sim \Lambda^{-\frac{n}{2}}, \quad (4.22)$$

characterizing the typical spacing between the few lowest-lying states of a Wilson chain of finite length n with n sufficiently large.

For a non-interacting Fermi sea with M particles (and size $L \propto M$) the mean single-particle level spacing at the Fermi energy scales like $1/M$. According to Fermi liquid theory (see Sec. 2.1) this also holds for the interacting case. Thus, we may conclude that $\delta_n \propto 1/M$ and so

$$M \propto \Lambda^{\frac{n}{2}} \Leftrightarrow L \propto \Lambda^{\frac{n}{2}}, \quad (4.23)$$

³For historical reasons we are using the exact formula in Eq. (4.17) which does not make any difference as it is only an estimate anyway.

i.e. the effective number of particles (i.e. the number of particles of the *original* model represented by the Wilson chain) or rather the size of the system scales exponentially with the Wilson site index n . In particular, this is the foundation of the shell structure of the Wilson chain, cf. Fig. 4.1(d), and means that we have access to exponentially large system sizes which will be of particular importance in the context of Anderson orthogonality, see Sec. 6.1.

4.4 NRG solution of the Wilson chain

Finally, we can turn to the NRG solution of the problem. For a solution in the spirit of RG we introduce a sequence of Hamiltonians

$$\hat{H}_N = \delta_N^{-1}(\hat{H}_{\text{imp}} + \hat{H}_{\text{imp-sea}} + \sum_{\mu} \sum_{n=0}^{N-1} t_n(\hat{f}_{n\mu}^{\dagger} \hat{f}_{n+1\mu} + \hat{f}_{n+1\mu}^{\dagger} \hat{f}_{n\mu})), \quad (4.24)$$

which approaches the Hamiltonian in Eq. (4.19) like

$$\hat{H} = \lim_{N \rightarrow \infty} \delta_N \hat{H}_N. \quad (4.25)$$

The factor of δ_N^{-1} has been chosen such that it cancels the N -dependence of t_{N-1} . The sequence can also be written in an iterative fashion, starting with

$$\hat{H}_0 = \delta_0^{-1}(\hat{H}_{\text{imp}} + \hat{H}_{\text{imp-sea}}), \quad (4.26)$$

and the recursion relation

$$\hat{H}_{N+1} = \sqrt{\Lambda} \hat{H}_N + \sum_{\mu} (\delta_{N+1}^{-1} t_N)(\hat{f}_{N\mu}^{\dagger} \hat{f}_{N+1\mu} + \hat{f}_{N+1\mu}^{\dagger} \hat{f}_{N\mu}). \quad (4.27)$$

Defining the RG transformation

$$\hat{H}_{N+1} = R(\hat{H}_N), \quad (4.28)$$

we have finally arrived at a formulation which contains all characteristics of Wilson's RG. Our goal is to obtain the full energy eigenspectrum with corresponding eigenstates of the Hamiltonian in Eq. (4.19), or at least a good approximation thereof. We do so by successively diagonalizing the series of Hamiltonians \hat{H}_N given above.

Starting with the impurity, we successively consider fluctuations of energy δ_N or, equivalently, size δ_N^{-1} (cf. Eq. (4.23)) until we reach a stable low-energy fixed point. Thus, the energy resolution δ_N plays the role of the cutoff in terms of the conventional RG theory. The presence of a stable low-energy fixed point can be anticipated - even though it is not guaranteed - from the fact that after the energy resolution is well below any inherent (e.g. impurity parameters) or arising (e.g. Kondo temperature) energy scales, the RG transformation tends to show self-similarity, cf. Sec. 2.3. In practice, we apply the renormalization

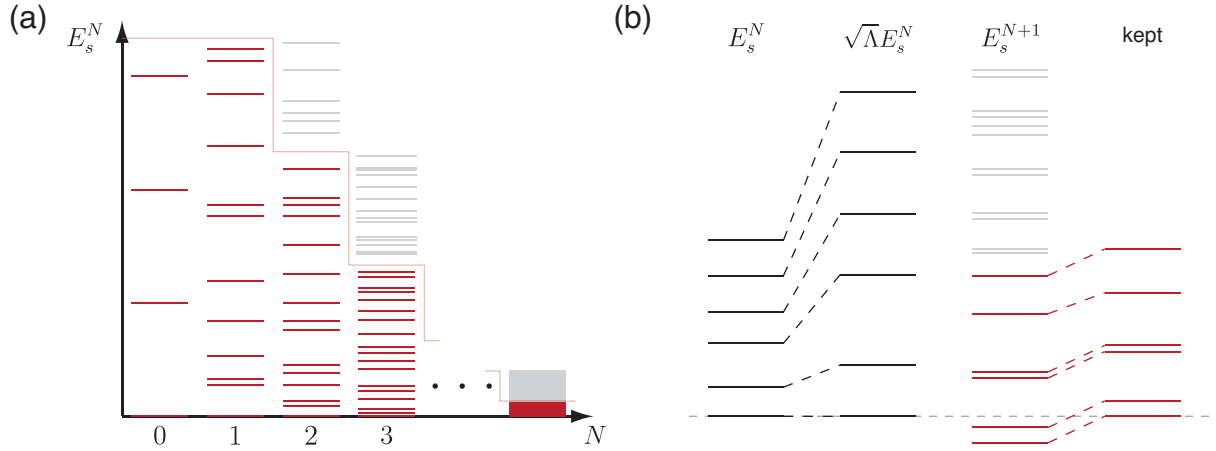


Figure 4.2: Panel (a) shows the unscaled (but shifted w.r.t. energy zero point) energy level diagram of the renormalization steps, i.e. the shifted eigenspectra of $\delta_N \hat{H}_N$. We see that the states of one iteration are refined w.r.t. energy in the following iteration. As soon as the number of states is truncated, only the low-energy states are further refined. For a better representation the ratio between kept and truncated states is shifted in favour of the kept states, because actually D states are kept while $(d-1)D$ states are discarded. In Panel (b) the steps during one RG iteration are depicted (adopted from [23]): the many-particle spectrum E_s^N of the previous iteration is rescaled by $\sqrt{\Lambda}$ and subject to the perturbation of the new site. The new system is diagonalized, yielding eigenenergies E_s^{N+1} , truncated and the energies are shifted such that the new ground state has zero energy.

procedure for Wilson chain length up to $N_{\max} \approx 80 - 120$ depending on the desired energy resolution,⁴ ensuring that we went below all relevant energy scales and reached a stable low-energy fixed point, see Sec. 4.4.2.

In each renormalization step, the Hamiltonian \hat{H}_{N+1} is diagonalized by an unitary transformation $A^{[N]}$ (see Sec. 4.4.3 for details) and the form of the energy renormalization is such that the eigenenergies of \hat{H}_{N+1} are of order 1. Thus, having a closer look onto the structure of \hat{H}_{N+1} , we see that a term with level spacing of the order $\sqrt{\Lambda}$ (namely $\sqrt{\Lambda} \hat{H}_N$) is subject to a perturbation of order 1 (remember $\delta_{N+1}^{-1} t_N \sim 1$), i.e. each additional site works as an perturbation of order $1/\sqrt{\Lambda}$, thereby lifting the degeneracy of the states of the former system, see Fig. 4.2.

So far, we have not addressed the thinning out of degrees of freedom. If we keep all degrees of freedom during the RG transformation, the Hilbert space of the Hamiltonian \hat{H}_N will have the dimension $d_{\text{imp}} d^{N+1}$ (d_{imp} being the dimension of \hat{H}_{imp}), which will be beyond a numerical treatment even for small values of N . Thus, we need to truncate parts of the Hilbert space and we do so by keeping only the D lowest energy eigenstates of \hat{H}_N . There is no guarantee that this *ad hoc* truncation works and we have to check on the validity

⁴A naturally arising stopping value N_{\max} is when $\delta_{N_{\max}}$ reaches machine precision, which in the case of double-precision is 10^{-16} .

of this approach by varying D while keeping all other parameters fixed. However, the exponentially decreasing energy scale gives some justification to this scheme: as already said, one may see the addition of a site as a perturbation of order $1/\sqrt{\Lambda}$, and we know from perturbation theory that the influence of high-energy states on the low-energy states will be small provided that the perturbation is weak enough. Thus, for a smaller value of Λ we need larger values of D to keep the truncation error small. Usually, D is chosen such that the first few ($\lesssim 5$) Wilson sites are included without truncation. Summarizing, this procedure results in an increasing resolution of low-energy states as smaller and smaller energy scales are considered for those states which had small energy initially, while high-energy states are not refined any more, Fig. 4.2(a).

4.4.1 Description of the iteration procedure

Finally, we give the full iteration procedure, starting with the Hamiltonian \hat{H}_{imp} (where the first renormalization has a slightly different form) and the transformation from a given, diagonalized Hamiltonian \hat{H}_N to the renormalized \hat{H}_{N+1} . The RG transformation steps are in detail (see Fig. 4.2(b) for a pictorial explanation):

- We start by diagonalizing $\delta_0^{-1}(\hat{H}_{\text{imp}} + \hat{H}_{\text{imp-sea}})$ but without shifting its energy. We continue with \hat{H}_1 which we fully consider as it is questionable for the early iterations whether the new terms can be treated as a perturbation.
- Given \hat{H}_N with eigenstates $|s\rangle_N$ and their respective energies $\hat{H}_N|s\rangle_N = E_s^N|s\rangle_N$, we rescale the energies E_s^N , initially with level spacing of order 1, by $\sqrt{\Lambda}$. Then, we introduce the next Wilson site with basis states $|\sigma_{N+1}\rangle$ which act as a perturbation of size $1/\sqrt{\Lambda}$, thus forming the new Hamiltonian \hat{H}_{N+1} with dimension a factor of d larger than that of \hat{H}_N . Therefore, in the regime where \hat{H}_N has already been truncated \hat{H}_{N+1} has dimension dD .
- We diagonalize \hat{H}_{N+1} , obtaining a new set of eigenstates $|s\rangle_{N+1}$ with energies E_s^{N+1} , where the typical level spacing is of order 1. The energies are shifted by $E_0^{(N+1)}$ such that the ground state of \hat{H}_{N+1} has zero energy.
- If the number of states $|s\rangle_{N+1}$ is larger than D , only those are kept with lowest energy. It is useful to be not too strict, e.g. if the D th and $(D+1)$ th states are degenerate, keep $D+1$ states in total. The states are classified as $|s\rangle_{N+1}^X$ with X either K or D for kept and discarded, respectively.
- Finally, the renormalized Hamiltonian is given as

$$\hat{H}_{N+1} = \sum_s^K E_s^{N+1} |s\rangle_{N+1}^K \langle s|_{N+1}^K, \quad (4.29)$$

where s is restricted to the kept states only, indicated by the K over the sum.

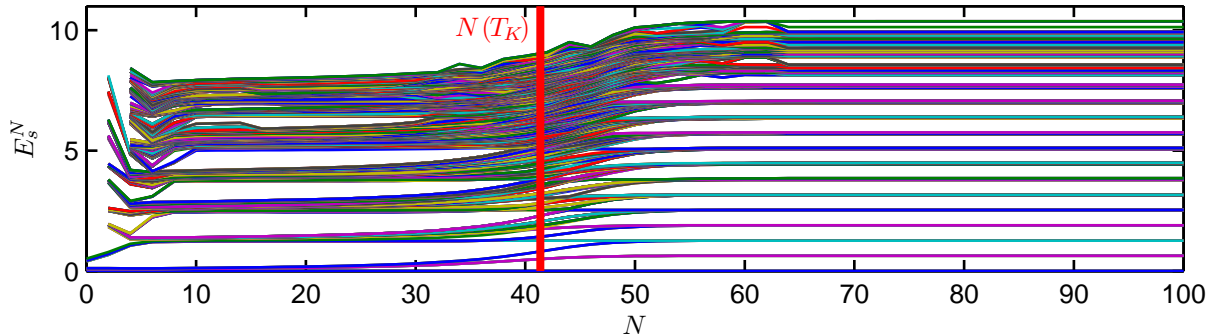


Figure 4.3: Energy flow diagram [22] for the symmetric SIAM with $U = 0.6$, $\varepsilon_d = -U/2$ and $\Gamma = 0.02$, where we choose $D = 256$ (i.e. we show $dD = 1024$ levels per iteration). We show only even values of N (with a similar picture for odd N) and connect the data points by lines to depict the flow. The energy scale δ_N corresponding to $T_K = 5.9 \cdot 10^{-7}$ is reached for $N \approx 41$ (for $\Lambda = 2$). For the SIAM, one finds essentially three regimes, see [22] for an extensive explanation: the free orbital regime for very small $N \lesssim 5$ (the impurity behaves as if not coupled to the Fermi sea), the local moment regime for $10 \lesssim N \lesssim 30$ (the impurity has a definite spin, subject to fluctuations) and finally a crossover (characterized by T_K) to the strong coupling regime corresponding to the low-energy fixed point (the impurity spin is completely screened by the Fermi sea). We conclude from this energy flow diagram that we captured all relevant physics in our calculation.

- When we reach our stopping value N_{\max} , consistently, all states are discarded, which thus stops the RG transformations and we have

$$\hat{H}_{N_{\max}} = \sum_s^D E_s^{N_{\max}} |s\rangle_{N_{\max}}^D \langle s|_{N_{\max}}^D. \quad (4.30)$$

After stopping the RG transformations at N_{\max} , we have roughly dD energy eigenstates for the Wilson chain of length N_{\max} with full Hilbert space dimension $d_{\text{imp}} d^{N_{\max}+1}$. This is, of course, not at all a complete basis set. However, we show in Sec. 4.5 how it is possible to construct a complete basis by considering the *discarded* states of *all* iterations.

4.4.2 Renormalization group flow

The very first check on an actual NRG calculation is the energy flow diagram. In a standard RG transformation, the renormalized Hamiltonians are characterized by an effective description of a Hamiltonian with a fixed set of parameters which change under the RG flow, see Sec. 2.3. In [22] we find an extensive discussion of flowing parameters for the SIAM. However, the sequence of Hamiltonians in Eq. (4.24) cannot, in general, be described that way and thus, equivalently, the flow in terms of the eigenenergies E_s^N is taken, instead, as these also reflect the parameter flow [22].

Before we discuss the energy flow diagram in more detail, we need to mention a peculiarity of fermionic finite-size systems: they typically show even-odd alternations, i.e. while convergence has been reached in terms of even and odd system sizes individually, these still differ from each other. The even-odd alternation immediately shows up in the energy flow diagram but, of course, also affects some properties of the system, e.g. this turned out to influence some calculations concerning Anderson orthogonality, see Sec. 6.1. So, strictly speaking, all fixed point discussions need to be made in terms of R^2 including two iterations rather than R . In particular, N_{\max} introduces a source for undesired even-odd effects as one needs to make a definite choice for it.

Investigating the energy flow diagram shows us whether the RG transformations still change the system or whether we approached a stable fixed point. In Fig. 4.3 we show the energy flow diagram of the symmetric SIAM. The flow reflects the fixed points of the SIAM and we conclude that the system will not change any more well below T_K . For other models the energy flow diagram will, of course, look different in the high- and intermediate-energy regime, but finally needs to approach a stable low-energy fixed point.

4.4.3 Matrix product state structure of the basis states

To round up the details of the RG transformations, we point out the structure of the unitary transformations mapping the kept part of the energy eigenbasis from the previous iteration $|s\rangle_{N-1}^K$ and the basis states of the new site $|\sigma_N\rangle$ onto the new energy eigenbasis $|s\rangle_N^X$. It has been shown only recently that these transformations feature the structure of matrix product states (MPS), a unified framework for RG methods [62]. We give an extensive introduction about matrix product states as used in the context of DMRG in [the appendix](#) of the publication on the CDM, see Chap. 5. However, this is only useful for a deeper understanding of MPS and is not needed for the present discussion.

To be specific, the unitary transformation $A^{[N]}$ has the following form:

$$|s'\rangle_N^X = \sum_{\sigma_N^s}^K [A_{\text{KK}}^{[\sigma_N]}]_{ss'} |\sigma_N\rangle \otimes |s\rangle_{N-1}^K, \quad (4.31)$$

where we have introduced several new notations. By MPS convention, we split the unitary transformation $A^{[N]}$ into the d matrices $A^{[\sigma_N]}$ (one per site degree of freedom; henceforth called A-matrices), where the first notation is still used to refer to all of them at once. In mathematical terms, the $[A_{\text{KK}}^{[\sigma_N]}]_{ss'}$ are three-dimensional tensors in the space spanned by $|\sigma_N\rangle$, $|s\rangle_{N-1}^K$, and $|s'\rangle_N^X$.

Furthermore, these matrices are partitioned into a part for kept and a part for discarded states, respectively. Note that the index corresponding to the previous site only consists of kept states as we are refining only these.

The term MPS becomes clear when we trace the iterative structure of the states $|s\rangle_N^X$ back to the impurity by reinserting the definition given above:

$$|s\rangle_N^X = \sum_{\sigma_N \dots \sigma_0 \sigma_{\text{imp}}} [A_{\text{KK}}^{[\sigma_0]} \dots A_{\text{KK}}^{[\sigma_{N-1}]} A_{\text{KK}}^{[\sigma_N]}]_{\sigma_{\text{imp}} s} |\sigma_N\rangle \otimes |\sigma_{N-1}\rangle \otimes \dots \otimes |\sigma_0\rangle \otimes |\sigma_{\text{imp}}\rangle, \quad (4.32)$$

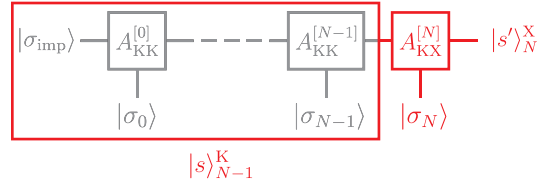


Figure 4.4: Graphical representation of the MPS structure of the NRG transformations. The highlighted part depicts how in Eq. (4.31) $[A_{\text{KK}}^{[\sigma_N]}]_{ss'}$ transforms the states $|\sigma_N\rangle$ and $|s\rangle_{N-1}^K$ into $|s'\rangle_N^X$. The indices s , σ_N and s' belong to the legs to the left, bottom and right of $A_{\text{KK}}^{[N]}$, respectively. In the following we will explicitly write the indices and states only when it is instructive, but otherwise skip them when it is clear in context which leg represents which index. Furthermore, we show in the interior of the highlighted box how $|s'\rangle_N^X$ is represented in Eq. (4.32) in terms of the basis states of all previous sites.

where $|\sigma_{\text{imp}}\rangle$ is the basis of the impurity which is included in $A^{[0]}$ as “previous iteration” (note that $A^{[0]}$ has σ_{imp} as index for the previous iteration). For a single choice of $\sigma_N \dots \sigma_0 \sigma_{\text{imp}}$ its contribution to the state $|s\rangle_N^X$ is given as a matrix-product.

The great advantage of the MPS is that we have access to a description of the state $|s\rangle_N^X$ in the full $d_{\text{imp}} d^{N+1}$ -dimensional Hilbert space according to Eq. (4.32), but partitioned into smaller blocks $A^{[N]}$ which makes a numerical treatment possible. In particular, the application of an operator onto the state can be performed very efficiently, see below.

MPS possesses a very intuitive graphical representation (cf. page 36 of the appendix of the publication on the CDM in Chap. 5). Each “object” is represented as a box with small legs representing indices, where connected legs represent contractions over the respective indices, see Fig. 4.4.

Fermion signs

Equation (4.31) reveals how another important complication in the treatment of Fermions has been dealt with: Fermion signs. The numerical treatment of Fermions in second quantization requires an order that defines how the creation operators constitute with positive sign a certain state due to their anti-commutation relations. We define for a single electron species ($\mu = 1$, see Sec. 4.1) and a single degree of freedom on the impurity (given by \hat{d}^\dagger) that

$$\hat{f}_N^\dagger \hat{f}_{N-1}^\dagger \dots \hat{f}_0^\dagger \hat{d}^\dagger |\text{vac}\rangle = +|\text{all occupied}\rangle. \quad (4.33)$$

This choice determines how we obtain from the operators of the site Hilbert space their $d_{\text{imp}} d^{N+1} \times d_{\text{imp}} d^{N+1}$ -dimensional representation:

$$\hat{d}^{(\dagger)} \cong \hat{d}_{\text{loc}}^{(\dagger)} \otimes_{0 \leq m \leq N} \hat{Z}_m, \quad (4.34)$$

$$\hat{f}_n^{(\dagger)} \cong \mathbf{1}_{\text{imp}} \otimes_{0 \leq m < n} \mathbf{1}_m \otimes \hat{f}_{n,\text{loc}}^{(\dagger)} \otimes_{n < m \leq N} \hat{Z}_m, \quad (4.35)$$

$$\hat{Z}_m \equiv (-1)^{\hat{n}_m}, \quad (4.36)$$

with $\hat{d}_{\text{loc}}^{(\dagger)}$ the $d_{\text{imp}} \times d_{\text{imp}}$ -dimensional representation in the impurity Hilbert space, $\hat{f}_{n,\text{loc}}^{(\dagger)}$ the $d \times d$ -dimensional representation in the site Hilbert space, which is the same for all Wilson sites, and $\hat{n}_m = \hat{f}_{m,\text{loc}}^\dagger \hat{f}_{m,\text{loc}}$. The operators \hat{Z}_m constitute the so-called Jordan-Wigner string $\otimes_{n < m \leq N} \hat{Z}_m$, which derives from the order in Eq. (4.33). Thus, in each RG iteration the operators of the previous sites obtain an extra factor in their Jordan-Wigner string, but otherwise remain unchanged.

This scheme is easily generalized to several electron species:

$$\hat{Z}_m = \otimes_{\mu} (-1)^{\hat{n}_{m\mu}} , \quad (4.37)$$

with $\hat{n}_{m\mu} = \hat{f}_{m\mu,\text{loc}}^\dagger \hat{f}_{m\mu,\text{loc}}$. Moreover, we additionally need to establish an order of the different channels on one site. For example, for the SIAM we choose

$$\hat{f}_{N\uparrow}^\dagger \hat{f}_{N\downarrow}^\dagger \hat{f}_{N-1\uparrow}^\dagger \hat{f}_{N-1\downarrow}^\dagger \cdots \hat{f}_{0\uparrow}^\dagger \hat{f}_{0\downarrow}^\dagger \hat{d}_{\uparrow}^\dagger \hat{d}_{\downarrow}^\dagger |\text{vac}\rangle = +|\text{all occupied}\rangle . \quad (4.38)$$

In particular, this means that $\hat{f}_{n\sigma,\text{loc}}$ represented in the basis $|0\rangle = (1, 0, 0, 0)$, $|\uparrow\rangle = (0, 1, 0, 0)$, $|\downarrow\rangle = (0, 0, 1, 0)$, and $|\uparrow\downarrow\rangle = (0, 0, 0, 1)$ has the following form:

$$\hat{f}_{n\uparrow,\text{loc}} = \begin{pmatrix} 0 & 1 & 0 & 0 \\ 0 & 0 & 0 & 0 \\ 0 & 0 & 0 & 1 \\ 0 & 0 & 0 & 0 \end{pmatrix} , \quad \hat{f}_{n\downarrow,\text{loc}} = \begin{pmatrix} 0 & 0 & 1 & 0 \\ 0 & 0 & 0 & -1 \\ 0 & 0 & 0 & 0 \\ 0 & 0 & 0 & 0 \end{pmatrix} . \quad (4.39)$$

Note that in this definition the ‘‘site-internal’’ fermionic sign has been absorbed into the representation of $\hat{f}_{n\downarrow,\text{loc}}$.

During the RG iterations only the hopping term between the (old) site N and the added site $N + 1$ arises, cf. Eq. (4.27):

$$\hat{f}_{N\mu}^\dagger \hat{f}_{N+1\mu} = \mathbb{1}_{\text{imp}} \otimes_{0 \leq m < N} \mathbb{1}_m \otimes \hat{f}_{N\mu,\text{loc}}^\dagger \otimes \hat{Z}_{N+1} \hat{f}_{N+1\mu,\text{loc}} , \quad (4.40)$$

with the additional Z -operator on site $N + 1$ arising from our order of the fermionic operators.

Operators

When we apply an operator onto a MPS we do not need to evaluate it globally in the $d_{\text{imp}} d^{N+1}$ -dimensional Hilbert space. Instead the site representation of the operator itself and the z -operators of all later sites are applied individually on the A -matrices. This is a great simplification even for a long Jordan-Wigner string, e.g. in case of impurity operators (however, in this case there exists another simplification, see Sec. 4.7).

The most important task within the iterative procedure is the diagonalization of the Hamiltonian \hat{H}_{N+1} in the product space of $|s\rangle_N^K$ and $|\sigma_{N+1}\rangle$. However, as can be seen from Eq. (4.40) we only know how the hopping term acts on the site Hilbert space of site N and $N + 1$, respectively. Thus, we need to transform the operator $\hat{f}_{N\mu,\text{loc}}^{(\dagger)}$ into the basis $|s\rangle_N^K$:

$$[\hat{f}_{N\mu,\text{K}}^{(\dagger)}]_{ss'} = \sum_{\sigma_N \sigma'_N s''}^{\text{K}} [A_{\text{KK}}^{[\sigma_N]}]_{s''s}^* [\hat{f}_{N\mu,\text{loc}}^{(\dagger)}]_{\sigma_N \sigma'_N} [A_{\text{KK}}^{[\sigma'_N]}]_{s''s'} , \quad (4.41)$$

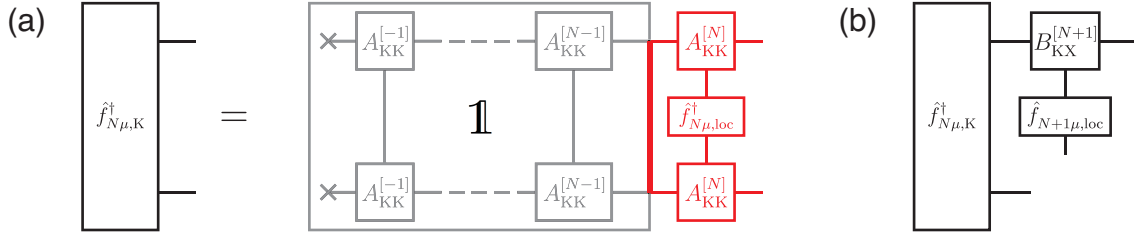


Figure 4.5: Panel (a) shows the graphical representation of Eq. (4.41): the operator $\hat{f}_{N\mu,\text{loc}}^\dagger$, acting on the site Hilbert space of site N , is transformed into the basis $|s\rangle_N^K$ via the unitary transformation $A_{KK}^{[N]}$. However, this transformation includes not only the basis $|\sigma_N\rangle$ but also $|\sigma_{N-1}\rangle^K$ where $\hat{f}_{N\mu,\text{loc}}^\dagger$ does not act (therefore the unit matrix in the box). Thus, we may directly connect the legs corresponding to the $|\sigma_{N-1}\rangle^K$ states (thick line). In panel (b) we show how the hopping term acts on a state: based on $[\hat{f}_{N\mu,K}^\dagger]_{ss'}$ the application of the hopping term on a state reduces to the manipulation of a single A -matrix

where s'' runs over the states $|\sigma_{N-1}\rangle^K$. This formula is much easier understood when depicted in the graphical representation in Fig. 4.5(a).

In the numerical procedure of finding the eigenbasis of \hat{H}_{N+1} we need to apply several times the hopping term onto intermediate states, described by intermediate A -matrices $B_{KK}^{[N+1]}$ converging to $A_{KK}^{[N+1]}$. However, due to the structure of the MPS as presented above we need to manipulate the A -matrix of site $N+1$ only (see Fig. 4.5(b)), even though we obtain an effective description of the states in the full many-body space.

Symmetries of the Hamiltonian

MPS can be easily adapted to properly account for conserved quantum numbers, representing the global symmetries of the Hamiltonian. We will limit ourselves to Abelian symmetries, meaning that the irreducible representation of the symmetry group is Abelian, as these are easily implemented, which is not necessarily the case for non-Abelian symmetries. However, as already in [2] the total spin as a representation of a non-Abelian symmetry was considered, recent development allows for the implementation of arbitrary non-Abelian symmetries [63, 64].

An Abelian symmetry allows a quantum number Q to be attached to every state. The property that the symmetry is Abelian manifests itself in that this quantum number is strictly additive. For two states $|Q_1\rangle$ and $|Q_2\rangle$, the quantum number of the direct product of these two states is given by $|Q_1\rangle \otimes |Q_2\rangle = |Q_1 + Q_2\rangle$. For example, if the Hamiltonian commutes with the number operator for the full system, the quantum number Q could represent particle number. Of course, the treatment of Abelian symmetries is generic and not limited to only one symmetry. We may incorporate as many symmetries as exist for a given Hamiltonian, by writing Q as a vector of the corresponding quantum numbers.

For the handling of MPS, quantum numbers imply a significant amount of bookkeeping, i.e. for every coefficient block we have to store its quantum numbers. The benefit is

that we can deal with large effective state spaces at a reasonable numerical cost. The diagonalization of \hat{H}_N , in particular, takes advantage of the block structure.

Due to our finite description of the system we always have conservation of total particle number

$$Q = Q_{\text{imp}} + \sum_{\mu} \sum_{n=0}^N (\hat{f}_{n\mu}^{\dagger} \hat{f}_{n\mu} - \frac{1}{2}), \quad (4.42)$$

where Q_{imp} is given relative to half-filling, similar to the Fermi sea. In many cases the μ -summands are conserved individually. For example, for the SIAM each spin species is conserved individually, i.e. we have two quantum numbers Q_{\uparrow} and Q_{\downarrow} which are usually written in terms of conservation of total charge and the z component of the total spin:

$$Q = Q_{\uparrow} + Q_{\downarrow} = \sum_{\sigma} ((\hat{d}_{\sigma}^{\dagger} \hat{d}_{\sigma} - \frac{1}{2}) + \sum_{n=0}^N (\hat{f}_{n\sigma}^{\dagger} \hat{f}_{n\sigma} - \frac{1}{2})), \quad (4.43)$$

$$S_z = \frac{1}{2}(Q_{\uparrow} - Q_{\downarrow}) = \frac{1}{2}[(\hat{d}_{\uparrow}^{\dagger} \hat{d}_{\uparrow} + \sum_{n=0}^N \hat{f}_{n\uparrow}^{\dagger} \hat{f}_{n\uparrow}) - (\hat{d}_{\downarrow}^{\dagger} \hat{d}_{\downarrow} + \sum_{n=0}^N \hat{f}_{n\downarrow}^{\dagger} \hat{f}_{n\downarrow})]. \quad (4.44)$$

Thus, the site basis states can be labelled as $|Q, 2S_z\rangle$ ($2S_z$ to avoid fractions, for convenience): $|0\rangle = |-1, 0\rangle$, $|\uparrow\rangle = |0, 1\rangle$, $|\downarrow\rangle = |0, -1\rangle$, and $|\uparrow\downarrow\rangle = |1, 0\rangle$.

4.5 Anders-Schiller basis

After finishing the RG procedure we turn to the calculation of physical properties of the system like spectral functions and expectation values. However, the MPS cover only a limited range of energy eigenstates, that is for a given chain length we have at most dD energy eigenstates. However, Anders and Schiller proposed a way to obtain from the A -matrices a full but approximate energy eigenbasis [65, 66].

Henceforth, in summations over s we will usually not write explicitly whether the sum runs over K or D as it is mostly apparent from the context.

4.5.1 Definition

As long as we do not truncate, say up to iteration n_0 , the states $|s\rangle_n^K$ with $n \leq n_0$ provide a complete basis set for \hat{H}_n , i.e. for the chain of length n . However, for later sites the necessary thinning out of degrees of freedom inherently includes that the states $|s\rangle_N^X$ do not span the whole Hilbert space. Thus, to obtain a complete basis for the full chain we need to include the discarded states $|s\rangle_n^D$ of previous iterations n , $n_0 < n < N$ which are, however, too short for the full system as they are defined only for a chain of length n . Consequently, we supplement them with a set of d^{N-n} degenerate ‘‘environmental’’ states

$$|e_n\rangle \equiv |\sigma_N\rangle \otimes \cdots \otimes |\sigma_{n+1}\rangle, \quad (4.45)$$

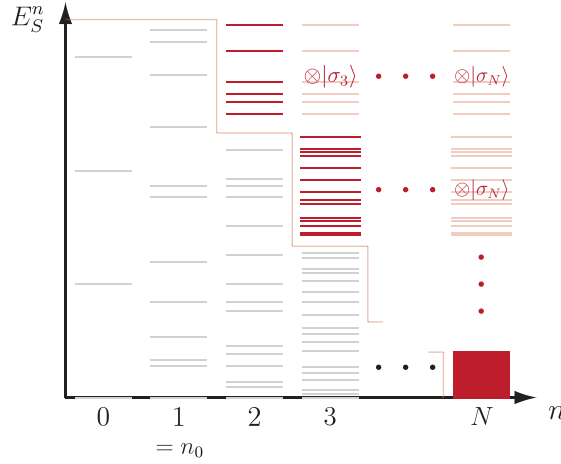


Figure 4.6: Similar figure as Fig. 4.2 but here the states of interest are not the kept states at each iteration as these are further considered in later iterations, but rather the discarded states. These are, together with their environmental states, part of the complete basis set for the chain of length N . Kept states are only indirectly part of the complete basis set in that they contribute to the discarded states of later iterations.

spanning the remainder of the chain.

In general, for states (kept and discarded) of previous iterations we define their extension to the full Hilbert space as

$$|se\rangle_n^X \equiv |e_n\rangle \otimes |s\rangle_n^X, \quad (4.46)$$

which are approximate eigenstates to the Hamiltonian \hat{H}_N of the full chain:

$$\hat{H}_N |se\rangle_n^X \simeq E_s^n |se\rangle_n^X. \quad (4.47)$$

This is justified by the so called “NRG approximation”: as elucidated above, a Wilson site corresponds to a characteristic energy scale δ_n (cf. Eq. (4.22)) and each following site acts as a perturbation of order $1/\sqrt{\Lambda}$. Thus, the states $|se\rangle_n^X$ are approximate eigenstates of \hat{H}_N within an accuracy of δ_n while the degeneracy lifting due to the later sites is ignored.

Apparently, the discarded states of different iterations are orthogonal to each other,

$${}^D_n \langle se | s' e' \rangle_m^D = \delta_{nm} \delta_{ss'} \delta_{e_n e'_n}, \quad (4.48)$$

and orthogonal to any kept states of later iterations (upper line in Eq. (4.49)) while their overlap to kept states of earlier iterations depends on how the following A -matrices mapped them on in later iterations (lower line in Eq. (4.49)):

$${}^D_n \langle se | s' e' \rangle_m^K = \begin{cases} 0 & n \leq m \\ \delta_{e_n e'_n} [A_{\text{KK}}^{[\sigma_{m+1}]} \dots A_{\text{KD}}^{[\sigma_n]}]_{ss'} & n > m \end{cases}. \quad (4.49)$$

Having defined the extension of the MPS of previous iterations onto the chain of length N , we now show which of these form the ‘‘Anders-Schiller basis’’ spanning the full $d_{\text{imp}}d^{N+1}$ -dimensional Hilbert space:

$$\mathbb{1}^{(d_{\text{imp}}d^{N+1})} = \sum_{se} |se\rangle_{n_0}^{\text{K}} \langle se|_{n_0}^{\text{K}} \quad (4.50a)$$

$$= \sum_{n>n_0}^N \sum_{se} |se\rangle_n^{\text{D}} \langle se|_n^{\text{D}} \quad (4.50b)$$

The first line in this equation trivially extends the complete kept basis from iteration n_0 (the last iteration where we do not truncate) by the environmental states to the chain of length N . However, usually the accuracy δ_{n_0} to which Eq. (4.47) holds in this case is not enough to obtain meaningful results. The best accuracy achievable from a given NRG run for an approximate eigenbasis of \hat{H}_N gives the second line of the equation, where the eigenstates obtained in the N th iteration are supplemented by the discarded states of the previous iterations. For simplicity, the states of the N th iteration are treated as discarded. Henceforth, a sum over n will always be considered as $n_0 < n \leq N$ unless stated otherwise.

4.5.2 Local operators

During the iteration procedure we took advantage of the fact that the action of the involved operators could be determined locally, cf. Eq. (4.41). However, in other context we need a description of operators in the full basis introduced above, which can be achieved in a straightforward manner [67].

We consider an operator \hat{B} acting non-trivially only on sites up to n_0 (i.e. a ‘‘local’’ operator) which means that we may calculate exactly numerically its representation in the basis $|s\rangle_{n_0}^{\text{K}}$ and thus in $|se\rangle_{n_0}^{\text{K}}$:

$$\hat{B} = \sum_{ss'e} |se\rangle_{n_0}^{\text{K}} [B_{\text{KK}}^{[n_0]}]_{ss'} \langle s'e|_{n_0}^{\text{K}}. \quad (4.51)$$

(To be precise, we could allow for operators acting on sites up to $n_0 + 1$ which becomes apparent in the derivation below. In this case the sum in Eq. (4.51) would not only include kept but also discarded states.) To actually calculate these matrix elements we have to distinguish between the cases where \hat{B} consists of an even and odd number of fermionic operators, respectively.

Even number

If the operator consists of an even number of fermionic creation and annihilation operators, e.g. $\hat{B} = \hat{d}_{\mu}^{\dagger} \hat{f}_{0\mu}$, the matrix elements can be easily calculated from (cf. Sec. 4.4.3):

$$\hat{B} = \hat{d}_{\mu, \text{loc}}^{\dagger} \otimes \hat{Z}_0 \hat{f}_{0\mu, \text{loc}} \otimes \mathbb{1}_{1 \leq m \leq N}. \quad (4.52)$$

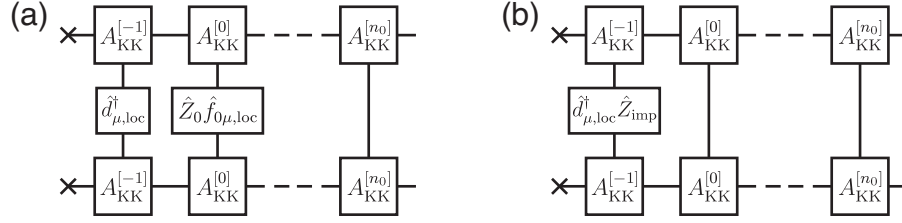


Figure 4.7: Graphical depiction of how to calculate the matrix elements $[B_{\text{KK}}^{[n_0]}]_{ss'}$ for (a) $\hat{B} = \hat{d}_{\mu}^{\dagger} \hat{f}_{0\mu}$, an even number of fermionic operators, and (b) $\hat{B} = \hat{d}_{\mu}^{\dagger}$, an odd number of fermionic operators. In the first case the Fermion sign problem is fully taken care of by the additional operator \hat{Z}_0 . In the second case we choose to evaluate Eq. (4.54b), i.e. we need to additionally apply the operator \hat{Z}_{imp} to obtain the matrix elements $[B_{\text{KK}}^{[n_0]}]_{ss'}$. However, the factor Z_{tot} still needs to be attached to each basis state, but will cancel out in the end, cf. Eq. (4.55).

The locally acting operators $\hat{d}_{\mu, \text{loc}}^{\dagger}$ and $\hat{Z}_0 \hat{f}_{0\mu, \text{loc}}$ need to be transformed stepwise into the basis $|s\rangle_{n_0}^{\text{K}}$ (the subscripts of the operators on the left hand side indicate the iteration for which they are calculated):

$$[(\hat{d}_{\mu}^{\dagger})_{-1}]_{ss'} = {}_{-1}^{\text{K}} \langle s | \hat{d}_{\mu}^{\dagger} | s' \rangle_{-1}^{\text{K}} = \sum_{\sigma_{-1} \sigma'_{-1}}^{\text{K}} [A_{\text{KK}}^{[\sigma_{-1}]}]_{1s}^* [\hat{d}_{\mu, \text{loc}}^{\dagger}]_{\sigma_{-1} \sigma'_{-1}} [A_{\text{KK}}^{[\sigma'_{-1}]}]_{1s'}, \quad (4.53a)$$

$$[(\hat{d}_{\mu}^{\dagger} \hat{Z}_0 \hat{f}_{0\mu})_0]_{ss'} = \sum_{\sigma_0 \sigma'_0 s'' s'''}^{\text{K}} [A_{\text{KK}}^{[\sigma_0]}]_{s'' s}^* [(\hat{d}_{\mu}^{\dagger})_{-1}]_{s'' s'''} [\hat{Z}_0 \hat{f}_{0\mu, \text{loc}}]_{\sigma_0 \sigma'_0} [A_{\text{KK}}^{[\sigma'_0]}]_{s''' s'}, \quad (4.53b)$$

$$[(\hat{d}_{\mu}^{\dagger} \hat{Z}_0 \hat{f}_{0\mu})_n]_{ss'} = \sum_{\sigma_n s'' s'''}^{\text{K}} [A_{\text{KK}}^{[\sigma_n]}]_{s'' s}^* [(\hat{d}_{\mu}^{\dagger} \hat{Z}_0 \hat{f}_{0\mu})_{n-1}]_{s'' s'''} [A_{\text{KK}}^{[\sigma_n]}]_{s''' s'}, \quad (4.53c)$$

where the last equation is valid for $1 \leq n \leq n_0$. This procedure is easier to understand when depicted graphically, see Fig. 4.7(a). Thus, applying this transformation up to site n_0 and introducing the environmental states at that site yields Eq. (4.51).

Odd number

The situation is a bit more complicated when the operator consists of an odd number of fermionic operators, e.g. $\hat{B} = \hat{d}_{\mu}$:

$$\hat{B} = \hat{d}_{\mu, \text{loc}}^{\dagger} \otimes_{0 \leq m \leq N} \hat{Z}_m \quad (4.54a)$$

$$= (\hat{d}_{\mu, \text{loc}}^{\dagger} \hat{Z}_{\text{imp}}) \otimes_{0 \leq m \leq N} \mathbf{1}_m \cdot \hat{Z}_{\text{tot}} \quad (4.54b)$$

$$= \hat{Z}_{\text{tot}} \cdot (\hat{Z}_{\text{imp}} \hat{d}_{\mu, \text{loc}}^{\dagger}) \otimes_{0 \leq m \leq N} \mathbf{1}_m \quad (4.54c)$$

$$\hat{Z}_{\text{tot}} \equiv (-1)^{\hat{N}_{\text{tot}}}. \quad (4.54d)$$

We have taken advantage of the fact that each state in our finite size description has a fixed total particle number \hat{N}_{tot} . Thus, instead of calculating the full Jordan-Wigner string we only need to calculate the sign operator on the impurity: $\prod_{0 \leq m \leq N} Z_m = Z_{\text{imp}} Z_{\text{tot}}$. The generalization to operators acting on several sites $0 \leq n \leq n_0$ is straightforward.

Finally, the matrix elements of the operator \hat{B} in the basis $|s\rangle_{n_0}^{\text{K}}$ are calculated similar to Eqs. (4.53), see Fig. 4.7(b). Moreover, we need to supply each state in Eq. (4.51) with an additional factor Z which is (-1) to the power of the states total particle number.

However, the expectation value of operators with an odd number of fermionic operators will always vanish due to particle conservation and thus we will only consider products of such operators, $\hat{B}\hat{C}$ (cf. Sec. 4.7), where the sign factors cancel:

$$\begin{aligned} \hat{B}\hat{C} &= \left(\sum_{ss'e} |se\rangle_{n_0}^{\text{K}} [B_{\text{KK}}^{[n_0]}]_{ss'} Z_{s'e}^{[n_0] \text{K}} \langle s'e| \right) \left(\sum_{s''s''e} |s''e\rangle_{n_0}^{\text{K}} Z_{s''e}^{[n_0]} [C_{\text{KK}}^{[n_0]}]_{s''s''} \langle s''e| \right) \\ &= \sum_{ss's''e} |se\rangle_{n_0}^{\text{K}} [B_{\text{KK}}^{[n_0]}]_{ss'} [C_{\text{KK}}^{[n_0]}]_{s''s''} \langle s''e|. \end{aligned} \quad (4.55)$$

In this representation we have chosen Eq. (4.54b) for \hat{B} and Eq. (4.54c) for \hat{C} because then the sign factors of the states appear only quadratically and thus cancel! The Fermion sign factor is fully taken care for in the calculation of the matrix elements $[B_{\text{KK}}^{[n_0]}]_{ss'}$ and $[C_{\text{KK}}^{[n_0]}]_{s''s''}$ via the operator Z_{imp} . Therefore, in practice we do not need to consider fermionic signs any more after having calculated Eq. (4.51).

Technical details

Having arrived at Eq. (4.51) we now want to express the operator \hat{B} in the full Anders-Schiller basis. Starting with $\hat{B}_{\text{KK}}^{[n_0]}$ we iteratively refine the part of the operator which solely consists of kept states (in case of the iteration n_0 this is the complete operator). According to Eq. (4.41) we have

$$\hat{B}_{\text{KK}}^{[n-1]} = \sum_{\text{XX}'} \sum_{ss'e} |se\rangle_n^{\text{X}} [B_{\text{XX}'}^{[n]}]_{ss'} \langle s'e| = \sum_{\text{XX}'} \hat{B}_{\text{XX}'}^{[n]} \quad (4.56)$$

$$[B_{\text{XX}'}^{[n]}]_{ss'} = [A_{\text{XK}}^{[\sigma_n] \dagger} B_{\text{KK}}^{[n-1]} A_{\text{KK}'}^{[\sigma_n]}]_{ss'}. \quad (4.57)$$

Thus, starting at n_0 we refine the complete description of the operator, Eq. (4.51), obtaining an expression as in Eq. (4.57) for n_0+1 . Splitting off all terms with $\text{XX}' \neq \text{KK}$, we continue to refine the $\text{XX}' = \text{KK}$ terms until we reach the end of the chain, arriving at

$$\hat{B} = \sum_{n > n_0} \sum_{\text{XX}' \neq \text{KK}'} \hat{B}_{\text{XX}'}^{[n]}, \quad (4.58)$$

a description of \hat{B} in the full Hilbert space using an approximate energy eigenbasis. This procedure features two important properties: (i) there is no double-counting of basis states

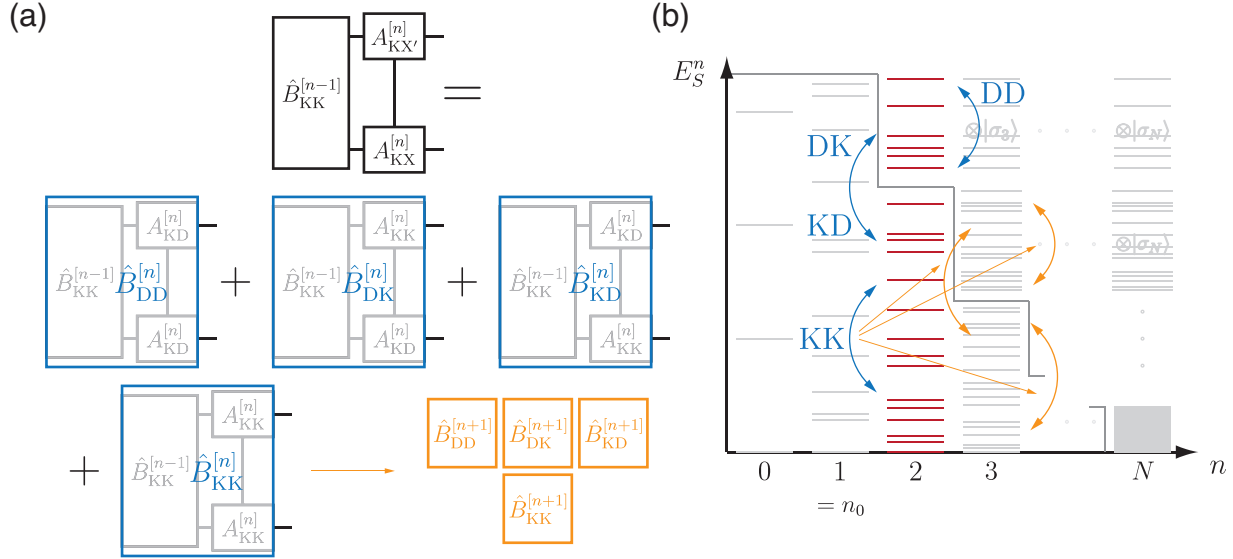


Figure 4.8: (a) Graphical depiction of the refinement of the KK-part at iteration $n - 1$ of the operator \hat{B} in MPS-notation. We see that the operator $\hat{B}_{\text{KK}}^{[n-1]}$ is mapped onto either the kept or discarded space of iteration n resulting in DD-, DK-, KD-part which connect states of iteration n only and an KK-part which will be further refined in later iterations. (b) In the energy level diagram one nicely sees that this way of refining the operator \hat{B} does not lead to double-counting of basis states. Each of the discarded states yields exactly one matrix element with each other state at that iteration (blue arrows with DD, DK, KD) while the matrix elements between kept states only (blue arrow with KK) are taken care of only in the next iteration which do not connect to the discarded states at iteration n (yellow arrows).

as happened in previous approaches and (ii) we only consider matrix elements between states within the same Wilson shell (i.e. of the same iteration) which are calculated with the same level of accuracy. In particular, the latter implies that the time evolution of the operator, $\hat{B}(t) = e^{i\hat{H}t} \hat{B} e^{-i\hat{H}t}$, evaluated within the NRG approximation contains only differences of eigenenergies of the same shell:

$$[\hat{B}_{\text{XX}}^{[n]}(t)]_{ss'} \simeq [\hat{B}_{\text{XX}}^{[n]}]_{ss'} e^{it(E_s^n - E_{s'}^n)}. \quad (4.59)$$

4.6 Density matrix

Having obtained an energy eigenbasis of \hat{H}_N we can finally turn towards the calculation of physical properties of the system. The starting point is to express the full density matrix $\hat{\rho} = e^{-\beta\hat{H}_N}/Z$ at temperature T , $\beta^{-1} = k_B T$, in terms of the Anders-Schiller basis:

$$\hat{\rho} \simeq \sum_{n>n_0}^N \sum_{se} \frac{e^{-\beta E_s^n}}{Z} |se\rangle_n^D \langle se|_n = \sum_{n>n_0}^N w_n \hat{\rho}_{\text{DD}}^{[n]}, \quad (4.60)$$

using the NRG approximation. We have

$$\hat{\rho}_{\text{DD}}^{[n]} = \frac{1}{Z_n} \sum_s e^{-\beta E_s^n} |s\rangle_n^{\text{D}} \langle s|_n^{\text{D}}, \quad (4.61\text{a})$$

$$Z_n = \sum_s^{\text{D}} e^{-\beta E_s^n} \rightarrow \text{tr} \hat{\rho}_{\text{DD}}^{[n]} = 1, \quad (4.61\text{b})$$

$$w_n = \frac{Z_n d^{N-n}}{Z} \rightarrow \sum_n w_n = 1, \quad (4.61\text{c})$$

which means that the environmental states are taken care of by the degeneracy factor d^{N-n} in w_n and otherwise do not need to be considered. To be precise, the $\hat{\rho}_{\text{DD}}^{[n]}$ on the r.h.s. of Eq. (4.60) are not defined in the same Hilbert space as $\hat{\rho}$ because we skipped the environmental states, as these contribute in the form of the degeneracy factor only. Note that here we need the physical value of the energies E_s^N , i.e. we need to undo the rescaling and energy shifting from the renormalization procedure, cf. Sec. 4.4.1.

The definitions above were chosen such that the $\hat{\rho}_{\text{DD}}^{[n]}$ have the interpretation of a proper density matrix at iteration n with typical energy scale δ_n which contribute to the full density matrix with weight w_n . The latter consist of two competing elements: the degeneracy factor d^{N-n} and the sum of the Boltzmann weights Z_n . The first will decrease with increasing iteration number n while the latter increases as the energy scale δ_n approaches $k_B T$, reflecting the fact that for $\delta_n \lesssim k_B T$ the thermal fluctuations are strong enough to excite the system. Thus we expect that the weights w_n are peaked at $\delta_n \approx k_B T$, see Fig. 4.9.

Even for calculations at zero temperature, it is advisable to use a finite temperature. The reason is that for zero temperature the density matrix reduces to the ground states only (ignoring degeneracy for the moment) which has a certain set of symmetries, in particular some particle number Q which has an *integer* value due to our finite size description. Moreover, due to the even-odd alternations (cf. Sec. 4.4.2) this value will possibly vary for even and odd iterations as Q_1 and $Q_2 \neq Q_1$, respectively. Per construction, the ground state will have zero overlap to any state with a particle number $Q' \neq Q$ different from its own. In particular, it may be that the ground state at even iterations has finite overlap to some state with particle number Q_1 while the ground state at odd iterations has zero overlap to the very same state. Being interested in thermodynamic quantities in the limit $T \rightarrow 0$, we choose some effective temperature T which is much smaller than any inherent or emerging energy scales of the system to circumvent the problem above while still simulating essentially zero temperature physics.

If one wants to stick to strictly zero temperature for finite chain length N or is interested in the properties of the ground state at iteration N only, the density matrix acquires the following form:

$$\hat{\rho}_{\text{G}} \equiv \frac{1}{d_{\text{G}}} \sum_{s \in \text{G}} |s\rangle_N^{\text{D}} \langle s|_N^{\text{D}}, \quad (4.62)$$

where G represents the d_{G} -fold degenerate ground state space.

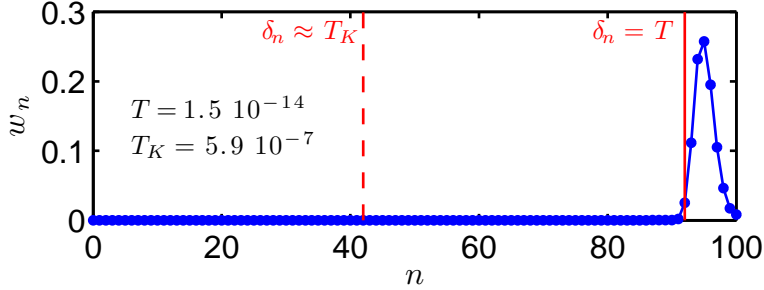


Figure 4.9: Distribution of the weights w_n along the chain of length N at temperature T for the symmetric SIAM with $U = 0.6$, $\varepsilon_d = -U/2$ and $\Gamma = 0.02$. We see that the distribution has significant values only for $\delta_n \lesssim T$ (indicated by the red vertical solid line with $k_B \equiv 1$). The value for T is deliberately chosen such that the peak is close to the end of the chain to simulate zero temperature. Indeed we have $T \ll T_K$, the lowest physical energy scale in the problem.

4.7 Spectral functions

The dynamics of the impurity in thermal equilibrium can be described well in terms of spectral functions. These have the general form

$$\mathcal{A}_{BC}(\omega) = \int \frac{dt}{2\pi} e^{i\omega t} \langle \hat{B}(t) \hat{C} \rangle_T, \quad (4.63)$$

for two operators \hat{B} and \hat{C} acting on the first n_0 sites only. The thermal average is given by the general Lehmann representation:

$$\langle \hat{B}(t) \hat{C} \rangle_T \equiv \text{tr}(\rho \hat{B}(t) \hat{C}) = \sum_{i,j} \frac{e^{-\beta E_i}}{Z} \langle i | \hat{B}(t) | j \rangle \langle j | \hat{C} | i \rangle. \quad (4.64)$$

Plugging in the time-evolution $\hat{B}(t) = e^{i\hat{H}t} \hat{B} e^{-i\hat{H}t}$ and Fourier transforming yields

$$\mathcal{A}_{BC}(\omega) = \sum_{i,j} \frac{e^{-\beta E_i}}{Z} \langle i | \hat{B} | j \rangle \langle j | \hat{C} | i \rangle \delta(\omega - (E_j - E_i)). \quad (4.65)$$

Local density of states

Another useful quantity is the local density of states $A(\omega)$, defined as the Fourier transform of the retarded Green's function $\mathcal{G}^R(t) = -i\theta(t) \langle \{ \hat{d}_\mu(t), \hat{d}_\mu^\dagger \} \rangle_T$:

$$A(\omega) \equiv -\frac{1}{\pi} \Im[\mathcal{G}^R(\omega)]. \quad (4.66)$$

The details of this definition are a bit different from that of Eq. (4.63), cf. Sec. 8.3.3 in [68]. However, its Lehmann representation is similar to that of Eq. (4.65):

$$A(\omega) = \sum_{i,j} \frac{e^{-\beta E_i} + e^{-\beta E_j}}{Z} |\langle i|\hat{d}|j\rangle|^2 \delta(\omega - (E_j - E_i)). \quad (4.67)$$

A particularly useful property of the local density of states is that for $T = 0$ (or $T \approx 0$, see Sec. 4.6) its negative frequency part gives the local occupation of the dot level

$$\langle \hat{n}_\mu \rangle_{T=0} = \langle \hat{d}_\mu^\dagger \hat{d}_\mu \rangle = \sum_{\omega < 0} A(\omega). \quad (4.68)$$

Spectral functions and quantum quenches

In this thesis, we study the effect of quantum quenches, i.e. the abrupt change from an initial Hamilton operator \hat{H}_i to a final Hamilton operator \hat{H}_f , see Sec. 3.5. To this end we consider spectral functions as in Eq. (4.63), but with slightly changed definitions. First of all, we assume that initially the system is in thermal equilibrium with respect to the Hamilton \hat{H}_i . Then, at $t = 0$ the operator \hat{C} switches the system from \hat{H}_i to \hat{H}_f , while at time t the operator \hat{B} switches the system back to \hat{H}_i . This results in a *mixed* time-evolution (see Sec. 3.5.2 for a motivation) with initial states given by the density matrix $\hat{\rho}_i$:

$$\langle \hat{B}(t)\hat{C} \rangle_T \equiv \text{tr}(\hat{\rho}_i \hat{B}(t)\hat{C}) = \text{tr}(\hat{\rho}_i e^{i\hat{H}_i t} \hat{B} e^{-i\hat{H}_f t} \hat{C}), \quad (4.69)$$

and a corresponding spectral function of the form

$$\mathcal{A}_{BC}(\omega) = \sum_{i,f} \frac{e^{-\beta E_i^{(i)}}}{Z} \langle i|\hat{B}|f\rangle \langle f|\hat{C}|i\rangle \delta(\omega - (E_f^{(f)} - E_i^{(i)})), \quad (4.70)$$

where the states $|i\rangle$ and $|f\rangle$ are energy eigenstates of \hat{H}_i and \hat{H}_f , respectively. Thus, we need two NRG calculations for the Hamilton operators \hat{H}_i and \hat{H}_f and in the following derivations one uses two sets of A -matrices instead of one, e.g. in Eq. (4.72) the states corresponding to s and s' are (approximate) eigenstates of \hat{H}_i and \hat{H}_f , respectively.

Technical details

To depict the technical details of the calculation of the spectra we focus on Eq. (4.63) and write it in terms of the density matrix in Eq. (4.60):

$$\mathcal{A}_{BC}(\omega) = \sum_n w_n \mathcal{A}_{BC}^{(n)}(\omega) \equiv w_n \sum_n \int \frac{dt}{2\pi} e^{i\omega t} \text{tr}(\hat{B}(t)\hat{C}\hat{\rho}_{\text{DD}}^{[n]}), \quad (4.71)$$

Smooth curves

A numerical calculation of a spectral function will always yield a set of discrete data points (ω_j, a_j) , i.e. we obtain a “raw” spectral function

$$\mathcal{A}_{\text{raw}}(\omega) = \sum_j a_j \delta(\omega - \omega_j), \quad (4.75)$$

consisting of a series of delta-peaks. In order to obtain a smooth curve from this data we broaden the raw spectral function [69] in that we convolve it with a broadening kernel $K(\omega, \omega')$:

$$\mathcal{A}(\omega) \equiv \int d\omega' K(\omega, \omega') \mathcal{A}_{\text{raw}}(\omega'). \quad (4.76)$$

Throughout this thesis we use the choice of [67] where for $|\omega'| \gtrsim \omega_0$ a log-Gaussian kernel is applied, while in the regime around zero frequency, $|\omega'| \lesssim \omega_0$, a regular Gaussian is applied to obtain finite values for $\omega \rightarrow 0$. The threshold frequency ω_0 is chosen such that the inevitable low-frequency oscillations which come from the underlying logarithmic discretization are smeared out. Optimal values for ω_0 are around the temperature T , where we used $\omega_0 = T/2$. However, the transition from log-Gaussian to regular Gaussian is not abrupt but smooth in that for $|\omega'| < \omega_0$ a mixture between both is applied where the log-Gaussian fraction is suppressed exponentially with decreasing ω' [70].

The log-Gaussian, which is a regular Gaussian with width σ on a logarithmic scale, is defined as

$$L(\omega, \omega') \equiv \frac{\theta(\omega\omega')}{\sqrt{\pi}\sigma|\omega|} e^{-\left(\frac{\log|\omega/\omega'|}{\sigma} - \frac{\sigma}{4}\right)^2} \quad (4.77)$$

i.e. it treats high- and low-frequency data in the same way and conserves the overall spectral weight, $\int d\omega \mathcal{A}(\omega) = \int d\omega' \mathcal{A}_{\text{raw}}(\omega')$. The influence of the broadening parameter σ is such that larger values lead to a stronger smearing of spectral features, where it needs to be adjusted such that it does not obscure physical details but still suppresses signatures of the discretization. In most cases $\sigma \approx 0.6$ produced good results, but the best choice highly depends on Λ and the specific kind of spectral features which one physically expects (peaks at certain frequencies, power-law behaviour for small or large frequencies, etc.).

Self-energy representation

Another improvement of the spectral data is obtained by the self-energy representation [71]. However, as this technique was not applied throughout this thesis we will just note that the improvement is based on an equation of motion approach. There, the correlator constituting the spectral function is related to the self-energy which in turn is given by the ratio of two correlators. Therefore, by calculating two correlators and dividing one by the other a lot of unwanted dependencies on the discretization and other artificial parameters cancel.

4.8 Expectation values

Apart from spectral functions one might also be interested in the expectation value of some operator, say \hat{F} , which necessarily consists of an even number of fermionic creation and annihilation operators, so that we do not need to care about fermionic signs. We have two possibilities for the calculation of such expectation values.

Via spectral functions

In Eq. (4.68) we already showed how to calculate an expectation value from a spectral function, but only in a special case. Generally, an expectation value can be obtained from Eq. (4.63) by setting $\hat{B} = \hat{F}$ and $\hat{C} = \mathbb{1}$ ($\mathbb{1}$ being the unit operator in the space where \hat{F} is defined) or vice versa, where \hat{F} typically acts only on the first n_0 sites. We have

$$\langle \hat{F} \rangle_T = \int d\omega \mathcal{A}_{F\mathbb{1}} = \int d\omega \mathcal{A}_{\mathbb{1}F}, \quad (4.78)$$

which can be easily seen from Eq. (4.65). Conceptual this is an easy way to calculate an expectation value as no new technique needs to be implemented.

Of course it is also possible to simplify the procedure from the previous section to expectation values,

$$\langle \hat{F} \rangle_T = \sum_n w_n \langle \hat{F} \rangle_{(n)} \equiv \sum_n w_n \text{tr}(\hat{F} \hat{\rho}_{\text{DD}}^{[n]}), \quad (4.79)$$

with

$$\langle \hat{F} \rangle_{(n)} = \sum_{m > n_0}^n \sum_X \sum_s [F_{\text{XX}}^{[m]} \rho_{\text{XX}}^{[mn]}]_{ss}, \quad (4.80)$$

and all other definitions as before.

Approximation for small temperatures

Consider an operator \hat{F} which acts in the local Hilbert space of site m_0 only. If the temperature is much smaller than the energy scale δ_{m_0} such that

$$\hat{\rho}_{\text{DD}}^{[m \leq m_0]} \approx 0, \quad (4.81)$$

we may neglect these parts of the density matrix and Eq. (4.79) reduces to

$$\langle \hat{F} \rangle_T = \sum_{n > m_0}^N \sum_s [(A_{\text{KK}}^{[m_0] \dagger} F A_{\text{KK}}^{[m_0]}) \rho_{\text{KK}}^{[m_0 n]}]_{ss}, \quad (4.82)$$

with definitions as in Eq. (4.74). This can be explained as follows: instead of expressing the operator \hat{F} in the full AS basis, determining its action in all following iterations, we

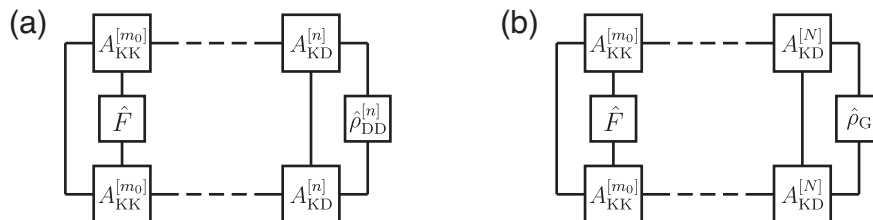


Figure 4.11: (a) A single term of the sum in Eq. (4.82). We see how the density matrix at iteration n is traced back into the kept space of iteration m_0 and how the operator \hat{F} is transformed from the local space of that iteration into the kept space. (b) At zero temperature this reduces to only a single term with $n = N$ where the density matrix representing the ground state space is applied.

only express it in the kept space of iteration m_0 and determine how the density matrix acts in that space, see Fig. 4.11(a) for a pictorial explanation.

In particular, Eq. (4.82) is exact when considering zero temperature. Then the only non-zero contribution to the density matrix comes from the ground state space of iteration N , $\hat{\rho}_{\text{G}}$ from Eq. (4.62), and the sum reduces to the $n = N$ term, see Fig. 4.11(b).

This procedure is easily generalized to operators acting on several sites up to iteration m_0 . The only difference is that one first needs to map these operators from the local spaces of previous iterations into the kept space of iteration m_0 , similar to the mapping from the local space of iteration m_0 to the kept space at iteration m_0 in Eq. (4.82) (the expression in parentheses).

4.9 Overlap calculations in the context of Anderson Orthogonality

A major task of this work is to investigate the various manifestations of Anderson Orthogonality (see Sec. 3.5). In this context we need to calculate the overlap between two ground states as a function of system size, which means as a function of iteration number, cf. Sec. 4.3. In Sec. 6.1 we present an extensive study on how this can be achieved. Thus, here we will show only the technical details of the final version thereof.

Consider two Hamiltonians, \hat{H}_i and \hat{H}_f , which we want to investigate in terms of Anderson Orthogonality. We calculate the overlap $z(n)$ with $n < N$ between their respective ground states as a function of system size like

$$\begin{aligned}
 z^2(n) &\equiv \text{tr}_{\text{K}}^{\text{F}}(\hat{\rho}_{\text{G}}^{\text{I}}) \\
 &= \frac{1}{d_{\text{G,I}}} \sum_{s \in \text{G}} \sum_{s'} | \langle s | s' \rangle_n^{\text{K,I}} \langle s | s' \rangle_n^{\text{K,F}} |^2, \tag{4.83}
 \end{aligned}$$

where the superscripts I and F denote from which Hamiltonian the respective quantity is derived from. Note that we take the ground state space for \hat{H}_i , but the full kept space for

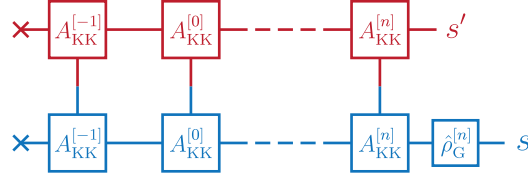


Figure 4.12: Graphical depiction of the ground state overlap in Eq. (4.83). The states of \hat{H}_i and \hat{H}_f are depicted in blue and red, respectively, and $\hat{\rho}_G^{[n]}$ is the density matrix of the ground state space at iteration n .

\hat{H}_f , for technical reasons elucidated in Sec. 6.1. The actual calculation of the overlap is best depicted graphically, see Fig. 4.12.

4.10 Scattering phase shifts from the energy flow diagram

A useful feature of the energy flow diagram is that one can easily deduce the scattering phase shifts (see Sec. 3.5) of the problem, given the system is still a Fermi liquid. We know that the excitation spectrum of a Fermi liquid resembles that of the free Fermi gas, cf. Sec. 2.1. In particular, it can be described in terms of a shifted equidistant free-particle spectrum.

When the stable low-energy fixed point is approached the spectrum of the Hamiltonian \hat{H}_N is self-similar w.r.t. the addition of an additional site. In particular, the spectrum is that of a system of size $L \propto \Lambda^{n/2}$ in units of $2\pi v_F/L$. Taking insights from boundary conformal field theory [72, 73], we find that this fixed-point spectrum is universal and, in case of a Fermi liquid, the full many-body spectrum can be written in terms of a simple fixed-point Hamiltonian in Fourier space [73]:

$$\hat{H}_{\text{fp}} = \frac{2\pi}{L} \sum_{\mu} \sum_q \left(q - \frac{\delta_{\mu}}{\pi} \right) \hat{c}_{\mu q}^{\dagger} \hat{c}_{\mu q}, \quad (4.84)$$

where the $\hat{c}_{\mu q}^{(\dagger)}$ represent effectively free particles and q takes integer (half-integer) values for even (odd) values of N . The shift by $\Delta_{\mu} \equiv \delta_{\mu}/\pi$ represents the influence of the impurity, where an attractive phase shift shifts the spectrum downwards. This allows us to identify (up to a multiplicative constant C) how a certain energy level can be constructed from the excitation spectrum of \hat{H}_{fp} , by attaching the quantum numbers to the spectrum of \hat{H}_N . To be more precise:

$$\lim_{N \rightarrow \infty} \hat{H}_N = C \frac{L}{2\pi} \hat{H}_{\text{fp}}, \quad (4.85)$$

where C is some constant to be determined from the NRG spectra. Thus for sufficiently

large N (for example in Fig. 4.3 for $N \gtrsim 70$) we may set

$$\hat{H}_N = C \sum_{\mu} \sum_q (q - \Delta_{\mu}) \hat{c}_{\mu q}^{\dagger} \hat{c}_{\mu q}, \quad (4.86)$$

where at iteration N the system consists of $N + 2$ sites, cf. Fig. 4.1(c). The ground state is

$$|G\rangle = \prod_{\mu} \prod_{q, (q - \Delta_{\mu}) \leq 0} \hat{c}_{\mu q}^{\dagger} |0\rangle, \quad (4.87)$$

with particle number Q_0 . For simplicity, in the following we will consider even N and therefore the lowest excitations are those with an extra particle in the first level above the Fermi level ($Q = Q_0 + 1$) or a hole at the first level below the Fermi level ($Q = Q_0 - 1$), having energy $C(1 - \Delta_{\mu})$ and $C\Delta_{\mu}$, respectively. Another excitation is the particle-hole pair, consisting of the latter, with energy C , see Fig. 4.13(a). Thus, identifying these three excitations per electron species allows us to calculate all phase shifts δ_{μ} , see Fig. 4.13(b). If we have as many quantum numbers as electron species this procedure is easily applied, while for less symmetries one has to sample which excitation belongs to which electron species [73].

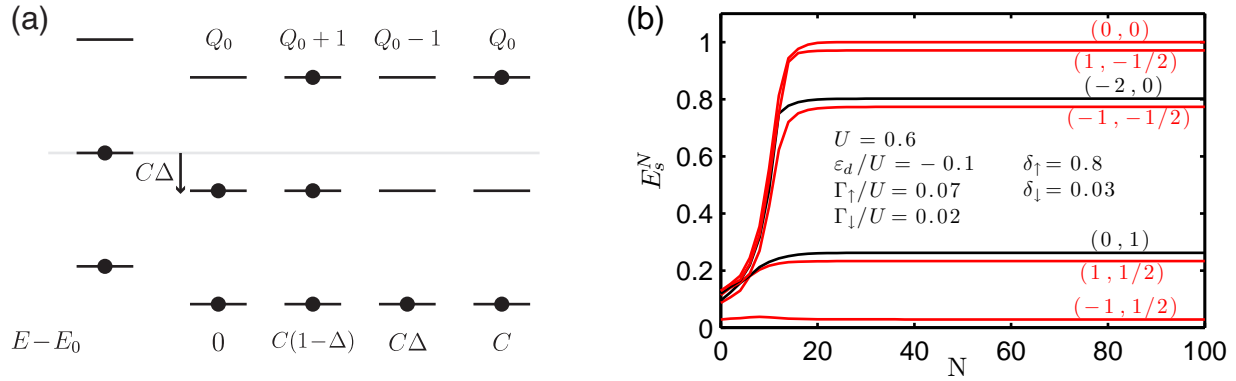


Figure 4.13: In panel (a) we consider, for simplicity, $n_c = 1$, even N and an attractive phase shift δ . The first level diagram shows a real free-particle spectrum, showing a level at the Fermi energy with zero energy and thus the ground state, in this case, is degenerate. The interaction-induced phase shift shifts the levels down by $\Delta = \delta/\pi$, thereby lifting the degeneracy. For this case, the ground state with energy E_0 and particle number Q_0 is given by the second level diagram. The other three level diagrams show the first three excitations (together with their respective particle number and energy $E - E_0$): an additional particle directly above the Fermi level, a hole directly below the Fermi level and a particle-hole pair consisting of these two. In panel (b) we show how to extract the phase shifts from the even- N fixed-point spectrum for an asymmetric SIAM (cf. Eqs. (4.3a) and (4.21)) with parameters specified in the figure legend. The symmetries of the levels are given as (Q, S_z) , where the ground state (with energy 0) has symmetry $(0, 0)$. The red lines have energy (from top to bottom): C (degenerate level corresponding to spin up and down particle-hole pair, respectively), $C(1 - \Delta_\downarrow)$ (additional spin down particle), $C\Delta_\uparrow$ (spin up hole), $C(1 - \Delta_\uparrow)$ (additional spin up particle) and $C\Delta_\downarrow$ (spin down hole). The extracted values for δ_\uparrow and δ_\downarrow (see figure legend) can be used to determine the energy of the other levels for consistency, which holds with good accuracy.

Part II

Results

Chapter 5

The correlation density matrix

In this chapter we present our results for the correlation density matrix (CDM) [3] as already introduced in Chap. 1. As our publication in the New Journal of Physics presents an extensive study of the CDM we will only give an outline to the paper here:

- The general motivation to establish the concept of the CDM is given in the introductory part of the paper. It outlines the usefulness of a method to find the dominant correlations in a quantum ladder system in an unbiased way without using prior knowledge.
- The second section becomes concrete in proposing the *dominant operator basis* (DOB) method, motivated from Luttinger Liquid theory. This method extracts from the CDM a short list of operators that carry the dominant correlations, together with the set of their mutual correlation functions.
- In the third section we introduce our model, a class of spinless extended Hubbard models for fermions, which contains rich physics and its treatment can readily be generalized to other models. We shortly outline the expectations for simple limiting cases and introduce the smooth boundary conditions, an adoption from open boundary conditions to improve the numerical simulation of infinite systems.
- The fourth section deals with the technical complexities of the calculation of the CDM using DMRG like finite size effects and numerically broken symmetries (e.g. translational invariance).
- The fifth section shows how we decompose the CDM into the DOB and investigate the long-range behaviour of their mutual correlation functions. Moreover, we propose a way to further reduce the number of operators by further analysing the distance dependence of the correlation functions.
- In sections six to eight we show how we calculate the CDM for our model and apply the DOB method. We investigate all arising operators and compare our results to previous results for that model.

- Sections nine and ten give conclusions and an outlook to previous applications, followed by an extensive appendix about the details of our implementation of DMRG.

New Journal of Physics

The open-access journal for physics

Correlation density matrices for one-dimensional quantum chains based on the density matrix renormalization group

W M \ddot{u} nder^{1,3}, A Weichselbaum¹, A Holzner¹, Jan von Delft¹
and C L Henley²

¹ Physics Department, Arnold Sommerfeld Center for Theoretical Physics and Center for NanoScience, Ludwig-Maximilians-Universit \ddot{a} t, 80333 Munich, Germany

² Laboratory of Atomic and Solid State Physics, Cornell University, Ithaca, NY, 14853-2501, USA

E-mail: wolfgang.muender@physik.uni-muenchen.de

New Journal of Physics **12** (2010) 075027 (50pp)

Received 4 February 2010

Published 28 July 2010

Online at <http://www.njp.org/>

doi:10.1088/1367-2630/12/7/075027

Abstract. A useful concept for finding numerically the dominant correlations of a given ground state in an interacting quantum lattice system in an unbiased way is the correlation density matrix (CDM). For two disjoint, separated clusters, it is defined to be the density matrix of their union minus the direct product of their individual density matrices and contains all the correlations between the two clusters. We show how to extract from the CDM a survey of the relative strengths of the system's correlations in different symmetry sectors and the nature of their decay with distance (power law or exponential), as well as detailed information on the operators carrying long-range correlations and the spatial dependence of their correlation functions. To achieve this goal, we introduce a new method of analysing the CDM, termed the dominant operator basis (DOB) method, which identifies in an unbiased fashion a small set of operators for each cluster that serve as a basis for the dominant correlations of the system. We illustrate this method by analysing the CDM for a spinless extended Hubbard model that features a competition between charge density correlations and pairing correlations, and show that the DOB method successfully identifies their relative strengths and dominant correlators. To calculate the ground state of

³ Author to whom any correspondence should be addressed.

2

IOP Institute of Physics Φ DEUTSCHE PHYSIKALISCHE GESELLSCHAFT

this model, we use the density matrix renormalization group, formulated in terms of a variational matrix product state (MPS) approach within which subsequent determination of the CDM is very straightforward. In an extended [appendix](#), we give a detailed tutorial introduction to our variational MPS approach for ground state calculations for one-dimensional quantum chain models. We present in detail how MPSs overcome the problem of large Hilbert space dimensions in these models and describe all the techniques needed for handling them in practice.

Contents

1. Introduction	3
2. Goals of the DOB method	4
3. Model	6
3.1. Definition of the model	6
3.2. Expectations for simple limiting cases	7
3.3. Smooth boundary conditions	8
4. Calculation of the CDM	8
4.1. Definition of the CDM	8
4.2. DMRG calculation of the CDM	9
4.3. Symmetry sectors	10
4.4. ‘Restoration’ of numerically broken symmetries	10
5. Finding a distance-independent DOB	11
5.1. Need for operator bases for clusters A and B	11
5.2. Construction of the DOB	12
5.3. Definition of f -matrix	13
5.4. Fourier analysis and decay of f -matrix	14
6. Numerical results: general remarks	15
6.1. Specification of clusters A and B	15
6.2. Average site occupation	16
6.3. Rms net correlations $w_{\Delta N}(r)$	17
7. Numerical results: symmetry sectors	18
7.1. Charge-density correlations	18
7.2. One-particle correlations	23
7.3. Two-particle correlations	26
8. Comparison to previous results	27
9. Conclusions	30
10. Outlook: larger cluster sizes	31
Acknowledgments	31
Appendix. The variational MPS approach	32
References	50

1. Introduction

In an interacting quantum lattice model, the ground state may have several kinds of correlations, such as long-range order, power-law or exponentially decaying correlations. In the numerical treatment of such a model, it is not clear *a priori* what kind of correlation will be dominant and what kind of operators corresponds to these correlations. Before calculating correlation functions, one typically chooses in advance which operators to consider, using prior knowledge and making initial assumptions. The need to make such choices introduces a certain bias into the investigation, which can be somewhat unsatisfying, especially when hidden or exotic correlations are present.

The correlation density matrix (CDM) has been proposed by Cheong and Henley [1] as an unbiased tool to discover the dominant kind of correlations between two separated clusters, given the density matrix for their union (obtained by tracing out the rest of the system). For two disjoint, separated clusters A and B the CDM is defined to be the density matrix of their union minus the direct product of their respective density matrices to get rid of trivial correlations,

$$\hat{\rho}^C \equiv \hat{\rho}^{A \cup B} - \hat{\rho}^A \otimes \hat{\rho}^B, \quad (1.1)$$

which is completely unbiased except for the specification of the clusters. If the two clusters were not correlated at all, this would imply $\hat{\rho}^{AB} = \hat{\rho}^A \otimes \hat{\rho}^B$ and therefore $\hat{\rho}^C = 0$. The CDM encodes all possible correlations between clusters A and B , as can be seen from the fact that

$$\begin{aligned} \text{tr}(\hat{\rho}^C \hat{O}^A \otimes \hat{O}'^B) &= \text{tr}(\hat{\rho}^{A \cup B} (\hat{O}^A \otimes \hat{O}'^B)) - \text{tr}((\hat{\rho}^A \hat{O}^A) \otimes (\hat{\rho}^B \hat{O}'^B)) \\ &= \langle \hat{O}^A \hat{O}'^B \rangle - \langle \hat{O}^A \rangle \langle \hat{O}'^B \rangle \equiv C_{\hat{O} \hat{O}'}, \end{aligned} \quad (1.2)$$

where \hat{O}^A and \hat{O}'^B are operators acting on clusters A and B , respectively.

The very fact that the CDM encodes all possible correlations between two clusters also implies that it is a rather complex, unwieldy object. Indeed, if clusters A and B each have n sites and the local Hilbert space per site is d , the CDM can be represented as a matrix with d^{2n} elements. Moreover, this matrix will typically be calculated as a function of separation r between the clusters. Thus, even if the CDM is already known (e.g. via a highly accurate method for calculating ground states, such as DMRG), it is a highly nontrivial challenge to extract useful, easily digestible information from the mass of data that constitutes the CDM.

The goal of this paper is to propose a systematic method for meeting this challenge. It will be referred to as the dominant operator basis (DOB) method below. The DOB method extracts from the CDM only the dominant correlations of the model, does so in an unbiased fashion and efficiently truncates all information pertaining to correlations of negligible weight. In particular, the DOB method produces a short (!) list of operators per cluster that carry the dominant correlations, together with the set of their mutual correlation functions. This list constitutes the model's DOB (hence the method's proposed name). It turns out that it is possible to formulate the DOB method rather succinctly in general, abstract terms: we do so in the space of just more than three pages, in section 5, which constitutes the heart of this paper and presents its central conceptual advances. Moreover, the general formulation of the DOB method does not depend on cluster size; although in this paper 'cluster' refers to a small number of contiguous sites and we have tried and tested the method only for small clusters, we formulate the method in full generality for clusters of arbitrary size.

To illustrate how the DOB method works in practice, we have chosen to apply it to a certain extended Hubbard model, due to Cheong and Henley [2], involving correlated hopping of

spinless fermions on a two-leg chain. We have two main reasons for this particular choice: firstly, the model shows a rather nontrivial competition between charge density (CD) correlations and pairing correlations, providing a challenging test for a method designed to discover a model's dominant correlations without prior information. Secondly, exact results on this model are available in various limiting regions of parameter space, obtained in [2] using nontrivial mappings to hardcore bosons and free fermions. This information serves as a useful consistency check for the results of our numerical analysis. We would like to emphasize, however that it is *not* our purpose to analyse this model in comprehensive detail (indeed, we study only one particular regime of its large parameter space), nor to calculate its dominant correlation functions with very high accuracy (e.g. to determine the exponents characterizing power-law decays with very small error bars). While the DOB is certainly capable of producing such information (the only prerequisite is that the CDM that is fed into the DOB method needs to be calculated with sufficient accuracy), such a study is beyond the scope of the present work and is left for a separate investigation. Instead, since our interest here is primarily in methodology, we will be content to use this model as a vehicle for illustrating the DOB method in action.

The CDM in [1] was calculated using the full ground state obtained from exact diagonalization. This limits the system size, so that the method was appropriate mainly in cases of rapidly decaying or non-decaying correlations—not for critical or slowly decaying ones. In the present work, we use the density matrix renormalization group (DMRG) [3, 4] (see the excellent review by Schollwöck [5]) to compute the ground state for a ladder system that is known to have algebraic correlations [2]. We use the matrix product state (MPS) formulation of DMRG [6] in which an efficient variational procedure is used to obtain the ground state.

The structure of the main body of the paper is as follows: in section 2, we outline the ideas behind the DOB method in general terms. In section 3, we introduce the model to be considered for explicit calculations. In section 4, we show how the CDM is defined, how to calculate it and explain how a first survey of the relative strengths of various types of correlations can be obtained. In section 5, we give a detailed exposition of the DOB method for constructing a DOB. Sections 6–8 present our numerical results. Our conclusions are given in section 9 and an outlook in section 10. In an extended appendix, we offer a tutorial introduction to the MPS formulation of DMRG and also explain how it can be used to efficiently calculate the CDM.

2. Goals of the DOB method

To extract useful information from the CDM, it will be helpful to develop some intuition of its general structure. To this end, let us recall some fundamental facts from one-dimensional critical fermion systems. They are described by the Luttinger liquid theory, in which one of the key parameters is the Fermi wave vector k_F . The asymptotic behaviour of any kind of correlation or Green's function is typically an oscillation inside a power-law envelope,

$$C(r) \sim \cos(mk_F r + \phi) / r^\gamma, \quad (2.1)$$

for some exponent γ , where m is some integer. For the particular model to be used in this study, a nontrivial mapping is known to a free fermion chain [2], a special case of a Luttinger liquid.

The renormalization group theory [7] quite generally implies the existence of *scaling operators* in any critical system such as a Luttinger liquid. They are eigenvectors of the renormalization transformation and, consequently, their correlations are purely of a form like (2.1) for all r , not just asymptotically. The scaling operators usually have complicated forms.

The correlation of a simple operator (e.g. fermion density $n(x)$ at position x along a chain) has overlap with various scaling operators, and correspondingly the correlation function of that simple operator is a linear combination of contributions like (2.1) from those scaling operators.

Our aim is to discover the leading scaling operators numerically. The leading scaling operator encodes all the local fluctuations that are correlated with faraway parts of the system. Intuitively, for a given cluster A , that operator does not depend significantly on the exact position of the (distant) cluster B . That is particularly obvious in a one-dimensional system: any correlation at distances $r' > r$ must be propagated through some sort of correlation at r , so we expect the same operators from cluster A to be involved in $\hat{\rho}^C(r)$, irrespective of the distance r .

This suggests an ansatz for leading contributions in the CDM:

$$\hat{\rho}^C(r) = \sum_s \hat{O}^{A,s} \otimes \hat{O}^{B,s} c_s \frac{e^{ik_s r}}{r^{\gamma_s}}. \quad (2.2)$$

Here $\hat{O}^{A,s}$ and $\hat{O}^{B,s}$ are a pair of (distance-independent) scaling operators acting on clusters A and B , respectively, k_s is the characteristic wave vector for oscillations in their correlation, and γ_s is the corresponding scaling exponent. When $k_s \neq 0$, the operator pairs must themselves come in pairs, labelled, say, by s and $s+1$, with $k_{s+1} = -k_s$, $c_{s+1} = c_s^*$, and $\gamma_{s+1} = \gamma_s$, so that $\hat{\rho}^C$ is Hermitian. The scaling operators for each cluster form an orthonormal set. We expect that only a few terms in the sum in (2.2) capture most of the weight. Correspondingly, it may be feasible to truncate the complete basis sets $\hat{O}^{A,s}$ and $\hat{O}^{B,s}$ to a smaller set of ‘dominant operators’, whose correlators carry the dominant correlations of the system. The ansatz (2.2) will guide our steps in the ensuing analysis; at the end, we shall check how well it is satisfied by the actual CDMs calculated for the model studied in this paper (see section 7.1.2).

Note that although a particular correlation function may have nodes, see (2.1), for a CDM of the form (2.2) the norm

$$\|\hat{\rho}^C(r)\|^2 = \sum_s \frac{|c_s|^2}{r^{2\gamma_s}} \quad (2.3)$$

is monotonically decaying with r . This expresses the fact that information can only be lost with increasing distance, never restored, in a one-dimensional system.

In [1], the operators entering the dominant correlation were found by a kind of singular value decomposition (SVD), which was done independently for each separation. However, the operators obtained from the SVD will in general be different for different separations r . This does not correspond to the form (2.2), where the operators are distance independent and only the coefficients are r dependent. Therefore, we shall explore in this paper a new scheme to decompose the CDMs for all separations in concert, so as to obtain a small set of scaling operators characterizing the dominant correlations at any (sufficiently large) separation. We decompose $\hat{\rho}^C$ in the form

$$\hat{\rho}^C(r) = \sum_{S_i} \left(\sum_{\mu\mu'} f^{\mu,\mu'}(r) \hat{O}^{A,\mu} \otimes \hat{O}^{B,\mu'} \right)_{S_i}, \quad (2.4)$$

where the S_i represent the symmetry sectors of the discrete, Abelian symmetries of the Hamiltonian (see section 4.3). The subscript of the brackets indicates that the decomposition within the brackets is done for each symmetry sector individually. This decomposition is

6

IOP Institute of Physics Φ DEUTSCHE PHYSIKALISCHE GESELLSCHAFT

possible for any two complete, r -independent operator sets $\hat{O}^{A,\mu}$ and $\hat{O}^{B,\mu'}$ acting on the part of the Hilbert space of clusters A and B , respectively, which correspond to the symmetry sector S_i . The goal is to find two operator sets $\hat{O}^{A,\mu}$ and $\hat{O}^{B,\mu'}$ such that these operator sets may be truncated to a small number of operators each, while still bearing the dominant correlations of the system. These truncated sets of operators will constitute the desired DOBs for the two clusters. The distance dependence of the CDM is then only contained in the matrix $f^{\mu,\mu'}(r)$. Then, all the analysis concerning the distance-dependence of correlations can be done in terms of this f -matrix.

3. Model

To be concrete in the following analysis of the CDM, we begin by introducing the model for which we did our numerical calculations. This model contains rich physics and its treatment below can readily be generalized to other models.

3.1. Definition of the model

We analyse the CDM for a class of spinless extended Hubbard models for fermions, which was intensely studied by Cheong and Henley [2]. They computed correlation functions up to separations of about $r = 20$, using nontrivial mappings to free fermions and hardcore bosons. The correlation functions are calculated with an intervening-particle expansion [2], which expresses the correlation functions in terms of one-dimensional Fermi-sea expectation values (an evaluation of the CDM for that model has also been done by Cheong and Henley [1], using exact diagonalization, but the system sizes are too short to be conclusive). For spinless fermions on a two-leg ladder with length N , we use the following Hamiltonian:

$$\begin{aligned}
 H = & -t_{\parallel} \sum_{a=1}^2 \sum_{x=1}^{N-1} (\hat{c}_{a,x}^{\dagger} \hat{c}_{a,x+1} + \text{h.c.}) - t_{\perp} \sum_{x=1}^N (\hat{c}_{1,x}^{\dagger} \hat{c}_{2,x} + \text{h.c.}) \\
 & - t_c \sum_{x=2}^{N-1} (\hat{c}_{1,x-1}^{\dagger} \hat{n}_{2,x} \hat{c}_{1,x+1} + \hat{c}_{2,x-1}^{\dagger} \hat{n}_{1,x} \hat{c}_{2,x+1} + \text{h.c.}) \\
 & + V \sum_{a=1}^2 \sum_{x=1}^{N-1} \hat{n}_{a,x} \hat{n}_{a,x+1} + V \sum_{x=1}^N \hat{n}_{1,x} \hat{n}_{2,x}, \tag{3.1}
 \end{aligned}$$

where $\hat{c}_{a,x}$ destroys a spinless fermion on leg a and rung x and $\hat{n}_{a,x} = \hat{c}_{a,x}^{\dagger} \hat{c}_{a,x}$ is the corresponding number operator. Effectively, the model corresponds to a one-dimensional pseudo-spin chain, where the $a = 1$ leg is denoted by spin \uparrow and the $a = 2$ leg by spin \downarrow . Hence, in the following sections, which generally apply to quantum chain models, we will treat this model as a quantum chain consisting of N sites and return to view the system as a ladder model in the sections where we discuss our results. We define the filling ν to be the average number of particles per site (see equation (3.2) below).

We will focus on infinite nearest-neighbour repulsion $V \rightarrow \infty$, which we implement differently along the legs and the rungs in our numerical calculations. In the pseudo-spin description, we can enforce the nearest-neighbour exclusion along the rungs by removing double occupancy from the local Hilbert space of the pseudo-spin sites. The nearest-neighbour

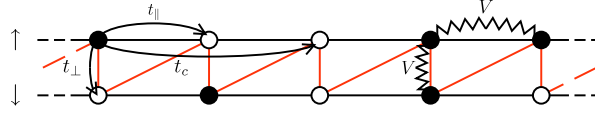


Figure 1. Ladder model with the terms of the Hamiltonian in (3.1). Fermions are depicted by black circles and empty lattice positions by white circles. The ordering used for our Jordan–Wigner transformation of fermionic creation and annihilation operators is depicted by the red line.

exclusion along the legs cannot be implemented so easily and we mimic $V \rightarrow \infty$ by a value of V that is much larger than all the other energies in the Hamiltonian (typically $V/t_{\parallel} = 10^4$).

For fermionic systems, the fermionic sign due to the anti-commutation relations of the fermionic creation and annihilation operators needs to be taken into account. Specifically, we have to choose an order in which we pick the Fock basis, where we have to keep in mind that this choice produces a so-called Jordan–Wigner string of the form $\sum_{x'=x+1}^{x'-1} e^{i\pi n_{x'}}$ when evaluating correlators $\langle \hat{c}_x \hat{c}_{x'}^{\dagger} \rangle$ at distance $r = |x - x'|$. In the present system, it is convenient to choose this order such that the operators of the two sites of a rung are succeeding each other (see figure 1), as this choice yields the shortest Jordan–Wigner strings.

3.2. Expectations for simple limiting cases

Setting $t_{\parallel} \equiv 1$ as a reference scale, we are left with two parameters in the Hamiltonian: the rung hopping t_{\perp} and the correlated hopping t_c . The physics of the system is governed by the competition of t_{\perp} to localize the fermions on the rungs and t_c to pair the fermions. There are three limiting cases that have been studied in detail by Cheong and Henley [1, 2].

- (i) The paired limit, $t_c \gg t_{\parallel}$, t_{\perp} (we used $t_c/t_{\parallel} = 10^2$ and $t_{\perp} = 0$ for our calculations). In this limit, the fermions form tight pairs that behave similarly to hardcore bosons [2]. For two given rungs x and $x + 1$, there are two possibilities to create a pair of fermions, due to infinite nearest-neighbour repulsion: $\hat{c}_{\uparrow x}^{\dagger} \hat{c}_{\downarrow, x+1}^{\dagger}$ and $\hat{c}_{\downarrow x}^{\dagger} \hat{c}_{\uparrow, x+1}^{\dagger}$. It has been shown in [2] that, based on these two bound pairs, one may classify the bound pairs in two flavours along the ladder and that the ground state has only one definite flavour, causing a twofold symmetry breaking in the ground state. This symmetry breaking introduces complications that will be addressed below. The dominant correlations are expected to be charge-density correlations at short distances and two-particle correlations at long distances. These charge-density and two-particle correlations decay as power laws, oscillating with $k = 2k_F$, where the Fermi wavelength k_F is related to the filling as $k_F = \pi\nu$ [2]. In this system, the one-particle correlations are suppressed and are expected to decay exponentially, as a nonzero expectation value depends on a local fluctuation completely filling the rungs between the clusters (as elaborated in section 7.2).
- (ii) The two-leg limit, $t_{\perp} \ll t_{\parallel}$, $t_c = 0$. In this limit, the two legs are decoupled with respect to hopping, but still the infinite nearest-neighbour repulsion introduces correlations between the two legs. At large distances, power-law charge-density correlations dominate, while

two-particle correlations show much faster power-law decay and one-particle correlations decay exponentially.

- (iii) The rung-fermion limit, $t_{\perp} \gg t_{\parallel}$, $t_c = 0$. In this limit, the particles are delocalized along the rungs. For fillings smaller than quarter filling, charge-density, one-particle and two-particle correlations all decay as power laws where charge-density correlations dominate at large distances.

Our analysis in this paper is limited to case (i), where DMRG also showed the best performance.

3.3. Smooth boundary conditions

For a ladder of length N (treated as a pseudo-spin chain), we have attempted to reduce effects from the boundaries by implementing *smooth boundary conditions*, adapting a strategy proposed in [8] for a spin chain to our present fermionic system. (Alternatively, it is possible to use periodic boundary conditions [6]. However, this leads to some difficulties, since it is not possible to work with orthonormal basis sets describing the left or right part of the chain with respect to a given site.) Smooth boundary conditions are open boundary conditions together with an artificial decay of all terms of the Hamiltonian over the last M rungs at each end of the chain. We shall calculate expectation values only of operators located in the central part of the system (sites x , with $M < x \leq N - M$); thus the system's effective length is $N' = N - 2M$. For the numerical results presented in this paper, we choose the following combinations of chain length and boundary size: $(N, M) = (100, 20)$, $(150, 30)$ and $(200, 40)$.

For both smooth and open boundary conditions, the average site filling strongly decreases near the boundaries. To determine the average filling ν , which influences the system's correlations in an important manner, we thus use only the central N' sites:

$$\nu = \sum_{x=M+1}^{N-M} (\langle \hat{n}_{\uparrow x} \rangle + \langle \hat{n}_{\downarrow x} \rangle) / (2N'). \quad (3.2)$$

Due to the infinite nearest-neighbour repulsion, this implies that $\nu \in [0, 0.5]$.

4. Calculation of the CDM

Throughout the paper we will use the Frobenius inner product and norm for any matrices M_{ij} and M'_{ij} of matching dimension,

$$\langle M, M' \rangle \equiv \sum_{ij} M_{ij}^* M'_{ij} = \text{tr}(M^{\dagger} M'), \quad (4.1)$$

$$\|M\| \equiv \langle M, M \rangle^{1/2}. \quad (4.2)$$

4.1. Definition of the CDM

We take two disjoint, separated clusters A and B of equal size from a one-dimensional quantum chain, i.e. two sets of adjacent sites x_1^A, \dots, x_n^A and x_1^B, \dots, x_n^B , where n is the size of the clusters and all the indices x are distinct from each other. In the present study, both clusters will comprise only two rungs, i.e. they support only 'local' operators. While the formulation of the DOB method is independent of cluster size, the version presented here has been tailored to

situations where the cluster used is the smallest possible one consistent with the symmetries of the important operators. We have not tested its performance for larger clusters.

The local Hilbert spaces of clusters A and B with dimension d^n are described in terms of sets of basis states $|\alpha\rangle$ and $|\beta\rangle$, which are product states of the local states of each site in the cluster. The CDM of the two clusters, defined by (1.1), can be expanded in this basis as

$$\hat{\rho}^C = \rho_{\alpha\beta\alpha'\beta'}^C |\alpha\rangle|\beta\rangle\langle\alpha'|\langle\beta'|. \quad (4.3)$$

For processing the CDM we fuse the two indices of each cluster [1]:

$$\tilde{\rho}_{\tilde{\alpha}\tilde{\beta}}^C \equiv \tilde{\rho}_{(\alpha\alpha')(\beta\beta')}^C |\alpha\rangle\langle\alpha'| |\beta\rangle\langle\beta'| \quad (4.4)$$

with $\tilde{\alpha} = (\alpha\alpha')$ and $\tilde{\beta} = (\beta\beta')$, and denote the reshaped object $\tilde{\rho}^C$ itself by an extra tilde. This corresponds to a partial transpose of the CDM (note that $\tilde{\rho}^C$ is no longer a symmetric tensor). For the CDM expressed in the indices $\tilde{\alpha}$ and $\tilde{\beta}$, we may use the Frobenius inner product (4.1) and norm (4.2).

To study the distance dependence of the correlations, we vary the position of clusters A and B , resulting in a position-dependent CDM $\tilde{\rho}^C(x_1^A, x_1^B)$. If the system is translationally invariant, this object depends only on the distance $r = |x_1^A - x_1^B|$ (the minimal distance for two adjacent clusters is equal to the cluster size n). For a finite system, however, $\tilde{\rho}^C$ will also depend on $(1/2)(x_1^A + x_1^B)$, at best weakly if the system is long. Strategies for minimizing the dependence on $(1/2)(x_1^A + x_1^B)$ by taking suitable averages will be discussed in section 4.4.

4.2. DMRG calculation of the CDM

The fact that the Hamiltonian in (3.1) is a one-dimensional pseudo-spin chain allows us to calculate ground state properties with the DMRG [3, 4]. Using the variational MPS formulation of that method (see the appendix for a detailed description), we calculated the ground state of the Hamiltonian in (3.1) for several values of t_\perp and t_c . The framework of MPS also allows the CDM to be calculated efficiently (see section A.2.7 for details). Limiting ourselves to the case $t_\perp = 0$ in this paper, we have calculated the CDM derived from the ground state for distances up to 40 rungs, which is significantly larger than in previous approaches.

We used chain lengths of $N = 100, 150$ and 200 and limited the maximal Hilbert space dimension during the DMRG sweeps to less than ~ 200 . This dimension is sufficient to retain all contributions larger than 10^{-6} , with respect to the singular value spectrum on each bond (see section A.2.5), which means that the discarded part of the reduced density matrix at each step is less than 10^{-12} . We believe that this choice is sufficient to represent the ground state good enough to extract power-law correlations. We can trust the CDMs calculated from these ground states up to distances of $r \approx 37$, because for larger r all correlations start to decay exponentially (even if they showed power-law decay for $r \lesssim 37$). This is a well-known artefact of DMRG (see [5], in particular section III.A and figure 12, for an example). The reason for the exponential decay is the limited Hilbert space dimension for the effective state spaces. Even if the dimension is large enough to represent the ground state faithfully, it still imposes an upper bound on the entanglement entropy going through the bond between two sites. Thus, correlations between clusters close to this bond are represented faithfully, while for larger distances the correlations between two clusters are not well captured any more. The distance up to which correlations are represented faithfully can be increased, if desired, by allowing for a larger Hilbert space dimension [9], but for present purposes this was not necessary (as illustrated by figure 12 below).

4.3. Symmetry sectors

All the symmetries of the Hamiltonian are reflected in the CDM, making the CDM block-diagonal, where each block can be labeled uniquely by a set of quantum numbers that are conserved by the Hamiltonian. This means, for Abelian symmetries (which are the only ones we are considering in practice), that the CDM in the original form $\rho_{\alpha\beta,\alpha'\beta'}^C$ fulfills $Q_\alpha + Q_\beta = Q_{\alpha'} + Q_{\beta'}$, where Q_α corresponds to the quantum numbers of state $|\alpha\rangle$, etc. The rearrangement of the CDM into $\tilde{\rho}_{\tilde{\alpha}\tilde{\beta}}^C$ then implies $\Delta Q_{\tilde{\alpha}} = -\Delta Q_{\tilde{\beta}}$ with $\Delta Q_{\tilde{\alpha}} \equiv Q_\alpha - Q_{\alpha'}$ and $\Delta Q_{\tilde{\beta}} \equiv Q_\beta - Q_{\beta'}$. Since $\hat{\rho}^{AB}$ is Hermitian, for every block of the CDM involving $\Delta Q_{\tilde{\alpha}}$ ($\Delta Q_{\tilde{\beta}}$) there has to be a block involving $-\Delta Q_{\tilde{\alpha}}$ ($-\Delta Q_{\tilde{\beta}}$), respectively. Therefore, it is convenient to sort the various parts of the CDM in terms of their change in quantum numbers $\Delta Q \equiv |\Delta Q_{\tilde{\alpha}}| = |\Delta Q_{\tilde{\beta}}|$ and to analyse each symmetry sector individually.

To obtain a general classification of the CDM, we sort the various contributions of the CDM according to the conserved quantum number(s) Q . In the case of the Hamiltonian in (3.1), we consider particle conservation ($Q = \hat{N}_{\text{tot}}$) which breaks the CDM into blocks with well-defined particle transfer $\Delta N \equiv |\Delta N_{\tilde{\alpha}}| = |\Delta N_{\tilde{\beta}}|$ between clusters A and B . The following rms net correlations then are a measure of the correlations with transfer of ΔN particles between A and B (with $\Delta N = 0, 1, 2$):

$$w_{\Delta N}^2(r) = \sum_{\tilde{\alpha}\tilde{\beta} \in \mathcal{S}_{\Delta N}} |\tilde{\rho}_{\tilde{\alpha}\tilde{\beta}}^C(r)|^2, \quad (4.5)$$

where $\sum_{\Delta N=0}^2 w_{\Delta N}^2(r) = \|\rho^C(r)\|^2$. Here the notation $\tilde{\alpha} \equiv (\alpha\alpha') \in \mathcal{S}_{\Delta N}$ indicates that only pairs of states $(\alpha\alpha')$ are considered that differ by ΔN in particle number (similarly for $\tilde{\beta} \equiv (\beta\beta') \in \mathcal{S}_{\Delta N}$). In the following, we will call correlations involving $\Delta N = 0, 1, 2$ particles *charge-density* correlations (CD), *one-particle* correlations (1P) and *two-particle* correlations (2P), respectively. The following analysis is done for each symmetry sector individually. Depending on the decay of the rms net correlations (4.5), some symmetry sectors may become irrelevant with increasing distance.

4.4. 'Restoration' of numerically broken symmetries

Although we have tried to minimize the effect of boundaries, our numerical methods for calculating the ground state and CDM do not produce strictly translationally invariant results. (In contrast, analyses based on exact diagonalization start from a ground state wave function in which the symmetry (in a finite system) is restored even if there is a symmetry breaking in the thermodynamic limit.) Therefore, we construct the CDM $\tilde{\rho}^C(r)$ for a given distance r from an average over several CDMs $\tilde{\rho}^C(x, x')$ with constant $r = |x - x'|$, where x and x' give the position of the first site of clusters A and B , respectively.

Moreover, if the exact ground state is degenerate under a discrete symmetry, we expect that DMRG breaks this symmetry unless it is implemented explicitly in the code. As mentioned in section 3.2 for the specific models of this paper, we expect a discrete symmetry under interchange of legs for some parameter regimes. Since we did not implement this symmetry explicitly in our code, we also average the CDM by interchanging the legs of the ladder. Thus, all the data analysis presented in subsequent sections will be based on using the following

‘symmetry-restored’ form of the CDM:

$$\tilde{\rho}^C(r) = \frac{1}{\mathcal{N}} \sum_{xx', |x-x'|=r} (\tilde{\rho}^C(x, x') + \tilde{\rho}'^C(x, x')), \quad (4.6)$$

where $\tilde{\rho}'^C$ is obtained from $\tilde{\rho}^C$ by interchanging the legs of the ladder, and \mathcal{N} is some normalization factor.

One might argue that it is not sufficient to average over the broken symmetry w.r.t. leg-interchange on the level of the density matrix, but that instead the symmetry should be restored on the level of the ground state wave function. Specifically, for a ground state $|\psi_1\rangle$ (however it is calculated) that breaks this symmetry, we could restore the symmetry in the following way:

$$|\psi^+\rangle = \frac{1}{\sqrt{2}}(|\psi_1\rangle + |\psi_2\rangle), \quad (4.7)$$

where $|\psi_2\rangle = \hat{S}|\psi_1\rangle$ and \hat{S} describes the action of interchanging the legs. This would lead to a total density matrix

$$|\psi^+\rangle\langle\psi^+| = \frac{1}{2} (|\psi_1\rangle\langle\psi_1| + |\psi_2\rangle\langle\psi_2| + |\psi_1\rangle\langle\psi_2| + |\psi_2\rangle\langle\psi_1|). \quad (4.8)$$

Now, for two clusters A and B , the first two terms on the rhs yield the CDM of (4.6), whereas the last two terms turn out to be negligible when traced out over all sites except for the two *local* clusters A and B . This follows from $|\psi_1\rangle$ and $|\psi_2\rangle$ being orthogonal, hence $\text{tr}(|\psi_1\rangle\langle\psi_2|) = \langle\psi_2|\psi_1\rangle = 0$, implying that for a long chain with local clusters A and B , the reduced density matrix $\hat{\rho}^{AB,12} \equiv \text{tr}_{x \notin A, B}(|\psi_1\rangle\langle\psi_2|)$ will be very close to zero, since the wave functions of $|\psi_1\rangle$ and $|\psi_2\rangle$ are essentially orthogonal on the sites outside clusters A and B . Consequently, it is sufficient to retain only the first two terms of (4.8), i.e. to restore the broken symmetry on the level of the density matrices only, as done in (4.6).

The preceding arguments could, in principle, be verified explicitly by implementing the rung symmetry in the numerical DMRG code (i.e. excluding the possibility of symmetry breaking by construction).

5. Finding a distance-independent DOB

The goal of this section is to extract a (likely) small set of operators from the CDM, which constitute the system’s DOB and whose correlators describe the system’s dominant correlations. We will assume in this section that the CDM does not include any broken symmetries as indicated in section 4.4.

5.1. Need for operator bases for clusters A and B

As already mentioned, the CDM (obtained from (4.6)) may be investigated by applying a SVD for each distance individually [1]:

$$\tilde{\rho}_{\tilde{\alpha}\tilde{\beta}}^C = \sum_s w^s O_{\tilde{\alpha}}^{A,s} \otimes O_{\tilde{\beta}}^{B,s}, \quad (5.1)$$

or in operator notation:

$$\hat{\rho}^C = \sum_s w^s \hat{O}^{A,s} \otimes \hat{O}^{B,s}, \quad (5.2)$$

where $\hat{O}^{A,s}$ and $\hat{O}^{B,s}$ act on clusters A and B , respectively. Here the singular values w^s are strictly positive real numbers. By construction, $\hat{O}^{A,s}$ and $\hat{O}^{B,s}$ form orthonormal sets in their corresponding Hilbert spaces, i.e. $O_{\alpha}^{A,s} = O_{\alpha\alpha'}$ and $O_{\beta}^{B,s} = O_{\beta\beta'}$ form a complete set in the operator space of clusters A and B , respectively, using the inner product as in (4.1). The set includes operators with $w_s = 0$, such as the identity operator, since these will be produced by the SVD. The SVD (5.2) yields for each specific distance r a set of operators $\hat{O}^{A,s}(r)$ and $\hat{O}^{B,s}(r)$ acting on clusters A and B , respectively.

However, the dominant operators so obtained, i.e. the ones with large weight from the SVD of $\tilde{\rho}^C(r)$, are likely not the same as each other for different distances and hence not convenient for characterizing the ‘dominant correlations’ of the system. What is needed, evidently, is a strategy for reducing the numerous sets of operators $\hat{O}^{A,s}(r)$ and $\hat{O}^{B,s}(r)$ to two ‘basis sets of operators’ for clusters A and B , respectively, the DOB $\hat{O}^{A,\mu}$ and $\hat{O}^{B,\mu}$, which are r -independent and whose correlators yield the dominant correlations in the system in the spirit of (2.2). (For a translationally invariant system the two sets have to be equal for both clusters A and B , but we will treat them independently in the analysis.) Following the ansatz (2.2) from the Luttinger liquid theory, these operators ought to be distance independent, carrying common correlation content for all distances. Thus, we seek an expansion of $\tilde{\rho}^C(r)$ of the form (2.4), in which *only* the coefficients, not the operators, are r -dependent.

5.2. Construction of the DOB

We have explored a number of different strategies for extracting operators from the CDM which carry common information for all distances. We will discuss in detail only one of these, which is rather simple to formulate and reliably yields operator sets with the desired properties. (Several other strategies yielded equivalent results, but in a somewhat more cumbersome fashion.)

The simplest possible strategy one may try is to average over all the CDMs at different distances and to singular-value decompose the resulting crude ‘average CDM’. However, since the elements for the CDM are expected to be oscillating functions of r , such a crude average can cancel out important contributions of the CDM. Thus we need a procedure that avoids such possible cancellations. To this end, we construct the following operators, bi-linear in the CDM:

$$\hat{K}^A(r) \equiv \text{tr}_B(\hat{\rho}^{C\dagger}(r)\hat{\rho}^C(r))/\|\hat{\rho}^C\|^2, \quad (5.3a)$$

$$\hat{K}^B(r) \equiv \text{tr}_A(\hat{\rho}^C(r)\hat{\rho}^{C\dagger}(r))/\|\hat{\rho}^C\|^2, \quad (5.3b)$$

with matrix elements

$$K_{\alpha\alpha'}^A(r) = \sum_{\beta} \tilde{\rho}_{\alpha\beta}^C(r)\tilde{\rho}_{\alpha'\beta}^{C*}(r)/\|\tilde{\rho}^C(r)\|^2, \quad (5.4a)$$

$$K_{\beta\beta'}^B(r) = \sum_{\alpha} \tilde{\rho}_{\alpha\beta}^C(r)\tilde{\rho}_{\alpha\beta'}^{C*}(r)/\|\tilde{\rho}^C(r)\|^2. \quad (5.4b)$$

We normalize by $\|\tilde{\rho}^C(r)\|^2$ in order to treat the operator correlations of $\tilde{\rho}^C(r)$ for different distances on an equal footing. Note that the eigenvalue decomposition on the Hermitian matrices $K^A(r)$ and $K^B(r)$ (in short K -matrices) yields the same operators $\hat{O}^A(r)$ and $\hat{O}^B(r)$ as the SVD of $\tilde{\rho}^C(r)$, with eigenvalues being equal to singular values squared, up to the additional

normalization factor $\|\tilde{\rho}^C(r)\|^2$. (The reason is that for a matrix of the form $M = uv^\dagger$ we have $MM^\dagger = us^2u^\dagger$ and $M^\dagger M = vs^2v^\dagger$.)

The object \hat{K}^X (for $X = A, B$) is positive-definite, and according to ansatz (2.2), it is expected to have the form

$$\hat{K}^X(r) = \mathcal{N}_K^{-1} \sum_s \frac{|c_s|^2}{r^{2\gamma_s}} \hat{O}^X \hat{O}^{X\dagger}. \quad (5.5)$$

In particular, it no longer contains any oscillating parts (in contrast to (2.2)) and, hence, is suitable for being averaged over r .

Summing up the \hat{K}^X -matrices over a range R of distances ($r \in R$, where R will be specified below) gives a mean \bar{K}^X -matrix for cluster $X (= A, B)$, namely $\bar{K}^{X,R} \equiv \sum_{r \in R} \hat{K}^X(r)$. We do not divide the latter expression by the number of terms in the sum (as would be required for a proper mean), as at this stage we are only interested in the operator eigendecomposition,

$$\bar{K}^{X,R} = \sum_{\mu} w^{R,\mu} (\hat{O}^{X,R,\mu} \otimes \hat{O}^{X,R,\mu\dagger}), \quad (5.6)$$

with the operators normalized such that $\|\hat{O}^{X,R,\mu}\| = 1$. The operator set $\hat{O}^{X,R,\mu}$ gives an orthonormal, r -independent basis for cluster X . In practice, however, many of the $w^{R,\mu}$ (which turn out to be the same for $X = A$ or B) will be very small. Thus, it will be sufficient to work with a truncated set of these operators having significant weight.

To explore the extent to which \bar{K}^X depends on the summation range, we shall study several such ranges: R_{all} includes all distances, R_{short} short distances (first third of distances analysed), R_{int} intermediate distances (second third) and R_{long} long distances (last third). The resulting (truncated) sets of operators can be compared via their mutual overlap matrix $O_{\mu\mu'}^{RR'} = \text{tr}(\hat{O}^{R,X,\mu} \hat{O}^{R',X,\mu'})$, or more simply, by the single number $O^{RR'} = \sum_{\mu\mu'} (O_{\mu\mu'}^{RR'})^2$, which may be interpreted as the dimension of the common subspace of the two operator sets. The value of $O^{RR'}$ ranges from 0 to $\text{dim}(\hat{O}^{R,X,\mu})$. By comparing $O^{RR'}$ for the different distance ranges, additional clues can be obtained about how the relative weight of correlations evolves from short to long distances. (Such a comparison is carried out in table 1 below.)

5.3. Definition of f -matrix

Once two convenient DOBs for each cluster, the sets of operators $\hat{O}^{A,\mu}$ and $\hat{O}^{B,\mu}$, have been found, the CDM can be expanded in terms of these bases as in (2.4),

$$\tilde{\rho}_{\alpha\beta}^C(r) = \sum_{\mu\mu'} f^{\mu,\mu'}(r) O_{\alpha}^{A,\mu} O_{\beta}^{B,\mu'}, \quad (5.7)$$

with matrix elements

$$f^{\mu,\mu'}(r) \equiv \sum_{\alpha\beta} \tilde{\rho}_{\alpha\beta}^C(r) O_{\alpha}^{A,\mu} O_{\beta}^{B,\mu'}. \quad (5.8)$$

For complete operator bases $\hat{O}^{A,\mu}$ and $\hat{O}^{B,\mu'}$, by definition, the set of amplitudes squared sum up to the norm of the CDM:

$$\sum_{\mu\mu'} |f^{\mu,\mu'}(r)|^2 = \|\tilde{\rho}^C(r)\|^2. \quad (5.9)$$

Table 1. Comparison of the operator sets on cluster A for a filling of $\nu = 0.286$, calculated for chain length $N = 100$. (The results for $\nu = 0.248$ and other chain lengths are similar, with only minor differences.) The first and second columns of the table give the number of operators kept and the corresponding smallest singular value of the set of operators $\hat{O}^{A, R_{\text{all}}, \mu}$ obtained from the full range of distances R_{all} . The other three columns show $O^{R_{\text{all}} R_{\text{short}}}$, $O^{R_{\text{all}} R_{\text{int}}}$ and $O^{R_{\text{all}} R_{\text{long}}}$ for the given number of operators.

Number of operators	$w^{R_{\text{all}}, \mu} / w^{R_{\text{all}}, 1}$	$O^{R_{\text{all}} R_{\text{short}}}$ (short)	$O^{R_{\text{all}} R_{\text{int}}}$ (intermediate)	$O^{R_{\text{all}} R_{\text{long}}}$ (long)
1	1	1	0.99	1
2	0.784 122	1.99	2	2
3	0.579 242	2.99	3	3
4	0.176 043	3.99	4	4
5	0.011 250	5	5	4.99
6	0.003 040	6	6	5.99
7	0.000 004	7	6	6
8	0.000 001	8	6	6
9	0.000 001	9	6	6
10	0.000 001	10	6	6

However, as alluded to above, we expect that the dominant correlators can be expressed in terms of a *truncated* set of dominant operators. If the sum on the lhs of (5.9) is restricted to this truncated set, its deviation from the rhs gives an estimate of how well $\tilde{\rho}^C$ is represented by the DOB. It will turn out that only a handful of dominant operators (typically 4 or 6) are needed, implying very significant simplifications in the analysis. Thus, the data analysis will be done in terms of the matrices $f^{\mu, \mu'}(r)$ (in short ‘*f*-matrix’) based on the DOB.

5.4. Fourier analysis and decay of *f*-matrix

According to the expectations expressed in (2.2), the elements of the *f*-matrix are expected to be products of oscillating and decaying functions of r . The corresponding dominant wave vectors can be identified via Fourier transform on each element of the *f*-matrix. For an oscillating function times a monotonically decaying envelope, the peaks of the Fourier spectrum of the oscillating function will be broadened by the presence of the envelope. To minimize this unwanted broadening, we introduce a rescaled *f*-matrix (denoted by a tilde), $\tilde{f}^{\mu, \mu'}(r) = u(r) f^{\mu, \mu'}(r)$, where the positive weighting-function $u(r)$ is chosen such that all values of $|\tilde{f}^{\mu, \mu'}(r)|$ are of the same order, and we Fourier decompose the rescaled \tilde{f} -matrix as $\tilde{f}^{\mu, \mu'}(k) = \sum_r e^{-ikr} \tilde{f}^{\mu, \mu'}(r)$. Its norm $\|\tilde{f}(k)\|^2 = \sum_{\mu, \mu'} |\tilde{f}^{\mu, \mu'}(r)|^2$, plotted as a function of k , will contain distinct peaks that indicate which wave vectors characterize the dominant correlations. Subsequently, the elements of the *f*-matrix can be fitted to the form

$$f^{\mu, \mu'}(r) = \sum_j A_{\mu, \mu'}^{[j]} e^{ik_j r} f_j(r), \quad (5.10)$$

	$ 00\rangle$	$ 0\uparrow\rangle$	$ 0\downarrow\rangle$	$ \uparrow 0\rangle$	$ \downarrow 0\rangle$	$ \uparrow\downarrow\rangle$	$ \downarrow\uparrow\rangle$
$\langle 00 $	0			1			2
$\langle \uparrow 0 $							
$\langle \downarrow 0 $							
$\langle 0\uparrow $	1			$\Delta N = 0$			1
$\langle 0\downarrow $							
$\langle \downarrow\uparrow $							
$\langle \uparrow\downarrow $	-2			1			0

Figure 2. The symmetry sectors of an operator acting on a cluster of two rungs in the basis $|00\rangle, |0\uparrow\rangle, |0\downarrow\rangle, |\uparrow 0\rangle, |\downarrow 0\rangle, |\uparrow\downarrow\rangle, |\downarrow\uparrow\rangle$ in pseudo-spin notation.

where $A_{\mu,\mu'}^{[j]}$ are complex amplitudes, $f_j(r)$ describes the decay with distance (e.g. $f_j(r) = r^{-\gamma_j}$ or e^{-r/r_j} for power-law or exponential decay, respectively) and k_j is a set of dominant wave vectors. The latter appear pairwise in combinations $(+k; -k)$, since $f^{\mu,\mu'} \in \mathbb{R}$, which implies $A_{\mu,\mu'}^{[j]} = A_{\mu,\mu'}^{[j]*}$ for $k_i = -k_j$. The results of such a fit for each pair of dominant operators $\hat{O}^{A,\mu}$ and $\hat{O}^{B,\mu'}$ are the final outcome of our analysis, since it contains the information needed to check the applicability of ansatz (2.1).

6. Numerical results: general remarks

In this section, we illustrate the analysis proposed above for the model introduced in section 3. We will focus on the limiting case of large t_c (called ‘paired limit’ in [2], see section IV.B therein), which we expect to have the most complex behaviour among all three limiting cases introduced in [1, 2]. After some preliminary analysis, we will discuss in section 7 each of the three symmetry sectors (CD, 1P and 2P) characterized by the operators’ fermion number and, in section 8, compare our present results with those found in [2] using a different method.

6.1. Specification of clusters A and B

For the following analysis, it is convenient to take the size of clusters A and B to be two rungs, because clusters of at least that size allow for up to two particles in one cluster (due to infinite nearest-neighbour repulsion). Thus, correlations involving $\Delta N = 0, 1, 2$ are possible, i.e. CD, 1P and 2P correlations, respectively. Note that larger clusters can be studied, but that would significantly increase numerical costs. Taking into account the infinite nearest-neighbour repulsion, clusters of size two have a seven-dimensional Hilbert space spanned by the kets $|00\rangle, |0\uparrow\rangle, |0\downarrow\rangle, |\uparrow 0\rangle, |\downarrow 0\rangle, |\uparrow\downarrow\rangle, |\downarrow\uparrow\rangle$, where the first (second) entry corresponds to the first (second) rung, 0 represents an empty rung and \uparrow and \downarrow a fermion on the upper and lower legs in pseudo-spin notation (recall that we are dealing with spinless fermions). The space of operators acting on a cluster has dimension $7^2 = 49$, where the subspaces for $\Delta N = 0, 1$ or 2 have dimensions 21, 24 and 4, respectively, as depicted schematically in figure 2.

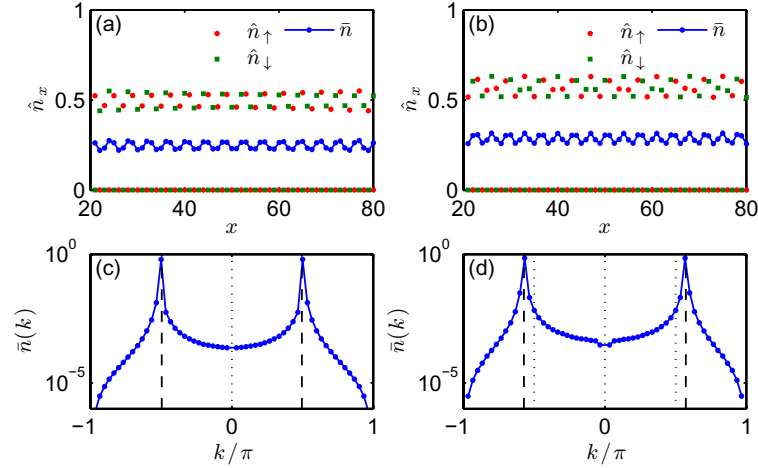


Figure 3. The average occupation along the legs of the ladder for a filling of $\nu = 0.248$ ((a) and (c)) and a filling of $\nu = 0.286$ ((b) and (d)). In ((a) and (b)), we show the average occupation \hat{n}_\uparrow on the upper leg (red) and \hat{n}_\downarrow on the lower leg (green), with every second value being zero. The end regions $i = 1, \dots, 20$ and $i = 81, \dots, 100$ were excluded in the figures and also in the analysis, as these are affected by the smooth open boundary condition. The leg symmetrized occupation $\bar{n} = \frac{1}{2}(\hat{n}_\uparrow + \hat{n}_\downarrow)$ (blue, the same for the upper and lower legs) eliminates this strong even–odd alternation but still shows small modulations. This can be seen in detail in the Fourier transform of the symmetrized occupation in (c) and (d). There is a clear peak at $k = \pm 2k_F$ (dashed vertical lines).

6.2. Average site occupation

As a first check of the influence of the boundaries, we investigate the average site occupation on the ladder. It is expected to be uniform in a translationally invariant system. However, there are two ways in which our calculation breaks translational symmetry, which cause residual oscillations in the density of particles along the ladders.

Firstly, there is the spontaneous breaking of the pair flavour symmetry described in section 3.2. In the ground state produced by DMRG, all pairs have the same flavour, so only one of the two sublattices actually has any fermions on it. Thus a strong alternation in the density is observed between one leg for even rungs and the other leg for odd rungs; this can be taken care of by the symmetrization with respect to legs (as in (4.6)).

Secondly, translational symmetry is broken due to finite size in the DMRG calculation. This induces oscillations in the average occupation as a function of x (see figure 3), whose period is clearly dependent on the filling. In fact, their period is $2k_F$, so they may be interpreted as Friedel-like oscillations caused by the boundaries. Although the amplitude of density oscillation appears rather flat in the central portion of the system, it does have a minimum there; so we expect that the amplitude in the centre of the system would vanish in a sufficiently large system.

Although the intent of the smooth boundary conditions is to minimize effects such as these oscillations, in fact, their amplitude appeared to be of about the same strength independent of whether we used smooth or plain open boundary conditions. We suspect, however, that the amplitude could be reduced by further careful optimization (not attempted here) of the parameters of the smooth boundary conditions.

6.3. Rms net correlations $w_{\Delta N}(r)$

The next basic step is to identify the leading correlations in terms of the rms net correlations $w_{\Delta N}$ defined in (4.5). These reveal which sectors of correlations dominate at large distances. The results (see figure 4) show that the rms net correlations decay exponentially in the 1P sector, whereas they decay algebraically in both the CD and 2P sectors, consistent with Cheong and Henley's work [2]. The latter two correlations are comparable in size over a significant range of distances, but for the fillings that we investigated, 2P correlations ultimately dominate over CD correlations at the largest distances.

Both the CD and 2P rms net correlations can be fitted to power laws, with the exponent dependent on the filling. The fitting of oscillating data—even if weakly oscillating—to a monotonic power law has to be done very carefully. As the correlations have the largest absolute value at short distances, the fitting is sensitive to these values and thus to the precise range of the fitting interval $[r_1, r_2]$ (compare the oscillations of the rms net correlations within the first ten sites in figure 4). Thus, we perform fits for \mathcal{N}_{r_1} different values of r_1 between 2 and $2 + \pi/k_F$ (i.e. covering one period of the oscillation), with r_2 fixed to the maximal distance available. Denoting the fitting result for a given r_1 by $\gamma[r_1]$, we take the mean value of the latter as our fitting result and the variance as the error of our fitting:

$$\gamma = \frac{1}{\mathcal{N}_{r_1}} \sum_{r_1=2}^{2+\pi/k_F} \gamma[r_1], \quad \delta\gamma = \left[\frac{1}{\mathcal{N}_{r_1}} \sum_{r_1=2}^{2+\pi/k_F} (\gamma - \gamma[r_1])^2 \right]^{1/2}. \quad (6.1)$$

The rms net correlations in each sector are monotonic and only weakly modulated, even though the dominant correlation functions and the dominant parts of the CDM itself are oscillating (as will be discussed in more detail in section 7.1; see e.g. figure 7). This implies that the correlations in each sector can be represented by a linear combination of correlation functions (associated with different operators) that oscillate out of phase, in such a way that in the sum of their squared moduli the oscillations more or less average out, resulting in an essentially monotonic decay with r , as expected according to (2.3).

We will next apply the analysis proposed in section 5.2 to the respective symmetry sectors (which will provide more exact fits of the exponents of the power law decays). The analysis in any sector consists of two stages. Firstly, following section 5.2, we try to find an optimal truncated basis that describes best the dominant correlations. Secondly, we examine the f -matrix of section 5.3 (i.e. represent the CDM in the truncated basis) to see the nature of its r dependence and to fit this to an appropriate form, following section 5.4.

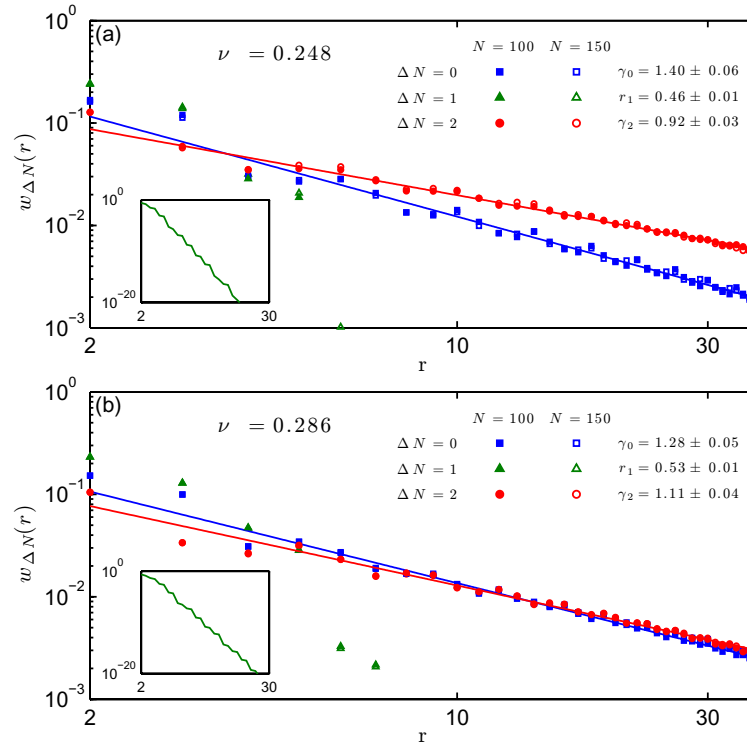


Figure 4. The rms net correlations of (4.5), plotted as a function of distance for a filling of (a) $\nu = 0.248$ and (b) $\nu = 0.286$, for chain lengths $N = 100$ (filled symbols) and $N = 150$ (open symbols). The symmetry sectors are $\Delta N = 0$ (squares, no particle transfer, CD), $\Delta N = 1$ (triangles, transfer of one particle, 1P) and $\Delta N = 2$ (dots, transfer of two particles, 2P). We see that CD and 2P correlations decay as power laws ($r^{-\gamma}$, solid lines) with small residual oscillations at $k = 2k_F$, while the 1P correlations show exponential decay (e^{-r/r_1} , see the semi-logarithmic plot in the inset). The results for different chain lengths differ only slightly (for most data points no open symbols are visible, because they overlap fully with filled symbols). Consequently, the values obtained for γ_0 , r_1 and γ_2 are the same for both chain lengths.

7. Numerical results: symmetry sectors

7.1. Charge-density correlations

7.1.1. Operator basis. The following analysis to obtain the DOB for the charge-density correlations is independent of filling and chain length. We obtain exactly the same DOB for

different fillings and chain lengths, but of course the coefficients of the f -matrix depend on the filling (not on the chain length). The functional form of the f -matrix is investigated in the next section.

First, we calculated the mean K -matrices $\bar{K}^{A,R}$ and $\bar{K}^{B,R}$ from $\bar{\rho}_R^C$ defined in (5.3a) and (5.3b) and obtained operator sets from their eigenvalue decomposition, using various distance ranges. In order to construct the DOB, we used the diagnostic described in section 5.2. In presenting the results, we limit ourselves to cluster A as the results for cluster B are completely analogous. The operator set $\hat{O}^{A,R_{\text{all}},\mu}$ corresponding to the full range of distances R_{all} (specified in section 5.2) is used as a reference set to be compared with the operator sets obtained from R_{short} , R_{int} and R_{long} . The results are given in table 1. We see that, for intermediate or long distances, the effective dimension ($O^{R_{\text{all}},R_{\text{int}}}$ and $O^{R_{\text{all}},R_{\text{long}}}$) of the common operator space shared between the operator set $\hat{O}^{A,R_{\text{all}},\mu}$ and the operator sets $\hat{O}^{A,R_{\text{int}},\mu}$ and $\hat{O}^{A,R_{\text{long}},\mu}$, respectively, saturates at six even if a larger operator space is allowed. Similarly, also the short-distance operator set $\hat{O}^{A,R_{\text{short}},\mu}$ agrees best with the other three operator sets at dimension six: a further increase of the number of operators, however, adds only operators in the short-range sector of the CDM. Hence, we construct the DOB as a six-dimensional operator set. Within this reduced operator space, all dominant correlations are well captured, as can be seen from the relative weights of table 1. For the resulting truncated basis set, equation (5.9) holds up to a relative deviation of the order of $\mathcal{O}(10^{-5})$.

Investigating the DOB in more detail reveals that it can be split into two sectors, classified by their symmetry with respect to interchanging the legs of the ladder, i.e. the operators obey $\hat{S}\hat{O}^{A,R_{\text{all}},\mu} = \pm\hat{O}^{A,R_{\text{all}},\mu}$, with \hat{S} describing the action of interchanging legs. The two subsets contain three operators each, which have positive or negative parity with respect to \hat{S} , respectively. It turns out that all six operators are linear combinations of operators having matrix elements on the diagonal only, in the representation of figure 2. Moreover, together with the unit matrix they span the full space of diagonal operators (therefore the dimension of $6 = 7 - 1$). Explicitly, the symmetric operators are given by

$$\hat{O}^1 = \frac{1}{\sqrt{12}} (-\hat{n}_{0,x}\hat{n}_{\uparrow,x+1} - \hat{n}_{\uparrow,x}\hat{n}_{0,x+1} + 2\hat{n}_{\uparrow,x}\hat{n}_{\downarrow,x+1} + \text{leg symmetrized}), \quad (7.1a)$$

$$\hat{O}^2 = \frac{1}{2} (\hat{n}_{0,x}\hat{n}_{\uparrow,x+1} - \hat{n}_{\uparrow,x}\hat{n}_{0,x+1} + \text{leg symmetrized}), \quad (7.1b)$$

$$\hat{O}^3 = \frac{1}{\sqrt{42}} [-6\hat{n}_{0,x}\hat{n}_{0,x+1} + (\hat{n}_{0,x}\hat{n}_{\uparrow,x+1} + \hat{n}_{\uparrow,x}\hat{n}_{0,x+1} + \hat{n}_{\uparrow,x}\hat{n}_{\downarrow,x+1} + \text{leg symmetrized})] \quad (7.1c)$$

and the antisymmetric operators by

$$\hat{O}^4 = \frac{1}{\sqrt{2}}\hat{n}_{0,x} (\hat{n}_{\uparrow,x+1} - \hat{n}_{\downarrow,x+1}), \quad (7.2a)$$

$$\hat{O}^5 = \frac{1}{\sqrt{2}} (\hat{n}_{\uparrow,x} - \hat{n}_{\downarrow,x}) \hat{n}_{0,x+1}, \quad (7.2b)$$

$$\hat{O}^6 = \frac{1}{\sqrt{2}} (\hat{n}_{\uparrow,x}\hat{n}_{\downarrow,x+1} - \hat{n}_{\downarrow,x}\hat{n}_{\uparrow,x+1}), \quad (7.2c)$$

20

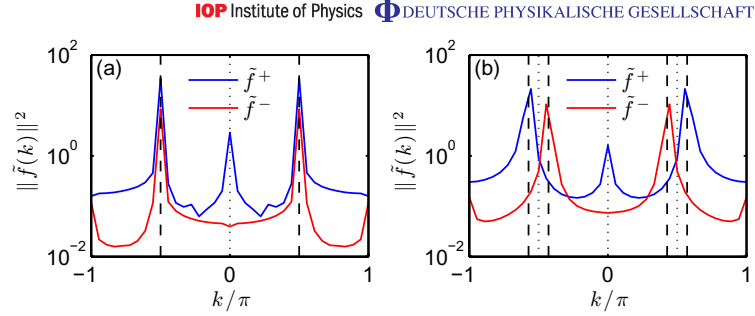


Figure 5. Fourier transform of the rescaled f -matrix \tilde{f} for CD correlations based on operators chosen from a reduced six-dimensional operator space, for a filling of (a) $\nu = 0.248$ and (b) $\nu = 0.286$. We obtain these Fourier spectra from the rescaled f -matrix $\tilde{f}^{\mu,\mu'}(r) = r^{\gamma''} f^{\mu,\mu'}(r)$, with γ'' extracted from a power law fit on $|f^{\mu,\mu'}(r)|$. The Fourier spectrum breaks up into a contribution coming from the operators symmetric or antisymmetric under leg interchange, labelled \tilde{f}^+ (blue) and \tilde{f}^- (red), respectively. The spectrum of \tilde{f}^+ shows strong peaks at $k = \pm 2k_F$ (dashed lines) and a smaller peak at $k = 0$ with $k_F/\pi = \nu$. The spectrum of \tilde{f}^- , having peaks at $k = \pm 2k_F + \pi$ (dashed lines) and $k = \pi$, is shifted w.r.t. \tilde{f}^+ by π . For a filling close to $\frac{1}{4}$ the dominant peaks of \tilde{f}^\pm , at $k = \pm 2k_F$ and $k = \pm 2k_F + \pi$, are nearly at the same position.

where $\hat{n}_0 = (1 - \hat{n}_\uparrow - \hat{n}_\downarrow)$. We use this operator basis for both cluster A and cluster B . If we calculate the f -matrix (5.7) based on these operators, we see that it breaks into two blocks corresponding to their symmetry with respect to leg interchange.

7.1.2. f -matrix elements: oscillations and decay. We now turn to extracting the distance dependence of the dominant correlation in this symmetry sector, which is now visualizable since we have drastically reduced the operator space to six dimensions. All the relevant information is contained in the f -matrix and its Fourier transform. The first step is to identify the oscillation wave vector(s) k to be used as initial guesses in the fit. A general method is to plot the Fourier spectrum $\|\tilde{f}(k)\|$ of the rescaled f -matrix (figure 5). When using a logarithmic scale for the vertical axis, even sub-leading contributions show up clearly. We find that the spectra belonging to the symmetric and anti-symmetric operators are shifted against each other by π . This relative phase shift implies a trivial additional distance dependence of $e^{i\pi r}$ of $f^-(r)$ with respect to $f^+(r)$, reflecting the different parity under leg interchange of the two operator sets. We have found it convenient to undo this shift by redefining $f^-(r)$, the part of the f -matrix belonging to the anti-symmetric operators, to $e^{i\pi r} f^-(r)$. The resulting combined Fourier spectrum for f^+ and $e^{i\pi r} f^-$ has strong peaks at $k = 2k_F$ and a smaller peak at $k = 0$, in agreement with the result of [2].

Based on the Fourier spectrum, we rewrite the fitting form (5.10) as

$$f^{\mu,\mu'}(r) = A_{\mu\mu'} r^{-\gamma} \cos(kr + \phi_{\mu\mu'}) + B_{\mu\mu'} r^{-\gamma'}, \quad (7.3)$$

with real numbers $A_{\mu\mu'} > 0$ and $B_{\mu\mu'}$, where we expect $\gamma' > \gamma$, due to the relative sharpness of the peaks in the Fourier spectrum. The nonlinear fitting is done in several steps to also include

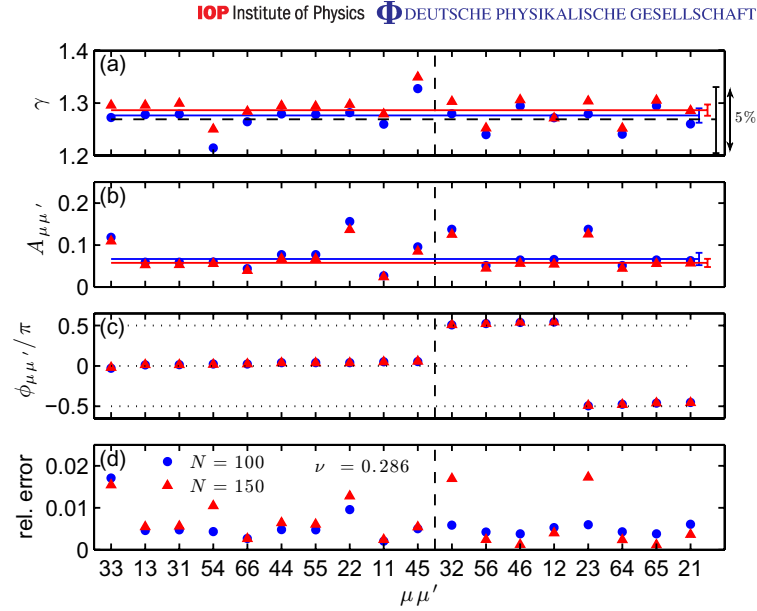


Figure 6. The results of the fit in (7.3) to the 18 independent elements $f^{\mu,\mu'}$ of the f -matrix, labelled along the horizontal axis by the index pair $\mu\mu'$, for $\Delta N = 0$ at filling $\nu = 0.286$ for chains with length $N = 100$ (blue circles) and $N = 150$ (red triangles). The results for $\nu = 0.248$ are qualitatively the same. (a) γ , (b) $A_{\mu\mu'}$, (c) $\phi_{\mu\mu'}$ and (d) the overall fit error ϵ of (7.4). The phase $\phi_{\mu\mu'}$ is defined such that it lies in the interval $[-\pi, \pi]$. The matrix elements have been grouped according to their relative phases $\phi_{\mu\mu'}$ (separated by the vertical dashed line), which clearly indicate cos and sin behaviour for $\phi_{\mu\mu'} = 0$ and $\phi_{\mu\mu'} = \pm\frac{\pi}{2}$, respectively. The exponent $\gamma_0 = 1.277$ and the amplitude $A = 0.066$ obtained from the single fit (7.5) (which was averaged over fitting ranges $[r_1, r_2]$ according to (6.1)), are shown by the solid lines in (a) and (b), respectively; the small error bars on the right of these panels show the corresponding variances $\delta\gamma_0 = \pm 0.013$ and $\delta A = \pm 0.003$. For comparison, (a) also shows the rms exponent $\gamma_0^{\text{rms}} = 1.28$ (dashed line) and its uncertainty ± 0.05 (largest error bar on the right), as determined in figure 4(b).

the decaying part at long distances on an equal footing. Firstly, the data are multiplied by $r^{+\gamma''}$, where we obtained γ'' from a simple power-law fit, in order to be able to fit the oscillations for all distances with comparable accuracy. Then we fit the rescaled data to (7.3), where initially we use the information from the Fourier spectrum in keeping k fixed to $k = 2k_F$, but finally also release the constraint on k . As in section 6.3, we average the results of this procedure for fitting ranges $[r_1, r_2]$, with r_1 ranging from 2 to $2 + \pi/k_F$, see (6.1).

The results of this fitting procedure are depicted in figure 6 for $\nu = 0.286$, for all 18 nonzero elements of the f -matrix. Figure 6(a) shows the leading power-law exponents γ ;

they are distributed within a window of about 5% around the corresponding rms value $\gamma_0^{\text{rms}} = 1.28 \pm 0.05$ (figure 6(a), dashed line) obtained in figure 4(b). The k -vectors from the nonlinear fit are close to $k = 2k_{\text{F}}$ and deviate from this by less than 1%. The fit results for γ' (not shown) always yielded $\gamma' > \gamma$ (with γ' ranging between 2 and 10), but are less reliable than for γ , because the quicker decay implies a comparatively stronger influence from the small- r regime. The relative errors ϵ for the individual matrix elements $f^{\mu,\mu'}$, defined as

$$\epsilon^2 = \sum_r (f^{\mu,\mu'}(r) - f^{\text{fit}}(r))^2 / r^{-2\gamma'}, \quad (7.4)$$

are depicted in figure 6(d) and are always smaller than 2%.

Since most of the exponents γ and amplitudes $A_{\mu\mu'}$ are of comparable size, we have also performed a fit of the f -matrix elements to a *single* γ_0 and A (as well as a single γ'_0 and B for the second term) for all the f -matrix elements, using the ansatz:

$$f(r) = Ar^{-\gamma_0} \left(\begin{array}{ccc} \cos(kr) & \sin(kr) & \cos(kr) \\ -\sin(kr) & \cos(kr) & -\sin(kr) \\ \cos(kr) & \sin(kr) & \cos(kr) \end{array} \right) \begin{array}{c} 0 \\ 0 \\ 0 \end{array} + Br^{-\gamma'_0} e^{i\pi r} \left(\begin{array}{ccc} \cos(kr) & \cos(kr) & \sin(kr) \\ \cos(kr) & \cos(kr) & \sin(kr) \\ -\sin(kr) & -\sin(kr) & \cos(kr) \end{array} \right) \quad (7.5)$$

The form of the matrices in the two blocks was obtained by inserting into (7.3) the explicit values of the phases $\phi_{\mu\mu'}$ determined from the previous fit and summarized in figure 6. Fitting to (7.5) gives an error of about 10%, with the largest errors arising for the f -matrix elements where $A_{\mu\mu'}$ deviates strongly from A (see figure 6). Averaging over fitting ranges $[r_1, r_2]$ according to (6.1), we find $\gamma_0 = 1.277 \pm 0.013$ and $A = 0.066 \pm 0.003$ (indicated by solid lines and small error bars in figures 6(a) and (b), respectively). The values of γ'_0 and B are unreliable in that the results from several fittings differ by about 30%, but still it holds that $\gamma'_0 > \gamma_0$, with γ'_0 ranging between 1.7 and 2.3. The overall error estimate of (7.4) yields $\epsilon \approx 0.1$, i.e. an error of order 10%, the largest contributions arising from those f -matrix elements for which $A_{\mu\mu'}$ deviates most strongly from the average A .

The form of (7.5) allows us to understand why the rms net correlations displayed in figure 4 show some residual oscillations, instead of decaying completely smoothly, as anticipated in section 2. The reason is that (7.5) contains ten $\cos(kr)$ terms but only eight $\sin(kr)$ terms. Although any two such terms oscillate out of phase, as illustrated in figure 7, the cancellation of oscillations will thus not be complete. Instead, the rms net correlations contain a factor $[8 + 2\cos^2(kr)]^{1/2}$ (compare with (4.5)), which produces relative oscillations of about 10%, in accord with figure 4. (The fact that the total numbers of $\cos(kr)$ and $\sin(kr)$ terms are not equal is to be expected: the total operator Hilbert space per cluster is limited, and its symmetry subspaces might have dimensions not a multiple of 4.)

For each pair of wave vectors $\pm k$ in each parity sector, the effective operator basis per cluster can be reduced even further, from three operators to one conjugate pair of operators. This can be seen by rewriting (7.5) as follows:

$$f(r) = Ar^{-\gamma_0} \left[e^{ikr} \begin{pmatrix} f_+ & 0 \\ 0 & e^{i\pi r} f_- \end{pmatrix} + \text{c.c.} \right] + Br^{-\gamma'_0}, \quad (7.6)$$

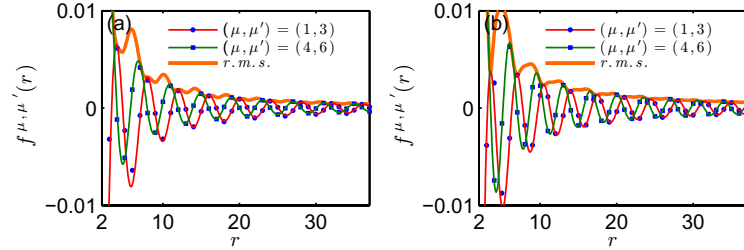


Figure 7. Two entries of the f -matrix for (a) $\nu = 0.248$ and (b) $\nu = 0.286$ fitted to the form in (7.3). The single points (blue circles and squares) are data points from the f -matrix and the lines (red and green) are the result of the fitting. They evidently oscillate with a relative phase of $\Delta\phi = \pi/2$. As a result, their contribution to the rms net correlations, $(|f^{1,3}|^2 + |f^{4,6}|^2)^{1/2}$, shown by the thick orange curve, has only small oscillations at large distances.

with the matrices f_+ and f_- defined as

$$f_+ = \frac{1}{2} \begin{pmatrix} 1 & -i & 1 \\ i & 1 & i \\ 1 & -i & 1 \end{pmatrix}, \quad f_- = \frac{1}{2} \begin{pmatrix} 1 & 1 & -i \\ 1 & 1 & -i \\ i & i & 1 \end{pmatrix}. \quad (7.7)$$

Note that both f_+ and f_- are matrices of rank one with eigenvalues $\frac{3}{2}$, 0 and 0. The eigenvectors with eigenvalue $\frac{3}{2}$ are $\frac{1}{\sqrt{3}}(1, i, 1)$ and $\frac{1}{\sqrt{3}}(1, 1, i)$, respectively. Thus, by transforming to an operator basis in which f_{\pm} is diagonal, one finds that in both the even and the odd sector, the dominant correlations are actually carried by only a pair of operators, namely $\frac{1}{\sqrt{3}}(\hat{O}^1 + i\hat{O}^2 + \hat{O}^3)$ and its Hermitian conjugate, and $\frac{1}{\sqrt{3}}(\hat{O}^4 + \hat{O}^5 + i\hat{O}^6)$ and its Hermitian conjugate, respectively. This result, whose precise form could hardly have been anticipated *a priori*, is a pleasing illustration of the power of a CDM analysis to uncover nontrivial correlations.

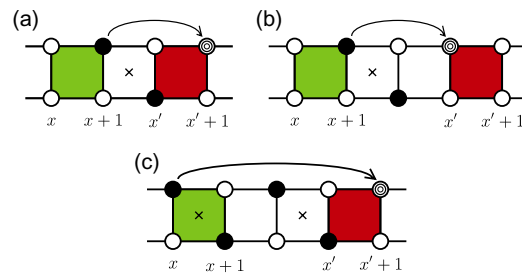
7.2. One-particle correlations

The correlations in the 1P sector are exponentially decaying, as already mentioned in section 6.3. The reason for this was given in [1] and is the key to understanding the operators and correlations in this sector. In the limit where the fermions are all paired, the only possible way to annihilate one at x and create one at $x' > x$, such that the initial and final states are both paired, is that every rung in the interval (x, x') has a fermion (necessarily on alternating legs). These fermions can be grouped as pairs in two different ways: $(x, x+1), (x+2, x+3), \dots, (x'-2, x'-1)$ in the initial state and $(x+1, x+2), \dots, (x'-1, x')$ in the final state. (Note that this requires that x and x' have the same parity.) Cheong and Henley [1] showed that the probability of such a run of filled sites decays exponentially with its length.

Applying the operator analysis in this sector using the eigenvalue decomposition in (5.6) gives a series of fourfold degenerate eigenvalues for both clusters; see table 2 for cluster A. The table for cluster B is exactly the same. For a specific eigenvalue, also the operators for cluster

Table 2. Comparison of the 1P operator sets on cluster A for a filling of $\nu = 0.286$, using the same conventions as for table 1.

Number of operators	$w^{R_{\text{all}}^{\mu}}/w^{R_{\text{all}}^1}$	$O^{R_{\text{all}}R_{\text{short}}}$ (short)	$O^{R_{\text{all}}R_{\text{int}}}$ (intermediate)	$O^{R_{\text{all}}R_{\text{long}}}$ (long)
4	1	4	4	4
8	0.297 162	8	8	8
12	0.014 661	12	12	12
16	0.000 402	16	16	16
20	0.000 001	19.97	19.95	19.31

**Figure 8.** Three configurations of bound pairs contributing to 1P correlations for a distance (a) $r = 2$ and ((b) and (c)) $r = 3$. Clusters A and B are depicted by the green and red squares, respectively. Fermions are depicted by black circles, empty lattice positions by white circles and the position where a fermion will be created is depicted by concentric circles. The crosses show the centre of mass of the bound pairs. In configuration (a), we have a correlation between an operator corresponding to the first four eigenvalues and an operator corresponding to the second four eigenvalues in clusters A and B , respectively. In contrast, configuration (b) shows a correlation between operators corresponding to the largest eigenvalue only and configuration (c) shows a correlation between operators corresponding to the second eigenvalue only.

B (residing at rungs $(x', x' + 1)$) are the same as for cluster A (residing at rungs $(x, x + 1)$), but with mirrored rungs, i.e. an operator acting on rungs $(x, x + 1)$ acts in the same fashion on rungs $(x' + 1, x')$.

Looking more closely, the first four operators annihilate or create a particle on rungs $x + 1$ or x' , respectively, thereby breaking or regrouping bound pairs residing on $(x + 1, x + 2)$ or $(x' - 1, x')$, respectively. The second set of four operators annihilates or creates a particle on rungs x or $x' + 1$, thereby breaking or regrouping bound pairs residing on rungs $(x, x + 1)$ or $(x', x' + 1)$. For a given odd separation $x' - x$, the combination of $x + 1$ with x' requires the smallest number of pairs to be present in between the two clusters. The alternative combination is x with $x' + 1$, which requires an additional pair in between (see figure 8). We could estimate

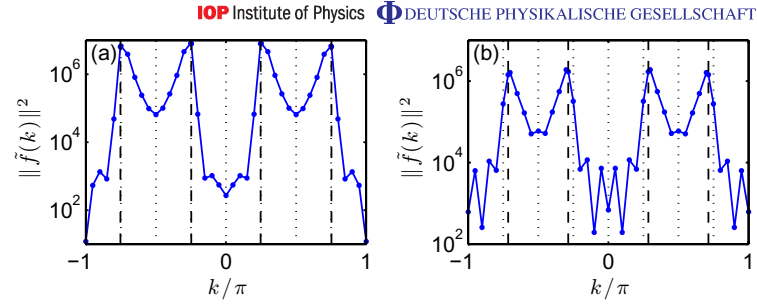


Figure 9. Fourier transform of the f -matrix obtained similarly to figure 5, for 1P correlations based on the four operators per cluster for a filling of (a) $\nu = 0.248$ and (b) $\nu = 0.286$. We find peaks at about $k = \pm k_F$ and $k = \pm k_F + \pi$ (dashed black lines).

their weights since the relative probability of an extra pair is the factor associated with increasing the separation by two. Since the correlations decay roughly as $\sim 10^{-r}$ (see figure 10), we predict two orders of magnitude. Similarly, when $x' - x$ is even, we get a mixture of the first four and the second four operators (see figure 8). This explains the difference in the weights of the two operator sets.

Thus, it turns out that for the 1P correlations, a cluster size of one rung would have already been large enough to reveal the dominant correlations. We will hence use as DOB:

$$\hat{O}^{A,\pm} = \mathbb{1}_x \otimes \frac{1}{\sqrt{2}} (\hat{c}_{\uparrow,x+1} \pm \hat{c}_{\downarrow,x+1}), \quad (7.8a)$$

$$\hat{O}^{B,\pm} = \frac{1}{\sqrt{2}} (\hat{c}_{\uparrow,x} \pm \hat{c}_{\downarrow,x}) \otimes \mathbb{1}_{x+1}, \quad (7.8b)$$

together with their Hermitian conjugates. (The fact that our operator basis consists only of operators acting on a single rung implies that it would have been sufficient to use single-rung clusters. However, for the sake of consistency with the rest of our analysis, we retain two-rung clusters here, too.)

The f -matrix based on these four operators (per cluster) is diagonal with equal entries for a given distance r . Its Fourier transform (see figure 9) gives a result distinct from the Fourier transform for CD and 2P correlations. The dominant wave vectors are $k = \pm k_F$ and $k = \pi \pm k_F$, where the latter is the product of an oscillation with $k = \pi$ and an oscillation with $k = \pm k_F$. In total, we have an oscillation in the correlations of the form $(1 + (-1)^r) e^{\pm i k_F r}$, i.e. an oscillation with $k = \pm k_F$, and every second term being close to zero. The dominant wave vector $k = \pm k_F$ is consistent with the usual behaviour of 1P Green's functions.

The reason for every second term being essentially zero is that the dominant hopping in the system, the correlated hopping, always changes the position of a particle by two rungs, so every second position is omitted. The small but finite value for hopping onto intermediate rungs is related to the finite $t_{\parallel}/t_c = 10^{-2}$ that we use. It results in a second oscillation at $k = \pm k_F$ located at intermediate rungs, whose relative strength compared with the dominant one is about 10^{-2} , which is consistent with the ratio t_{\parallel}/t_c that we used (see figure 10).

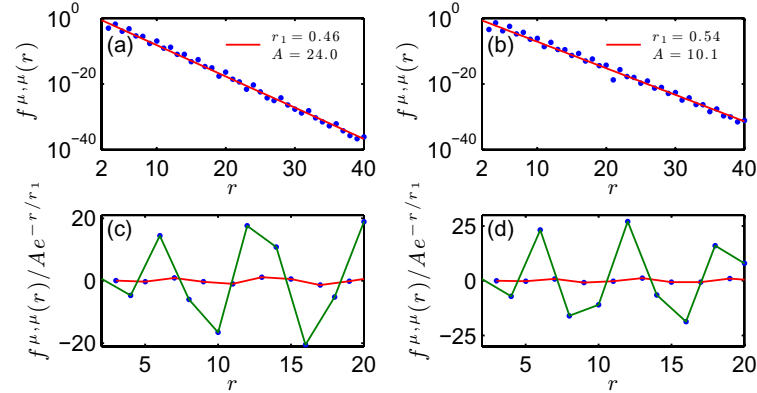


Figure 10. The 1P correlations for a filling of ((a) and (c)) $\nu = 0.248$ and ((b) and (d)) $\nu = 0.286$. ((a) and (b)) The 1P correlations (blue symbols) together with a fit of the form Ae^{-r/r_1} (red line). (b) and (d) The rescaled correlator $f^{\mu, \mu}(r)/Ae^{-r/r_1}$ (blue symbols) for distances up to $r = 20$. (Larger distances are omitted, because for them $f^{\mu, \mu}(r) < 10^{-16}$, which is the maximal computer precision.) One can see a strong oscillation (green curve) and a weak oscillation (red curve).

We fit the one independent f -matrix element $f^{\mu, \mu}$ to an exponential decay of the form Ae^{-r/r_1} (see figure 10), but apart from this we were not able to fit the exact functional dependence on r , especially the oscillations with $k = \pm k_F$. The reason for this is the existence of two oscillations where one is zero on every second rung, and that the data range for which reasonable 1P correlations are still present is too small and thus makes it susceptible to numerical noise. This can be seen already in the Fourier spectrum, where we find relatively broad peaks, as a result of the influence of the exponential envelope and the relatively short distance range available.

7.3. Two-particle correlations

The operator subspace for 2P ($\Delta N = 2$), in a cluster including two rungs, has the comparatively small dimension of four due to the infinite nearest-neighbour repulsion (see figure 2). These are $\hat{c}_{\uparrow, x} \hat{c}_{\downarrow, x+1}$, $\hat{c}_{\downarrow, x} \hat{c}_{\uparrow, x+1}$ and their Hermitian conjugates. In the present case of dominating t_c , these operators represent the creation and annihilation operators of bound pairs [2]. The operator analysis yields exactly the same four operators with degenerate weight for all distance regimes for both clusters A and B . The four operators are $1/\sqrt{2}(\hat{c}_{\uparrow, x} \hat{c}_{\downarrow, x+1} \pm \hat{c}_{\downarrow, x} \hat{c}_{\uparrow, x+1})$ together with their Hermitian conjugates, and they already represent the symmetric and antisymmetric combinations of the operators mentioned above.

The f -matrix (5.7) is diagonal in the basis of the four operators, with equal strength of correlations for a fixed distance apart from a possible sign. This may be expected, given the similar structure of the operators.

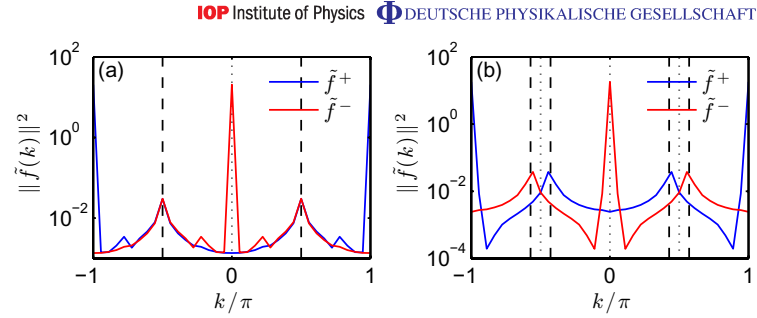


Figure 11. Fourier transform of the f -matrix for 2P correlations based on the operators chosen from the four-dimensional operator space for a filling of (a) $\nu = 0.248$ and (b) $\nu = 0.286$. For a detailed description see figure 5.

As for the CD correlations ($\Delta N = 0$), we apply a Fourier transform on the f -matrix (see figure 11) to identify the dominant wave vectors. Again, we find two spectra of similar form but shifted by π with respect to each other. Consequently, we redefine f^+ to $e^{i\pi r} f^+$, the part of the f -matrix belonging to the symmetric operators. Thus, we obtain one leading peak at $k = 0$ and sub-leading peaks at $k = 2k_F$. Given the similarity of the structure of the Fourier spectrum to that of the CD correlations, we fit the elements of the f -matrix to the form (7.3), but now expect $\gamma'_2 < \gamma_2$, since in the Fourier spectrum the peaks at $k = 0$ are sharper than those at $k = 2k_F$. Already at the level of the f -matrix elements, we find an overall leading decay with residual oscillations, whose relative magnitude becomes smaller at large distances (since $\gamma'_2 < \gamma_2$). Since all matrix elements are the same after redefining f^+ , it is sufficient to fit $|f^{\mu, \mu}|$ for a given μ , which will have dominant k -vectors $k = 0$ and $k = \pm 2k_F$. The fit has errors of less than 5% throughout, with results as shown in figure 12. The overall behaviour is very similar to the one already found from the rms net correlations of this sector (see figure 4), up to the oscillatory part from the second term in (7.3). We see that the oscillations clearly decay more strongly than the actual strength $|f^{\mu, \mu}|$, in accord with $\gamma'_2 < \gamma_2$.

In contrast to the CD correlations (see section 7.1.2), for the 2P correlations we do not find correlations that oscillate with phases shifted by $\Delta\phi = \pm\pi/2$. This may come from the fact that clusters with the size of two rungs have the minimal possible size to capture 2P correlations. The corresponding operator space has dimension four and the four possible operators are very similar in structure. We expect that for larger clusters and hence a larger operator space, we would find correlations, which also oscillate out of phase such that their oscillations cancel in the rms net correlations, in accord with (2.2).

8. Comparison to previous results

We are now ready to compare our CDM-based results with those obtained in [2] (see section IV.B therein) by Cheong and Henley (CH) from fitting simple correlation functions. The latter were computed exactly in [2] for accessible separations (up to 18 lattice sites) after mapping the large t_c model onto a hard-core bosonic system, evaluating the correlators numerically using a so-called interparticle expansion, and fitting the numerical results to simple functional forms in order to determine their leading and sub-leading r -dependences.

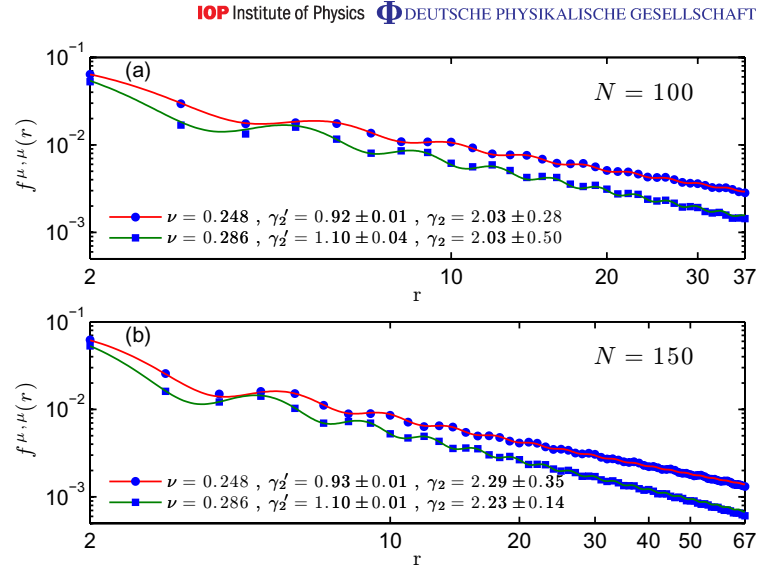


Figure 12. Fitting the 2P correlations to the form in (7.3) for a filling of $\nu = 0.248$ and 0.286 for a chain length of (a) $N = 100$ and (b) $N = 150$. The single points (blue circles and squares) are data points from the f -matrix and the lines (red and green) are the result of the fitting. The error of the exponents is calculated according to (6.1). Results in panels (a) and (b) were obtained from ground states calculated by retaining all contributions to bond singular spectra larger than 10^{-6} and 10^{-8} , respectively, which required maximal Hilbert space dimensions of $D \lesssim 200$ or $D \lesssim 500$, respectively. The increase in accuracy for (b) was needed to obtain good power-law behaviour out to distances about twice as large in (a). (The power laws turn to exponential decays beyond $r \simeq 37$ or 67 in (a) and (b), respectively, for reasons explained in section 4.2.) Since the exponents determined from (a) and (b) agree within the stated error margins, we conclude that the exponents for the power-law decay are converged with respect to the thermodynamic limit. Hence we used and deemed sufficient the accuracy chosen in (a) for all other results reported in this paper.

Overall, our results for the Hamiltonian (3.1) in the strongly correlated hopping regime agree qualitatively with [2], in that (i) 2P correlations and CD correlations show power-law behaviour, (ii) for the fillings we investigated, 2P correlations dominate at large distances, (iii) 1P correlations decay exponentially and are negligible over all distances except very short distances and (iv) the dominant and sub-dominant wave vectors are, respectively, $2k_F$ and 0 for the CD sector and 0 and $2k_F$ for the 2P sector.

However, our results for the power-law exponents γ_0 and γ_2 characterizing the decay of the dominant correlations in the CD and 2P sectors, respectively, are not in quantitative agreement with the exponents found by CH in [2] for CD and 2P correlators. Figure 13 compares the

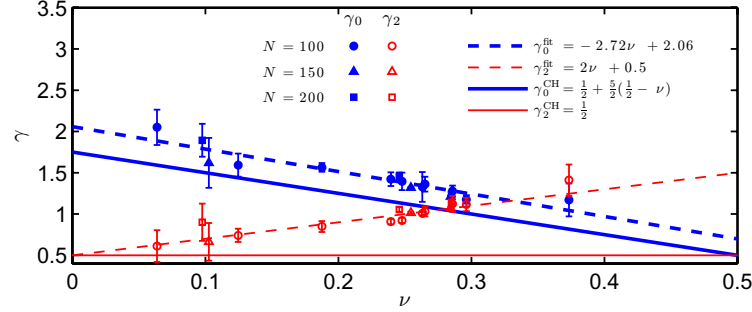


Figure 13. The power-law exponents for CD correlations (γ_0 , filled symbols) and 2P correlations (γ_2 , open symbols) obtained from the fitting in (7.3) for several fillings ν . We used chain lengths of $N = 100$ (circles), $N = 150$ (triangles) and $N = 200$ (squares). The errors of the exponents are defined as in (6.1) and are smallest for fillings around quarter filling. The reason for the somewhat larger errors in the CD exponent at small fillings is that there the wave length of Friedel-like oscillations caused by the boundaries (see section 6.2) becomes significant in comparison to the system sizes we are considering. The thick and thin dashed lines are linear fits to our numerical data for γ_0 and γ_2 , respectively. The thick and thin solid lines show the corresponding predictions of CH [2].

filling-dependence of our exponents γ_0 and γ_2 obtained from (7.3) with that predicted by CH [2]. Such a direct comparison is justified, since in both symmetry sectors, CD and 2P, the correlation functions considered by CH can be written as linear combinations of the f -matrix elements studied by us (for which equation (7.5) yields a good simultaneous fit, as shown in figure 6). Indeed, for the 2P sector, the linear combination is trivial, since the pair operator $\Delta_{j,g} = 1/\sqrt{2}(\hat{c}_{\uparrow x}\hat{c}_{\downarrow x+1} + \hat{c}_{\downarrow x}\hat{c}_{\uparrow x+1})$ appearing in CH's (4.4) is one of the basis elements of our DOB. For the CD sector, the number operator \hat{N}_x occurring in $\langle \hat{N}_x \hat{N}_{x+r} \rangle$ of CH's (4.7) can be expressed as a linear combination of the DOB elements given in our (7.1) and (7.2):

$$\hat{N}_x = \hat{n}_{\uparrow x} \hat{n}_{\downarrow x+1} = \frac{1}{\sqrt{3}} \hat{O}^1 + \frac{1}{\sqrt{42}} \hat{O}^3 + \frac{1}{\sqrt{2}} \hat{O}^6 + \frac{1}{\sqrt{7}} \mathbb{1}_x \otimes \mathbb{1}_{x+1}. \quad (8.1)$$

(The cluster identity operator $\mathbb{1}_x \otimes \mathbb{1}_{x+1}$ does not contribute to the CDM, due to the subtractions in (1.1) and (1.2).)

Consider first the exponent γ_0 for the CD correlations. CH [2] suggested it to depend on filling ν according to $\gamma_0^{\text{CH}} = (1/2) + (5/2)((1/2) - \nu)$ (figure 13, thick solid line). While our result for γ_0 (figure 13, thick dashed line) likewise decreases linearly with ν , the magnitude of its slope and its offset are larger than those of CH (slope: -2.72 versus -2.5 ; offset: 2.06 versus 1.75 , respectively).

For the dominant 2P correlations, CH predicted a constant power-law exponent of $\gamma_2^{\text{CH}} = 1/2$ independent of filling (figure 13, thin solid line), coming from a universal correlation exponent for a chain of tightly bound spinless fermion pairs [10]. In contrast, our data imply a linear ν -dependence (figure 13, thin dashed line), going from $1/2$ at $\nu = 0$ to $3/2$ at $\nu = (1/2)$.

(Such a crossover was asserted by CH for a sub-leading contribution, without giving an explicit functional dependence on ν .)

In light of the discrepancies between our results and those of CH [2], two comments are in order. Firstly, we do not believe that they stem from finite-size or boundary effects, since these hardly affect our results; this is illustrated, for example, by the fact that the exponents extracted for $N = 100$ and 150 (figures 6 and 12) or for $N = 100, 150$ and 200 (figure 13) are essentially independent of N (they differ by at most a few per cent, which is within the margin of error of our fitting procedure).

Secondly, we note that the maximum distance studied by CH in [2], namely $r_{\max} = 18$, is significantly smaller than in our case, where $r_{\max} = 40$ for N ranging over 100, 150 and 200. We speculate that this is the main reason for the discrepancies—it is rather difficult to extract from numerical data an accurate power law for distances ranging only up to 18, in particular in the presence of superimposed oscillations, such as those depicted in figures 7 and 12. In figure 12, for example, the difference in the power-law decays depicted for two different fillings (circles and squares) becomes unambiguously evident only in the regime of largest distances shown, say between 25 and 37.

We conclude with some comments about the exponents in the limit of large fillings ($\nu \rightarrow 0.5$). By linear extrapolation of the behaviour shown in figure 13 for smaller fillings, we conjecture that for fillings larger than ~ 0.35 , eventually the CD correlations dominate over 2P correlations (see figure 13). This conclusion has also been found in [11], which similarly addresses diatomic real space pairing in the context of superconductivity. Their discussion, however, is not specifically constrained to one-dimensional systems, and one may wonder how the specific choice of parameters compares.

As the filling approaches 0.5 in an excluded-fermion chain, it is appropriate to think of the degrees of freedom as impurity states or holes in the crystalline matrix of pairs [11]. Then the natural length scale is the spacing between holes. The longer that spacing gets (it diverges as $\nu \rightarrow 0.5$), the larger also the system under investigation must be in order to reach the asymptotic limit. In other words, to see proper scaling behaviour in a uniform way, the system size should increase proportional to $1/(0.5 - \nu)$. In our case, the data became unreliable for $\nu \gtrsim 0.4$ (see figure 13); hence we cannot make definite statements about that regime. (For $\nu < 0.4$ however, we are confident that the data in figure 13 are essentially independent of system size, as emphasized above.)

9. Conclusions

In summary, we demonstrated that the DOB method for analysing the CDM is a useful tool to detect dominant correlations in a quantum lattice system. Starting from a ground state calculated with DMRG, we extracted all the important correlations present in our model system. Our proposed DOB method, firstly, determines a distance-independent basis of dominant operators on each cluster that carry the dominant correlations of the system, and secondly, encodes the distance dependence of the correlations in the f -matrix, the correlation matrix of the DOB operators. The f -matrix is then analysed in terms of decaying and oscillatory terms to extract the long-range behaviour of the correlations.

Overall, DMRG is a suitable method to calculate the CDM. The latter is easily and efficiently calculated within the framework of the MPS. The explicit breaking of (i) translational invariance by using finite system DMRG and (ii) a discrete symmetry of the model lead us to

develop certain strategies to restore these broken symmetries. The smoothing of the boundaries can still be further optimized or be replaced by periodic boundary conditions. However, we do not expect that this will have a significant influence on the conclusions drawn.

10. Outlook: larger cluster sizes

The size of clusters A and B is a limitation of the present implementation of the DOB method, as it constrains the analysis towards local operators. For some kinds of correlations however, larger clusters may be needed to capture the relevant physics [12]. Even for correlations approximately captured by a certain cluster size, the results may still show some dependence on the actual cluster size. For this purpose, an alternative strategy, which we leave as an outlook, appears viable: instead of the pair of local clusters used in the present work, one could use two ‘super clusters’ representing large contiguous parts of the system, including the left and right boundaries respectively.

Since MPS technology can be used to construct orthonormal effective basis sets to describe the left and right parts of the chain with respect to any specified site (as described in section A.2), it should also be possible to use these basis sets to obtain an efficient description of both super clusters (this is illustrated in figure A.9(c)). To be specific, let cluster A be the set of sites $1, \dots, x$ (‘left’ cluster), while cluster B is the set of sites x', \dots, N (‘right’ cluster) with $x' - x = r > 0$. (The cluster sizes, x and $N - x' + 1$, should be similar; they should also be chosen rather large, to ensure that boundary effects at the very ends of the chains do not contaminate the analysis.) The MPS formulation of DMRG provides an effective set of basis states, $|l_{x+1}\rangle$ and $|r_{x'-1}\rangle$ (see section A.2 for details, in particular figure A.1), that can be used to construct an economical description of the left and right super clusters, respectively (as illustrated in figure A.9(c)). The CDM can then be defined with respect to these effective MPS basis states. A DOB analysis of such a CDM would then yield operator sets $\hat{O}^{A,\mu}$ and $\hat{O}^{B,\mu}$ acting on the system to the left of site $x+1$ and to the right of site $x'-1$, respectively (i.e. each $\hat{O}^{A,\mu}$ or $\hat{O}^{B,\mu}$ is a linear operator on the set of basis states $|l_{x+1}\rangle$ or $|r_{x'-1}\rangle$, respectively). Using the MPS in these parts as maps to the local Hilbert spaces, the action of these operators can be investigated on individual sites, thus determining the actual range of the dominant operator correlations without bias to some predetermined cluster size.

Acknowledgments

We thank S-A Cheong and A Läuchli for discussions and comments on the paper. This work was supported by DFG (SFB 631, SFB-TR 12, De-730/4-1 and De-730/4-2), Center for NanoScience (CENS; LMU) and Nanosystems Initiative Munich (NIM). CLH acknowledges the NSF for support through grant number DMR-0552461. This research was partially supported by the NSF under grant no. NSF PHY05-51164. JvD acknowledges the hospitality of the Kavli Institute for Theoretical Physics, UCSB, and of the Institute for Nuclear Theory, University of Washington, Seattle.

Appendix. The variational MPS approach

This [appendix](#) offers a tutorial introduction to the variational formulation of DMRG for finding the ground state of a one-dimensional quantum lattice model, based on MPS. It also explains how this approach can be used to efficiently calculate the CDM. We point out all the important properties of the MPS and explain how to perform basic quantum calculations such as evaluating scalar products and expectation values, as well as determining the action of local operators on the MPS and constructing a reduced density matrix. We explain how a given MPS can be optimized in an iterative fashion to find an excellent approximation for the global ground state. We also indicate briefly how the efficiency of the method can be enhanced by using Abelian symmetries.

We would like to emphasize that we make no attempt below at a complete historical overview of the DMRG approach or at a complete set of references, since numerous detailed expositions of this approach already exist in the literature (see the excellent review by Schollwöck [5]). Our aim is much more modest, namely to describe the strategy implemented in our code in enough detail to be understandable for interested non-experts.

A.1. Introduction

Quantum many-body systems deal with very large Hilbert spaces even for relatively small system sizes. For example, a one-dimensional quantum chain of N spin- $\frac{1}{2}$ particles forms a Hilbert space of dimension 2^N , which is exponential in system size. For quantum lattice models in 1D a very efficient numerical method is the DMRG, introduced by Steven R White [3, 4]. The problem of large Hilbert space dimension is avoided by an efficient description of the ground state, which discards those parts of the Hilbert space that have negligible weight in the ground state. In this manner, the state space dimension of the effective description becomes tractable, and it has been shown that this produces excellent results in many quasi one-dimensional systems. In the meantime, the method has been extended to time dependence, and various time-dependent Hamiltonians have been studied [13]–[16].

The original DMRG formulation did not rely on MPS but used ‘block states’ to represent the effective Hilbert spaces of one or more targeted states. The notion of MPS was introduced independently of DMRG [17]–[21] before it was realized that the algebraic structure of the ground state for one-dimensional systems calculated with DMRG can be described in terms of position-dependent MPS [6, 19], [22]–[27]. The MPS-based formulation of DMRG has proven to be very enlightening and fruitful, in particular the observation that DMRG is in essence a variational method [6] opened up rich connections to quantum information theory. A firmer theoretical grounding was based on the observation that the numerical effort depends strongly on the entanglement of the wavefunction [28]–[31]. Also some new fields of application arose like periodic systems [6] and finite temperature calculations through purification of the density operator [32, 33].

The origin of the MPS structure underlying the DMRG approach can be understood as follows (a detailed description will follow later): pick any specific site of the quantum lattice model, say site k , representing a local degree of freedom whose possible values are labelled by an index σ_k (e.g. for a chain of spinless fermions, $\sigma_k = 0$ or 1 would represent an empty or

occupied site). Any many-body state $|\psi\rangle$ of the full chain can be expressed in the form

$$|\psi\rangle = \sum_{l_k r_k \sigma_k} A_{l_k r_k}^{[\sigma_k]} |l_k\rangle |\sigma_k\rangle |r_k\rangle, \quad (\text{A.1})$$

where $|l_k\rangle$ and $|r_k\rangle$ are sets of states (say N_l and N_r in number) describing the parts of the chain to the left and right of the current site k , respectively, and for each σ_k , $A^{[\sigma_k]}$ is a matrix with matrix elements $A_{l_k r_k}^{[\sigma_k]}$ and dimension $N_l \times N_r$. Since such a description is possible for any site k , the state $|\psi\rangle$ can be specified in terms of the set of all matrices $A^{[\sigma_k]}$, resulting in an MPS of the form

$$|\psi\rangle = \sum_{\sigma_1 \dots \sigma_N} (A^{[\sigma_1]} \dots A^{[\sigma_N]})_{l_1 r_N} |\sigma_1\rangle \dots |\sigma_N\rangle. \quad (\text{A.2})$$

One may now seek to minimize the ground state energy within the space of all MPS, treating the matrix elements of the A -matrices as variational parameters to minimize the expectation value $\langle \psi | H | \psi \rangle$. If this is done by sequentially stepping through all matrices in the MPS and optimizing one matrix at a time (while keeping the other matrices fixed), the resulting procedure is equivalent to a strictly variational minimization of the ground state energy within the space of all MPS of the form (A.2) [6, 19, 23, 25, 26]. If instead the optimization is performed for two adjacent matrices at a time, the resulting (quasi-variational) procedure is equivalent to White's original formulation of DMRG [6, 19, 23, 25, 26].

In general, such an approach works for both bosonic and fermionic systems. However, to be efficient the method needs a local Hilbert space with finite and small dimension, limiting its applicability to cases where the local Hilbert space is finite dimensional *a priori* (e.g. fermions or hard-core bosons) or effectively reduced to a finite dimension, e.g. by interactions. For example, such a reduction is possible if there is a large repulsion between bosons on the same site such that only a few states with small occupation number will actually take part in the ground state. For fermions, on the other hand, the fermionic sign must be properly taken care of. The anti-commutation rules of fermionic creation and annihilation operators cause the action of an operator on a single site to be non-local because the occupations of the other sites have to be accounted for. To simplify the problem, a Jordan–Wigner transformation [34] can be used to transform fermionic creation and annihilation operators to new operators that obey bosonic commutation relations for any two operators referring to different sites. This greatly simplifies the numerical treatment of these operators as fermionic signs can be (almost) ignored.

Before outlining in more detail the above-mentioned optimization scheme for determining the ground state (see section A.3), we present in section A.2 various technical ingredients needed when working with MPS.

A.2. MPSs

A.2.1. Construction of MPSs. We consider a chain with open boundary conditions consisting of N equal sites with a local Hilbert space dimension of d . A state $|\psi\rangle$ is described by

$$|\psi\rangle = \sum_{\sigma_1 \dots \sigma_N} \psi_{\sigma_1 \dots \sigma_N} |\sigma_1\rangle \dots |\sigma_N\rangle, \quad (\text{A.3})$$

where $\sigma_i = 1, \dots, d$ labels the local basis states of site i . In general, the size of the coefficient space ψ scales with $\mathcal{O}(d^N)$. This can be rewritten in a matrix decomposition of the form

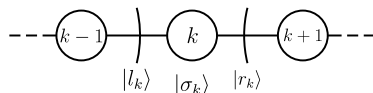


Figure A.1. The current site with effective basis sets.

(A.2) with a set of N times d matrices $A^{[\sigma_k]}$ (see section A.2.3 for details). Formally, this decomposition has two open indices, namely the first index of $A^{[\sigma_1]}$ and the second index of $A^{[\sigma_N]}$, as $A^{[\sigma_1]}$ and $A^{[\sigma_N]}$ are not multiplied onto a matrix to the left and the right, respectively. For periodic boundary conditions these two indices would be connected by a trace over a matrix decomposition, giving a scalar. In the case of open boundary conditions, the two indices range only over one value (see section A.2.3), i.e. the matrix decomposition is a 1×1 matrix, which is a scalar.

If these A -matrices are sufficiently large this decomposition is formally exact, but since that would require A -matrices of exponentially large size, such an exact description is only of academic interest. The reason why the A -matrices are introduced is that they offer a very intuitive strategy for reducing the numerical resources needed to describe a given quantum state. This strategy involves limiting the dimensions of these matrices by systematically using SVD and retaining only the set of largest singular values. The A -matrices can be chosen much smaller while still giving a very good approximation of the state $|\psi\rangle$.

Selecting a certain site k , the state can be rewritten in the form (A.1). The effective ‘left’ basis $|l_k\rangle = \sum_{\sigma_1 \dots \sigma_{k-1}} A^{[\sigma_1]} \dots A^{[\sigma_{k-1}]} |\sigma_1\rangle \dots |\sigma_{k-1}\rangle$ describes the sites $j = 1, \dots, k-1$; the effective ‘right’ basis $|r_k\rangle$ similarly describes the sites $j = k+1, \dots, N$. Site k is called the *current* site, as the description of the state makes explicit only the A -matrix of this site (see figure A.1).

So far (A.3) and (A.1) are equivalent, but now we have a representation of the state that allows a convenient truncation of the total Hilbert space, used for the description of an MPS. For example, if we introduce a parameter D and truncate all effective Hilbert spaces of all sites to the dimension D , each $A^{[\sigma_k]}$ -matrix has at most the dimension $D \times D$. This reduces the resources used to describe a state from $\mathcal{O}(d^N)$ for the full many-body Hilbert space down to $\mathcal{O}(ND^2d)$. This is linear in the system size, assuming that the size required for D to accurately describe the state grows significantly slower than linearly in N . This, in fact, turns out to be the case for ground state calculations [35]. Details of this truncation procedure and estimates of the resulting error are described in section A.2.5.

A.2.2. Global view and local view. MPSs can be viewed in two alternative ways: a global view and a local view. Both views are equivalent and both have their applications. In the global view the state is expressed as in (A.2), i.e. the effective Hilbert spaces have been used ‘only’ to reduce resources. The state is stored in the A -matrices, but the effective basis sets will be contracted out. This perception has to be handled very carefully, because contracting out the effective basis sets leads to higher costs in resources! In the local view the state is expressed as in (A.1). It is called local because there is one special site, the *current* site, and all other sites are combined in effective orthonormalized basis sets. Usually, the local view is used iteratively for every site. In this perception, we need effective descriptions of operators contributing to the Hamiltonian acting on other sites than the current site (see section A.2.8).

A.2.3. Details of the A-matrices. The A -matrices have some useful properties that hold independently of the truncation scheme used to limit the effective Hilbert spaces. First of all, we note that by construction $\dim(\mathcal{H}^{r_{k-1}}) \equiv \dim(\mathcal{H}^k)$; otherwise the matrix products in (A.2) would be ill-defined. Based on this, we can find another interpretation of the A -matrices in the local view. The part of the chain to the left of site k (where k is far from the ends for simplicity) is described by the effective basis $|l_k\rangle$, which is built of truncated A -matrices:

$$\begin{aligned} |l_k\rangle &= \sum_{\sigma_1, \dots, \sigma_{k-1}} (A^{[\sigma_1]} \dots A^{[\sigma_{k-1}]})_{l_k} |\sigma_1\rangle \dots |\sigma_{k-1}\rangle \\ &= \sum_{\sigma_{k-1}} \sum_{l_{k-1}} \underbrace{\sum_{\sigma_1, \dots, \sigma_{k-2}} (A^{[\sigma_1]} \dots A^{[\sigma_{k-2}]})_{l_{k-1}} |\sigma_1\rangle \dots |\sigma_{k-2}\rangle}_{|l_{k-1}\rangle} A_{l_{k-1}, l_k}^{[\sigma_{k-1}]} |\sigma_{k-1}\rangle \\ &= \sum_{\sigma_{k-1}, l_{k-1}} A_{l_{k-1}, l_k}^{[\sigma_{k-1}]} |l_{k-1}\rangle |\sigma_{k-1}\rangle. \end{aligned} \quad (\text{A.4})$$

The $A^{[\sigma_{k-1}]}$ -matrix maps the effective left basis $|l_{k-1}\rangle$ together with the local $|\sigma_{k-1}\rangle$ basis onto the effective left basis $|l_k\rangle$! The same argument applied on the effective right basis of site k leads to the transformation of $|r_{k+1}\rangle$ and $|\sigma_{k+1}\rangle$ into $|r_k\rangle$ via the $A^{[\sigma_{k+1}]}$ -matrix:

$$|r_k\rangle = \sum_{\sigma_{k+1}, r_{k+1}} A_{r_k, r_{k+1}}^{[\sigma_{k+1}]} |\sigma_{k+1}\rangle |r_{k+1}\rangle. \quad (\text{A.5})$$

So far, this may be any transformation, but in order to deal with properly orthonormal basis sets, we may impose unitarity on the transformation (see below).

The A -matrices towards the ends of the chain have to be discussed separately. The use of open boundary conditions implies that we have a one-dimensional effective state space to the left of site 1 and the right of site N , respectively, both representing the empty state. This implies that $\dim(\mathcal{H}^1) = 1 = \dim(\mathcal{H}^N)$. Moving inwards from the ends of the chain, the effective Hilbert spaces acquire dimension d^1, d^2, \dots until they become larger than D and need to be truncated. Correspondingly, the dimension of matrix $A^{[\sigma_k]}$ is $D_{k-1} \times D_k$, where $D_k = \min(d^k, d^{N-k}, D)$. There is no truncation needed if $\dim(\mathcal{H}^k) * d = \dim(\mathcal{H}^k)$ or $\dim(\mathcal{H}^k) * d = \dim(\mathcal{H}^k)$. In these cases we simply choose $A_{(l_k \sigma_k) r_k} = \mathbb{1}$ and $A_{l_k (r_k \sigma_k)} = \mathbb{1}$, respectively.

Summarizing, the A -matrices have two functions. If site i is the current site in (A.1), the $A^{[\sigma_i]}$ -matrices represent the state, i.e. its coefficients specify the linear combination of basis states $|l_k\rangle$, $|\sigma_k\rangle$ and $|r_k\rangle$. On the other hand, if not the current site, the A -matrices are used as a mapping to build the effective orthonormal basis for the current site, as we describe next:

Orthonormal basis sets. In the local view, the whole system is described by the A -matrices of the current site k in the effective left basis, the effective right basis and the local basis of site k . *A priori*, the basis states form an orthonormal set only for the local basis set, but we may ask for the effective basis sets $|l\rangle$ and $|r\rangle$ ⁴ to be orthonormal, too, i.e. require them to obey:

$$\begin{aligned} \langle l' | l \rangle &= \delta_{l'l}, \\ \langle r' | r \rangle &= \delta_{r'r}. \end{aligned} \quad (\text{A.6})$$

⁴ From now on, the index k is only displayed when several sites are involved. For the current site or in the case when only one A -matrix is considered, the index will be dropped.

36

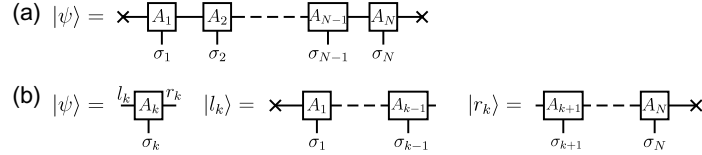
IOP Institute of Physics Φ DEUTSCHE PHYSIKALISCHE GESELLSCHAFT

Figure A.2. Graphical representation of an MPS in (a) the global view and (b) the local view.

This immediately implies the following condition on the $A^{[\sigma_j]}$ -matrices, using (A.4) and (A.5) (for a derivation, see section A.5.1):

$$\begin{aligned} \sum_{\sigma_j} A^{[\sigma_j]^\dagger} A^{[\sigma_j]} &= \mathbb{1} \quad \text{for } j < k, \\ \sum_{\sigma_j} A^{[\sigma_j]} A^{[\sigma_j]^\dagger} &= \mathbb{1} \quad \text{for } j > k. \end{aligned} \quad (\text{A.7})$$

The orthonormality (A.6) for both the left and right basis states holds only for the current site. For the other sites there is always only one orthonormal effective basis.

Graphical representation. MPSs can be depicted in a convenient graphical representation (see figure A.2). In this representation, A -matrices are displayed as boxes and $A^{[\sigma_k]}$ is replaced by A_k for brevity. Indices correspond to links from the boxes. The left link connects to the effective left basis, the right link to the right one, and the link at the bottom to the local basis. Sometimes indices are explicitly written on the links to emphasize the structure of the sketch. Connected links denote a summation over the indices (also called contraction) of the corresponding $A^{[\sigma]}$ -matrices. At the boundaries of the chain, a cross is used to indicate the vacuum state.

A.2.4. Orthonormalization of effective basis states. We now describe how an arbitrary MPS state can be rewritten into a form where its local view with respect to a given site has orthonormal left and right basis states. It should be emphasized that this really just amounts to a reshuffling of information among the state's A -matrices without changing the state itself, by exploiting the freedom that we can always insert any $X^{-1}X = \mathbb{1}$ at any position in the MPS without altering it.

Assume site k to be the current site and assume that it has an orthonormal left basis (the latter is automatically fulfilled for $k = 1$). We need a procedure to ensure that when the current site is switched to site $k + 1$, this site, too, will have an orthonormal left basis. (This is required for the orthonormality properties used in the proof in section A.5.1. A similar procedure can be used to ensure that site $k - 1$ has an orthonormal right basis provided k has such a basis.) For this purpose we use the singular value decomposition (SVD; see section A.5.2) for which we have to rewrite $A_{l_k r_k}^{[\sigma_k]}$ by *fusing* the indices l_k and σ_k :

$$A_{l_k r_k}^{[\sigma_k]} \hat{=} A_{(l_k \sigma_k) r_k} = \sum_{m, n} u_{(l_k \sigma_k) m} s_{mn} (v^\dagger)_{nr_k} \hat{=} \sum_m u_{l_k m}^{[\sigma_k]} (s v^\dagger)_{mr_k}, \quad (\text{A.8})$$

$$l_k \begin{array}{|c|} \hline A_k \\ \hline \end{array} r_k \underset{\sigma_k}{\cong} (l_k \sigma_k) \begin{array}{|c|} \hline A_k \\ \hline \end{array} r_k \stackrel{\text{SVD}}{\cong} (l_k \sigma_k) \begin{array}{|c|} \hline u \\ \hline \end{array} \begin{array}{|c|} \hline S \\ \hline \end{array} \begin{array}{|c|} \hline v^\dagger \\ \hline \end{array} r_k \underset{\sigma_k}{\cong} l_k \begin{array}{|c|} \hline u \\ \hline \end{array} \begin{array}{|c|} \hline S v^\dagger \\ \hline \end{array} r_k$$

Figure A.3. SVD of the A -matrices.

$$l_k \begin{array}{|c|} \hline A_k \\ \hline \end{array} r_k = l_{k+1} \begin{array}{|c|} \hline A_{k+1} \\ \hline \end{array} r_{k+1} \stackrel{\text{SVD}}{\cong} l_k \begin{array}{|c|} \hline u \\ \hline \end{array} \begin{array}{|c|} \hline S v^\dagger \\ \hline \end{array} r_k = l_{k+1} \begin{array}{|c|} \hline A_{k+1} \\ \hline \end{array} r_{k+1} = l_k \begin{array}{|c|} \hline u \\ \hline \end{array} \tilde{r}_k = \tilde{l}_{k+1} \begin{array}{|c|} \hline S v^\dagger A_{k+1} \\ \hline \end{array} r_{k+1} = l_k \begin{array}{|c|} \hline \tilde{A}_k \\ \hline \end{array} \tilde{r}_k = \tilde{l}_{k+1} \begin{array}{|c|} \hline \tilde{A}_{k+1} \\ \hline \end{array} r_{k+1}$$

Figure A.4. Rearrangement of the A -matrices to switch the current site from site k to $k + 1$.

$$l_{k-1} \begin{array}{|c|} \hline A_{k-1} \\ \hline \end{array} \begin{array}{|c|} \hline A_k \\ \hline \end{array} r_k = l_{k-1} \begin{array}{|c|} \hline A_{k-1} u s \\ \hline \end{array} \begin{array}{|c|} \hline v^\dagger \\ \hline \end{array} r_k$$

Figure A.5. Orthonormal effective right basis for site $k - 1$.

where m , n and r_k have the same index range (see figure A.3). Specifically, u fulfills

$$\mathbb{1} = u^\dagger u = \sum_{(l_k \sigma_k)} u_{(l_k \sigma_k), m}^* u_{(l_k \sigma_k), m}, \quad (\text{A.9})$$

which is equivalent to the orthonormality condition (A.7) for the $A^{[\sigma_k]}$ -matrices.

As u replaces $A^{[\sigma_k]}$ and $s v^\dagger$ is contracted onto $A^{[\sigma_{k+1}]}$, this leaves the overall state unchanged (for a graphical depiction see figure A.4):

$$\begin{aligned} A^{[\sigma_k]} A^{[\sigma_{k+1}]} &= \sum_{(r_k = l_{k+1})} A_{l_k r_k}^{[\sigma_k]} A_{l_{k+1} r_{k+1}}^{[\sigma_{k+1}]} = \sum_{(r_k = l_{k+1})} \sum_m u_{l_k m}^{[\sigma_k]} (s v^\dagger)_{m r_k} A_{l_{k+1} r_{k+1}}^{[\sigma_{k+1}]} \\ &= u^{[\sigma_k]} (s v^\dagger A_{k+1})^{[\sigma_{k+1}]} \equiv \tilde{A}^{[\sigma_k]} \tilde{A}^{[\sigma_{k+1}]}. \end{aligned} \quad (\text{A.10})$$

Site $k + 1$ now has an orthonormal effective left basis. A similar procedure works for the effective right basis, see figure A.5. To obtain an orthonormal effective left basis for the current site k , we start with the first site, update $A^{[\sigma_1]}$ and $A^{[\sigma_2]}$, move to the next site, update $A^{[\sigma_2]}$ and $A^{[\sigma_3]}$, and so on until site $k - 1$. For an orthonormal effective right basis, we start from site N and apply an analogous procedure in the other direction.

If the state $|\psi\rangle$ is in the local description of site k with orthonormal basis sets $|l_k\rangle$, $|\sigma_k\rangle$ and $|r_k\rangle$, it is now very easy to change the current site to site $k \pm 1$, with corresponding new orthonormal basis sets $|l_{k \pm 1}\rangle$, $|\sigma_{k \pm 1}\rangle$ and $|r_{k \pm 1}\rangle$. Suppose we want to change the current site from site k to site $k + 1$. Following the procedure described above, site $k + 1$ already has an orthonormal right basis and all the sites left of site k fulfill the orthonormality condition. All that is left to do is to update sites k and $k + 1$ to obtain an orthonormal left basis for site $k + 1$. This is called a *switch* of the current site from site k to site $k + 1$. The switch from site k to site $k - 1$ is done analogously.

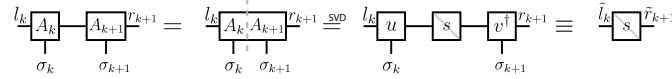


Figure A.6. Procedure for site update within two-site DMRG. The grey line through the s indicates that s is the diagonal matrix of singular values.

A.2.5. Hilbert space truncation. A central ingredient in the variational optimization of the ground state (see section A.3.1 below) is the truncation of the effective Hilbert spaces associated with a given A -matrix. The strategy for truncating the effective Hilbert spaces is completely analogous to the original DMRG formulation [25]. The DMRG truncation scheme is based on discarding that part of the Hilbert space on which a certain density matrix has sufficiently small weight. There are two ways to obtain an appropriate reduced density matrix: two-site DMRG [3]–[5] and one-site DMRG [5]. The crucial difference between the two is that one-site DMRG is strictly variational in the sense that the energy is monotonically decreasing with each step, whereas in two-site DMRG the energy may (slightly) increase in some steps, but with the advantage that the cutoff dimension can be chosen dynamically in each step.

Two-site DMRG. Two-site DMRG arises when variationally optimizing two sites at a time. We consider two current sites, say k and $k+1$, and we may choose the cutoff dimension site-dependent: $D \rightarrow D_k \equiv \dim(\mathcal{H}^k)$. Following section A.2.4, we assume site k to have an orthonormal left basis and site $k+1$ to have an orthonormal right basis. After contracting the indices connecting $A^{[\sigma_k]}$ and $A^{[\sigma_{k+1}]}$ (see figure A.6), the state is described by $A_{l_k r_{k+1}}^{[\sigma_k \sigma_{k+1}]}$. In this description, we may optimize the ground state locally by variationally minimizing the ground state energy with respect to $A_{l_k r_{k+1}}^{[\sigma_k \sigma_{k+1}]}$ (see section A.3.1). Afterwards, we need to decompose $A_{l_k r_{k+1}}^{[\sigma_k \sigma_{k+1}]}$ into $A^{[\sigma_k]}$ and $A^{[\sigma_{k+1}]}$ again. This can be accomplished via SVD (see section A.5.2) by fusing the indices $l_k, \sigma_k \rightarrow (l_k \sigma_k)$ and $r_{k+1}, \sigma_{k+1} \rightarrow (r_{k+1} \sigma_{k+1})$ (see figure A.6) to obtain $A_{l_k r_{k+1}}^{[\sigma_k \sigma_{k+1}]} = \sum_i u_{l_k i}^{[\sigma_k]} s_i (v^\dagger)_{i r_{k+1}}^{[\sigma_{k+1}]}$, where $i = 1 \dots \min(dD_k, dD_{k+1})$. Using the column unitarity of u and the row unitarity of v^\dagger (see section A.5.2), we rewrite the state as

$$\begin{aligned}
 |\psi\rangle &= \sum_{l_k r_{k+1} \sigma_k \sigma_{k+1}} \left(\sum_i u_{l_k i}^{[\sigma_k]} s_i (v^\dagger)_{i r_{k+1}}^{[\sigma_{k+1}]} \right) |l_k\rangle |\sigma_k\rangle |\sigma_{k+1}\rangle |r_{k+1}\rangle \\
 &= \sum_i s_i \underbrace{\left(\sum_{l_k \sigma_k} u_{l_k i}^{[\sigma_k]} |l_k\rangle |\sigma_k\rangle \right)}_{|\tilde{l}_i\rangle} \underbrace{\left(\sum_{r_{k+1} \sigma_{k+1}} (v^\dagger)_{i r_{k+1}}^{[\sigma_{k+1}]} |\sigma_{k+1}\rangle |r_{k+1}\rangle \right)}_{|\tilde{r}_i\rangle} \\
 &= \sum_i s_i |\tilde{l}_i\rangle |\tilde{r}_i\rangle, \tag{A.11}
 \end{aligned}$$

where the new set of basis states $|\tilde{l}_i\rangle$ and $|\tilde{r}_i\rangle$ is orthonormal with $\langle \tilde{l}_i | \tilde{l}_i \rangle = \delta_{i i'}$ and $\langle \tilde{r}_i | \tilde{r}_i \rangle = \delta_{i i'}$. This representation of the state may be seen as residing on the bond between k and $k+1$, with effective orthonormal basis sets for the parts of the system to the left and right of the bond. Reduced density matrices for these parts of the system, obtained by tracing out the respective

complementary part, have the form:

$$\rho^{[L]} = \sum_i s_i^2 |\tilde{l}_i\rangle \langle \tilde{l}_i|, \quad \rho^{[R]} = \sum_i s_i^2 |\tilde{r}_i\rangle \langle \tilde{r}_i|. \quad (\text{A.12})$$

The standard DMRG truncation scheme amounts to truncating $\rho^{[L]}$ and $\rho^{[R]}$ according to their singular values s_i . We could either keep all singular values greater than a certain cutoff, thereby specifying a value for D_{k+1} between 1 and $\min(dD_k, dD_{k+2})$, or alternatively choose $D_k = D$ to be site independent for simplicity. This step makes the method not strictly variational, since we discard some part of the Hilbert space, which could increase the energy. It turns out that this potential increase of energy is negligible in practice. We can obtain a measure for the information lost due to truncation by using the von Neumann entropy $S = -\text{tr}(\rho \ln \rho)$, given by

$$\varepsilon \equiv - \sum_{i>D} s_i^2 \ln(s_i^2), \quad (\text{A.13})$$

where $\sum s_i^2 = 1$ due to the normalization of $|\psi\rangle$.

One-site DMRG. One-site DMRG arises when variationally optimizing one site at a time. In contrast to two-site DMRG, one-site DMRG does not easily allow for dynamical truncation during the calculation. (It is possible in principle to implement the latter, but if one decides to use dynamical truncation, it would be advisable to do so using two-site DMRG.) The truncation is fixed by the initial choice of D , but it is still possible to determine an estimate on the error of this truncation by analysing the reduced density matrix. Starting from an expression for the full density matrix in the local view (the current site k with orthonormal effective basis sets)

$$\begin{aligned} \rho &= |\psi\rangle \langle \psi| = \left(\sum_{l,r,\sigma} A_{lr}^{[\sigma]} |l\rangle |\sigma\rangle |r\rangle \right) \left(\sum_{l',r',\sigma'} A_{l'r'}^{[\sigma']*} \langle l'| \langle \sigma'| \langle r'| \right) \\ &= \sum_{l,r,\sigma,l',r',\sigma'} A_{lr}^{[\sigma]} A_{l'r'}^{[\sigma']*} |l\rangle \langle l'| |\sigma\rangle \langle \sigma'| |r\rangle \langle r'|, \end{aligned} \quad (\text{A.14})$$

we trace out the effective right basis and obtain a reduced density matrix for the current site and the left part of the system:

$$\rho^{[k+1]} = \sum_{l,r,\sigma,l',\sigma'} A_{lr}^{[\sigma]} A_{l'r}^{[\sigma']*} |l\rangle \langle l'| |\sigma\rangle \langle \sigma'|. \quad (\text{A.15})$$

This reduced density matrix carries the label l_{k+1} because it corresponds precisely to the density matrix $|l_{k+1}\rangle \langle l'_{k+1}|$. So if we switch the current site from site k to site $k+1$, we can check the error of the truncation of $\mathcal{H}^{l_{k+1}}$. Fusing the indices l and σ , we obtain

$$\begin{aligned} \rho^{[k+1]} &= \sum_{l,r,\sigma,l',\sigma'} A_{(l\sigma)r} A_{(l'\sigma')r}^* |(l\sigma)\rangle \langle (l'\sigma')| \\ &= \sum_{l,r,\sigma,l',\sigma'} A_{(l\sigma)r} (A^\dagger)_{r(l'\sigma')} |(l\sigma)\rangle \langle (l'\sigma')| \\ &= \sum_{l\sigma,l'\sigma'} (AA^\dagger)_{(l\sigma)(l'\sigma')} |(l\sigma)\rangle \langle (l'\sigma')|. \end{aligned} \quad (\text{A.16})$$

We do not need to diagonalize the coefficient matrix AA^\dagger to obtain the largest weights in the density matrix, because we obtain its eigenvalues as a byproduct of the following manipulations

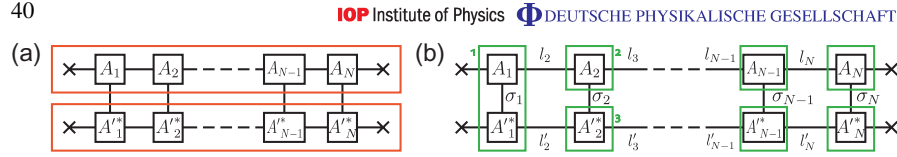


Figure A.7. Scalar product, computed in two different orders. (a) First, all A -matrices of $|\psi\rangle$ and $|\psi'\rangle$ are contracted and then contraction over the local indices is carried out. (b) First, for site 1, we contract over the local indices of A_1 and A'_1 . Then we contract over the effective index between A_1 and A_2 and afterwards over the indices between the resulting object and $(A'_2)^*$. Proceeding over the whole chain yields the scalar product.

anyway [5]. To switch the current site we need to apply a SVD (see section A.2.4) and obtain $A = usv^\dagger$ (this is not the usual A -matrix, but the index-fused form). This directly yields $AA^\dagger = usv^\dagger vsu^\dagger = us^2u^\dagger$, which corresponds to the diagonalization of $\rho^{[k+1]}$, implying that the weights of the density matrix are equal to s^2 . Of course this works also for the right effective basis. With such an expression, we can check whether the effective Hilbert space dimension D of $\mathcal{H}^{[k+1]}$ is too small or not. For example, we could ask for the smallest singular value s_D to be at least n orders of magnitude smaller than the largest one s_1 , i.e. the respective weights in the density matrix would be $2n$ orders of magnitude apart. If the singular values do not decrease that rapidly, we have to choose a greater D .

A.2.6. Scalar product. The scalar product of two states $|\psi\rangle$ and $|\psi'\rangle$ is one of the simplest operations we can perform with MPSs. It is calculated most conveniently in the global view because then we do not need to care about orthonormalization of the A -matrices:

$$\begin{aligned} \langle \psi' | \psi \rangle &= \langle \sigma'_1 | \dots \langle \sigma'_N | \sum_{\sigma'_1 \dots \sigma'_N} (A'^{[\sigma'_1]} \dots A'^{[\sigma'_N]})^* \sum_{\sigma_1 \dots \sigma_N} (A^{[\sigma_1]} \dots A^{[\sigma_N]}) |\sigma_1\rangle \dots |\sigma_N\rangle \\ &= \sum_{\sigma_1 \dots \sigma_N} (A^{[\sigma_1]} \dots A^{[\sigma_N]})^* (A^{[\sigma_1]} \dots A^{[\sigma_N]}), \end{aligned} \quad (\text{A.17})$$

using the orthonormality of the local basis $\langle \sigma'_k | \sigma_l \rangle = \delta_{kl} \delta_{\sigma'_k \sigma_k}$. In principle, the order in which these contractions are carried out is irrelevant, but in practice it is possible to choose an order in which this summation over the full Hilbert space is carried out very efficiently by exploiting the one-dimensional structure of the matrix product state (see figure A.7 for a graphical explanation). For details of the numerical costs, see section A.5.3. In method (a), after contracting all A -matrices of $|\psi\rangle$ and $|\psi'\rangle$, we have to perform a contraction over the full Hilbert space, i.e. a $1 \times d^N$ matrix is multiplied with a $d^N \times 1$ matrix. This contraction is of order $\mathcal{O}(d^N)$, which is completely unfeasible for practical purposes. In method (b), the most 'expensive' contraction is in the middle of the chain, say at site k , and it is of order $\mathcal{O}(dD^3)$. Here the A -matrices are viewed as three-index objects $A_{l_k r_k \sigma_k}$ with dimension $D \times D \times d$. All sites left of site k are represented by a $D \times D$ matrix, say $L_{l'_k}^k$. Contracting this with the matrix at site k yields the object $\sum_{l_k} L_{l'_k}^k A_{l_k r_k \sigma_k}$, which has dimensions $D \times D \times d$, and since the sum contains D terms, the overall cost is $\mathcal{O}(dD^3)$. Thus, in practice, method (b) is rather efficient and renders such calculations feasible in practice.

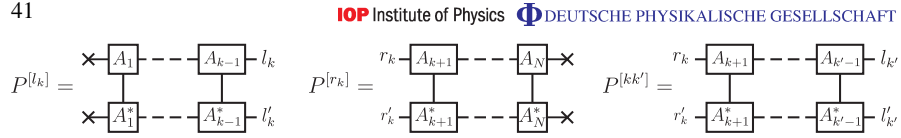


Figure A.8. Partial products associated with site k .

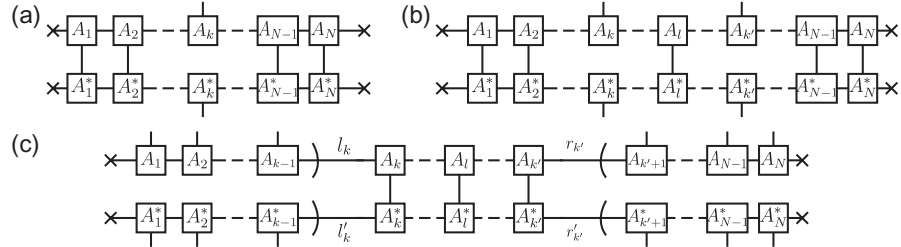


Figure A.9. Reduced density matrix (a) $\rho_{(k)}$ for site k , (b) $\rho_{(k k')}$ for sites k and k' , where $k < l < k'$, and (c) for two superclusters to the left of site k and the right of site k' , respectively, which are described in terms of MPS basis states $|l_k\rangle$ and $|r_{k'}\rangle$, respectively, where $k < l < k'$.

Partial product. Sometimes it is required to calculate a product over only a part of the MPS. This is done the same way as the scalar product

$$(P^{[L_k]})_{l'_k l_k} \equiv \sum_{\sigma_1 \dots \sigma_{k-1}} (A^{[\sigma_1]} \dots A^{[\sigma_{k-1}]})_{l'_k}^* (A^{[\sigma_1]} \dots A^{[\sigma_{k-1}]})_{l_k}, \quad (\text{A.18})$$

$$(P^{[R_k]})_{r'_k r_k} \equiv \sum_{\sigma_{k+1} \dots \sigma_N} (A^{[\sigma_{k+1}]} \dots A^{[\sigma_N]})_{r'_k}^* (A^{[\sigma_{k+1}]} \dots A^{[\sigma_N]})_{r_k}, \quad (\text{A.19})$$

$$(P^{[k k']})_{r'_k l'_k, l_k r'_k} \equiv \sum_{\sigma_{k+1} \dots \sigma_{k'-1}} (A^{[\sigma_{k+1}]} \dots A^{[\sigma_{k'-1}]})_{r'_k l'_k}^* (A^{[\sigma_{k+1}]} \dots A^{[\sigma_{k'-1}]})_{l_k r'_k}. \quad (\text{A.20})$$

Note that $P^{[L_k]}$ and $P^{[R_k]}$ are matrices in the indices l_k and r_k , respectively (see figure A.8). In fact, they correspond to the overlap matrices $\langle l'_k | l_k \rangle$ and $\langle r'_k | r_k \rangle$, respectively.

A.2.7. Reduced density matrix. The pure density matrix given by the MPS $|\psi\rangle$ is defined as $\rho = |\psi\rangle\langle\psi|$. To describe only a part of the system, we need to calculate the reduced density matrix. Let I be a set of sites and $\sigma_s = \{\sigma_{k \in I}\}$ a fused index for their local states. Tracing out all other sites with combined index $\sigma_b = \{\sigma_{k \notin I}\}$, we obtain

$$\rho_I = \sum_{\sigma_1 \dots \sigma_N \sigma'_1 \dots \sigma'_N} \delta_{\sigma_b \sigma'_b} (A^{[\sigma'_1]} \dots A^{[\sigma'_N]})^* (A^{[\sigma_1]} \dots A^{[\sigma_N]}) |\sigma_s\rangle \langle \sigma'_s|. \quad (\text{A.21})$$

This is a completely general expression, but in the cases where $I = \{k\}$ or $I = \{k, k'\}$ it reduces to (see figure A.9)

$$\rho_{(k)} = P^{[L_k]} (A^{[\sigma_k]} \otimes A^{[\sigma'_k]}) P^{[R_k]} |\sigma_k\rangle \langle \sigma'_k|, \quad (\text{A.22})$$

42

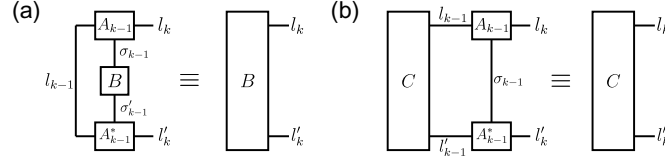
IOP Institute of Physics Φ DEUTSCHE PHYSIKALISCHE GESELLSCHAFT

Figure A.10. The k -left representation of (a) the operator B , obtained from its $(k-1)$ -local-representation, and (b) the operator C , obtained from its $(k-1)$ -left-representation.

$$B_{\sigma'_i \sigma_i} \longrightarrow B_{l'_{i+1} l_{i+1}} \longrightarrow B_{l'_{i+2} l_{i+2}} \longrightarrow \dots \longrightarrow B_{l'_k l_k}$$

Figure A.11. Iterative calculation of the k -left-description of an operator B , given in the i -local-description, by (A.24) and (A.25) for any $k > i$.

$$\rho_{\{kk'\}} = P^{[L_k]}(A^{[\sigma_k]} \otimes A^{[\sigma'_k]^*}) P^{[kk']}(A^{[\sigma_{k'}]} \otimes A^{[\sigma'_{k'}]^*}) P^{[R_{k'}]} |\sigma_k\rangle |\sigma_{k'}\rangle \langle \sigma'_k| \langle \sigma'_{k'}|. \quad (\text{A.23})$$

A similar strategy can be used to calculate the density matrices needed for the main text, by contracting out the σ_k 's for all sites except those involved in the clusters A , B or $A \cup B$. In fact, (A.23) gives $\hat{\rho}^{A \cup B}$ for two clusters of size 1 at sites k and k' .

A.2.8. Operators in an effective basis. Let k be the current site with orthonormal effective basis sets $|l_k\rangle$ and $|r_k\rangle$. Consider an operator B , which acts on the local basis of site $k-1$ only, with matrix elements $B_{\sigma'_{k-1} \sigma_{k-1}} = \langle \sigma'_{k-1} | B | \sigma_{k-1} \rangle$. We call this the $(k-1)$ -local-representation of B . To represent B in the effective left basis of site k , called the k -left-representation of B , we use the transformation properties of $A^{[\sigma_{k-1}]}$ (see figure A.10),

$$\begin{aligned} \langle l'_k | B | l_k \rangle &= \left(\langle l'_{k-1} | \langle \sigma'_{k-1} | \sum_{l'_{k-1} \sigma'_{k-1}} A_{l'_{k-1} l'_k}^{[\sigma'_{k-1}]^*} \right) B_{\sigma'_{k-1} \sigma_{k-1}} \left(\sum_{l_{k-1} \sigma_{k-1}} A_{l_{k-1} l_k}^{[\sigma_{k-1}]} | l_{k-1} \rangle | \sigma_{k-1} \rangle \right) \\ &= \sum_{l_{k-1} \sigma_{k-1}} A_{l_{k-1} l'_k}^{[\sigma'_{k-1}]^*} A_{l_{k-1} l_k}^{[\sigma_{k-1}]} B_{\sigma'_{k-1} \sigma_{k-1}}, \end{aligned} \quad (\text{A.24})$$

where the only condition to derive these results was that site $k-1$ has an orthonormal effective left basis. Similarly, if the $(k-1)$ -left-representation of an operator C is known, its k -left-representation can be obtained via (see figure A.10)

$$\langle l'_k | C | l_k \rangle = \sum_{l'_{k-1} \sigma'_{k-1}} A_{l'_{k-1} l'_k}^{[\sigma'_{k-1}]^*} A_{l_{k-1} l_k}^{[\sigma_{k-1}]} C_{l'_{k-1} l_{k-1}}. \quad (\text{A.25})$$

Equations (A.24) and (A.25) can be used iteratively to transcribe the i -local-representation of B into its k -left-representation for any $k > i$ (see figure A.11). This reasoning also applies to the right site of site k and hence it is possible to obtain a description of any local operator on any site.

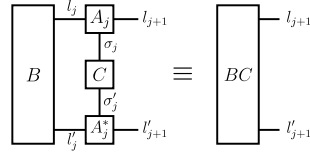


Figure A.12. The $(j+1)$ -left-representation of the operators C , given in the j -local-representation, and B , given in the j -left-representation.

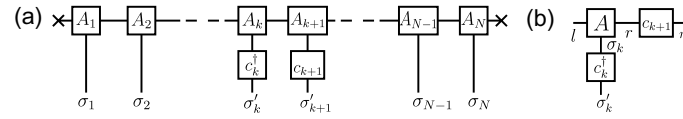


Figure A.13. The nearest-neighbour hopping term $c_k^\dagger c_{k+1}$ acting on $|\psi\rangle$ in (a) the global view and (b) the local view.

To obtain a description of a pair of local operators acting on different sites, we have to transcribe them step by step. Let site k be the current site with orthonormal effective basis sets and B and C two operators acting locally on sites i and j , respectively ($i < j < k$). Firstly, we obtain the j -left-representation of B , namely $B_{l'_j l_j}$, as described above. Then both operators are transformed together into the $(j+1)$ -left-representation (see figure A.12),

$$\langle l'_{j+1} | (BC) | l_{j+1} \rangle = \sum_{l'_j l_j \sigma'_j \sigma_j} A_{l'_j l_{j+1}}^{[\sigma'_j]} * A_{l_j l_j}^{[\sigma_j]} B_{l'_j l_j} C_{\sigma'_j \sigma_j}, \quad (\text{A.26})$$

which in turn can be transformed iteratively into the desired k -left-representation of the operators B and C .

A.2.9. Local operators acting on $|\psi\rangle$. Any combination of operators can be calculated directly in the global view or in the local view via the effective descriptions introduced in the previous section.

Global view. The operators, known in the local basis of the site they are acting on, are contracted directly with the corresponding A -matrix. For example, the formula for a nearest-neighbour hopping term $c_k^\dagger c_{k+1}$ (see figure A.13) reads as

$$\begin{aligned} c_k^\dagger c_{k+1} |\psi\rangle &= \sum_{\sigma_1 \dots \sigma_N} \left(\sum_{\sigma'_k} (c_k^\dagger)_{\sigma'_k \sigma_k} \right) \left(\sum_{\sigma'_{k+1}} (c_{k+1})_{\sigma'_{k+1} \sigma_{k+1}} \right) (A^{[\sigma_1]} \dots A^{[\sigma_N]}) \\ &\times |\sigma_1\rangle \dots |\sigma_{k-1}\rangle |\sigma'_k\rangle |\sigma'_{k+1}\rangle |\sigma_{k+2}\rangle \dots |\sigma_N\rangle. \end{aligned} \quad (\text{A.27})$$

Local view. Let k be the current site with orthonormal effective basis sets. If we want to evaluate operators acting on other sites than the current site k , we need an effective description

44

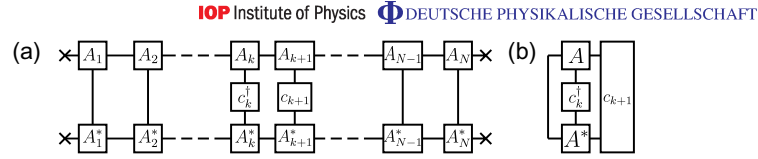


Figure A.14. The expectation value of the nearest-neighbour hopping $c_k^\dagger c_{k+1}$ in (a) the global view and (b) the local view.

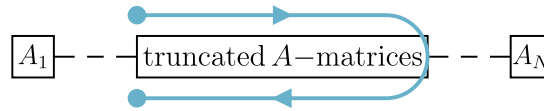


Figure A.15. One complete sweep.

of these operators in one of the effective basis sets of site k to contract these operators with the A -matrix of the current site. For example, to calculate the action of the nearest-neighbour hopping term $c_k^\dagger c_{k+1}$ on $|\psi\rangle = A_{lr}^{[\sigma_k]} |l\rangle |\sigma_k\rangle |r\rangle$, we need $(c_k^\dagger)_{\sigma'_k \sigma_k}$ and $(c_{k+1})_{r'r}$ to obtain (see figure A.13)

$$c_k^\dagger c_{k+1} |\psi\rangle = \sum_{r\sigma_k} \left(\sum_{\sigma'_k} (c_k^\dagger)_{\sigma'_k \sigma_k} \right) \left(\sum_{r'} (c_{k+1})_{r'r} \right) A_{lr}^{[\sigma_k]} |l\rangle |\sigma'_k\rangle |r'\rangle. \quad (\text{A.28})$$

A.2.10. Expectation values. Expectation values are merely the scalar product between the state with itself including the action of an operator and can be easily worked out in both the global view and the local view (see figure A.14). Since both methods are equivalent, the local variant is much more efficient as it involves many fewer matrix multiplications. However, it requires careful orthonormalization of the remainder of the A -matrices. The iterative scheme, introduced in section A.3, allows for that and works in the local picture.

A.3. Variational optimization scheme

The basic techniques introduced in the previous sections are the building blocks for DMRG sweeps, an iterative scheme to determine the ground state in the usual DMRG sense. This scheme starts at some site as current site, for example the first site where truncation occurs, and minimizes the energy of $|\psi\rangle$ with respect to that site. Afterwards the current site is shifted to the next site, and the energy of $|\psi\rangle$ with respect to that site is minimized. This is repeated until the last site where truncation occurs is reached and the direction of the switches is reversed. When the starting site is reached again, one *sweep* has been finished (see figure A.15). These sweeps are repeated until $|\psi\rangle$ converges.

A.3.1. Energy minimization of the current site. In order to find the ground state of the system we have to minimize the energy $E = \langle \psi | H | \psi \rangle$ of the matrix product state $|\psi\rangle$ with the constraint that the norm of $|\psi\rangle$ must not change. Introducing λ as Lagrange multiplier to ensure

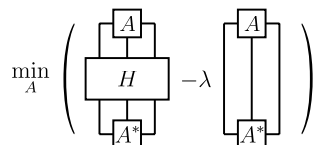


Figure A.16. The minimization problem expressed in the current site.

proper normalization, we arrive at the problem of determining

$$\min_{|\psi\rangle} (\langle \psi | H | \psi \rangle - \lambda \langle \psi | \psi \rangle). \quad (\text{A.29})$$

In the sweeping procedure introduced above, the current site is changed from one site to the next and the energy is minimized in each local description. Thus, we need (A.29) in terms of the parameters of the current site. Let us describe how to do this for the case of one-site DMRG, where the A -matrices are optimized one site at a time. (The procedure for two-site DMRG is entirely analogous, except that it involves combining A -matrices of two neighbouring sites by fusing their indices to obtain a combined two-site A -matrix; see section A.2.5.) Inserting (A.1) into (A.29) yields (see figure A.16)

$$\min_{A^{[\sigma]}} \left(\sum_{l'r\sigma'l'r\sigma'} A_{l'r'}^{[\sigma]*} H_{l'r'\sigma'l'r\sigma} A_{l'r}^{[\sigma]} - \lambda \sum_{l'r\sigma} A_{l'r}^{[\sigma]*} A_{l'r}^{[\sigma]} \right), \quad (\text{A.30})$$

where $H_{l'r'\sigma'l'r\sigma} = \langle l' | \langle \sigma' | \langle r' | H | l | \sigma \rangle | r \rangle$ is the Hamiltonian expressed in the two orthonormal effective basis sets and the local basis of the current site.

The multidimensional minimization problem (A.29) has been transformed to a local minimization problem where one A -matrix (or two) is optimized at a time and all others are kept constant. Such a procedure could, in principle, cause the system to get stuck in a local minimum in energy, but experience shows that the procedure works well [5], especially in the presence of a gap.

To obtain a solution for (A.30), we differentiate the equation with respect to $A_{l'r'}^{[\sigma]*}$ (this is possible because the Hilbert space has a Hermitian scalar product) and obtain

$$0 = \sum_{l'r'\sigma'} H_{l'r'\sigma'l'r\sigma} A_{l'r}^{[\sigma]} - \lambda A_{l'r'}^{[\sigma]}. \quad (\text{A.31})$$

The matrix elements $H_{l'r'\sigma'l'r\sigma}$ may be calculated easily using the techniques introduced in section A.2 (see section A.3.2 for details). Changing to matrix notation and replacing λ with E_0 in anticipation of its interpretation as an energy, we obtain an eigenvalue equation:

$$H A_{l'r}^{[\sigma]} | l \rangle | \sigma \rangle | r \rangle = E_0 A_{l'r}^{[\sigma]} | l \rangle | \sigma \rangle | r \rangle. \quad (\text{A.32})$$

The minimization problem reduces to a local eigenvalue problem, which can be solved by standard techniques. The full Hilbert space of the current site has dimension dD^2 and may become large, but it is not necessary to determine the full spectrum of H , since we are interested only in the ground state. The Lanczos algorithm is an effective algorithm to achieve exactly

46

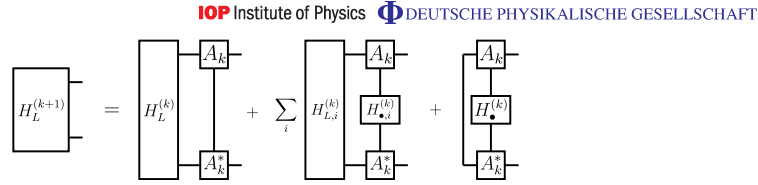


Figure A.17. Iterative calculation of the operator $H_L^{(k+1)}$. The sum over i indicates that $H_{L,\bullet}^{(k)}$ has the form $\sum_i H_{L,i}^{(k)} \otimes H_{\bullet,i}^{(k)}$, where $H_{L,i}^{(k)}$ acts only on sites $k' < k$ and $H_{i,\bullet}^{(k)}$ acts only on site k . The calculation of $H_R^{(k-1)}$ works analogously.

that. The advantage of this algorithm is that we only have to compute $H|\psi\rangle$, which saves much effort. The Lanczos algorithm produces as output the ground state eigenvalue and eigenvector. The latter gives the desired optimized version of the matrix $A_{l,r}^\sigma$, which then has to be rewritten (with or without Hilbert space truncation, as needed) into a form that satisfies the orthonormality requirements of the left and right basis sets, as described in section A.2.4.

A.3.2. Sweeping details. Before the actual sweeping may be started we have to set up an initial state, prepare a current site with orthonormal effective basis sets and calculate effective descriptions of operators that are part of the Hamiltonian. After this initialization we may determine the ground state with respect to this current site and shift the current site to the next site. That current site again has orthonormal effective basis sets due to the switching procedure introduced in section A.2.4, but we also need effective representations of the operators acting in the Hamiltonian. At this step the structure of the MPS saves much effort, as most of the needed representations are already calculated.

Structure of the Hamiltonian terms. The Hamiltonian $H_{l'r'\sigma'l r\sigma}$, acting in the space spanned by the states $|l\rangle$, $|\sigma\rangle$ and $|r\rangle$, breaks up into several terms:

$$\begin{aligned} H_{l'r'\sigma'l r\sigma} = & \mathbb{1}_{l'l} \otimes (H_{\bullet})_{\sigma'\sigma} \otimes \mathbb{1}_{r'r} + (H_L)_{l'l} \otimes \mathbb{1}_{\sigma'\sigma} \otimes \mathbb{1}_{r'r} + \mathbb{1}_{l'l} \otimes \mathbb{1}_{\sigma'\sigma} \otimes (H_R)_{r'r} \\ & + (H_{L,\bullet})_{l'l\sigma'\sigma} \otimes \mathbb{1}_{r'r} + \mathbb{1}_{l'l} \otimes (H_{\bullet R})_{r'r\sigma'\sigma} + (H_{L,\bullet R})_{l'l r'r\sigma'\sigma}, \end{aligned} \quad (\text{A.33})$$

where the indices denote on which parts of the system the respective term acts on (L and R indicate left and right of the current site, respectively, and \bullet indicates action on the current site). Of course, the six terms of (A.33) depend on the current site k : $H_{\bullet}^{(k)}$, $H_L^{(k)}$, $H_R^{(k)}$, $H_{L,\bullet}^{(k)}$, $H_{\bullet R}^{(k)}$ and $H_{L,\bullet R}^{(k)}$. The terms $(H_L)_{l'l}$ and $(H_R)_{r'r}$ contain all terms that involve only sites $k' < k$ and $k' > k$, respectively. The iterative structure of the method directly yields the following equalities:

$$H_L^{(k+1)} = H_L^{(k)} + H_{L,\bullet}^{(k)} + H_{\bullet}^{(k)}, \quad (\text{A.34})$$

$$H_R^{(k-1)} = H_{\bullet}^{(k)} + H_{\bullet R}^{(k)} + H_R^{(k)}, \quad (\text{A.35})$$

where the terms on the rhs are meant to be expressed in the effective basis of the operator on the lhs (see figure A.17).

Initialization. First of all we need an initial MPS, which is most conveniently chosen to consist of identity transformations at the ends of the chain (see section A.2.3) and random A -matrices for the rest of the chain. We take the first site where Hilbert space truncation is applied as current site k and obtain an orthonormal effective right basis (the effective left basis is already orthonormal) using the orthonormalization procedure introduced in section A.2.4 starting from site N . Additionally, it is convenient, while dealing with site N , to calculate and store the operator $H_R^{(N-1)}$ (see equation (A.35)) and the effective description of all operators of site N that contribute to $H_{\bullet R}^{(k)}$ and $H_{L\bullet R}^{(k)}$ in the effective right basis of site $N-1$ (see section A.2.8). This ensures, when the sweeping procedure reaches site $N-1$, that all necessary operators are already calculated. This is repeated from site N down to site $k+1$ and similarly for the sites $k' < k$ in the other direction. The result of these initialization steps is that we have a current site k with orthonormal effective basis sets, effective descriptions of the Hamiltonian terms $H_L^{(k)}$ and $H_R^{(k)}$ and effective descriptions of all operators contributing to $H_{L\bullet}^{(k)}$, $H_{\bullet R}^{(k)}$ and $H_{L\bullet R}^{(k)}$. Moreover, with an appropriate extension to the switching procedure of section A.2.4, all effective descriptions for other current sites are available for use when needed in future sweeping steps.

Extended switching procedure. The switching procedure of section A.2.4 is applied as before. Additionally, depending on the direction of the switch, $H_L^{(k+1)}$ or $H_R^{(k-1)}$ are calculated and stored as well as the operators needed for the Hamiltonian (A.33). This extended switching ensures that for the new current site all required operators are calculated if they had been for the old current site.

Complete ground state calculation. The methods introduced above make the procedure for determining the ground state very efficient as the global problem is mapped onto many local problems involving only a few terms to calculate. The iterative structure of the MPSs and the effective Hamiltonian terms strongly increase the efficiency. A full ground state calculation consists of:

- (i) Initialization as described above.
- (ii) Full sweeps from site K to site K' and back to site K , with sites K and K' being the first and last sites where the effective Hilbert spaces are truncated.
- (iii) After each sweep i the overlap $\langle \psi_{i-1} | \psi_i \rangle$ between the state before and after the sweep is calculated. If the MPS does not change any more, stop the sweeping. A criterion, for example, for when to stop would be to require that

$$\frac{|\langle \psi_{i-1} | \psi_i \rangle - \langle \psi_{i-2} | \psi_{i-1} \rangle|}{|\langle \psi_{i-1} | \psi_i \rangle|} \leq \epsilon, \quad (\text{A.36})$$

where ϵ is a small control parameter, typically of order 10^{-10} .

Numerical costs. The step with the most impact on the numerical costs of the algorithm is the calculation of $H|\psi\rangle$ in the Lanczos method. This method is an iterative scheme using several *Lanczos steps*, of which usually less than 100 are needed for one ground state calculation. Each Lanczos step calculates $H|\psi\rangle$ exactly once. This calculation basically consists of elementary matrix multiplications, see section A.5.3 for details of the numerical costs of such calculations.

All of the six terms introduced in (A.33) are not equally time consuming. Most of them contain identity maps that do not need to be carried out and thus the term $H_{L,R}$ is the most time consuming, requiring operations of order $\mathcal{O}(dD^2(2D+d))$. The total numerical cost for the minimization process is

$$C = N_{\text{Sweep}} \times 2N \times N_{\text{Lanczos}} \times (dD^2(2D+d)), \quad (\text{A.37})$$

where N_{Sweep} is the number of sweeps, N the chain length and N_{Lanczos} the number of Lanczos steps. In practice the cutoff dimension is significantly higher than the local Hilbert space dimension d and thus (A.37) is nearly linear in d .

A.4. Abelian symmetries

MPSs can be easily adapted to properly account for conserved quantum numbers, representing the global symmetries of the Hamiltonian. We will limit ourselves to Abelian symmetries, meaning that the irreducible representation of the symmetry group is Abelian, as these are easily implemented, which is not necessarily the case for non-Abelian symmetries [36].

An Abelian symmetry allows a quantum number Q to be attached to every state. The property that the symmetry is Abelian manifests itself in that this quantum number is strictly additive. For two states $|Q_1\rangle$ and $|Q_2\rangle$, the quantum number of the direct product of these two states is given by $|Q_1\rangle \otimes |Q_2\rangle = |Q_1 + Q_2\rangle$. For example, if the Hamiltonian commutes with the number operator for the full system, the quantum number Q could represent particle number.

For MPSs, the introduction of Abelian symmetries has the consequence that the A -matrix $A_r^{[\sigma]}$ may be written as $(A_{Q_l, Q_r}^{Q_\sigma})_{\alpha_l \beta_r}^{\gamma_\sigma}$. Here Q_σ , Q_l and Q_r are the quantum numbers attached to the local, left effective and right effective basis, respectively. The index α_l distinguishes different states $|Q_l, \alpha_l\rangle$ characterized by the same quantum number Q_l , and similarly for $|Q_r, \beta_r\rangle$ and $|Q_\sigma, \gamma_\sigma\rangle$. If A describes, for example, the mapping of the $|l\rangle$ -basis of the left block together with the local basis to a combined (truncated) $|r\rangle$ -basis, then the only nonzero blocks of the A -matrix are those for which $Q_\sigma + Q_l = Q_r$. For the current site, the total symmetry Q_{tot} of the full quantum many-body state manifests itself in that the corresponding A -matrix fulfills $Q_l + Q_r + Q_\sigma = Q_{\text{tot}}$.

For the handling of MPSs, quantum numbers imply a significant amount of bookkeeping, i.e. for every coefficient block we have to store its quantum number. The benefit is that we can deal with large effective state spaces at a reasonable numerical cost. The Lanczos algorithm, in particular, takes advantage of the block structure.

Of course, the treatment of Abelian symmetries is generic and not limited to only one symmetry. We may incorporate as many symmetries as exist for a given Hamiltonian, by writing Q as a vector of the corresponding quantum numbers.

A.5. Additional details

A.5.1. Derivation of the orthonormality condition. The orthonormality condition (A.7) is easily derived by induction. The starting point is condition (A.6) and we confine ourselves to the derivation for the left basis. The derivation for the right basis is analogous.

The induction argument can be initialized with site $k = 1$ because its effective left basis is already orthonormal as it consists only of the vacuum state. Now, consider the case that site k has an orthonormal effective left basis and construct the condition for site $k + 1$ to have an

orthonormal effective left basis:

$$\begin{aligned}
 \langle l'_{k+1} | l_{k+1} \rangle &= \left(\sum_{l'_k \sigma'_k} \langle l'_k | \langle \sigma'_k | A_{l'_k l'_{k+1}}^{[\sigma'_k]} \rangle^* \right) \left(\sum_{l_k \sigma_k} A_{l_k l_{k+1}}^{[\sigma_k]} | l_k \rangle | \sigma_k \rangle \right) \\
 &= \sum_{l'_k l'_k \sigma'_k} A_{l'_k l'_{k+1}}^{[\sigma'_k]} A_{l_k l_{k+1}}^{[\sigma_k]} \underbrace{\langle l'_k | l_k \rangle}_{\delta_{l'_k l_k}} \underbrace{\langle \sigma'_k | \sigma_k \rangle}_{\delta_{\sigma'_k \sigma_k}} = \sum_{l_k \sigma_k} A_{l_k l'_{k+1}}^{[\sigma_k]} A_{l_k l_{k+1}}^{[\sigma_k]} \\
 &= \left(\sum_{\sigma_k} A^{[\sigma_k]} \right)^\dagger A^{[\sigma_k]} \Big|_{l'_{k+1} l_{k+1}}. \tag{A.38}
 \end{aligned}$$

Condition (A.7) follows with $\langle l'_{k+1} | l_{k+1} \rangle \stackrel{!}{=} \delta_{l'_{k+1} l_{k+1}}$.

A.5.2. SVD. The SVD can be seen as a generalization of the spectral theorem, i.e. of the eigenvalue decomposition. It is valid for any real or complex $m \times n$ rectangular matrix. Let M be such a matrix; then it can be written in an SVD

$$M = USV^\dagger, \tag{A.39}$$

where U is an $m \times m$ unitary matrix, S is an $m \times n$ matrix with real, non-negative entries on the diagonal and with zeros off the diagonal and V is an $n \times n$ unitary matrix. The numbers on the diagonal of S are called *singular values*, and there are $p = \min(n, m)$ of them. The singular values are unique, but U and V are not, in general. It is convenient to truncate and reorder these matrices in such a fashion that their dimensions are $m \times p$ for U , $p \times p$ for S (with the singular values ordered in a non-increasing fashion) and $n \times p$ for V (i.e. $p \times n$ for V^\dagger). A consequence of this truncation is that U or V is no longer quadratic and unitarity is not defined for such matrices. This property is replaced by *column unitarity* (orthonormal columns) of U and *row unitarity* (orthonormal rows) for V^\dagger —no matter which one is no longer quadratic. In this paper, all SVDs are understood to be ordered in this fashion.

A.5.3. Numerical costs of index contractions. The numerical costs of matrix multiplications and index contractions of multi-index objects depend on the dimension of both the resulting object and of the contracted indices. In the case of matrix multiplications this is quite simple. Consider an $n \times m$ matrix M_1 multiplied by an $m \times p$ matrix M_2 . The result is an $n \times p$ matrix M :

$$M_{ij} = \sum_{k=1}^m (M_1)_{ik} (M_2)_{kj}. \tag{A.40}$$

Evidently, each of the $n * p$ matrix elements M_{ij} requires a sum over m products of the form $(M_1)_{ik} (M_2)_{kj}$. Thus the process for calculating $M_1 M_2$ is of order $\mathcal{O}(nmp)$.

The numerical costs of multi-index objects are obtained analogously. Consider two multi-index objects, M_1 with indices i_1, \dots, i_n and dimensions $p_1 \times \dots \times p_n$ and M_2 with indices j_1, \dots, j_m and dimensions $q_1 \times \dots \times q_m$. If we contract the indices i_1 and i_2 of M_1 with the indices j_1 and j_2 of M_2 (assuming that $p_1 = q_1$ and $p_2 = q_2$), we obtain the multi-index object M :

$$M_{i_3 \dots i_n j_3 \dots j_m} = \sum_{k=1}^{p_1} \sum_{l=1}^{p_2} (M_1)_{kl i_3 \dots i_n} (M_2)_{kl j_3 \dots j_m}. \tag{A.41}$$

Thus, for every entry of M , p_1 times p_2 multiplications have to be done, so that the process is of order $\mathcal{O}((p_3 \dots p_n)(p_1 p_2)(q_3 \dots q_m))$.

References

- [1] Cheong S A and Henley C L 2009 *Phys. Rev. B* **79** 212402
- [2] Cheong S A and Henley C L 2009 *Phys. Rev. B* **80** 165124
- [3] White S R 1992 *Phys. Rev. Lett.* **69** 2863–6
- [4] White S R 1993 *Phys. Rev. B* **48** 10345–56
- [5] Schollwöck U 2005 *Rev. Mod. Phys.* **77** 259–315
- [6] Verstraete F, Porras D and Cirac J I 2004 *Phys. Rev. Lett.* **93** 227205
- [7] Wilson K G 1975 *Rev. Mod. Phys.* **47** 773–840
- [8] Vekić M and White S R 1993 *Phys. Rev. Lett.* **71** 4283–6
- [9] Andersson M, Boman M and Östlund S 1999 *Phys. Rev. B* **59** 10493–503
- [10] Efetov K B and Larkin A I 1976 *Sov. Phys. JETP* **42** 390–6
- [11] Micnas R, Ranninger J and Robaszkiewicz S 1988 *J. Phys. Colloq.* **49** C8-2221–6
- [12] Furukawa S, Pasquier V and Shiraishi J 2009 *Phys. Rev. Lett.* **102** 170602
- [13] Vidal G 2004 *Phys. Rev. Lett.* **93** 040502
- [14] White S R and Feiguin A E 2004 *Phys. Rev. Lett.* **93** 076401
- [15] Daley A J, Kollath C, Schollwöck U and Vidal G 2004 *J. Stat. Mech.* P04005
- [16] García-Ripoll J J 2006 *New J. Phys.* **8** 305
- [17] Affleck I, Kennedy T, Lieb E H and Tasaki H 1987 *Phys. Rev. Lett.* **59** 799
- [18] Klümper A, Schadschneider A and Zittartz J 1991 *J. Physique A* **24** L955
- [19] Fannes M, Nachtergaele B and Werner R F 1992 *Commun. Math. Phys.* **144** 443–90
- [20] Klümper A, Schadschneider A and Zittartz J 1992 *Z. Phys. B* **87** 281
- [21] Derrida B, Evans M R, Hakim V and Pasquier V 1993 *J. Physique A* **26** 1493
- [22] Rommer S and Östlund S 1997 *Phys. Rev. B* **55** 2164
- [23] Östlund S and Rommer S 1995 *Phys. Rev. Lett.* **75** 3537–40
- [24] Martín-Delgado M A and Sierra G 1996 *Int. J. Mod. Phys. A* **11** 3145
- [25] Dukelsky J, Martín-Delgado M A, Nishino T and Sierra G 1998 *Europhys. Lett.* **43** 457–62
- [26] Takasaki H, Hikihara T and Nishino T 1999 *J. Phys. Soc. Japan* **68** 1537–40
- [27] McCulloch I P 2007 *J. Stat. Mech.* **2007** P10014
- [28] Chung M-C and Peschel I 2001 *Phys. Rev. B* **64** 064412
- [29] Vidal G, Latorre J I, Rico E and Kitaev A 2003 *Phys. Rev. Lett.* **90** 227902
- [30] Schuch N, Wolf M M, Verstraete F and Cirac J I 2008 *Phys. Rev. Lett.* **100** 040501
- [31] Korepin V E 2004 *Phys. Rev. Lett.* **92** 096402
- [32] Verstraete F, García-Ripoll J J and Cirac J I 2004 *Phys. Rev. Lett.* **93** 207204
- [33] Feiguin A E and White S R 2005 *Phys. Rev. B* **72** 220401
- [34] Jordan P and Wigner E 1928 *Z. Phys.* **47** 631–51
- [35] Verstraete F and Cirac J I 2006 *Phys. Rev. B* **73** 094423
- [36] McCulloch I P and Gulácsi M 2002 *Europhys. Lett.* **57** 852–8

Chapter 6

Anderson orthogonality

In this section we present our results about Anderson orthogonality, as introduced in Sec. 3.5. Our first publication *Anderson Orthogonality and the Numerical Renormalization Group* deals with static quantities related to AO (see Sec. 3.5.1) that is we show (i) how to extract the AO factor Δ_{AO} from decaying overlaps between two separate NRG calculations, (ii) how to calculate the displaced charge Δ_{ch} for a single state calculated with NRG, and (iii) that all consistency checks between Δ_{AO} , Δ_{ch} , and Δ_{ph} (the calculation of the latter is known for a long time) hold with great accuracy even for complex models.

Our second publication concerning AO, *Anderson Orthogonality in the Dynamics After a Local Quantum Quench*, deals with dynamical quantities related to AO (see Sec. 3.5.2). We establish a formalism of how AO leaves its imprints in optical absorption spectra and apply it to a simple model to illustrate some effects which will be of more importance in a more complex context like population switching in quantum dots. For the latter, we apply an extensive study to clarify the influence of AO.

6.1 Anderson Orthogonality and the Numerical Renormalization Group

PHYSICAL REVIEW B **84**, 075137 (2011)**Anderson orthogonality and the numerical renormalization group**

Andreas Weichselbaum, Wolfgang Munder, and Jan von Delft

Physics Department, Arnold Sommerfeld Center for Theoretical Physics, and Center for NanoScience, Ludwig-Maximilians-Universitat, DE-80333 Munich, Germany

(Received 20 April 2011; published 10 August 2011)

Anderson orthogonality (AO) refers to the fact that the ground states of two Fermi seas that experience different local scattering potentials, say $|G_I\rangle$ and $|G_F\rangle$, become orthogonal in the thermodynamic limit of large particle number N , in that $|\langle G_I|G_F\rangle| \sim N^{-\frac{1}{2}\Delta_{AO}^2}$ for $N \rightarrow \infty$. We show that the numerical renormalization group offers a simple and precise way to calculate the exponent Δ_{AO} : the overlap, calculated as a function of Wilson chain length k , decays exponentially $\sim e^{-k\alpha}$, and Δ_{AO} can be extracted directly from the exponent α . The results for Δ_{AO} so obtained are consistent (with relative errors typically smaller than 1%) with two other related quantities that compare how ground-state properties change upon switching from $|G_I\rangle$ to $|G_F\rangle$: the difference in scattering phase shifts at the Fermi energy, and the displaced charge flowing in from infinity. We illustrate this for several nontrivial interacting models, including systems that exhibit population switching.

DOI: 10.1103/PhysRevB.84.075137

PACS number(s): 02.70.-c, 05.10.Cc, 75.20.Hr, 78.20.Bh

I. INTRODUCTION

In 1967, Anderson considered the response of a Fermi sea to a change in local scattering potential and made the following observation¹: The ground states $|G_I\rangle$ and $|G_F\rangle$ of the Hamiltonians \hat{H}_I and \hat{H}_F describing the system before and after the change, respectively, become orthogonal in the thermodynamic limit, decaying with total particle number N as

$$|\langle G_I|G_F\rangle| \sim N^{-\frac{1}{2}\Delta_{AO}^2}, \quad (1)$$

because the single-particle states comprising the two Fermi seas are characterized by different phase shifts.

Whenever the Anderson orthogonality (AO) exponent Δ_{AO} is finite, the overlap of the two ground-state wave functions goes to zero as the system size becomes macroscopic. As a consequence, matrix elements of the form $|\langle G_I|\hat{O}|G_F\rangle|$, where \hat{O} is a local operator acting at the site of the localized potential, necessarily also vanish in the thermodynamic limit. This fact has far-reaching consequences, underlying several fundamental phenomena in condensed matter physics involving quantum impurity models, i.e., models describing a Fermi sea coupled to localized quantum degrees of freedom. Examples are the Mahan exciton (ME) and the Fermi-edge singularity²⁻⁵ (FES) in absorption spectra, and the Kondo effect⁶ arising in magnetic alloys⁷ or in transport through quantum dots.⁸ For all of these, the low-temperature dynamics is governed by the response of the Fermi sea to a sudden switch of a local scattering potential. More recently, there has also been growing interest in inducing such a sudden switch, or quantum quench, by optical excitations of a quantum dot tunnel-coupled to a Fermi sea, in which case the post-quench dynamics leaves fingerprints, characteristic of AO, in the optical absorption or emission line shape.⁹⁻¹¹

The intrinsic connection of local quantum quenches to the scaling of the Anderson orthogonality with system size can be intuitively understood as follows. Consider an instantaneous event at the location of the impurity at time $t = 0$ in a system initially in equilibrium. This local perturbation will spread out spatially, such that for $t > 0$, the initial wave function is affected only within a radius $L \simeq v_f t$ of the impurity, with

v_f the Fermi velocity. The AO finite-size scaling in Eq. (1) therefore directly resembles the actual experimental situation and, in particular, allows the exponent Δ_{AO} to be directly related to the exponents seen in experimental observables at long-time scales, or at the threshold frequency in Fourier space.¹²

A powerful numerical tool for studying quantum impurity models is the numerical renormalization group (NRG),^{13,14} which allows numerous static and dynamical quantities to be calculated explicitly, also in the thermodynamic limit of infinite bath size. The purpose of this paper is to point out that NRG also offers a completely straightforward way to calculate the overlap $|\langle G_I|G_F\rangle|$ and hence to extract Δ_{AO} . The advantage of using NRG for this purpose is that NRG is able to deal with quantum impurity models that in general also involve local *interactions*, which are usually not tractable analytically. Although Anderson himself did not include local interactions in his considerations,¹ his prediction (1) still applies, provided the ground states $|G_{I,F}\rangle$ describe Fermi liquids. This is the case for most impurity models (but not all; the two-channel Kondo model is a notable exception). Another useful feature of NRG is that it allows consistency checks on its results for overlap decays since Δ_{AO} is known to be related to a change of scattering phase shifts at the Fermi surface. These phase shifts can be calculated independently, either from NRG energy flow diagrams, or via Friedel's sum rule from the displaced charge, as will be elaborated below.

A further concrete motivation for the present study is to develop a convenient tool for calculating AO exponents for quantum dot models that display the phenomenon of population switching.¹⁵⁻¹⁹ In such models, a quantum dot tunnel-coupled to leads contains levels of different widths, and is capacitively coupled to a gate voltage that shifts the levels energy relative to the Fermi level of the leads. Under suitable conditions, an (adiabatic) sweep of the gate voltage induces an inversion in the population of these levels (a so-called population switch), implying a change in the local potential seen by the Fermi seas in the leads. In this paper, we verify that the method of extracting Δ_{AO} from $\langle G_I|G_F\rangle$ works reliably also for such models. In a separate publication,¹² we will use

this method to analyze whether AO can lead to a quantum phase transition in such models, as suggested in Ref. 19.

The remainder of this paper is structured as follows: In Sec. II, we define the AO exponent Δ_{AO} in general terms, and explain in Sec. III how NRG can be used to calculate it. Section IV presents numerical results for several interacting quantum dot models of increasing complexity: first the spinless interacting resonant level model (IRLM), then the single-impurity Anderson model (SIAM), followed by two models exhibiting population switching, one for spinless and the other for spinful electrons. In all cases, our results for Δ_{AO} satisfy all consistency checks to within less than 1%.

II. DEFINITION OF ANDERSON ORTHOGONALITY

A. AO for a single channel

To set the stage, let us review AO in the context of a free Fermi sea involving a single species or channel of noninteracting electrons experiencing two different local scattering potentials. The initial and final systems are described in full by the Hamiltonians \hat{H}_I and \hat{H}_F , respectively. Let $\hat{c}_{\varepsilon,X}^\dagger|0\rangle$ be the single-particle eigenstates of \hat{H}_X characterized by the scattering phase shifts $\delta_X(\varepsilon)$, where $X \in \{I, F\}$ and $\hat{c}_{\varepsilon,X}^\dagger$ are fermion creation operators, and let ε^f be the same Fermi energy for both Fermi seas $|G_X\rangle$. Anderson showed that in the thermodynamic limit of large particle number $N \rightarrow \infty$, the overlap

$$\langle G_I | G_F \rangle = \langle 0 | \prod_{\varepsilon < \varepsilon^f} \hat{c}_{\varepsilon,I} \prod_{\varepsilon < \varepsilon^f} \hat{c}_{\varepsilon,F}^\dagger | 0 \rangle \quad (2)$$

decays as in Eq. (1),^{1,4} where Δ_{AO} is equal to the difference in single-particle phase shifts at the Fermi level

$$\Delta_{\text{AO}} = \Delta_{\text{ph}} \equiv [\delta_F(\varepsilon^f) - \delta_I(\varepsilon^f)]/\pi. \quad (3)$$

The relative sign between Δ_{AO} and Δ_{ph} (+, not $-$) does not affect the orthogonality exponent Δ_{AO}^2 , but follows standard convention [Ref. 20, Eq. (7), or Ref. 21, Eq. (21)].

In this paper, we will compare three independent ways of calculating Δ_{AO} . (i) The first approach calculates the overlap $|\langle G_I | G_F \rangle|$ of Eq. (1) explicitly as a function of (effective) system size. The main novelty of this paper is to point out that this can easily be done in the framework of NRG, as will be explained in detail in Sec. III.

(ii) The second approach is to directly calculate Δ_{ph} via Eq. (3), since the extraction of phase shifts $\delta_X(\varepsilon^f)$ from NRG finite-size spectra is well known¹³; Provided that \hat{H}_X describes a Fermi liquid, the (suitably normalized) fixed point spectrum of NRG can be reconstructed in terms of equidistant free-particle levels shifted by an amount determined by $\delta_X(\varepsilon^f)$. The many-body excitation energy of an additional particle, a hole and a particle-hole pair, thus allow the phase shift $\delta_X(\varepsilon^f)$ to be determined unambiguously.

(iii) The third approach exploits Friedel's sum rule,²⁰ which relates the difference in phase shifts to the so-called *displaced charge* Δ_{ch} via $\Delta_{\text{ch}} = \Delta_{\text{ph}}$. Here the displaced charge Δ_{ch} is defined as the charge in units of e (i.e., the number of electrons) flowing inward from infinity into a region of large but finite

volume, say V_{large} , surrounding the scattering location, upon switching from \hat{H}_I to \hat{H}_F :

$$\begin{aligned} \Delta_{\text{ch}} &\equiv \langle G_F | \hat{n}_{\text{tot}} | G_F \rangle - \langle G_I | \hat{n}_{\text{tot}} | G_I \rangle \\ &\equiv \Delta_{\text{sea}} + \Delta_{\text{dot}}. \end{aligned} \quad (4)$$

Here, $\hat{n}_{\text{tot}} \equiv \hat{n}_{\text{sea}} + \hat{n}_{\text{dot}}$, where \hat{n}_{sea} is the total number of Fermi-sea electrons within V_{large} , whereas \hat{n}_{dot} is the local charge of the scattering site, henceforth called "dot."

To summarize, we have the equalities

$$\Delta_{\text{AO}}^2 = \Delta_{\text{ph}}^2 = \Delta_{\text{ch}}^2, \quad (5)$$

where all three quantities can be calculated independently and straightforwardly within the NRG. Thus, Eq. (5) constitutes a strong consistency check. We will demonstrate below that NRG results satisfy this check with good accuracy (deviations are typically below 1%).

B. AO for multiple channels

We will also consider models involving several independent and conserved channels (e.g., spin in spin-conserving models). In the absence of interactions, the overall ground-state wave function is the product of those of the individual channels. With respect to AO, this trivially implies that each channel *adds* independently to the AO exponent in Eq. (1),

$$\Delta_{\text{AO}}^2 = \sum_{\mu=1}^{N_c} \Delta_{\text{AO},\mu}^2, \quad (6)$$

where $\mu = 1, \dots, N_c$ labels the N_c different channels. We will demonstrate below that the additive character in Eq. (6) generalizes to systems with *local interactions*, provided that the particle number in each channel remains conserved. This is remarkable since interactions may cause the ground-state wave function to involve entanglement between local and Fermi-sea degrees of freedom from different channels. However, our results imply that the asymptotic tails of the ground-state wave function far from the dot still factorize into a product of factors from individual channels. In particular, we will calculate the displaced charge for each individual channel [cf. Eq. (4)]

$$\begin{aligned} \Delta_{\text{ch},\mu} &\equiv \langle G_F | \hat{n}_{\text{tot},\mu} | G_F \rangle - \langle G_I | \hat{n}_{\text{tot},\mu} | G_I \rangle \\ &\equiv \Delta_{\text{sea},\mu} + \Delta_{\text{dot},\mu}, \end{aligned} \quad (7)$$

where $\hat{n}_{\text{tot},\mu} = \hat{n}_{\text{sea},\mu} + \hat{n}_{\text{dot},\mu}$. Assuming no interactions in the respective Fermi seas, it follows from Friedel's sum rule that $\Delta_{\text{AO},\mu}^2 = \Delta_{\text{ch},\mu}^2$, and therefore

$$\Delta_{\text{AO}}^2 = \sum_{\mu=1}^{N_c} \Delta_{\text{ch},\mu}^2 \equiv \Delta_{\text{ch}}^2, \quad (8)$$

where Δ_{ch}^2 is the total sum of the squares of the displaced charges of the separate channels. Equation (8) holds with great numerical accuracy, too, as will be shown below.

III. TREATING ANDERSON ORTHOGONALITY USING NRG

A. General impurity models

The problem of a noninteracting Fermi sea in the presence of a local scatterer belongs to the general class of quantum impurity models treatable by Wilson's NRG.¹³ Our proposed approach for calculating Δ_{AO} applies to *any* impurity model treatable by NRG. To be specific, however, we will focus here on generalized Anderson impurity type models. They describe N_c different (and conserved) species or channels of fermions that hybridize with local degrees of freedom at the dot, while all interaction terms are local.

We take both the initial and final ($X \in \{I, F\}$) Hamiltonians to have the generic form $\hat{H}_X = \hat{H}_b + \hat{H}_{d,X} + \hat{H}_{\text{int}}^{\text{IRLM}}$. The first term

$$\hat{H}_b = \sum_{\mu=1}^{N_c} \sum_{\epsilon} \epsilon \hat{c}_{\epsilon\mu}^{\dagger} \hat{c}_{\epsilon\mu} \quad (9)$$

describes a noninteracting Fermi sea involving N_c channels. (N_c includes the spin index, if present.) For simplicity, we assume a constant density of states $\rho_{\mu}(\epsilon) = \rho_{0,\mu} \theta(D - |\epsilon|)$ for each channel with half-bandwidth D . Moreover, when representing numerical results, energies will be measured in units of half-bandwidth, hence $D := 1$. The Fermi sea is assumed to couple to the dot only via the local operators $\hat{f}_{0\mu} = \frac{1}{\sqrt{N_b}} \sum_{\epsilon} \hat{c}_{\epsilon\mu}$ and $\hat{f}_{0\mu}^{\dagger}$, that, respectively, annihilate or create a Fermi-sea electron of channel μ at the position of the dot $\vec{r} = 0$, with a proper normalization constant N_b to ensure $[\hat{f}_{0\mu}, \hat{f}_{0\mu'}^{\dagger}] = \delta_{\mu\mu'}$.

The second term $\hat{H}_{d,X}$ contains the noninteracting local part of the Hamiltonian, including the dot-lead hybridization

$$\hat{H}_{d,X} = \sum_{\mu=1}^{N_c} \epsilon_{d\mu,X} \hat{n}_{d\mu} + \sum_{\mu=1}^{N_c} \sqrt{\frac{2\Gamma_{\mu}}{\pi}} [\hat{d}_{\mu}^{\dagger} \hat{f}_{0\mu} + \text{H.c.}] \quad (10)$$

Here, $\epsilon_{d\mu,X}$ is the energy of dot level μ in the initial or final configuration, and $\hat{n}_{d\mu} = \hat{d}_{\mu}^{\dagger} \hat{d}_{\mu}$ is its electron number. $\Gamma_{\mu} \equiv \pi \rho_{\mu} V_{\mu}^2$ is the effective width of level μ induced by its hybridization with channel μ of the Fermi sea, with V_{μ} the μ -conserving matrix element connecting the d -level with the bath states $\hat{c}_{\epsilon\mu}$, taken independent of energy, for simplicity.

Finally, the interacting third term is given in the case of the single-impurity Anderson model (SIAM) by the uniform Coulomb interaction U at the impurity

$$\hat{H}_{\text{int}}^{\text{SIAM}} = \frac{1}{2} U \hat{n}_d (\hat{n}_d - 1), \quad (11)$$

with $\hat{n}_d = \sum_{\mu} \hat{n}_{d\mu}$, while in the case of the interacting resonant-level model (IRLM), the interacting part is given by

$$\hat{H}_{\text{int}}^{\text{IRLM}} = U' \hat{n}_d \hat{n}_0, \quad (12)$$

with $\hat{n}_0 = \sum_{\mu} \hat{f}_{0\mu}^{\dagger} \hat{f}_{0\mu} \equiv \sum_{\mu} \hat{n}_{0,\mu}$. In particular, most of our results are for the one- or two-lead versions of the SIAM for spinful or spinless electrons

$$\hat{H}_X^{\text{SIAM}} = \hat{H}_b + \hat{H}_{d,X} + \hat{H}_{\text{int}}^{\text{SIAM}}. \quad (13)$$

We consider either a single dot level coupled to a single lead (spinful, $N_c = 2 : \mu \in \{\uparrow, \downarrow\}$), or a dot with two levels

coupled separately to two leads (spinless, $N_c = 2 : \mu \in \{1, 2\}$; spinful, $N_c = 4 : \mu \in \{1\uparrow, 1\downarrow, 2\uparrow, 2\downarrow\}$). A splitting of the energies $\epsilon_{d\mu,X}$ in the spin label (if any) will be referred to as magnetic field B . We also present some results for the IRLM, for a single channel of spinless electrons ($N_c = 1$):

$$\hat{H}_X^{\text{IRLM}} = \hat{H}_b + \hat{H}_{d,X} + \hat{H}_{\text{int}}^{\text{IRLM}}. \quad (14)$$

In this paper, we focus on the case that \hat{H}_I and \hat{H}_F differ only in the local level positions ($\epsilon_{d\mu,I} \neq \epsilon_{d\mu,F}$). It is emphasized, however, that our methods are equally applicable for differences between initial and final values of any other parameters, including the case that the interactions are channel specific, e.g., $\sum_{\mu\mu'} U_{\mu\mu'} \hat{n}_{d\mu} \hat{n}_{d\mu'}$ or $\sum_{\mu\mu'} U'_{\mu\mu'} \hat{n}_{d\mu} \hat{n}_{0\mu'}$.

B. AO on Wilson chains

Wilson discretized the spectrum of \hat{H}_b on a logarithmic grid of energies $\pm D \Lambda^{-k}$ (with $\Lambda > 1, k = 0, 1, 2, \dots$), thereby obtaining exponentially high resolution of low-energy excitations. He then mapped the impurity model onto a semi-infinite "Wilson tight-binding chain" of sites $k = 0$ to ∞ , with the impurity degrees of freedom coupled only to site 0. To this end, he made a basis transformation from the set of sea operators $\{\hat{c}_{\epsilon\mu}\}$ to a new set $\{\hat{f}_{k\mu}\}$, chosen such that they bring \hat{H}_b into the tridiagonal form

$$\hat{H}_b \simeq \sum_{\mu=1}^{N_c} \sum_{k=1}^{\infty} t_k (\hat{f}_{k\mu}^{\dagger} \hat{f}_{k-1,\mu} + \text{H.c.}). \quad (15)$$

The hopping matrix elements $t_k \propto D \Lambda^{-k/2}$ decrease exponentially with site index k along the chain. Because of this separation of energy scales for sufficiently large Λ , typically $\Lambda \gtrsim 1.7$, the Hamiltonian can be diagonalized iteratively by solving a Wilson chain of length k [restricting the sum in Eq. (15) to the first k terms] and increasing k one site at a time: Starting with a short Wilson chain, a new *shell* of many-body eigenstates for a Wilson chain of length k , say $|s\rangle_k$, is constructed from the states of site k and the M_k lowest-lying eigenstates of shell $k-1$. The latter are the so-called *kept* states $|s\rangle_{k-1}^k$ of shell $k-1$, while the remaining higher-lying states $|s\rangle_{k-1}^k$ from that shell are *discarded*.

The typical spacing between the few lowest-lying states of shell k , i.e., the energy scale dE_k , is set by the hopping matrix element t_k to the previous site, hence,

$$dE_k \simeq t_k \propto D \Lambda^{-k/2}. \quad (16)$$

Now, for a noninteracting Fermi sea with N particles, the mean single-particle level spacing at the Fermi energy scales as $dE \propto D/N$. This also sets the energy scale for the mean level spacing of the few lowest-lying many-body excitations of the Fermi sea. Equating this to Eq. (16), we conclude that a Wilson chain of length k represents a Fermi sea with an actual size $L \propto N$, i.e., an *effective* number of electrons N , that grows *exponentially* with k ,

$$N \propto \Lambda^{k/2}. \quad (17)$$

Now consider two impurity models that differ only in their local terms $\hat{H}_{d,X}$, and let $|G_X\rangle_k$ be the ground states of their respective Wilson chains of length k , obtained via

two separate NRG runs.⁹ Combining Anderson's prediction (1) and Eq. (17), the ground-state overlap is expected to decay exponentially with k as

$$|{}_k\langle G_I|G_F\rangle_k| \propto \Lambda^{-k\Delta_{\text{AO}}^2/4} \equiv e^{-\alpha k} \quad (18)$$

with

$$\Delta_{\text{AO}}^2 = \frac{4\alpha}{\log \Lambda}. \quad (19)$$

Thus, the AO exponent can be determined by using NRG to directly calculate the left-hand side of Eq. (18) as a function of chain length k , and extracting Δ_{AO} from the exponent α characterizing its exponential decay with k .

For *noninteracting* impurity models ($U = U' = 0$), a finite Wilson chain represents a single-particle Hamiltonian for a finite number of degrees of freedom that can readily be diagonalized numerically, without the need for implementing NRG truncation. The ground state is a Slater determinant of those single-particle eigenstates that are occupied in the Fermi sea. The overlap $\langle G_I|G_F\rangle$ is then given simply by the determinant of a matrix whose elements are overlaps between the I and F versions of the occupied single-particle states. It is easy to confirm numerically in this manner that $\langle G_I|G_F\rangle \sim e^{-\alpha k}$, leading to the expected AO in the limit $k \rightarrow \infty$. We will thus focus on interacting models henceforth, which require the use of NRG.

In the following three sections, we discuss several technical aspects needed for calculating AO with NRG on Wilson chains.

C. Ground-state overlaps

The calculation of state space overlaps within the NRG is straightforward, in principle,^{9,22} especially considering its underlying matrix product state structure.^{23–25} Now, the overlap in Eq. (18), which needs to be calculated in this paper, is with respect to ground states as a function of Wilson chain length k . As such, two complications can arise. (i) For a given k , the system can have several degenerate ground states $\{|s\rangle_k^X : s \in G\}$, with the degeneracy $d_{X,k}$ typically different for even and odd k . (ii) The symmetry of the ground-state space may actually differ with alternating k between certain initial and final configurations $X \in \{I, F\}$, leading to strictly zero overlap there. A natural way to deal with (i) is to essentially average over the degenerate ground-state spaces, while (ii) can be ameliorated by partially extending the ground-state space to the full kept space $\{|s\rangle_k^X : s \in K\}$, as will be outlined in the following.

The $d_{X,k}$ -fold degenerate ground-state subspace is described by its projector, written in terms of the fully mixed density matrix

$$\hat{\rho}_{G,k}^X \equiv \frac{1}{d_{X,k}} \sum_{s \in G} |s\rangle_k^X \langle s|. \quad (20)$$

It is then convenient to calculate the overlap of the ground-state space as

$$\begin{aligned} z_{GK}^2(k) &\equiv \text{tr}_{K,k}^F(\hat{\rho}_{G,k}^I) \\ &= \frac{1}{d_{I,k}} \sum_{s \in G} \sum_{s' \in K} |{}_k\langle s|s'\rangle_k^F|^2, \end{aligned} \quad (21)$$

where $\text{tr}_{K,k}^F(\cdot)$ refers to the trace over the kept space at iteration k of the final system. The final expression can be interpreted, up to the prefactor, as the square of the Frobenius norm of the overlap matrix ${}_k\langle s|s'\rangle_k^F$ between the NRG states $s \in G$ and $s' \in K$ at iteration k for the initial and final Hamiltonians, respectively.

Note that the specific overlap in Eq. (21), as used throughout later in this paper, not only includes the ground space of the final system at iteration k , but rather includes the *full kept space* of that system. Yet, each such overlap scales as $e^{-\alpha k}$, with the same exponent α for all combinations of s and s' , because (i) the states $|s\rangle_k^I$ with $s \in G$ are taken from the initial ground-state space, and (ii) the states $|s'\rangle_k^F$ with $s' \in K$ from the final kept shell differ from a final ground state only by a small number of excitations. Therefore, Eq. (21) is essentially equivalent, up to an irrelevant prefactor, to strictly taking the overlap of ground-state spaces as in $z_{GG}^2(k) \equiv \text{tr}_{G,k}^F(\hat{\rho}_{G,k}^I)$. This will be shown in more detail in the following. In particular, the overlap in Eq. (21) can be easily generalized to

$$z_{P'P}^2(k) \equiv \text{tr}_{P',k}^F(\hat{\rho}_{P,k}^I), \quad 0 \leq z_{P'P}^2(k) \leq 1 \quad (22)$$

where $P^{(i)} \in \{G, K, \infty\}$ represents the ground-state space, the full kept space, or the ground state taken at $k \rightarrow \infty$ with respect to either the initial or final system, respectively. The overlap $z_{P'P}^2(k)$ in Eq. (22) then represents the fully mixed density matrix in space P of the initial system traced over space P' of the final system, all evaluated at iteration k .

A detailed comparison for several different choices of $z_{P'P}^2(k)$, including $z_{GG}^2(k)$, is provided in Fig. 1 for the standard SIAM with $\mu \in \{\uparrow, \downarrow\}$. The topmost line (identified with legend by heavy round dot) shows the overlap Eq. (2) used as default for calculating the overlap in the rest of the paper. This measure is most convenient, as it reliably provides data with a smooth k -dependence for large k , insensitive to alternating k -dependent changes of the symmetry sector and degeneracy of the ground-state sector of $\hat{H}_{X,k}$ (note that the exact ground-state symmetry is somewhat relative within the NRG framework, given an essentially gapless continuum of states of the full system). The overlap z_{GG} (data marked by triangle) gives the overlap of the initial and final *ground-state* spaces, but is sensitive to changes in symmetry sector; in particular, for $k \lesssim 28$, it is nonzero for odd iterations only. The reason as to why it can be vanishingly small for certain iterations is, in the present case, that the initial and final occupancies of the local level differ significantly, as seen from the values for $\langle n_{\text{dot}}^I \rangle$ and $\langle n_{\text{dot}}^F \rangle$ specified in the panel. Therefore, initial and final ground states can be essentially orthogonal, in the worst case throughout the entire NRG run. Nonetheless, the AO exponent is expected to be well defined and finite, as reflected in z_{GK} .

The AO measure z_{KK} (data marked by star) is smooth throughout, and although it is not strictly constrained to the ground-state space at a given iteration, in either the initial or final system, it gives the correct AO exponent, the reason being the underlying energy scale separation of the NRG. Finally, $z_{\infty,K} = \text{Tr}_{F,k}^K(\hat{\rho}_{I,\infty}^G)$ (data marked by squares) refers to an AO measure that calculates the overlap of the ground-state space of an essentially infinite initial system (i.e., $k \rightarrow \infty$, or in practice, the last site of the Wilson chain), with the kept space

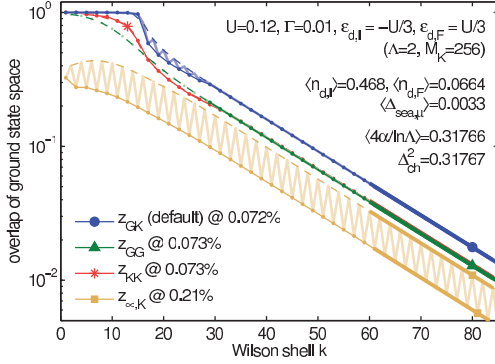


FIG. 1. (Color online) Anderson orthogonality for the spin-degenerate standard SIAM for a single lead [Eq. (10), $\mu \in \{\uparrow, \downarrow\}$], with μ -independent parameters ε_d and Γ for \hat{H}_I and \hat{H}_F as specified in the panel (the full ε_d^F dependence of Δ_{AO} for fixed ε_d^I is analyzed in more detail in Fig. 5). Several alternative measures for calculating the AO overlap are shown, using $z_{PP}(k)$ in Eq. (22) with $P^{(l)} \in \{G, K, \infty\}$, as defined in the text. All overlaps are plotted for even and odd iterations separately to account for possible even-odd behavior within the Wilson chain (thin solid lines with dots, and dashed lines, respectively), while heavy symbols identify lines with corresponding legends). If even and odd data from the same $z_{PP}(k)$ do not lie on the same smooth line, the combined data are also plotted (light zigzag lines) as guides to the eye. For large k , all AO overlaps exhibit exponential decay of equal strength. Separate fits of $e^{\lambda-ak}$ to even and odd sectors are shown as thick solid lines, the lengths of which indicate the fitting range used. The values for Δ_{AO}^2 extracted from these fits using Eq. (19) are in excellent agreement with the displaced charge Δ_{ch}^2 , as expected from Eq. (8). The relative error is less than 1% throughout, with the detailed values specified in the legend, and $(4\alpha/\ln\Lambda)$ representing the averaged value with regard to the four measures considered.

at iteration k of the final system. Since the latter experiences k -dependent even-odd differences, whereas the initial density matrix $\hat{\rho}_{L,\infty}^G$ is independent of k , $z_{\infty,K}$ exhibits rather strong k -dependent oscillations. Nevertheless, their envelopes for even and odd iterations separately decay with the same exponent α as the other AO measures.

In summary, Fig. 1 demonstrates that all AO measures decay asymptotically as $e^{\lambda-ak}$, as expected from Eq. (18), with the *same* exponent α , independent of the details of the construction. These details only affect the constant prefactor λ , which is irrelevant for the determination of Δ_{AO} .

D. Channel-specific exponents from chains of different lengths

Equation (6) expresses the exponent Δ_{AO} of the full system in terms of the AO exponents $\Delta_{AO,\mu}$ of the individual channels. This equation is based on the assumption (the validity of which, for the models studied here, is borne out by the results presented below) that for distances sufficiently far from the dot, the asymptotic tail of the ground-state wave function factorizes, in effect, into independent products, one for each channel μ . This can be exploited to calculate, in a straightforward fashion, the individual exponent $\Delta_{AO,\mu}$ for a

given channel μ : one simply constructs a modified Wilson chain, which, in effect, is much longer for channel μ than for all others. The overlap decay for large k is then dominated by that channel.

To be explicit, the strategy is as follows. First we need to determine when a Wilson chain is “sufficiently long” to capture the aforementioned factorization of ground-state tails. This will be the case beyond that chain length, say k_0 , for which the NRG energy flow diagrams for the kept space excitation spectra of the original Hamiltonians \hat{H}_I and \hat{H}_F are well converged to their $T = 0$ fixed point values. To calculate $\Delta_{AO,\mu}$, the AO exponent of channel μ , we then add an artificial term to the Hamiltonian that in effect depletes the Wilson chain beyond site k_0 for all other channels $\nu \neq \mu$ by drastically raising the energy cost for occupying these sites. This term has the form

$$H_{\text{art}}^{\mu} = C \sum_{\nu \neq \mu} \sum_{k > k_0} t_k \hat{f}_{k\nu}^{\dagger} \hat{f}_{k\nu}, \quad (23)$$

with $C \gg 1$. It ensures that occupied sites in the channels $\nu \neq \mu$ have much larger energy than the original energy scale t_k , so that they do not contribute to the low-energy states of the Hamiltonian. We then calculate a suitable AO measure (such as z_{GK}) using only k values in the range $k > k_0$. From the exponential decay found in this range, say $\sim e^{-\alpha_{\mu}k}$, the channel-specific AO exponent can be extracted [cf. Eq. (19)]:

$$\Delta_{AO,\mu}^2 = \frac{4\alpha_{\mu}}{\log \Lambda}. \quad (24)$$

This procedure works remarkably well, as illustrated in Fig. 2, for the spin-asymmetric single-lead SIAM of Eq. (13) (with $N_c = 2$, $\mu \in \{\uparrow, \downarrow\}$). Indeed, the values for $\Delta_{AO,\mu}$ and Δ_{AO} displayed in Fig. 2 fulfill the addition rule for squared exponents [Eq. (6)] with a relative error of less than 1%.

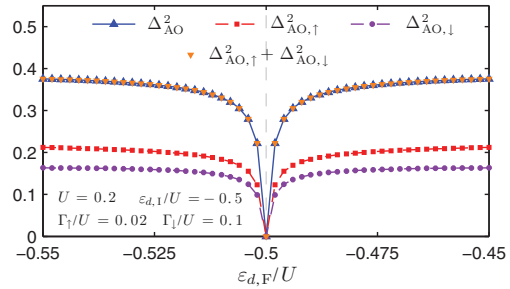


FIG. 2. (Color online) AO exponents for the standard spin-degenerate SIAM with spin-asymmetric hybridization [Eq. (13), with $\mu \in \{\uparrow, \downarrow\}$] as functions of $\varepsilon_{d,F}$ (all other parameters are fixed as specified in the panel). The vertical dashed line indicates $\varepsilon_{d,\uparrow}/U = -0.5$; at this line, the initial and final Hamiltonians are identical, hence all exponents vanish. The squared AO exponents for the individual channels $\Delta_{AO,\uparrow}^2$ (squares) and $\Delta_{AO,\downarrow}^2$ (dots) were calculated from Eq. (24). Their sum agrees (with a relative error of less than 1%) with Δ_{AO}^2 calculated from Eq. (19) (downward- and upward-pointing triangles coincide), confirming the validity of the addition rule for squared exponents in Eq. (6).

E. Displaced charge

The displaced charge $\Delta_{\text{ch},\mu}$ defined in Eq. (7) can be calculated directly within NRG. However, to properly account for the contribution from the Fermi sea $\Delta_{\text{sea},\mu}$, a technical difficulty has to be overcome: the Hamiltonians considered usually obey particle conservation and thus every eigenstate of \hat{H} is an eigenstate of the total number operator, with an integer eigenvalue. Consequently, evaluating Eq. (4) over the *full* Wilson chain *always* yields an integer value for the total $\Delta_{\text{ch},\mu}$. This integer, however, does not correspond to the charge within the large but finite volume V_{large} that is evoked in the definition of the displaced charge.

To obtain the latter, we must consider subchains of shorter length. Let

$$\hat{n}_{\text{sea},\mu}^{(k)} = \sum_{k'=0}^k \hat{f}_{k'\mu}^\dagger \hat{f}_{k'\mu} \quad (25)$$

count the charge from channel μ sitting on sites 0 to k . These sites represent, loosely speaking, a volume $V_{\text{large}}^{(k)}$ centered on the dot, the size of which grows exponentially with increasing k . The contribution from channel μ of the Fermi sea to the displaced charge within $V_{\text{large}}^{(k)}$ is

$$\Delta_{\text{sea},\mu}^{(k)} \equiv \langle G_F | \hat{n}_{\text{sea},\mu}^{(k)} | G_F \rangle - \langle G_I | \hat{n}_{\text{sea},\mu}^{(k)} | G_I \rangle, \quad (26)$$

where $|G_I\rangle$ and $|G_F\rangle$ are the initial and final ground states of the *full-length* Wilson chain of length N ($\geq k$).

Figure 3 shows $\Delta_{\text{sea}}^{(k)}$ for the spinless IRLM of Eq. (14), where we dropped the index μ , since $N_c = 1$. $\Delta_{\text{sea}}^{(k)}$ exhibits even-odd oscillations between two values, say $\Delta_{\text{sea}}^{\text{even}}$ and $\Delta_{\text{sea}}^{\text{odd}}$, but these quickly assume essentially constant values over a large intermediate range of k values. Near the very end of the chain, they change again rather rapidly, in such a way that the total displaced charge associated with the full Wilson chain of length N , $\Delta_{\text{ch}}^{(N)} = \Delta_{\text{sea}}^{(N)} + \Delta_{\text{dot}}$, is an integer (see Fig. 3) because the overall ground state has well-defined particle number. Averaging the even-odd oscillations in the intermediate regime yields the desired contribution of the Fermi sea to the displaced charge $\Delta_{\text{sea}} = \frac{1}{2}(\Delta_{\text{sea}}^{\text{even}} + \Delta_{\text{sea}}^{\text{odd}})$. The corresponding result for $\Delta_{\text{ch}} = \Delta_{\text{sea}} + \Delta_{\text{dot}}$ is illustrated by the black dashed line in Fig. 3.

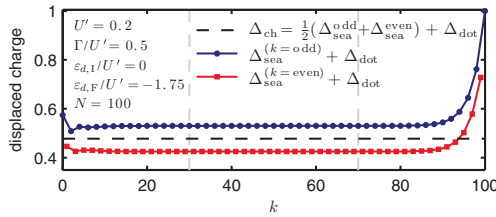


FIG. 3. (Color online) Determination of Δ_{ch} , for the interacting resonant-level model of Eq. (14), for a single specific set of parameters for \hat{H}_I and \hat{H}_F , specified in the figure legend (the $\varepsilon_{d,F}$ dependence of Δ_{AO} for fixed $\varepsilon_{d,I}$ is analyzed in more detail in Fig. 4). We obtain Δ_{ch} (dashed line) by calculating $\Delta_{\text{sea}}^{(k)} + \Delta_{\text{dot}}$ and averaging the results for even and odd k . To reduce the influence of chain's boundary regions, we take the average over the region between the vertical dashed lines.

IV. RESULTS

In this section, we present results for the single-channel interacting resonant-level model [Eq. (14)], and for single-lead and two-lead Anderson impurity models [Eq. (13)]. These examples were chosen to illustrate that the various ways of calculating AO exponents by NRG, via Δ_{AO} , Δ_{ph} , or Δ_{ch} , are mutually consistent with high accuracy, even for rather complex (multilevel, multilead) models with local interactions. In all cases, the initial and final Hamiltonians \hat{H}_I and \hat{H}_F differ only in the level position: $\varepsilon_{d,I}$ is kept fixed, while $\varepsilon_{d,F}$ is swept over a range of values. This implies different initial and final dot occupations $n_{d,\mu,X} = \langle G_X | \hat{n}_{d,\mu} | G_X \rangle$, and hence different local scattering potentials, causing AO.

AO exponents are obtained as described in the previous sections: We calculate the AO measure $z_{GK}(k)$ using Eq. (2), obtaining exponentially decaying behavior (as in Fig. 1). We then extract α by fitting to $e^{-\alpha k}$ and determine Δ_{AO} via Eq. (19). In the figures below, the resulting Δ_{AO}^2 is shown as function of $\varepsilon_{d,\mu,F}$, together with Δ_{ch}^2 , and also Δ_{ph}^2 in Fig. 4. The initial dot level position $\varepsilon_{d,I}$ is indicated by a vertical dashed line. When $\varepsilon_{d,\mu,F}$ crosses this line, the initial and final Hamiltonians are identical, so that all AO exponents vanish. To illustrate how the changes in $\varepsilon_{d,\mu,F}$ affect the dot, we also plot the occupancies $n_{d,\mu,F}$ of the dot levels.

A. Interacting resonant-level model

We begin with a model for which the contribution of the Fermi sea to the displaced charge is rather important, namely, the spinless fermionic interacting resonant-level model [Eq. (14), $N_c = 1$]. The initial and final Hamiltonians \hat{H}_I^{IRLM} and \hat{H}_F^{IRLM} differ only in the level position: the initial one is kept fixed at $\varepsilon_{d,I} = 0$, while the final one is swept over a range of values, $\varepsilon_{d,F} \in [-1, 1]$. The results

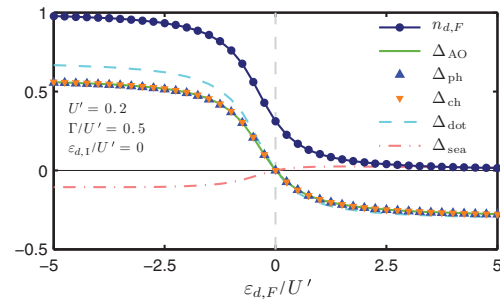


FIG. 4. (Color online) Verification that $\Delta_{\text{AO}} = \Delta_{\text{ph}} = \Delta_{\text{ch}}$ [Eq. (5)] for the spinless fermionic interacting resonant-level model [Eq. (14)]. All quantities are plotted as functions of $\varepsilon_{d,F}$, with all other parameters fixed (as specified in the panel). The vertical dashed line indicates $\varepsilon_{d,I}/U' = 0$. Heavy dots indicate the final occupation of the dot n_d . The exponent Δ_{AO} (light solid line) agrees well with Δ_{ph} and Δ_{ch} (triangles), with relative errors of less than 1%. The local and Fermi-sea contributions to the displaced charge Δ_{ch} are plotted separately, namely, Δ_{dot} (dashed line) and Δ_{sea} (dashed-dotted line). The latter is determined according to the procedure illustrated, for $\varepsilon_{d,F}/U' = -1.75$, in Fig. 3.

ANDERSON ORTHOGONALITY AND THE NUMERICAL ...

PHYSICAL REVIEW B **84**, 075137 (2011)

are shown in Fig. 4. The final dot occupancy $n_{d,F}$ (heavy dots) varies from $\simeq 1$ to 0, and $\Delta_{\text{dot}} = n_{d,F} - n_{d,I}$ (dashed line) decreases accordingly, too. The total displaced charge $\Delta_{\text{ch}} = \Delta_{\text{dot}} + \Delta_{\text{sea}}$ (downward-pointing triangles) decreases by a smaller amount since the depletion of the dot implies a reduction in the strength of the local Coulomb repulsion felt by the Fermi sea, and hence an increase in Δ_{sea} (dashed-dotted line). Throughout these changes, Δ_{AO} , Δ_{ph} , and Δ_{ch} mutually agree with errors of less than 1%, confirming that NRG results comply with Eq. (5) to high accuracy.

B. Single-impurity Anderson model

Next we consider the standard spin-degenerate SIAM for a single lead [Eq. (13), $\mu \in \{\uparrow, \downarrow\}$] with $\varepsilon_{d,\mu} = \varepsilon_d$ and $\Gamma_\mu = \Gamma$. This model exhibits well-known Kondo physics, with a strongly correlated many-body ground state.

In this model, the dot and Fermi sea affect each other only by hopping, and there is no direct Coulomb interaction between them ($U' = 0$). Hence, the contribution of the Fermi sea to the displaced charge is nearly zero, $\Delta_{\text{sea}} \simeq 0$. Apart from very small even-odd variations for the first ~ 35 bath sites corresponding to the Kondo scale, the sites of the Wilson chain are half-filled on average to a good approximation. Therefore, $\Delta_{\text{sea}} \ll \Delta_{\text{dot}}$ (explicit numbers are specified in the figure panels; see also Fig. 1), so that $\Delta_{\text{ch},\mu}$ in Eq. (7) is dominated by the change of dot occupation only,²¹

$$\Delta_{\text{ch}}^2 \simeq \Delta_{\text{dot}}^2 \equiv \sum_{\mu} (n_{d_{\mu,F}} - n_{d_{\mu,I}})^2. \quad (27)$$

As a consequence, despite the neglect of Δ_{sea} in some previous works involving Anderson impurity models, the Friedel sum rule ($\Delta_{\text{ph}} = \Delta_{\text{ch}}$) was nevertheless satisfied with rather good accuracy (typically with errors of a few percent). However, despite being small, Δ_{sea} in practice is on the order of $|\Delta_{\text{sea}}| \lesssim \Gamma/D$ and thus *finite*. Therefore, the contribution of Δ_{sea} to Δ_{ch} will be included throughout, while also indicating the overall smallness of Δ_{sea} . In general, this clearly improves the accuracy of the consistency checks in Eq. (5), reducing the relative errors to well below 1%.

The Anderson orthogonality is analyzed for the SIAM in detail in Fig. 5. The initial system is kept fixed at the particle-hole symmetric point $\varepsilon_{d,I} = -U/2$ [indicated also by vertical dashed line in Fig. 5(a)], where the initial ground state is a Kondo singlet. The final system is swept from double to zero occupancy by varying $\varepsilon_{d,F}/U$ from -2 to 1. The final ground state is a Kondo singlet in the regime $n_{d_{\mu,F}} \simeq 1/2$, corresponding to the intermediate shoulder in Fig. 5(a). Figure 5(b) shows the AO measure $z_{GK}(k)$ as function of k , for a range of different values of $\varepsilon_{d,F}$. Each curve exhibits clear exponential decay for large k (as in Fig. 1) of the form $e^{\lambda - \alpha k}$. The prefactor, parametrized by λ , carries little physical significance, as it also depends on the specific choice of z_{PP} ; its dependence on $\varepsilon_{d,F}$ is shown as a thick gray dashed line in Fig. 5(a), but it will not be discussed any further. In contrast, the decay exponent α directly yields the quantity of physical interest, namely, the AO exponent Δ_{AO}^2 via Eq. (19). Figure 5(a) compares the dependence on $\varepsilon_{d,F}$ of Δ_{AO}^2 (dashed line) with that of the displaced charge Δ_{ch}^2 (light thick line), that was calculated independently from Eqs. (7)

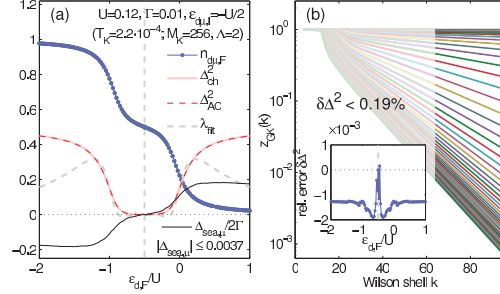


FIG. 5. (Color online) Anderson orthogonality for the single-lead, spin-symmetric SIAM [Eq. (13), with parameters as specified in the legend]. The energy of the d -level of the final system $\varepsilon_{d,F}$ is swept past the Fermi energy of the bath, while that of the initial reference system is kept fixed in the Kondo regime at $\varepsilon_{d,I} = -U/2$, indicated by vertical dashed line in panel (a) and in the inset to panel (b). Panel (a) shows, as function of $\varepsilon_{d,F}$, the dot occupation per spin $n_{d\mu}$ (dotted solid line), the contribution to the displaced charge by the Fermi sea $\Delta_{\text{sea}\mu}$ (thin black line), the displaced charge Δ_{ch}^2 (light solid line), and the parameters of the large- k exponential decay $e^{\lambda - \alpha k}$ of $z_{GK}(k)$ as extracted from panel (b), namely, λ (thick dashed line) and Δ_{AO} (dark dashed line), derived from α via Eq. (19). Panel (b) shows the AO measure $z_{GK}(k)$ in Eq. (2) (light lines) for the range of $\varepsilon_{d,F}$ values used in panel (a). The heavy lines shown on top for $k \geq 64$ are exponential fits, the results of which are summarized in panel (a). The inset shows the relative error in the AO exponents $\delta\Delta^2 \equiv (\Delta_{\text{AO}}^2 - \Delta_{\text{ch}}^2)/\Delta_{\text{ch}}^2$, i.e., the deviation between the light solid and dark dashed curves in panel (a); this error is clearly less than 1% over the full range of ε_d analyzed.

and (8). As expected from Eq. (5), they agree very well: the relative difference between the two exponents Δ_{AO}^2 and Δ_{ch}^2 is clearly below 1% throughout the entire parameter sweep, as shown in the inset of Fig. 5(b).

The contribution of the Fermi sea to the displaced charge is close to negligible, yet finite throughout [black line in Fig. 5(a)]. Overall, $\Delta_{\text{sea}} \lesssim 0.0037$, as indicated in Eq. (27). Nevertheless, by including it when calculating Δ_{ch} , the relative error $\delta\Delta^2$ is systematically reduced from a few percent to well below 1% throughout, thus underlining its importance.

C. Multiple channels and population switching

Figure 6 analyzes AO for lead-asymmetric two-level, two-lead SIAM models, with Hamiltonians of the form Eq. (13) (explicit model parameters are specified in the panels). Figure 6(a) considers a spinless case ($N_c = 2$, $\mu = j \in \{1, 2\}$), the dot levels of which have mean energy ε_d at fixed splitting δ ,

$$\varepsilon_{d1} = \varepsilon_d - \delta/2, \quad \varepsilon_{d2} = \varepsilon_d + \delta/2. \quad (28a)$$

Figure 6(b) considers a spinful case [$N_c = 4$, $\mu = (j\sigma)$ with $j \in \{1, 2\}$, $\sigma \in \{\uparrow, \downarrow\}$], where both the lower and upper levels have an additional (small) spin splitting $B \ll \delta$,

$$\varepsilon_{dj\uparrow} = \varepsilon_{dj} + B/2, \quad \varepsilon_{dj\downarrow} = \varepsilon_{dj} - B/2. \quad (28b)$$

Charge is conserved in each of the N_c channels since these only interact through the interaction on the dot. In both models,

WEICHELBAUM, MÜNDER, AND VON DELFT

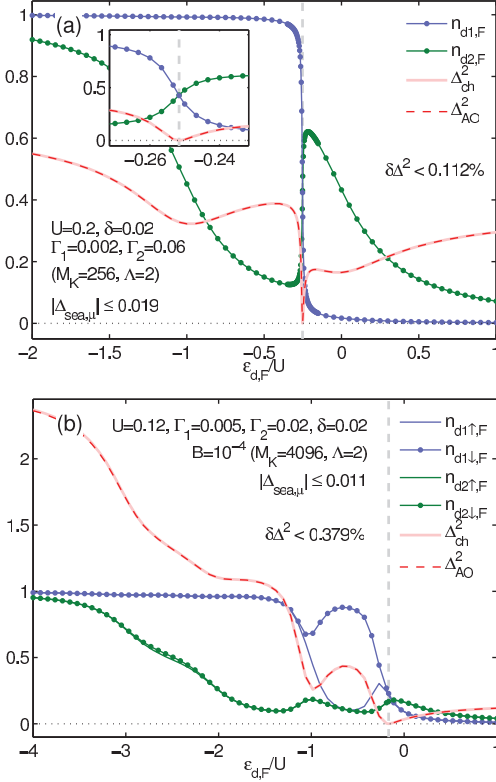
 PHYSICAL REVIEW B **84**, 075137 (2011)


FIG. 6. (Color online) Anderson orthogonality for a spinless (a) and spinful (b) two-lead SIAM, with dot levels of unequal width and a split level structure as defined in Eq. (28) (all relevant model parameters are specified in the legends). In both cases, the higher level 2 is broader than the lower level 1 ($\Gamma_2 > \Gamma_1$), leading to population switching as function of the average final level energy $\varepsilon_{d,F}$. The fixed value of $\varepsilon_{d,F}$ is indicated by the vertical dashed line. The inset to panel (a) shows a zoom into the switching region, clearly demonstrating that population switching occurs smoothly. For panel (b), a finite magnetic field B causes a splitting between spin-up and spin-down levels, resulting in a more complex switching pattern. In both panels, Δ_{AO}^2 and Δ_{ch}^2 agree very well throughout the sweep, with a relative error $\delta\Delta^2$ well below 1%.

the upper level 2 is taken to be broader than the lower level 1, $\Gamma_2 > \Gamma_1$ (for detailed parameters, see figure legends). As a consequence,^{15–19} these models exhibit population switching: When $\varepsilon_{d,F}$ is lowered (while all other parameters are kept fixed), the final state occupancies of upper and lower levels cross, as seen in both panels of Fig. 6.

Consider first the spinless case in Figure 6(a). The broader level 2 shows larger occupancy for large positive $\varepsilon_{d,F}$. However, once the narrower level 1 drops sufficiently far below the Fermi energy of the bath as $\varepsilon_{d,F}$ is lowered, it becomes energetically favorable to fill level 1, while the

Coulomb interaction will cause the level 2 to be emptied. At the switching point, occupations can change extremely fast, yet they do so smoothly, as shown in the zoom in the inset of Fig. 6(a).

Similar behavior is seen for the spinful case in Fig. 6(b), although the filling pattern is more complex, due to the nonzero applied finite magnetic field B (parameters are listed in the legend). The occupations $n_{d\sigma}$ of the narrower level 1 show a strong spin asymmetry since the magnetic field is comparable, in order of magnitude, to the level width ($B = \Gamma_1/2$). This asymmetry affects the broader level 2, which fills more slowly as ε_d is lowered. Due to the larger width of level 2, the asymmetry in its spin-dependent occupancies is significantly weaker. As in Fig. 6(a), population switching between the two levels occurs: as the narrower level 1 becomes filled, the broader level 2 gets depleted.

The details of population switching, complicated as they are [extremely rapid in Fig. 6(a) and involving four channels in Fig. 6(b)] are not the main point of Fig. 6. Instead, its central message is that despite the complexity of the switching pattern, the relation $\Delta_{AO}^2 = \Delta_{ch}^2$ is satisfied with great accuracy throughout the sweep (compare light thick and dark dashed lines). Moreover, since Δ_{ch} was calculated by adding the contributions from separate channels according to Eq. (8), this also confirms the additive character of AO exponents for separate channels.

As was the case for the single-channel SIAM discussed in Sec. IV B above, a direct interaction between dot and Fermi sea is not present in either of the models considered here ($U' = 0$). Consequently, the displaced charge Δ_{ch} is again dominated by Δ_{dot} , with $\Delta_{sea} \ll \Delta_{dot}$ [cf. Eq. (27)]. Specifically, for the spinless or spinful models, we find $\Delta_{sea} < 0.019$ or 0.011, respectively, for the entire sweep.

V. SUMMARY AND OUTLOOK

In summary, we have shown that NRG offers a straightforward, systematic, and self-contained way for studying Anderson orthogonality, and illustrated this for several interacting quantum impurity models. The central idea of our work is to exploit the fact that NRG allows the size dependence of an impurity model to be studied, in the thermodynamic limit of $N \rightarrow \infty$, by simply studying the dependence on Wilson chain length k . Three different ways of calculating AO exponents have been explored, using wave-function overlaps (Δ_{AO}), changes in phase shift at the Fermi surface (Δ_{ph}), and changes in displaced charge (Δ_{ch}). The main novelty in this paper lies in the first of these, involving a direct calculation of the overlap of the initial and final ground states themselves. This offers a straightforward and convenient way for extracting the overall exponent Δ_{AO} . Moreover, if desired, it can also be used to calculate the exponents $\Delta_{AO,\mu}$ associated with individual channels, by constructing a Wilson chain that is longer for channel μ than for the others. We have also refined the calculation of Δ_{ch} by showing how the contribution Δ_{sea} of the Fermi sea to the displaced charge can be taken into account in a systematic fashion.

The resulting exponents Δ_{AO} , Δ_{ph} , and Δ_{ch} agree extraordinarily well, with relative errors of less than 1% for a wide range of Λ . In particular, we have checked in the context of Fig. 1

that the resulting relative errors remain this small for a range of Λ values between 1.7 and 8.0. Moreover, this accuracy can be achieved using a remarkably small number of kept states M_K . For example, for the spinful SIAM analyzed above, for $\Lambda = 2$, a better than 5% agreement can be obtained already for $M_K \geq 32$. (For comparison, typically $M_K = 250$ is required to obtain an accurate description of the Kondo resonance of the d -level spectral function in the local moment regime of this model.)

Our analysis has been performed on models exhibiting Fermi liquid statistics at low temperatures. As an outlook, it would be interesting to explore to what extent the non-Fermi liquid nature of a model would change AO scaling properties, an example being the symmetric spinful two-channel Kondo model.

Finally, we note that nonequilibrium simulations of quantum impurity models in the time domain in response to quantum quenches are a highly interesting topic for studying AO physics in the time domain. The tools to do so using NRG have become accessible only rather recently.^{10,22,23,26} One considers a sudden change in some local term in

the Hamiltonian and studies the subsequent time evolution, characterized, for example, by the quantity $\langle G_1 | e^{-i\hat{H}t} | G_1 \rangle$. Its numerical evaluation requires the calculation of overlaps of eigenstates of \hat{H}_I and \hat{H}_F . The quantity of present interest $|\langle G_1 | G_F \rangle|$ is simply a particular example of such an overlap. As a consequence, the long-time decay of $\langle G_1 | e^{-i\hat{H}t} | G_1 \rangle$ is often governed by Δ_{AO} , too,^{3,5} showing power-law decay in time with an exponent depending on Δ_{AO} . This will be elaborated in a separate publication.¹²

ACKNOWLEDGMENTS

We thank G. Zaránd for an inspiring discussion that provided the seed for this work several years ago, and Y. Gefen for encouragement to pursue a systematic study of Anderson orthogonality. This work received support from the DFG (SFB 631, De-730/3-2, De-730/4-2, WE4819/1-1, SFB-TR12), and in part from the NSF under Grant No. PHY05-51164. Financial support by the Excellence Cluster "Nanosystems Initiative Munich (NIM)" is gratefully acknowledged.

-
- ¹P. W. Anderson, *Phys. Rev. Lett.* **18**, 1049 (1967).
²K. D. Mahan, *Phys. Rev.* **153**, 882 (1967).
³K. D. Schotte and U. Schotte, *Phys. Rev.* **182**, 479 (1969).
⁴K. D. Schotte and U. Schotte, *Phys. Rev.* **185**, 509 (1969).
⁵P. Nozières, J. Gavoret, and B. Roulet, *Phys. Rev.* **178**, 1084 (1969).
⁶G. Yuval and P. W. Anderson, *Phys. Rev. B* **1**, 1522 (1970).
⁷J. Kondo, *Prog. Theor. Phys.* **32**, 37 (1964).
⁸D. Goldhaber-Gordon, J. Göres, M. A. Kastner, H. Shtrikman, D. Mahalu, and U. Meirav, *Phys. Rev. Lett.* **81**, 5225 (1998).
⁹R. W. Helmes, M. Sindel, L. Borda, and J. von Delft, *Phys. Rev. B* **72**, 125301 (2005).
¹⁰H. E. Türeci, M. Hanl, M. Claassen, A. Weichselbaum, T. Hecht, B. Braunecker, A. Govorov, L. Glazman, A. Imamoglu, and J. von Delft, *Phys. Rev. Lett.* **106**, 107402 (2011).
¹¹C. Latta, F. Haupt, M. Hanl, A. Weichselbaum, M. Claassen, W. Wuester, P. Fallahi, S. Faelt, L. Glazman, J. von Delft, H. E. Türeci, and A. Imamoglu, e-print [arXiv:1102.3982v1](https://arxiv.org/abs/1102.3982v1).
¹²W. Mündler, A. Weichselbaum, M. Goldstein, Y. Gefen, and J. von Delft (unpublished).
¹³K. G. Wilson, *Rev. Mod. Phys.* **47**, 773 (1975).
¹⁴R. Bulla, T. A. Costi, and T. Pruschke, *Rev. Mod. Phys.* **80**, 395 (2008).
¹⁵G. Hackenbroich, W. D. Heiss, and H. A. Weidenmüller, *Phys. Rev. Lett.* **79**, 127 (1997); R. Baltin, Y. Gefen, G. Hackenbroich, and H. A. Weidenmüller, *Eur. Phys. J. B* **10**, 119 (1999).
¹⁶P. G. Silvestrov and Y. Imry, *Phys. Rev. Lett.* **85**, 2565 (2000).
¹⁷D. I. Golosov and Y. Gefen, *Phys. Rev. B* **74**, 205316 (2006).
¹⁸C. Karrasch, T. Hecht, A. Weichselbaum, Y. Oreg, J. von Delft, and V. Meden, *Phys. Rev. Lett.* **98**, 186802 (2007).
¹⁹M. Goldstein, R. Berkovits, and Y. Gefen, *Phys. Rev. Lett.* **104**, 226805 (2010).
²⁰J. Friedel, *Can. J. Phys.* **34**, 1190 (1956).
²¹D. C. Langreth, *Phys. Rev.* **150**, 516 (1966).
²²F. B. Anders and A. Schiller, *Phys. Rev. B* **74**, 245113 (2006).
²³A. Weichselbaum and J. von Delft, *Phys. Rev. Lett.* **99**, 076402 (2007).
²⁴A. Weichselbaum, F. Verstraete, U. Schollwöck, J. I. Cirac, and J. von Delft, *Phys. Rev. B* **80**, 165117 (2009).
²⁵U. Schollwöck, *Ann. Phys. (NY)* **326**, 96 (2011).
²⁶F. B. Anders and A. Schiller, *Phys. Rev. Lett.* **95**, 196801 (2005).

6.2 Anderson Orthogonality in the Dynamics After a Local Quantum Quench

Anderson Orthogonality in the Dynamics After a Local Quantum Quench

Wolfgang Munder,¹ Andreas Weichselbaum,¹ Moshe Goldstein,² Yuval Gefen,³ and Jan von Delft¹

¹ *Physics Department, Arnold Sommerfeld Center for Theoretical Physics, and Center for NanoScience, Ludwig-Maximilians-Universitat, Theresienstrasse 37, 80333 Munich, Germany*

² *Department of Physics, Yale University, 217 Prospect Street, New Haven, Connecticut 06520, USA*

³ *Department of Condensed Matter Physics, The Weizmann Institute of Science, Rehovot 76100, Israel*
(Dated: August 29, 2011)

We present a systematic study of the role of Anderson orthogonality for the dynamics after a quantum quench in quantum impurity models, using the numerical renormalization group. As shown by Anderson in 1967, the scattering phase shifts of the single-particle wave functions constituting the Fermi sea have to adjust in response to the sudden change in the local parameters of the Hamiltonian, causing the initial and final ground states to be orthogonal. This so-called Anderson orthogonality catastrophe also influences dynamical properties, such as spectral functions. Their low-frequency behaviour shows nontrivial power laws, with exponents that can be understood using a generalization of simple arguments introduced by Hopfield and others for the X-ray edge singularity problem. The goal of this work is to formulate these generalized rules, as well as to numerically illustrate them for quantum quenches in impurity models involving local interactions. As a simple yet instructive example, we use the interacting resonant level model as testing ground for our generalized Hopfield rule. We then analyse a model exhibiting population switching between two dot levels as a function of gate voltage, probed by a local Coulomb interaction with an additional lead serving as charge sensor. We confirm a recent prediction that charge sensing can induce a quantum phase transition for this system, causing the population switch to become abrupt. We elucidate the role of Anderson orthogonality for this effect by explicitly calculating the relevant orthogonality exponents.

PACS numbers: 02.70.-c, 05.10.Cc, 71.27.+a, 72.10.Fk, 73.21.La, 75.20.Hr, 78.20.Bh

I. INTRODUCTION

The Anderson orthogonality (AO) catastrophe¹ refers to the response of a Fermi sea to a change in a local scattering potential, described, say, by a change in Hamiltonian from \hat{H}_i to \hat{H}_f . Such a change induces changes in the scattering phase shifts of all single-particle wave functions. This causes the initial ground state $|G_i\rangle$ of \hat{H}_i and the final ground state $|G_f\rangle$ of \hat{H}_f , both describing a filled Fermi sea but w.r.t. different single-particle wave functions, to be orthogonal in the thermodynamic limit, even if the changes in the single-particle wave functions are minute. The overlap of the respective ground states scales as^{1,2}

$$|\langle G_i | G_f \rangle| \sim N^{-\frac{1}{2} \Delta_{AO}^2}, \quad (1)$$

where N is the number of particles in the system, and the exponent Δ_{AO} characterizes the degree of orthogonality.

AO underlies the physics of numerous dynamical phenomena such as the Fermi edge singularity,²⁻⁵ the Altshuler-Aronov zero bias anomaly⁶ in disordered conductors, tunnelling into strongly interacting Luttinger liquids,⁷⁻¹¹ and optical absorption involving a Kondo exciton,¹²⁻¹⁴ where photon absorption induces a local quantum quench, to name but a few. Recently, AO has also been evoked^{15,16} in an analysis of *population switching* (PS) in quantum dots (the fact that the population of individual levels of a quantum dot may vary non-monotonically with the gate voltage), and was argued to lead, under certain conditions involving a local Coulomb interaction with a nearby charge sensor, to a

quantum phase transition.

One of the goals of the present work is to analyse the latter prediction in quantitative detail. Another is to generalize arguments that were given in Refs. 12-14, for the role of AO for spectral functions of the excitonic Anderson model, to related models with a similar structure. Thus, we present a systematic study of the role of Anderson orthogonality for the dynamics after a quantum quench in quantum impurity models involving local interactions, using the numerical renormalization group (NRG).^{17,18} We thereby extend a recent study,¹⁹ which showed how Δ_{AO} can be calculated very accurately (with errors below 1%) by using NRG to directly evaluate overlaps such as $\langle G_i | G_f \rangle$, to the domain of dynamical quantities.

The spectral functions that characterize a local quantum quench typically show power-law behaviour, $\sim \omega^{-1+2\eta}$, in the limit of small frequencies, where η typically depends on Δ_{AO} .²⁻⁵ For the case of the X-ray edge singularity, Hopfield⁴ gave a simple argument to explain the relation between Δ_{AO} and η . We frame Hopfield's argument in a more general setting and numerically illustrate the validity of the resulting generalized Hopfield rule (Eq. (25) below) for several nontrivial models. In particular, we also analyse how this power-law behaviour is modified at low frequencies when one adds to the Hamiltonian an extra tunnelling term, that describes transitions between the Hilbert spaces characterizing the "initial" and "final" configurations. This effect plays a crucial role in understanding the abovementioned quantum phase transition for population switching.

The paper is organized as follows. In Sec. II we review

various consequences of AO in different but related settings, and formulate the abovementioned generalization of Hopfield's rule. In Sec. III we illustrate this rule for the spinless interacting resonant level model (IRLM), involving a single localized level interacting with the Fermi sea of a single lead. We consider this model without and with tunnelling, and study a quantum quench of the energy of its local level, focussing on signatures of AO in each case. Finally, in Sec. IV and Sec. V we discuss population switching without and with a charge sensor, respectively, confirming that if the sensor is sufficiently strongly coupled, AO indeed does cause population switching to become a sharp quantum phase transition. Section VI offers concluding remarks and outlines prospective applications of the present analysis.

II. VARIOUS CONSEQUENCES OF ANDERSON ORTHOGONALITY

In this section we review various consequences of AO, in different but related settings. We begin by recalling two well-known facts: first, the relation between the exponent Δ_{AO} and the charge that is displaced due to the quantum quench, Δ_{ch} ; and second, the role of Δ_{AO} in determining the asymptotic long-time power-law decay of correlation functions $\mathcal{G}_X(t)$ involving an operator \hat{X}^\dagger that connects the initial and final ground state.

Then we consider the spectral function $\mathcal{A}_X(\omega)$ associated with $\mathcal{G}_X(t)$, which correspondingly shows asymptotic power-law behaviour, $\sim \omega^{-1+2\eta}$, for small frequencies, where the exponent η depends on Δ_{AO} . We recall and generalize an argument due to Hopfield, that extends the relation between η and Δ_{AO} to composite local operators. Finally, we recapitulate how all these quantities can be calculated using NRG.

For simplicity, we assume in most of this section that the Fermi sea consists only of a single species of (spinless) electrons. The generalization to several channels needed in subsequent sections (in particular for discussing PS), is straightforward and will be introduced later as needed.

Although the concepts summarized in subsections II B to II E below apply quite generically to a wide range of impurity models, for definiteness we will illustrate them by referring to a particularly simple example, to be called the "local charge model" (LCM), which we define next.

A. Local charge model

The LCM describes a single spinless localized level, to be called dot level (alluding to a localized level in a quantum dot), interacting with a single Fermi sea of spinless electrons [see Fig. 1(a)]:

$$\hat{H}_{\text{LCM}}(\hat{n}_d) = U \hat{n}_d \hat{c}^\dagger \hat{c} + \sum_{\varepsilon} \varepsilon \hat{c}_{\varepsilon}^\dagger \hat{c}_{\varepsilon}. \quad (2)$$

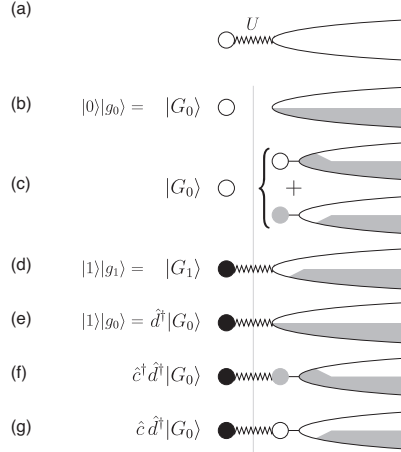


Figure 1: (a) Cartoon of the Hamiltonian (2) for the LCM. (b) to (g) Cartoons of the occupation of the dot and a half-filled lead, for $U > 0$, for several states discussed in the text. (b) and (c) give two equivalent depictions of the ground state $|G_0\rangle$ of \hat{H}_0 . (c) depicts the fact that $|g_0\rangle$ can be written as a superposition of the form $|0\rangle_c|Q\rangle_{\text{rest}} + |1\rangle_c|Q-1\rangle_{\text{rest}}$, indicating complementary occupations of the first site and the rest of a half-filled Wilson chain (defined in Sec. II E below). Here $|0\rangle_c$ (which obeys $\hat{c}|0\rangle_c = 0$) and $|1\rangle_c = \hat{c}^\dagger|0\rangle_c$ describe the first site of the Wilson chain being empty or filled, respectively; the charge in the rest of the Wilson chain is correspondingly distributed in such a way that both components of the superposition have the same total charge, Q . (d) depicts the ground state $|G_1\rangle$ of \hat{H}_1 , indicating that charge on the dot pushes charge in the lead away from the dot site. (e) shows the effect of applying \hat{d}^\dagger to $|G_0\rangle$, the latter depicted according to (b). Similarly, (f) and (g) show the effect of applying $\hat{c}^\dagger \hat{d}^\dagger$ or $\hat{c} \hat{d}^\dagger$ to $|G_0\rangle$, the latter depicted according to (c). The displaced charge flowing inwards from infinity towards the dot as each of the states (e) to (g) evolves to the final ground state $|G_1\rangle$ of (d) is $\Delta_d < 0$, $\Delta_d - 1 < 0$ or $\Delta_d + 1 > 0$, respectively. Comparison of (f) and (g) with (e) shows average charge differences of +1 and -1, respectively, in accord with the Hopfield-type argument summarized by Eq. (15).

Here \hat{c}_ε and \hat{d} are annihilation operators for Fermi sea states and the dot state, respectively, $\hat{n}_d = \hat{d}^\dagger \hat{d}$ counts the number of dot electrons, and $\hat{c} \equiv \hat{\psi}(0) \equiv \sum_{\varepsilon} \hat{c}_\varepsilon$ destroys a Fermi sea electron at the position of the dot. The interaction is taken to be repulsive, $U > 0$. There is no tunnelling between dot and sea. Therefore, the Hilbert space separates into two distinct sectors, in which the local charge operator \hat{n}_d has eigenvalues $n_d = 0$ and $n_d = 1$, respectively. The Hamiltonians describing the Fermi

sea in the two distinct sectors are

$$\hat{H}_0 = \hat{H}_{\text{LCM}}(n_d = 0) = \sum_{\varepsilon} \varepsilon \hat{c}_{\varepsilon}^{\dagger} \hat{c}_{\varepsilon}, \quad (3a)$$

$$\hat{H}_1(U) = \hat{H}_{\text{LCM}}(n_d = 1) = \sum_{\varepsilon} \varepsilon \hat{c}_{\varepsilon}^{\dagger} \hat{c}_{\varepsilon} + U \hat{c}^{\dagger} \hat{c}. \quad (3b)$$

We will denote their respective ground states [illustrated in Figs. 1(b,c) and 1(d), respectively] by

$$|G_0\rangle = |0\rangle|g_0\rangle, \quad |G_1\rangle = |1\rangle|g_1\rangle, \quad (4)$$

where $|0\rangle$ and $|1\rangle = \hat{d}^{\dagger}|0\rangle$ describe the dot state with charge 0 or 1, respectively, and $|g_0\rangle$ and $|g_1\rangle$ the corresponding Fermi sea ground states.

The LCM contains all ingredients needed for AO, hence we will repeatedly refer to it below as an explicit example of the general arguments to be presented. [Corresponding LCM passages will sometimes appear in square brackets, so as not to disrupt the general flow of the discussion.] Explicit numerical results for the LCM will be presented in Sec. III A below.

B. AO and the displaced charge

For the ensuing discussions, it will be useful to distinguish between two types of quenches, to be called type 1 and 2, which we now discuss in turn.

Type 1 quench: For a type 1 quench, some parameter of the Hamiltonian is changed abruptly (e.g. by a sudden change of gate voltage for one of the gates defining a quantum dot). Taking the LCM as an example, suppose that the value of the interaction in the LCM is changed suddenly from U to U' for a *fixed* local charge of $n_d = 1$. This corresponds to a type 1 quench with

$$\hat{H}_i = \hat{H}_1(U), \quad \hat{H}_f = \hat{H}_1(U'), \quad (5a)$$

$$|G_i\rangle = |1\rangle|g_{1,i}\rangle, \quad |G_f\rangle = |1\rangle|g_{1,f}\rangle. \quad (5b)$$

The overlap of initial and final ground states,

$$|\langle G_i|G_f\rangle| = |\langle g_{1,i}|g_{1,f}\rangle| \sim N^{-\frac{1}{2}\Delta_{\text{AO}}^2}, \quad (6)$$

will vanish in the thermodynamic limit due to AO, since the two Fermi sea states $|g_{1,i}\rangle$ and $|g_{1,f}\rangle$ feel scattering potentials of different strengths.

In his classic 1967 paper, Anderson showed that for this type of situation the exponent Δ_{AO} in Eq. (6) is equal to the change in scattering phase shifts at the Fermi surface divided by π , in reaction to the change in the strength of the scattering potential. According to the Friedel sum rule,^{20–23} the change in phase shifts divided by π , in turn, is equal to the *displaced charge* Δ_{ch} (in units of e) that flows inward from infinity into a large but finite volume (say V_{large}) surrounding the scattering site, in reaction to the change in scattering potential, so that $\Delta_{\text{AO}} = \Delta_{\text{ch}}$. To be explicit,

$$\Delta_{\text{ch}} \equiv \langle G_f|\hat{n}_{\text{tot}}|G_f\rangle - \langle G_i|\hat{n}_{\text{tot}}|G_i\rangle, \quad (7)$$

where $\hat{n}_{\text{tot}} \equiv \hat{n}_{\text{sea}} + n_{\text{dot}}$ counts the *total* number of electrons within V_{large} , with \hat{n}_{sea} counting the Fermi sea electrons and \hat{n}_{dot} counting the electrons on the dot. [For the LCM, $\hat{n}_{\text{dot}} = \hat{n}_d$.]

The relative sign between Δ_{AO} and Δ_{ch} (+ not $-$) is a matter of convention, which does not affect the orthogonality exponent Δ_{AO}^2 . Our convention,¹⁹ which agrees with standard usage,²⁴ is such that $\Delta_{\text{AO}} > 0$ (or < 0) if the change in local potential induces electrons to flow inward toward (outward away from) the scattering site.

For the LCM quench of Eq. (5) above, the initial and final states have the same dot charge, $n_d = 1$, hence the displaced charge reduces to $\Delta_{\text{ch}} \equiv \langle g_{1,f}|\hat{n}_{\text{sea}}|g_{1,f}\rangle - \langle g_{1,i}|\hat{n}_{\text{sea}}|g_{1,i}\rangle$. However, such a simplification will not occur for more complex impurity models involving tunneling between dot and lead [of the form $(\hat{d}^{\dagger}\hat{c} + \hat{c}^{\dagger}\hat{d})$], so that the local charge is not conserved. Examples are the interacting resonant level model [Eq. (36) below], or the single-impurity Anderson model [Eq. (47) below].

For such a model, consider a type 1 quench from \hat{H}_i to \hat{H}_f , implemented by a sudden change in one or several model parameters, in analogy to Eq. (5a). Although the corresponding ground states $|G_i\rangle$ and $|G_f\rangle$ will no longer have the simple factorized form of Eq. (5b), they will still exhibit AO as in Eq. (1). Moreover, the decay exponent is still equal to the displaced charge, $\Delta_{\text{AO}} = \Delta_{\text{ch}}$, given by Eq. (7). (For a NRG verification of this fact, see Ref. 19.)

Type 2 quench: For a type 2 quench, all model parameters are kept constant, but the system is switched suddenly between two dynamically disconnected sectors of Hilbert space characterized by different conserved quantum numbers. Taking again the LCM of Eq. (2) as an example, suppose that the local charge is suddenly changed, say from $n_d = 0$ to 1, while all model parameters are kept constant. This corresponds to a type 2 quench with

$$\hat{H}_i = \hat{H}_0, \quad \hat{H}_f = \hat{H}_1, \quad (8a)$$

$$|G_i\rangle = |0\rangle|g_0\rangle, \quad |G_f\rangle = |1\rangle|g_1\rangle. \quad (8b)$$

A physical example of such a quench would be core level X-ray photoemission spectroscopy (XPS), where an incident X-ray photon is absorbed by an atom in a crystal, accompanied by the ejection of a core electron from the material.²⁵ This amounts to the sudden creation of a core hole, which subsequently interacts with the Fermi sea of mobile conduction electrons (but does not hybridize with them). Thus, in this example \hat{n}_d would represent the hole number operator $\hat{n}_h = \hat{h}^{\dagger}\hat{h}$.

More generally, a type 2 quench presupposes a Hamiltonian $\hat{H}(\hat{n}_x)$ that depends on a conserved charge, say \hat{n}_x [such as \hat{n}_d for the LCM], with eigenvalues n_x [such as $n_d = 0$ or 1]. The Hilbert space can then be decomposed into distinct, dynamically disconnected sectors, labelled by n_x and governed by effective Hamiltonians $\hat{H}(n_x)$, whose ground states have the form $|G(n_x)\rangle = |n_x\rangle|g(n_x)\rangle$. A type 2 quench is induced by an operator, say \hat{X}^{\dagger} [such as \hat{d}^{\dagger} for the LCM], whose action changes the conserved charge, thereby connecting two distinct

sectors, say $\langle n'_x | \hat{X}^\dagger | n_x \rangle = 1$, with $n'_x \neq n_x$. For such a quench we make the identifications

$$\hat{H}_i = \hat{H}(n_x), \quad \hat{H}_f = \hat{H}(n'_x), \quad (9a)$$

$$|G_i\rangle = |n_x\rangle |g(n_x)\rangle, \quad |G_f\rangle = |n'_x\rangle |g(n'_x)\rangle. \quad (9b)$$

The overlap $\langle G_i | G_f \rangle = 0$ vanishes trivially, because $\langle n_x | n'_x \rangle = 0$. However, define

$$|\psi_i\rangle \equiv \hat{X}^\dagger |G_i\rangle \quad (10)$$

to be the ‘‘initial post-quench state’’ obtained by the action of the charge switching operator \hat{X}^\dagger on the initial ground state. [Fig. 1(e) illustrates this state for the LCM with $\hat{X}^\dagger = \hat{d}^\dagger$.] Then the overlap

$$\mathcal{O}_X \equiv |\langle \psi_i | G_f \rangle| = |\langle g(n_x) | g(n'_x) \rangle| \sim N^{-\frac{1}{2} \Delta_X^{\text{ch}}} \quad (11)$$

again shows AO, since it is equal to the overlap of two Fermi sea ground states corresponding to different local charges. The corresponding exponent in Eq. (11) can again be related to a displaced charge, $\Delta_X = \Delta_X^{\text{ch}}$, but now the latter should compare the total charge within V_{large} described by the states $|G_f\rangle$ and $|\psi_i\rangle$:

$$\Delta_X^{\text{ch}} \equiv \langle G_f | \hat{n}_{\text{tot}} | G_f \rangle - \langle \psi_i | \hat{n}_{\text{tot}} | \psi_i \rangle. \quad (12)$$

Δ_X^{ch} can be interpreted as the charge (in units of e) that flows into V_{large} during the post-quench time evolution from $|\psi_i\rangle$ to $|G_f\rangle$ subsequent to the action of \hat{X}^\dagger . To simplify notation, we will often omit the superscript ch distinguishing the displaced charge Δ_X^{ch} from the AO exponent Δ_X , since the two are equal in any case.

Composite type 2 quench: Let us now consider a more complicated version of a type 2 quench, induced by a composite operator of the form $\hat{Y}^\dagger = \hat{C}^\dagger \hat{X}^\dagger$. Here \hat{X}^\dagger switches between disconnected sectors of Hilbert space as above, while \hat{C}^\dagger does not; instead, \hat{C}^\dagger is assumed to be a *local* operator which acts on the dot or in the Fermi sea at the location of the dot, but commutes with \hat{n}_x . For the LCM, an example would be $\hat{C}^\dagger = \hat{c}^\dagger$, so that \hat{Y}^\dagger creates two electrons, one on the dot, one in the Fermi sea at the site of the dot.

A physical realization hereof is furnished by the edge-ray edge effect occurring in X-ray absorption spectroscopy (XAS), where an incident X-ray photon is absorbed by an atom in a crystal, accompanied by the creation of a core hole ($\hat{X}^\dagger = \hat{h}^\dagger$) and the transfer of a core electron into the conduction band of the metal ($\hat{C}^\dagger = \hat{c}^\dagger$).²⁵ Another example is the Kondo exciton discussed in Refs. 13,14, where the absorption of a photon by a quantum dot is accompanied by the creation of an electron-hole pair on the dot, described by $\hat{C}^\dagger = \hat{e}^\dagger$ and $\hat{X}^\dagger = \hat{h}^\dagger$, respectively. In this example, the hole number $\hat{n}_h = \hat{h}^\dagger \hat{h}$ is conserved, but the dot electron number $\hat{n}_e = \hat{e}^\dagger \hat{e}$ is not, since the Hamiltonian contains dot-lead hybridization terms of the form $(\hat{e}^\dagger \hat{c} + \hat{c}^\dagger \hat{e})$ (see Refs. 13,14 for details).

For a composite type 2 quench, the initial and final Hamiltonians and ground states are defined as in Eqs. (9), but the post-quench initial state is given by

$$|\psi'_i\rangle \equiv \hat{Y}^\dagger |G_i\rangle = \hat{C}^\dagger |\psi_i\rangle. \quad (13)$$

Its overlap with the final ground state $|G'_f\rangle$ to which it evolves in the long time limit has the form

$$\mathcal{O}_Y \equiv |\langle \psi'_i | G'_f \rangle| = |\langle g(n_x) | \hat{C} | g'(n'_x) \rangle| \sim N^{-\frac{1}{2} \Delta_Y^{\text{ch}}}. \quad (14)$$

The exponent Δ_Y arising here is related to Δ_X and can be found using the following argument, due to Hopfield.⁴ Due to the action of \hat{C}^\dagger , the states $|\psi'_i\rangle$ and $|\psi_i\rangle$ describe different amounts of initial post-quench charge within the volume V_{large} . We will denote the difference by

$$\Delta_C \equiv \langle \psi'_i | \hat{n}_{\text{tot}} | \psi'_i \rangle - \langle \psi_i | \hat{n}_{\text{tot}} | \psi_i \rangle. \quad (15)$$

For example, if \hat{C}^\dagger is a local electron creation or annihilation operator, then $\Delta_C = 1$ or -1 , respectively [as illustrated in Figs. 1(f) and (g)]. However, since an initial charge surplus or deficit at the scattering site is compensated, in the long-time limit, by charges flowing to or from infinity, the ground states $|G'_f\rangle$ and $|G_f\rangle$ towards which $|\psi'_i\rangle$ and $|\psi_i\rangle$ evolve, respectively, will differ only by one Fermi sea electron at infinity, and hence for practical purposes describe the same local physics. In particular, the charge within V_{large} is the same for both, $\langle G'_f | \hat{n}_{\text{tot}} | G'_f \rangle = \langle G_f | \hat{n}_{\text{tot}} | G_f \rangle$. Therefore, the *total* displaced charge associated with the action of \hat{Y}^\dagger is

$$\Delta_Y \equiv \langle G'_f | \hat{n}_{\text{tot}} | G'_f \rangle - \langle \psi'_i | \hat{n}_{\text{tot}} | \psi'_i \rangle = \Delta_X - \Delta_C, \quad (16)$$

where the second equality follows from Eqs. (15) and (12). The exponent governing the AO decay in Eq. (14) is thus given by Eq. (16). Since Δ_C is a trivially known integer, knowledge of Δ_X for a type 2 quench suffices to determine the AO exponents Δ_Y for an entire family of related composite quenches.

To conclude this section, we note that a type 1 quench can always be formulated as a type 2 quench, by introducing an auxiliary conserved degree of freedom (say \hat{n}_h), whose only purpose is to divide the Hilbert space into two sectors (labelled by $n_h = 0$ or 1), within which some parameters of the Hamiltonian take two different values. For example, if the quench involves changing U to U' , this can be modelled by replacing U by $U + \hat{n}_h(U' - U)$ in the Hamiltonian. For an example, see Sec. III C.

C. AO and post-quench time evolution

After a sudden change in the local Hamiltonian, AO also affects the long-time limit of the subsequent time evolution, and hence the low-frequency behaviour of corresponding spectral functions. A prominent example is optical absorption,^{2-5,12-14} for which AO leaves its imprint in the shape of the absorption spectrum, by reducing the probability for absorption. This is familiar

from the x-ray edge problem.³ In particular, in the limit of absorption frequency ω very close to (but above) the threshold for absorption, the zero-temperature absorption spectrum has a power-law form, with an exponent that is influenced by AO. Recent demonstrations of this fact can be found in studies, both theoretical^{12,13} and experimental,¹⁴ of exciton creation in quantum dots via optical absorption, whereby an electron is excited from a valence-band level to a conduction band level.

In this subsection, we will analyse the role of AO for the time evolution after a type 2 quench of the form (8). We consider the following generic situation: For $t < 0$, a system is in the ground state $|G_i\rangle$ of the initial Hamiltonian \hat{H}_i (with ground state energy E_i), describing a Fermi sea under the influence of a local scattering potential. At $t = 0$, a sudden change in the local potential occurs, described by the action of the local operator \hat{X}^\dagger . It switches sector n_x to n'_x , yielding the post-quench initial state $|\psi_i\rangle = \hat{X}^\dagger|G_i\rangle$ at time $t = 0^+$, and switches the Hamiltonian from \hat{H}_i to \hat{H}_f .

The subsequent dynamics can be characterized by the correlator

$$\mathcal{G}_X(t) \equiv -ie^{i\omega_0 t} \theta(t) \langle G_i | \hat{X}(t) \hat{X}^\dagger | G_i \rangle, \quad (17)$$

where $\hat{X}(t) = e^{i\hat{H}_f t} \hat{X} e^{-i\hat{H}_i t}$, reflecting the fact that \hat{X} switches \hat{H}_f to \hat{H}_i . The phase factor $e^{i\omega_0 t}$ is included for later convenience, with ω_0 to be specified below [after Eq. (22)].

Since the Fermi sea adjusts in reaction to the sudden change in local potential at $t = 0$, AO builds up and the overlap function $\mathcal{G}_X(t)$ decreases with time. It is known since 1969 that in the long-time limit it decays in power-law fashion as^{2,4}

$$\mathcal{G}_X(t) \sim t^{-\Delta_X}, \quad (18)$$

where Δ_X is the exponent governing the AO decay of \mathcal{O}_X in Eq. (11). This can be understood heuristically by expanding Eq. (17) as

$$ie^{-(E_i + \omega_0)t} \mathcal{G}_X(t) = \theta(t) \langle \psi_i | e^{-i\hat{H}_f t} | \psi_i \rangle \quad (19a)$$

$$= \theta(t) \langle \psi_i | \psi_i(t) \rangle \quad (19b)$$

$$= \theta(t) \sum_n e^{-iE_n t} |\langle \psi_i | n \rangle|^2, \quad (19c)$$

where $|\psi_i(t)\rangle = e^{-i\hat{H}_f t} |\psi_i\rangle$ describes the time-evolution for $t > 0$, and $|n\rangle$ and E_n represent a complete set of eigenstates and eigenenergies of \hat{H}_f . In the long-time limit Eq. (19c) will be dominated by the ground state $|G_f\rangle$ of \hat{H}_f (with eigenenergy E_f), yielding a contribution $|\langle \psi_i | G_f \rangle|^2$ that scales as $N^{-\Delta_X}$ [by Eq. (11)]. Now, as time increases, the effect of the local change in scattering potential is felt at increasing length scales $L(t) \sim v_f t$, with v_f the Fermi velocity; regarding $|G_f\rangle$ as the lowest eigenstate of \hat{H}_f in a box of size $N \sim L(t)$, the AO of $|\langle \psi_i | G_f \rangle|^2 \sim L(t)^{-\Delta_X}$ implies Eq. (18).

For a composite type 2 quench induced by $\hat{Y}^\dagger = \hat{C}^\dagger \hat{X}^\dagger$, we can conclude by analogous arguments that

$$\mathcal{G}_Y(t) \sim t^{-\Delta_Y}, \quad (20)$$

where Δ_Y is the displaced charge of Eq. (16).

For future reference, we also introduce the correlator

$$\mathcal{G}_C^{\text{eq}}(t) \equiv -i\theta(t) \langle G | e^{i\hat{H}t} \hat{C} e^{-i\hat{H}t} \hat{C}^\dagger | G \rangle \sim it^{-2\eta_C^{\text{eq}}} \quad (21)$$

of an operator \hat{C}^\dagger that does not switch between dynamically disconnected sectors, i.e. that commutes with \hat{n}_x [examples of such operators are given in the discussion before Eq. (13) above]. Then Eq. (21) is a standard *equilibrium* correlator, with $\hat{H}_i = \hat{H}_f$, in contrast to the *quench* correlator $\mathcal{G}_X(t)$ of Eq. (21), where $\hat{H}_i \neq \hat{H}_f$. For such an equilibrium correlator the decay exponent η_C^{eq} is called the scaling dimension of \hat{C}^\dagger . A local operator \hat{C}^\dagger is relevant, marginal or irrelevant under renormalization if $\eta_C^{\text{eq}} < 1, = 1$ or > 1 , respectively.²⁶

D. AO and spectral functions

Next we consider the spectral function corresponding to $\mathcal{G}_X(t)$,

$$\mathcal{A}_X(\omega) \equiv -\frac{1}{\pi} \Im \left(\int_0^\infty dt e^{i(\omega + i0^+)t} \mathcal{G}_X(t) \right) \quad (22a)$$

$$= \sum_n |\langle n | \hat{X}^\dagger | G_i \rangle|^2 \delta(\omega - E_n + E_i + \omega_0). \quad (22b)$$

It evidently has the form of a golden-rule transition rate for \hat{X}^\dagger -induced transitions with excitation energy $\omega + \omega_0$ and is nonzero only for ω above the threshold frequency $\omega_{\text{th}} = (E_f - E_i) - \omega_0$. For simplicity, we will here and henceforth set $\omega_{\text{th}} = 0$ by choosing $\omega_0 = E_f - E_i$. Note the sum rule $\int d\omega \mathcal{A}(\omega) = \langle G_i | \hat{X} \hat{X}^\dagger | G_i \rangle$, which can be used as consistency check for numerical calculations.

Equation (18) implies that in the limit $\omega \rightarrow \omega_{\text{th}} = 0$, the spectral function behaves as

$$\mathcal{A}_X(\omega) \sim \omega^{-1+2\eta_X}, \quad \eta_X = \frac{1}{2} \Delta_X^2. \quad (23)$$

The definition of η_X is deliberately chosen such that Eq. (23) parallels the form of the equilibrium spectral function corresponding to $\mathcal{G}_C^{\text{eq}}(t)$ of Eq. (21), namely

$$\mathcal{A}_C^{\text{eq}}(\omega) \sim \omega^{-1+2\eta_C^{\text{eq}}}. \quad (24)$$

Now consider the spectral function $\mathcal{A}_Y(\omega)$ involving the composite type 2 quench operator $\hat{Y}^\dagger = \hat{C}^\dagger \hat{X}^\dagger$. Equations (20) and (16) immediately lead to the prediction

$$\mathcal{A}_Y(\omega) \sim \omega^{-1+2\eta_Y}, \quad \eta_Y = \frac{1}{2} (\Delta_X - \Delta_C)^2, \quad (25)$$

to be called the *generalized Hopfield rule*, since the essence of the argument by which we have obtained it was first formulated by Hopfield.⁴

A physical situation for which Eq. (25) is relevant is the edge-ray edge effect occurring in X-ray absorption spectroscopy (XAS). There we have $\hat{Y}^\dagger = \hat{c}^\dagger \hat{h}^\dagger$ (as explained above), and $\Delta_C = 1$. Thus Eq. (25) yields

$$\mathcal{A}_{hc}(\omega) \sim \omega^{-1+(\Delta_h-1)^2} = \omega^{-2\Delta_h+\Delta_h^2} \quad (26)$$

reproducing a well-established result for the X-ray edge absorption spectrum [Ref. 4, p. 48; Ref. 5, Eq. (66)]. In the literature, $-2\Delta_h$ is often called the ‘‘Mahan contribution’’ to the exponent, and Δ_h^2 the AO contribution. Since $\Delta_h \leq 1$, one has $2\Delta_h > \Delta_h^2$, i.e. ‘‘Mahan wins’’, and $\mathcal{A}_{hc}(\omega)$ diverges at small frequencies. For present purposes, though, it is perhaps somewhat more enlightening to adopt Hopfield’s point of view, stated in Eq. (25), according to which both terms, $-2\Delta_h$ and Δ_h^2 arise from the AO exponent $(\Delta_h - 1)^2$.

Equations (11), (23) and (25) will play a central role in this work. Their message is that the near-threshold behaviour of spectral functions of the type defined in Eq. (22) is governed by an AO exponent that can be extracted from the overlap $\langle \psi_i | G_f \rangle$ between the initial post-quench state $|\psi_i\rangle$ and the ground state $|G_f\rangle$ to which it evolves in the long-time limit.

To conclude this section, we remark that the above analysis generalizes straightforwardly to models involving several species or channels of electrons, say with index μ , provided that the channel index is a conserved quantum number (i.e. no tunnelling between channels occurs).¹⁹ Then the initial and final ground states will be products of the ground states for each separate channel, so that Eq. (1) generalizes to

$$|\langle G_i | G_f \rangle| \sim \prod_{\mu} N_{\mu}^{-\frac{1}{2} \Delta_{\text{AO}, \mu}^2}. \quad (27)$$

All power laws discussed above that involve Δ_{AO}^2 (or quantities derived therefrom) in the exponent can be similarly generalized by including appropriate products over channels.

E. AO exponents and NRG

Results of the above type have been established analytically, in the pioneering papers from 1969, Refs. 2–5, only for the simple yet paradigmatic case of the X-ray edge effect. Nevertheless, Eq. (25) can be expected to hold for a larger class of models, as long as the setting outlined above applies. Indeed, it has recently been found to hold also in the context of the Kondo exciton.^{12–14} The purpose of this work, therefore, is to establish the validity of the connections between Eqs. (11), (23) and (25) for a series of models of increasing complexity. We shall do so numerically using NRG, since for most of these

models an analytical treatment along the lines of Refs. 2 and 5 would be exceedingly tedious, if not impossible. The requisite NRG tools have become accessible only recently.^{13,27,28}

NRG, developed in the context of quantum impurity models, offers a very direct way of evaluating the overlap, since it allows both ground states $|G_i\rangle$ and $|G_f\rangle$ to be calculated explicitly. Models treatable by NRG have the generic form $\hat{H} = \hat{H}_B + \hat{H}_d$. Here

$$\hat{H}_B = \sum_{\mu=1}^{n_c} \sum_{\varepsilon} \varepsilon \hat{c}_{\varepsilon\mu}^{\dagger} \hat{c}_{\varepsilon\mu}, \quad (28)$$

describes a free Fermi sea involving n_c channels of fermions, with constant density of states ρ per channel and half-bandwidth $D = 1/(2\rho)$. (When representing numerical results, energies will be measured in units of half-bandwidth by setting $D = 1$.) \hat{H}_d , which may involve interactions, describes local degrees of freedom and their coupling to the Fermi sea.

Wilson discretized the spectrum of \hat{H}_0 on a logarithmic grid of energies $\pm D\Lambda^{-k}$ (with $\Lambda > 1$, $k = 0, 1, 2, \dots$), thereby obtaining exponentially high resolution of low-energy excitations. He then mapped the impurity model onto a semi-infinite ‘‘Wilson tight-binding chain’’ of sites $k = 0$ to ∞ , with the impurity degrees of freedom coupled only to site 0. To this end, he made a basis transformation from the set of Fermi sea operators $\{\hat{c}_{\varepsilon\mu}\}$ to a new set $\{\hat{f}_{k\mu}\}$, with $\hat{f}_{0\mu} \propto \hat{c}_{\mu} \equiv \psi_{\mu}(0) \equiv \sum_{\varepsilon} \hat{c}_{\varepsilon\mu}$, chosen such that they bring \hat{H}_0 into the tridiagonal form

$$\hat{H}_B \simeq \sum_{\mu=1}^{n_c} \sum_{k=1}^{\infty} t_k (\hat{f}_{k\mu}^{\dagger} \hat{f}_{k-1,\mu} + \text{h.c.}), \quad (29)$$

with hopping matrix elements $t_k \propto D\Lambda^{-k/2}$ that decrease exponentially with site index k along the chain. Because of this separation of energy scales, the Hamiltonian can be diagonalized iteratively by solving a Wilson chain of length k (restricting the sum in Eq. (29) to the first k terms) and increasing k one site at a time. The number of kept states at each iteration will be denoted by N_k .

For a Wilson chain of length k , the effective level spacing of its lowest-lying energy levels is set by the smallest hopping matrix element of the chain, namely $\Lambda^{-k/2}$; such a Wilson chain thus represents a real space system of volume $V_{\text{large}} \sim \Lambda^{k/2}$. Thus, the overlap between the two ground states of a Wilson chain of length k can be expressed as¹⁹

$$|{}_k \langle G_i | G_f \rangle_k| \sim \Lambda^{-\frac{1}{2} \Delta_{\text{AO}}^2} \equiv e^{-\alpha k}, \quad (30)$$

where $\alpha \equiv (\log \Lambda / 4) \Delta_{\text{AO}}^2$. Explicit calculations show¹⁹ that an exponential decay of the form Eq. (30) applies for the overlap between any two states $|E_i\rangle_k$ and $|E_f\rangle_k$ representing low-lying excitations w.r.t. $|G_i\rangle_k$ and $|G_f\rangle_k$ at iteration k , respectively. More technically, ${}_k \langle E_i | E_f \rangle_k \sim e^{-\alpha k}$ holds whenever $|E_i\rangle_k$ and $|E_f\rangle_k$ represent NRG

eigenstates with matching quantum numbers from the k -th NRG shell for \hat{H}_i and \hat{H}_f , respectively, and their overlap is calculated for increasing k . For multi-chain models, we note that channel-specific exponents such as $\Delta_{\text{AO},\mu}$ [see Eq. (27)] can be calculated, if needed, by considering Wilson chains with channel-dependent lengths.¹⁹

Within the framework of NRG, a consistency check is available for the value of Δ_{AO} extracted from Eq. (30): Δ_{AO} should be equal to the displaced charge Δ_{ch} of Eq. (7), which can also be calculated directly from NRG by calculating the expectation value of \hat{n}_{tot} for $|G_i\rangle$ and $|G_f\rangle$ individually.¹⁹ This check was successfully performed, for example, in Refs. 12 and 13, within the context of the single impurity Anderson model; for a recent systematic study, see Ref. 19. We have also performed this check in the present work wherever it was feasible.

Within NRG, it is also possible to directly calculate spectral functions such as $\mathcal{A}_X(\omega)$ of Eq. (22). To this end, one uses two separate NRG runs to calculate the ground state $|G_i\rangle$ of \hat{H}_i and an approximate but complete set of eigenstates $|n\rangle$ of \hat{H}_f .^{27,28} The Lehmann sum in Eq. (22) can then be evaluated explicitly,^{29,30} while representing the δ -functions occurring therein using a log-Gaussian broadening scheme. To this end, we follow the approach of Ref. 30, which involves a broadening parameter σ . (The specific choice of NRG parameters Λ , N_k and σ used for spectral data shown below will be specified in the legends of the corresponding figures.) That this approach is capable of yielding spectral functions whose asymptotic behaviour shows power-law behaviour characteristic of AO has been demonstrated recently in the context of the Kondo exciton problem.¹²⁻¹⁴ In the examples to be discussed below, we will compare the power-law exponents extracted from the asymptotic behaviour of such spectral functions to the values expected from AO, thus checking relations such as Eq. (23) for $\mathcal{A}_X(\omega)$ and Eq. (25) for $\mathcal{A}_Y(\omega)$.

III. INTERACTING RESONANT LEVEL MODEL

In this section we consider the effect of AO on dynamical quantities in the context of the spinless interacting resonant level model (IRLM).^{11,31} (The effects of AO for some static properties of this model were studied in Ref. 32.) The purpose of this exercise is to illustrate several effects that will be found to arise also for more complex models considered in subsequent sections. The IRLM involves a single localized level, to be called dot level (alluding to localized levels in a quantum dot), interacting with and tunnel-coupled to a single Fermi sea. We consider first the case without tunnelling, in which case the IRLM reduces to the LCM introduced in Sec. II above, where adding an electron to the dot at time $t = 0$ constitutes a type 2 quench. This leads to AO between the initial and final ground states, and corresponding nontrivial AO power laws, $\omega^{-1+2\eta}$, in spectral functions.

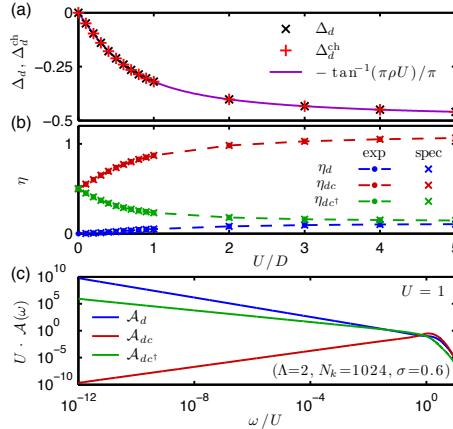


Figure 2: (Color online) Numerical results for the LCM of Eq. (2), for the type 2 quench of Eq. (8), whose initial, final and post-quench initial states $|G_i\rangle$, $|G_f\rangle$ and $|\psi_i\rangle$ are depicted in Figs. 1(b,c), 1(d) and 1(e-g), respectively. (a) Comparison of the decay exponent Δ_d obtained from Eq. (31) (crosses) with the displaced charge Δ_d^{ch} from Eq. (32) (pluses), for a number of different values of U . The two values agree very well (they differ by less than 0.1%), also with the analytic prediction Eq. (33) (solid line). As expected, $\Delta_d \rightarrow -1/2$ for $U \rightarrow \infty$. (b) Comparison of two ways of determining the AO exponents η that govern the low-energy asymptotic behaviour $\mathcal{A} \sim \omega^{-1+2\eta}$ of the spectral functions of Eqs. (35), related to Figs. 1(e-g): exponents obtained by fitting a power law to the corresponding spectra [shown in (c)] are shown as crosses (marked “spec”, for “spectra”); the corresponding exponents expected from Eq. (35), using the results of (a) for Δ_d , are shown as dots (marked “exp” for “expected”). We find a maximal deviation of less than 1%. Here and in all similar figures below, the dashed lines are only guides to the eye. (c) Asymptotic low-frequency dependence of the spectra Eqs. (35), for $U = 1$, on a double logarithmic plot, allowing the corresponding exponents η to be extracted.

We then turn on tunnelling, which connects the sectors of Hilbert space for which the dot is empty or filled, and hence counteracts AO. Correspondingly, the power-laws get modified at frequencies smaller than the renormalized level width, $\omega \lesssim \Gamma_{\text{ren}}$, where the AO behaviour is replaced by simple Fermi liquid behaviour; the effects of AO do survive, however, in a regime of intermediate frequencies, $\Gamma_{\text{ren}} < \omega < D$. Finally, we consider quenches of the position of the dot level, in which case AO reemerges.

A. Without tunnelling: LCM

In this subsection we present numerical results for the IRLM without tunnelling, corresponding to the lo-

8

cal charge model of Eq. (2), depicted in Fig. 1(a). We consider the type 2 quench of Eq. (8), with $\hat{X}^\dagger = \hat{d}^\dagger$. The initial and final ground states $|G_i\rangle$ and $|G_f\rangle$ are illustrated in Figs. 1(b,c) and 1(d), respectively, and the post-quench initial state $|\psi_i\rangle = \hat{d}^\dagger|G_i\rangle$ in Fig. 1(e). With these choices the overlap $|\langle\psi_i|G_f\rangle|$ of Eq. (11) becomes

$$\mathcal{O}_d \equiv |\langle G_0|\hat{d}|G_1\rangle| = |\langle g_0|g_1\rangle| \sim N^{-\frac{1}{2}\Delta_d^2}. \quad (31)$$

The corresponding displaced charge obtained from Eq. (12) is

$$\Delta_d^{\text{ch}} = \langle g_1|\hat{n}_{\text{sea}}|g_1\rangle - \langle g_0|\hat{n}_{\text{sea}}|g_0\rangle, \quad (32)$$

since $|G_f\rangle$ and $|\psi_i\rangle$ describe the same dot charge, $n_d = 1$.

We used NRG to calculate the overlap \mathcal{O}_d of Eq. (31) and extract the exponent Δ_d from its exponential decay with Wilson chain length [Eq. (30)], for several values of U . As consistency check, we also calculated the displaced charge Δ_d^{ch} [Eq. (32)]. As shown in Fig. 2(a), the results for Δ_d (crosses) and Δ_d^{ch} (pluses) agree very well. The displaced charge Δ_d^{ch} is < 0 , since the repulsive interaction pushes charge away from the local site. Its magnitude $|\Delta_d^{\text{ch}}|$ depends on the interaction strength: as U is increased from 0 to ∞ , the displaced charge goes from 0 to $-\frac{1}{2}$, reflecting the complete depletion of the initially half-filled Wilson chain site directly adjacent to the dot site [compare Figs. 1(b) and 1(d)]. Figure 2(a) shows that the numerical results for Δ_d and Δ_d^{ch} (symbols) also agree with the analytical result (solid line) obtained for the phase shift obtained from elementary scattering theory [see e.g. Ref. 11, Eq. (25.29)],

$$\Delta_d = -\frac{1}{\pi} \tan^{-1}(\pi\rho U), \quad (33)$$

with ρ the density of states in the Fermi sea (cf. Sec. II E).

To study the influence of AO on dynamical quantities, we consider simple and composite type 2 quenches induced by acting on the initial ground state $|G_i\rangle = |G_0\rangle$ with the operators

$$\hat{X}^\dagger = \hat{d}^\dagger, \quad \hat{Y}_1^\dagger = \hat{c}^\dagger \hat{d}^\dagger, \quad \hat{Y}_2^\dagger = \hat{c} \hat{d}^\dagger. \quad (34)$$

All three operators describe transitions between the $n_d = 0$ and 1 sectors. The analysis of Sec. II D applies directly, with the identifications $\hat{H}_i = \hat{H}_0$ and $\hat{H}_f = \hat{H}_1$, while $\Delta_C = \pm 1$ for \hat{Y}_1^\dagger or \hat{Y}_2^\dagger , respectively [see Figs. 1(e-g)]. In particular, Eqs. (23) and (25) imply:

$$\mathcal{A}_d(\omega) \sim \omega^{-1+2\eta_d} \quad \eta_d = \frac{1}{2}\Delta_d^2, \quad (35a)$$

$$\mathcal{A}_{dc}(\omega) \sim \omega^{-1+2\eta_{dc}} \quad \eta_{dc} = \frac{1}{2}(\Delta_d - 1)^2, \quad (35b)$$

$$\mathcal{A}_{dc^\dagger}(\omega) \sim \omega^{-1+2\eta_{dc^\dagger}} \quad \eta_{dc^\dagger} = \frac{1}{2}(\Delta_d + 1)^2. \quad (35c)$$

Using NRG, we calculated these three spectra for several values of U (cf. Fig. 2(c)). In the limit of small ω , the spectra show clear power law behaviour, $\omega^{-1+2\eta}$. The exponents η_d , η_{dc} , η_{dc^\dagger} extracted from these spectra are shown in Fig. 2(b) (crosses, marked “spec”, for “spectra”). They agree well with the values expected (dots,

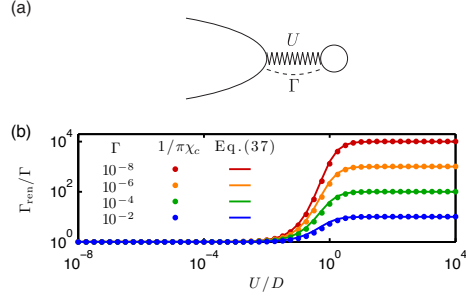


Figure 3: (Color online) (a) Cartoon of the Hamiltonian (36) for the IRLM. (b) The renormalized level width Γ_{ren} , calculated via the dot’s charge susceptibility, $1/\pi\chi_c$,³² (dots) or via Eq. (37) (solid line), shown as a function of U for $\varepsilon_d = 0$ and several values of Γ . As U increases from 0, $\Gamma_{\text{ren}}/\Gamma$ begins to differ significantly from its initial value, namely 1, only once U becomes comparable to the band-width, reaching its maximal value $(\Gamma/D)^{-1/2}$ for $U \gg D$.

marked “exp”, for “expected”) from Eqs. (35), based on the value for Δ_d extracted from Eq. (31). Thus, all ways of determining Δ_d are completely consistent, confirming the validity of the above analysis.

B. With tunnelling: IRLM

The previous subsection focused on a switch between two sectors of the Hilbert space, with $n_d = 0$ and $n_d = 1$, that were not coupled dynamically, but governed instead by two distinct Hamiltonians, \hat{H}_i and \hat{H}_f . In the present subsection, we consider the case that the sectors with $n_d = 0$ and $n_d = 1$ are coupled by tunnelling between dot and lead, so that the notion of an initial and final Hamiltonian, acting in decoupled sectors of Hilbert space, does not apply. The dynamics is governed instead by the single Hamiltonian $\hat{H}_i = \hat{H}_f = \hat{H}_{\text{IRLM}}$, given by [see Fig. 3(a)]

$$\hat{H}_{\text{IRLM}} = \varepsilon_d \hat{d}^\dagger \hat{d} + U(\hat{d}^\dagger \hat{d} - 1/2)(\hat{c}^\dagger \hat{c} - 1/2) + \sum_\varepsilon \varepsilon \hat{c}_\varepsilon^\dagger \hat{c}_\varepsilon + \sqrt{\frac{\Gamma}{\pi\rho}} \sum_\varepsilon (\hat{d}^\dagger \hat{c}_\varepsilon + \hat{c}_\varepsilon^\dagger \hat{d}). \quad (36)$$

We assume, here and in all later settings, that the hybridization of the dot level with the Fermi sea states is ε -independent, with Γ being the bare width of the dot level. Here, in contrast to the local charge model of Eq. (2), the interaction term is taken to be particle-hole symmetric, so that the model is particle-hole symmetric for $\varepsilon_d = 0$.

The presence of the interaction, U , is known to effectively modify the level width,^{31,32} both by reducing the density of states of the leads near the dot, and by inducing AO in the leads when the dot occupancy changes. The precise interplay between these effects can be quite

intricate and was studied in Ref. 32. A quantitative analysis can be performed by defining a renormalized level width in terms of the charge susceptibility, $\Gamma_{\text{ren}} \equiv 1/\pi\chi_c$. At the point of particle-hole (ph) symmetry ($\varepsilon_d = 0$), an analytic formula for the latter is available,³¹

$$\Gamma_{\text{ren}}/D = (\Gamma/D)^{1/(2-(1+\Delta_d^{\text{ph}})^2)}, \quad (37)$$

where Δ_d^{ph} is given by

$$\Delta_d^{\text{ph}} = -\frac{2}{\pi} \tan^{-1}(\pi\rho U/2). \quad (38)$$

Δ_d^{ph} can be interpreted as the change in scattering phase shift that a system with $\Gamma = 0$, $\varepsilon_d = 0$ experiences if the local occupancy is changed abruptly from $n_d = 0$ to 1. The form of Eq. (38) is analogous to Eq. (33) for Δ_d , with two differences: since the final scattering potentials being compared have amplitude $-U/2$ and $U/2$ (instead of 0 and U), the argument of \tan^{-1} has an extra factor of 1/2, and there is an extra prefactor of 2.

The dependence of Γ_{ren} on U is illustrated in Fig. 3(b), which shows good agreement between the NRG results for $1/\pi\chi_c$ (dots) and the analytic formula (37) (lines). For U much smaller than the bandwidth D , $\Gamma_{\text{ren}}/\Gamma$ is essentially equal to 1; it strongly increases once U becomes of the order D , and saturates to $(\Gamma/D)^{-1/2}$ for $U \gg D$.

Let us now consider the equilibrium spectral functions for the operators of Eq. (34), $\mathcal{A}_d^{\text{eq}}$, $\mathcal{A}_{dc}^{\text{eq}}$ and $\mathcal{A}_{dc^\dagger}^{\text{eq}}$. They are defined as in Eq. (22) but with $\hat{H}_f = \hat{H}_i$, because for the IRLM, where n_d is not conserved, none of these operators induces a quench. Therefore, the $\omega \rightarrow 0$ behaviour of their correlators is expected (and indeed found) to be independent of AO. However, quite remarkably, traces of AO *do show up* in an intermediate frequency regime, $\omega^* < \omega < D$, where $1/\omega^*$ corresponds to the time scale within which charge equilibration takes place. Below the energy scale ω^* the quantum impurity becomes strongly correlated with the Fermi sea and for the present model we have $\omega^* \simeq \Gamma_{\text{ren}}$. Let us therefore discuss the two regimes, ω below or above ω^* , separately.

In the regime $\omega \ll \omega^*$, the spectral functions are found to have the following asymptotic form $\mathcal{A}^{\text{eq}} \sim \omega^{-1+2\eta^{\text{eq}}}$ [cf. Figs. 4(a-c)]:

$$\mathcal{A}_d^{\text{eq}}(\omega) \sim \omega^0, \quad \eta_d^{\text{eq}} = 1/2, \quad (39a)$$

$$\mathcal{A}_{dc}^{\text{eq}}(\omega) \sim \omega^3, \quad \eta_{dc}^{\text{eq}} = 2, \quad (39b)$$

$$\mathcal{A}_{dc^\dagger}^{\text{eq}}(\omega) \sim \omega^3, \quad \eta_{dc^\dagger}^{\text{eq}} = 2. \quad (39c)$$

The exponents arising here can be understood analytically using elementary, though not entirely trivial arguments, based on the fact that the lowest-lying excitations of this model have Fermi liquid properties. We refer the reader to the Appendix for a detailed analysis.

Now consider the regime $\omega^* < \omega < D$. As shown in the corresponding regime of $\omega/\Gamma_{\text{ren}} > 1$ in Figs. 4(a-c), each of the equilibrium spectral functions $\mathcal{A}_d^{\text{eq}}$, $\mathcal{A}_{dc}^{\text{eq}}$ and $\mathcal{A}_{dc^\dagger}^{\text{eq}}$, exhibits another, different power-law there. For $\mathcal{A}_d^{\text{eq}}$ we

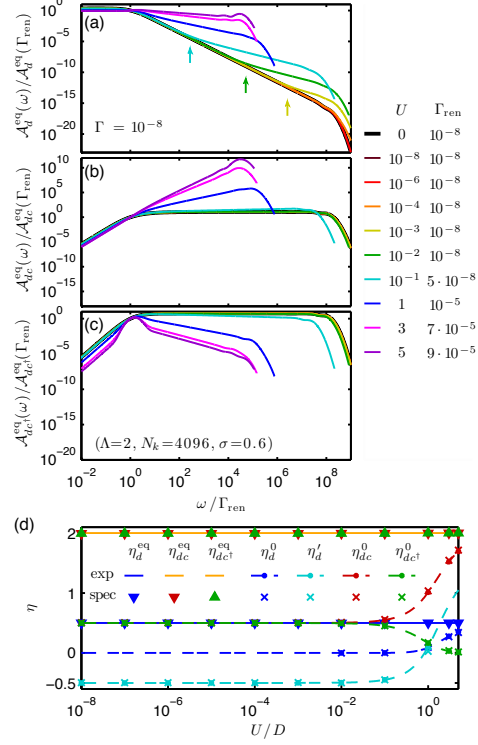


Figure 4: (Color online) (a)-(c) The equilibrium spectral functions $\mathcal{A}_d^{\text{eq}}(\omega)$, $\mathcal{A}_{dc}^{\text{eq}}(\omega)$ and $\mathcal{A}_{dc^\dagger}^{\text{eq}}(\omega)$ for the IRLM, showing a crossover from trivial power laws, $\omega^{-1+2\eta^{\text{eq}}}$, for $\omega < \omega^*$, to AO power laws, $\omega^{-1+2\eta^0}$, for $\omega^* < \omega < D$, with the crossover frequency ω^* given by Γ_{ren} . (d) Comparison of the exponents η_d^{eq} (triangles) and η^0 or η_d^0 (crosses) extracted from the spectra shown in (a-c), with the values expected from Eqs. (39) for η_d^{eq} (solid lines), and from Eqs. (41) for η^0 or from Eq. (40) for η_d^0 (dashed lines with dots), for several values of U . In (a), arrows indicate the scale $\bar{\omega}^*$ that separates the regimes $\omega^* < \omega < \bar{\omega}^*$ and $\bar{\omega}^* < \omega < D$, where $\mathcal{A}_d^{\text{eq}}$ scales according to Eqs. (40) or (41a), respectively.

actually find that within this regime two different power-laws can be discerned: First, in a regime $\omega^* < \omega < \bar{\omega}^*$ we find,

$$\mathcal{A}_d^{\text{eq}}(\omega) \sim \omega^{-1+2\eta'_d}, \quad \eta'_d = -\frac{1}{2} - \Delta_d^{\text{ph}} + (\Delta_d^{\text{ph}})^2, \quad (40)$$

where Δ_d^{ph} is given by Eq. (38). The exponent η'_d corresponds to the leading correction for weak interactions ($U/D \ll 1$) to the pure Lorentzian decay of the spectral function of the d -level (see Eq. (A.2) of the Appendix),

as can be shown using methods discussed in Refs. 33 and 34. The scale $\bar{\omega}^*$ that sets the upper limit for this behaviour is marked by arrows in Fig. 4(a) and decreases with increasing U/D . For U/D sufficiently small that $\bar{\omega}^*$ lies far below the bandwidth D , we find a second power law within the window $\bar{\omega}^* < \omega < D$, namely

$$\mathcal{A}_d^{\text{eq}}(\omega) \sim \omega^{-1+2\eta_d^0}, \quad \eta_d^0 = \frac{1}{2}(\Delta_d^{\text{ph}})^2. \quad (41a)$$

For the other two spectral functions we find throughout the regime $\omega^* < \omega < D$:

$$\mathcal{A}_{dc}^{\text{eq}}(\omega) \sim \omega^{-1+2\eta_{dc}^0}, \quad \eta_{dc}^0 = \frac{1}{2}(\Delta_d^{\text{ph}} - 1)^2, \quad (41b)$$

$$\mathcal{A}_{dc^\dagger}^{\text{eq}}(\omega) \sim \omega^{-1+2\eta_{dc^\dagger}^0}, \quad \eta_{dc^\dagger}^0 = \frac{1}{2}(\Delta_d^{\text{ph}} + 1)^2. \quad (41c)$$

Remarkably, Eqs. (41) have the same form as Eqs. (35), except that Δ_d is replaced by Δ_d^{ph} of Eq. (38), i.e. by the AO exponent involved in abruptly changing the local occupancy from 0 to 1 (in the absence of tunnelling). That this exponent should emerge is natural, since the corresponding correlators \mathcal{G}_d , \mathcal{G}_{dc} and \mathcal{G}_{dc^\dagger} all involve an operator \hat{d}^\dagger that places an electron on the dot at time $t = 0$. Although the dot occupancy $n_d(t)$ will relax back to its initial value n_d^i in the long time limit, this requires times $t \gg 1/\omega^*$. In contrast, the lead electrons react to the change in local charge on the much shorter time scale $1/D$. Thus, in the window of intermediate times, $1/D \ll t \ll 1/\omega^*$, corresponding to frequencies $\omega^* \ll \omega \ll D$, the situation is similar to that of the previous subsection, where we had $\Gamma = 0$ and a change in dot occupancy from 0 to 1 induced changes in the lead phase shifts, accompanied by AO. Thus, the exponents η^0 arising in Eq. (41) can be identified as the (equilibrium) scaling dimensions of the corresponding operators calculated in the *absence* of tunnelling (which is why we use a superscript 0 on such exponents, here and below). This explains the similarity between the behaviour described by Eqs. (41) and Eqs. (35). Note that the scaling dimension $\eta_{dc^\dagger}^0$ [Eq. (41c)] of the tunnelling operators $\hat{d}\hat{c}^\dagger$ and $\hat{c}^\dagger\hat{d}$ satisfy $0 \leq \eta_{dc^\dagger}^0 \leq 1/2$ [since for $U > 0$, we have $-1 \leq \Delta_d^{\text{ph}} \leq 0$, by Eq. (38)], thus tunnelling is always relevant for this model.

We conclude this subsection with a comment on the fact that $\mathcal{A}_d^{\text{eq}}(\omega)$ crosses over from non-AO behaviour [Eq. (40)] to AO behaviour [Eq. (41a)] as U/D is increased past 1. AO behaviour is absent for $U/D \ll 1$ because this situation corresponds essentially to a non-interacting resonant-level model, for which $\mathcal{G}_d^{\text{eq}}(t)$ does *not* show power-law behaviour of the type assumed in Eq. (18); instead it decays exponentially ($\sim e^{-\Gamma t}$), causing the spectral function $\mathcal{A}_d^{\text{eq}}(\omega)$ to have an essentially Lorentzian form. Equation (40) is the large-frequency limit of the latter, but including the leading corrections in U/D , calculated using methods discussed in Refs. 33 and 34. However, once U/D becomes $\gtrsim 1$, AO does begin to matter, implying a regime of power-law decay for $\mathcal{G}_d^{\text{eq}}(t)$ on intermediate time scales, leading to Eq. (41a) for $\mathcal{A}_d^{\text{eq}}(\omega)$.

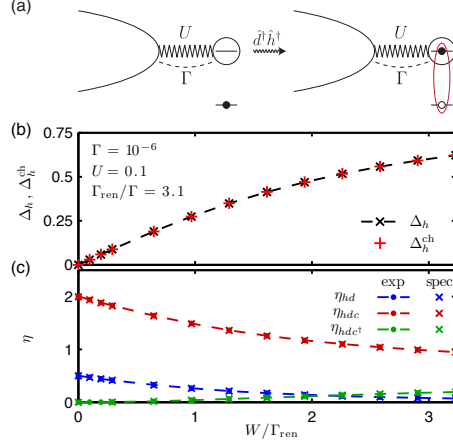


Figure 5: (Color online) (a) Cartoon of the quench which occurs when an electron-hole pair is created at time $t = 0$, see Eq. (43). (The cartoon depicts the situation relevant for exciton creation by absorption of a photon, which excited an electron from a valence-band to a conduction band level of a semiconducting quantum dot.) (b) The exponent Δ_h [from Eq. (11)] and the displaced charge Δ_h^{ph} [from Eq. (12)], for the quench of Eq. (42), as function of the quench range W . (c) Corresponding values of the AO exponents η_{hd} , η_{hdc} and η_{hdc^\dagger} , extracted from the asymptotic behaviour $\omega^{-1+2\eta}$ of spectral functions (crosses), or as expected from Eqs. (46) (dots). Typically, relative errors are less than 1%.

C. Quantum quench of level position

In the previous subsection we emphasized the importance of the scale ω^* , which separates the low- and intermediate-frequency regimes, showing trivial exponents or AO exponents, respectively. It is instructive to study the role of the scale ω^* in a slightly different but related context, namely quench spectral functions involving a quantum quench of the level position. This will shed further light on the AO between states with different local level occupancies.

Concretely, we consider initial and final Hamiltonians that both are of the form Eq. (36), but with initial and final level positions that are symmetrically spaced on opposite sides of the model's symmetry point at $\varepsilon_d = 0$:

$$\varepsilon_d^i = W/2 \xrightarrow{\text{quench}} \varepsilon_d^f = -W/2. \quad (42)$$

Although this is an example of a type 1 quench, it will be convenient (mainly for notational reasons) to reformulate this situation as a type 2 quench. To this end we use the

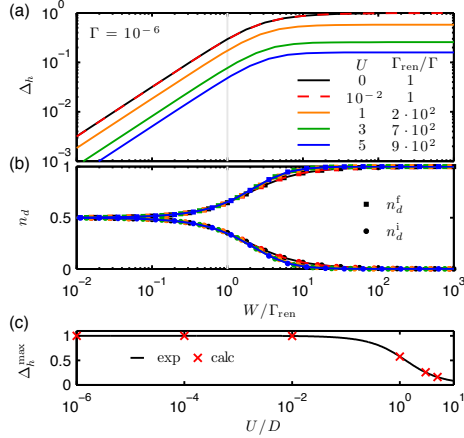


Figure 6: (Color online) (a) The AO exponent Δ_h [extracted according to Eq. (11)] as function of W/Γ_{ren} , for several values of U . For $W/\Gamma_{\text{ren}} \gg 1$, Δ_h approaches its maximal value Δ_h^{max} . As W is reduced below Γ_{ren} , Δ_h drops below its maximal value and decreases with W [linearly so for $W/\Gamma_{\text{ren}} \ll 1$]. (b) The final and initial occupancies n_d^f (squares, upper curves) and n_d^i (circles, lower curves) as functions of W/Γ_{ren} , for the same values of U [same color code as in (a)]. (c) The maximal value Δ_h^{max} of the AO exponent Δ_h , extracted from the $W/\Gamma_{\text{ren}} \gg 1$ regime of (a) (crosses, “calc”), or expected from Eq. (44) (solid line, “exp”); the relative deviations are well below 1%.

Hamiltonian

$$\hat{H} = W(1/2 - \hat{n}_h)\hat{n}_d + U(\hat{n}_d - 1/2)(\hat{c}^\dagger\hat{c} - 1/2) + \sum_{\epsilon} \epsilon \hat{c}_{\epsilon}^{\dagger}\hat{c}_{\epsilon} + \sqrt{\frac{\Gamma}{\pi\rho}} \sum_{\epsilon} (\hat{d}^{\dagger}\hat{c}_{\epsilon} + \hat{c}_{\epsilon}^{\dagger}\hat{d}), \quad (43)$$

where we have introduced an auxiliary degree of freedom, called “hole” (in analogy to the role of holes in exciton creation by optical absorption^{12–14}), with hole counting operator $\hat{n}_h = \hat{h}^{\dagger}\hat{h}$. The hole has no dynamics; its only role is to distinguish two distinct sectors of Hilbert space, in which the dynamics is described by \hat{H}_i or \hat{H}_f , with hole number $n_h = 0$ or 1, respectively [see Fig. 5(a)]. The type 2 quench that switches between these sectors is induced by $\hat{X}^{\dagger} = \hat{h}^{\dagger}$. The overlap $\mathcal{O}_h \sim N^{-\frac{1}{2}\Delta_h^2}$ between the initial and final ground states is characterized by an AO exponent Δ_h [Eq. (11)] that is equal to the charge Δ_h^{ch} displaced by the quench [Eq. (12)].

The magnitude of Δ_h increases with the range W of the quench, as shown in Fig. 5(b) (linear scale) and Fig. 6(a) (log-log scale). Note, in particular, that the scale on which the quenching range, W , needs to change in order for the AO exponents to change significantly, is given by Γ_{ren} . This is natural: when $W \gg \Gamma_{\text{ren}}$, the two states

$|G_i\rangle$ and $|G_f\rangle$ connected by the quench describe dots with strongly different occupancies, $n_d^i \simeq 0$ vs. $n_d^f \simeq 1$, see Fig. 6(b). Hence the AO [Eq. (11)] of the corresponding Fermi seas will be strong. The maximum possible value of the exponent Δ_h is

$$\Delta_h^{\text{max}} = 1 + \Delta_d^{\text{ph}}, \quad (44)$$

with $\Delta_d^{\text{ph}}(U) < 0$ given by Eq. (38). The first term simply gives the $U \rightarrow \infty$ value of the change in dot occupancy induced by the quench, namely 1; the second term reflects the reaction of the Fermi sea to this change, cf. Sec. III B.

Following the arguments of Sec. II D, the nonequilibrium spectral functions $\mathcal{A}_Y(\omega)$, defined for

$$\hat{Y}_1^{\dagger} = \hat{d}^{\dagger}\hat{h}^{\dagger}, \quad \hat{Y}_2^{\dagger} = \hat{c}^{\dagger}\hat{d}^{\dagger}\hat{h}^{\dagger}, \quad \hat{Y}_3^{\dagger} = \hat{c}\hat{d}^{\dagger}\hat{h}^{\dagger}, \quad (45)$$

are expected to show the following AO behaviour for $\omega \rightarrow 0$:

$$\mathcal{A}_{hd}(\omega) \sim \omega^{-1+2\eta_{hd}} \quad \eta_{hd} = \frac{1}{2}(\Delta_h - 1)^2, \quad (46a)$$

$$\mathcal{A}_{hdc}(\omega) \sim \omega^{-1+2\eta_{hdc}} \quad \eta_{hdc} = \frac{1}{2}(\Delta_h - 2)^2, \quad (46b)$$

$$\mathcal{A}_{hdct}(\omega) \sim \omega^{-1+2\eta_{hdct}} \quad \eta_{hdct} = \frac{1}{2}\Delta_h^2. \quad (46c)$$

The reason for the specific form of the exponents is that for the correlators \mathcal{G}_{hd} , \mathcal{G}_{hdc} or \mathcal{G}_{hdct} , at $t = 0$ the local charge (on the d-level or in the Fermi sea) is increased by one, two or zero, respectively [i.e. $\Delta_C = 1, 2$ or 0 in Eq. (16)]. Figure 5(c) shows that the exponents (crosses) extracted from the asymptotic behaviour $\mathcal{A}_Y(\omega)$ are indeed in good agreement with values expected (dots) from Eqs. (46).

IV. POPULATION SWITCHING WITHOUT SENSOR

The models investigated so far served as testing ground for the influence of AO on various types of spectral functions. The following two sections have the concrete motivation to clarify the role of AO in the context of quantum dot models that display the phenomenon of population switching (PS).^{15,16,35–40} In such models, a quantum dot, tunnel-coupled to leads, contains levels of different widths and is capacitively coupled to a gate voltage that shifts the levels energy relative to the Fermi level of the leads. Under suitable conditions, an (adiabatic) sweep of the gate voltage induces an inversion in the population of these levels (a so-called population switch), implying a change in the local potential seen by the Fermi seas in the leads. Goldstein, Berkovits and Gefen (GBG) have argued in Ref. 15,16 that in this context AO can play an important role. In particular, they pointed out that for a model involving a third lead acting as a charge sensor, the effects of AO can be enhanced to such an extent that population switching becomes abrupt, i.e. turns into a phase transition. Our goal is to elucidate the influence of AO by using the tools developed above in the context of the IRLM.

12

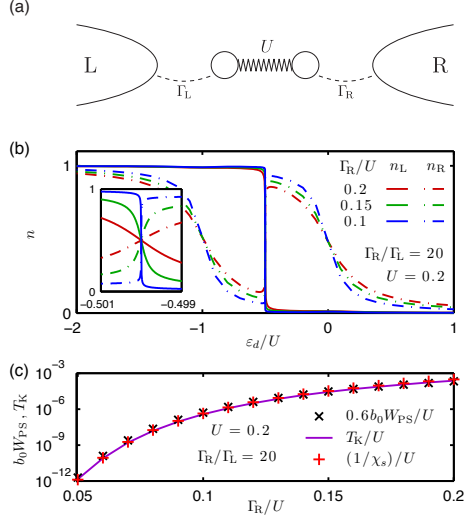


Figure 7: (Color online) (a) Cartoon of the Hamiltonian (47) for the asymmetric SIAM. (b) The occupations n_L (solid lines) and n_R (dashed lines) of the left and right level, respectively, as functions of ε_d , for several values of Γ_R , at a fixed ratio of $\Gamma_R/\Gamma_L = 20$. As ε_d is lowered past the particle-hole symmetric point at $\varepsilon_d = -U/2$, population switching occurs, with n_R changing from near 1 to near 0, and vice versa for n_L . Inset: zoom into the switching region around $\varepsilon_d = -U/2$, showing that the switch is continuous (as function of ε_d) even though the switching region becomes narrower for decreasing Γ_R . (c) Comparison of $b_0 W_{\text{PS}}$ [from Eqs. (48) and (51), crosses], T_K [from Eq. (52), solid], and the inverse pseudospin susceptibility $1/\chi_s$ (pluses). All three quantities evidently decrease similarly with decreasing Γ_R/U .

In the present section, we will study population switching in a two-lead model (without charge sensor), which is equivalent to an anisotropic Kondo model.^{15,16,41–44} The corresponding Kondo temperature, T_K , sets the width of the population switch as function of gate voltage. We calculate the spectral function $\mathcal{A}_\chi^{\text{SIAM}}(\omega)$ of the pseudospin-flip operator and show that T_K also acts as the crossover scale ω^* that separates a low-frequency regime showing Fermi-liquid power laws from an intermediate-frequency regime revealing AO exponents. We investigate the origin of the latter by a quantum quench analysis similar to that of Sec. III C above. In the following section, we will generalize the model by adding a charge sensor and analyse how this enhances the effects of AO.

A. Width of switching regime

We consider a model involving two single-level dots ($\mu = L, R$) and for convenience choose their level energies ε_d to be equal, so that the PS always occurs at the particle-hole symmetric point, $\varepsilon_d = -U/2$. (Note that PS occurs also for nondegenerate levels, as long as their level spacing is smaller than the difference of their level widths Γ_μ .) The levels have an electrostatic coupling $U > 0$ and are each tunnel-coupled to its own lead [see Fig. 7(a)]:

$$\hat{H}_{\text{SIAM}} = \sum_{\mu} \varepsilon_d \hat{d}_{\mu}^{\dagger} \hat{d}_{\mu} + U \hat{d}_{L}^{\dagger} \hat{d}_{L} \hat{d}_{R}^{\dagger} \hat{d}_{R} \quad (47)$$

$$+ \sum_{\varepsilon_{\mu}} \varepsilon \hat{c}_{\varepsilon_{\mu}}^{\dagger} \hat{c}_{\varepsilon_{\mu}} + \sum_{\mu} \sqrt{\frac{\Gamma_{\mu}}{\pi \rho}} \sum_{\varepsilon} (\hat{d}_{\mu}^{\dagger} \hat{c}_{\varepsilon_{\mu}} + \hat{c}_{\varepsilon_{\mu}}^{\dagger} \hat{d}_{\mu}),$$

(We use notation analogous to that of Sec. III B.) We choose the level widths to be strongly asymmetric and will use a fixed value of their ratio, $\Gamma_R/\Gamma_L = 20$, throughout. The model thus has the form of a spin-asymmetric single-impurity Anderson model (SIAM), where μ acts as pseudospin index.

As illustrated in Fig. 7(b), this model shows PS when ε_d is decreased past $\varepsilon_d = -U/2$ (the particle-hole symmetric point): as this “switching point” is crossed, the occupancy of the broad level (dashed lines) changes from near 1 to near 0, and vice versa for the narrow level (solid lines). We define the width of the switching regime, W_{PS} , as the difference,

$$W_{\text{PS}} \equiv \varepsilon_d(n_{R+}) - \varepsilon_d(n_{R-}), \quad (48)$$

between those two values of ε_d , located symmetrically on either side of the switching point, at which the occupation of the right level is $n_{R+} \equiv \frac{3}{4} n_{R+}^{\text{max}} (> \frac{1}{2})$ or $n_{R-} = 1 - n_{R+} (< \frac{1}{2})$, respectively, where n_{R+}^{max} is the largest value reached by n_R for $\varepsilon_d > -U/2$, to the right of the PS.

Figure 7(b) and its inset show that the width of the switching regime decreases with decreasing Γ_{μ} , without, however, dropping to zero as long as the level widths are nonzero. This behaviour can be understood as follows.^{15,16,41–44} In the vicinity of the particle-hole symmetric point, only two local charge configurations are relevant, namely those with occupancies (n_L, n_R) equal to $(0, 1)$ or $(1, 0)$. The spin-asymmetric SIAM can thus be mapped onto an anisotropic Kondo model by a Schrieffer-Wolff transformation. This leads to an anisotropic pseudospin exchange interaction of the form

$$\hat{H}_{\text{exch}} = (U_L + U_R)(\hat{d}_{L}^{\dagger} \hat{d}_{L} - \hat{d}_{R}^{\dagger} \hat{d}_{R})(\hat{c}_{L}^{\dagger} \hat{c}_{L} - \hat{c}_{R}^{\dagger} \hat{c}_{R})$$

$$+ 2\sqrt{U_L U_R}(\hat{c}_{L} \hat{c}_{R}^{\dagger} \hat{d}_{L}^{\dagger} \hat{d}_{R} + \text{h.c.})$$

$$+ B_{\text{eff}}(\hat{d}_{L}^{\dagger} \hat{d}_{L} - \hat{d}_{R}^{\dagger} \hat{d}_{R})/2, \quad (49)$$

respectively, with coupling constants given by

$$\rho \tilde{U}_{\mu} = \frac{\Gamma_{\mu}}{\pi} \left(\frac{1}{\varepsilon_d + U} + \frac{1}{|\varepsilon_d|} \right), \quad (50)$$

and effective magnetic field

$$B_{\text{eff}} = b_0(\varepsilon_d + U/2), \quad b_0 = \frac{4(\Gamma_R - \Gamma_L)}{\pi U}. \quad (51)$$

The corresponding Kondo temperature is given by the following expression:⁴¹

$$T_K = \frac{\sqrt{U(\Gamma_L + \Gamma_R)}}{\pi} \exp \left[\frac{\pi \varepsilon_d (U + \varepsilon_d)}{2U(\Gamma_L - \Gamma_R)} \ln \frac{\Gamma_L}{\Gamma_R} \right]. \quad (52)$$

Note that T_K decreases exponentially if Γ_μ is decreased with a fixed ratio of Γ_R/Γ_L and actually becomes zero for $\Gamma_\mu = 0$ (the argument of the exponent in Eq. (52) is negative, since $\varepsilon_d < 0$).

Now, T_K can be associated with the energy gained by forming a ground state involving a screened local pseudospin, which in the present setting translates to a ground state involving a coherent superposition of configurations with local occupancies (0, 1) and (1, 0). Screening will cease when ε_d deviates sufficiently from the symmetry point $-U/2$ that the effective magnetic field $|B_{\text{eff}}|$ exceeds T_K , in which case the ground state will be dominated solely by the (0, 1) or (1, 0) configuration, instead of involving a coherent superposition of both. Thus the switching width will be set by $b_0 W_{\text{PS}} \simeq T_K$, up to a numerical constant of order unity.

Figure 7(c) confirms this expectation. It shows that b_0 times the switching width W_{PS} [from Eq. (48)] (crosses) and the Kondo temperature T_K at $\varepsilon_d = -U/2$ [from Eq. (52)] (solid line), when plotted as functions of Γ_R/U at fixed Γ_R/Γ_L , are indeed almost perfectly proportional to each other. As a numerical consistency check, Fig. 7(c) also shows the inverse of the zero-temperature pseudospin susceptibility of the dot levels, $1/\chi_s$ (pluses), confirming that $T_K = 1/\chi_s$. (This is analogous to the relation $\Gamma_{\text{ren}} = 1/\pi\chi_c$ of Sec. III B.)

B. AO in dynamics of pseudospin-flip operator

Let us now explore the role of AO in population switching. To this end, we note that the effective exchange interaction \hat{H}_{exch} of Eq. (49) is similar in structure to the IRLM of Eq. (36): both involve two charge configurations (the former (0,1) and (1,0), the latter 0 and 1), which induce different phase shifts in the leads due to a dot-lead interaction term, and which are connected by a tunnelling term. More formally, the relation between the IRLM and PS is revealed by the equivalence of both models to the Kondo model (for the IRLM, this equivalence is discussed, e.g., in Refs. 11, 31, 32). Thus, we may expect AO to play a similar role for both models, and hence perform an analysis similar to that in Sections III B and III C.

Specifically, let us study the spectral function $\mathcal{A}_Y^{\text{eq}}(\omega)$ of the pseudospin-flip operators occurring in \hat{H}_{exch} ,

$$\hat{Y}^\dagger = \hat{c}_L \hat{c}_R^\dagger \hat{d}_L^\dagger \hat{d}_R, \quad \hat{Y} = \hat{d}_R \hat{d}_L \hat{c}_R \hat{c}_L^\dagger. \quad (53)$$

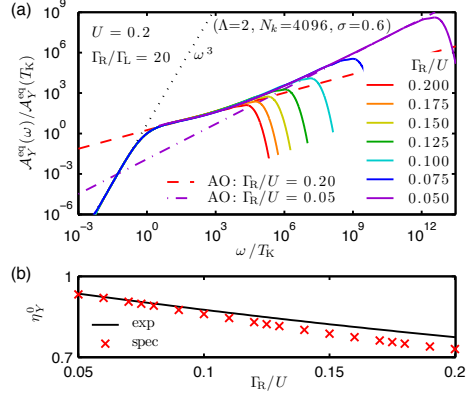


Figure 8: (Color online) (a) The pseudospin-flip spectral function $\mathcal{A}_Y^{\text{eq}}(\omega)$ [cf. Eq. (53)] for the PS model without charge sensor, for several values of Γ_R/U with fixed ratio Γ_R/Γ_L , calculated at $\varepsilon_d = -U/2$: plotting $\mathcal{A}_Y^{\text{eq}}(\omega)/\mathcal{A}_Y^{\text{eq}}(T_K)$ versus ω/T_K yields a scaling collapse. The frequency dependence of the curves qualitatively changes at T_K : for $\omega < T_K$ each curve shows a nontrivial AO power-law, $\sim \omega^{-1+2\eta_Y^*}$ [Eq. (54)], exemplified by the dashed and dash-dotted lines for $\Gamma_R/U = 0.2$ and 0.05 , respectively. (b) Comparison of the values for η_Y^* expected from Eq. (54b) (solid line), or extracted from the spectral function $\mathcal{A}_Y^{\text{eq}}(\omega)$ by using Eq. (54a) in the intermediate-frequency regime between T_K and the high frequency maximum (crosses). The accuracy of this extraction deteriorates with increasing Γ_R/U , since this reduces the width of the latter regime [see (a)], causing the relative error between crosses and solid line to increase from 1% for $\Gamma_R/U = 0.05$ to 10% for $\Gamma_R/U = 0.2$.

These induce transitions between the local charge configurations (0,1) and (1,0) and simultaneously add an electron to one lead while removing an electron from the other. (Such a transition does not constitute a quench, since for the present model n_d is not conserved.) $\mathcal{A}_Y^{\text{eq}}$ should, in some respects, be analogous to $\mathcal{A}_{d_{ct}}$ of Sec. III B. We have thus calculated $\mathcal{A}_Y^{\text{eq}}$ numerically, using the Hamiltonian \hat{H}_{SIAM} of Eq. (47). Indeed, Fig. 8(a), which shows $\mathcal{A}_Y^{\text{eq}}(\omega)$ for several values of Γ_R/U , exhibits several features reminiscent of Fig. 4(c) for $\mathcal{A}_{d_{ct}}(\omega)$: (i) A crossover scale ω^* , separating a regime of very low frequencies from one of intermediate frequencies, is clearly discernible; it is given by $\omega^* \simeq T_K$. (ii) When properly rescaled by plotting $\mathcal{A}_Y^{\text{eq}}(\omega)/\mathcal{A}_Y^{\text{eq}}(\omega^*)$ versus ω/ω^* , all curves collapse onto each other in the regime $\omega \lesssim D$. (iii) In the low-frequency regime $\omega \ll \omega^*$ we find the same Fermi-liquid power law, $\mathcal{A}_Y^{\text{eq}}(\omega) \sim \omega^3$ (dotted line), as for $\mathcal{A}_{d_{ct}}(\omega)$ [cf. Eq. (39c)]. (An analytical explanation for this fact is given in at the end of the Appendix.) (iv) In an intermediate-frequency regime $\omega^* \lesssim \omega \lesssim \omega_{\text{he}}$,

whose upper limit ω_{he} is a high-energy scale set by the minimum of the bandwidth or the cost of local charge fluctuations, we find an AO-dominated power law,

$$\mathcal{A}_Y^{\text{eq}}(\omega) \sim \omega^{-1+2\eta_Y^0}, \quad \omega^* \lesssim \omega \lesssim \omega_{\text{he}}. \quad (54a)$$

Though the numerical calculation of $\mathcal{A}_Y^{\text{eq}}(\omega)$ was performed using the full Hamiltonian \hat{H}_{SIAM} of Eq. (47), tunnelling is not important on the short time-scales that govern the frequency regime $\omega > \omega^*$. Hence, we expect the exponent η_Y^0 found from Eq. (54a) to be equal in value to that which one would obtain in the $\omega \rightarrow 0$ limit of a calculation performed in the *absence* of pseudospin-flips, i.e. using \hat{H}_{exch} without the pseudospin-flip terms in the second line of Eq. (49) (but retaining its first and third lines).

Without pseudospin-flips, the correlator involving \hat{Y} would actually constitute a type 2 quench correlator, because \hat{Y}^\dagger changes $(\hat{n}_L - \hat{n}_R)$, which is a conserved quantum number for Hamiltonians without pseudospin-flips. Therefore, the expected value of η_Y^0 can be predicted using the generalized Hopfield rule [Eq. (25)]. For the present case of two channels that are not interconnected by tunnelling, so that the total charge within each channel is conserved, it can be applied to each channel separately, adding the corresponding exponents¹⁹ [cf. Eq. (27)]:

$$\eta_Y^0 = \frac{1}{2}(\Delta_L + 1)^2 + \frac{1}{2}(-\Delta_R - 1)^2. \quad (54b)$$

Here Δ_μ describes the change in phase shift, divided by π , induced in lead μ by a pseudospin-flip; it is given by Eq. (38), with U replaced by U_μ [from Eq. (50)]. The applicability of these arguments is confirmed by Fig. 8(b), which shows that the exponents extracted from the numerical spectra (crosses) agree quite well with the values expected from Eq. (54b) (solid line). The quality of the agreement deteriorates with increasing Γ_R/U , because this reduces the width of the intermediate-frequency regime, making an accurate extraction of η_Y^0 from $\mathcal{A}_Y^{\text{eq}}(\omega)$ increasingly difficult.

Equation (54b) allows us to understand why PS is always continuous in this model: Since $-1 \leq \Delta_\mu \leq 0$, the scaling dimension of \hat{Y} satisfies $\eta_Y \leq 1$, implying that this operator always remains a relevant perturbation that does not flow to zero at low energy scales. This means that AO, although present, is not strong enough to completely suppress the amplitude for pseudospin-flip transitions. Hence, the two sectors (0,1) and (1,0) are always coupled by the effective low-energy Hamiltonian, so that population switching is continuous.^{15,16}

C. AO induced by quench of level positions

As mentioned above, the operators \hat{Y}^\dagger and \hat{Y} connect two configurations with different local occupancies, (0,1) and (1,0). To shed further light on the AO between such

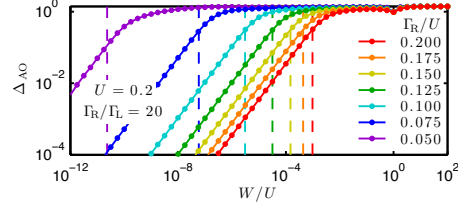


Figure 9: (Color online) AO for the PS model without charge sensing. The exponent Δ_{AO} [extracted from Eq. (1)] (solid lines with dots) is shown as function of quench size W/U [Eq. (55)], for several values of Γ_R/U with fixed ratio Γ_R/Γ_L , showing that AO becomes significant once W increases past T_K/b_0 (indicated by dashed vertical lines). The exponent Δ_{AO} increases linearly with W for $W \ll T_K/b_0$, and saturates to a maximal value of $\sqrt{2}$ [Eq. (56)] for $W \gg T_K/b_0$. The corresponding values of Δ_{ch} [from Eq. (7)] are not shown but agree with Δ_{AO} with relative errors of a few percent.

configurations, we now perform a quantum quench analysis similar to that of Sec. III C. We consider a type 1 quench, $\hat{H}_i \rightarrow \hat{H}_f$, induced by changing the level position ε_d from a value above the symmetry point, favouring (0,1), to one below, favouring (1,0):

$$\varepsilon_d^i = -U/2 + W/2 \xrightarrow{\text{quench}} \varepsilon_d^f = -U/2 - W/2. \quad (55)$$

The corresponding ground states, $|G_i\rangle$ and $|G_f\rangle$, will display AO as in Eq. (1). Based on the lessons learnt from Sec. III C, the corresponding exponent Δ_{AO} will increase with the width W of the quench. Indeed, Fig. 9 [to be compared with Fig. 6(a)] shows that Δ_{AO} increases from close to 0 for W much below T_K/b_0 (indicated by vertical dashed lines) to a maximal value of

$$\Delta_{\text{AO}}^{\text{max}} = \sqrt{(1)^2 + (1)^2} = \sqrt{2} \quad (56)$$

for $W \gg T_K/b_0$. This maximal value reflects the displaced charge Δ_{ch} [cf. Eq. (7)] induced by a very strong quench: both n_L and n_R are $\simeq 0$ (or $\simeq 1$) if the level position is far above (or below) the Fermi energy, $\varepsilon_d^i = -U/2 + W/2 \gg 0$ (or $\ll 0$), cf. Fig. 7(b), thus the displaced charge associated with both n_L and n_R is 1. (The contribution to Δ_{ch} from the leads turns out to be negligible here,¹⁹ since for sufficiently large W the Fermi sea is essentially decoupled from the dot.)

D. Summary for PS without sensor

The results of this section can be summarized as follows: (i) The energy scale setting the width of PS is proportional to T_K . (ii) This can directly be attributed to AO: as shown in Fig. 9, the ground states of two configurations on opposite sides of the switching points exhibit strong AO when their level positions differ by more than

T_K/b_0 . Thus, quantum fluctuations between them, induced by operators such as \hat{Y} and \hat{Y}^\dagger , are strongly suppressed. (iii) For the present model PS will always be continuous as a function of ε_d , because (for given U) T_K is nonzero for any fixed choice of Γ_L and Γ_R (although exponentially small), and AO ceases to be important ($\Delta_{AO} \simeq 0$) once ε_d comes within T_K/b_0 of the switching point. Conversely, however, it should now also be plausible that an essentially abrupt PS will be achievable if, by a suitable modification of the model, the degree of AO between the configurations (0,1) and (1,0) can be enhanced sufficiently to push T_K to zero even for finite Γ_L and Γ_R . As pointed out by GBG,^{15,16} this can be achieved by adding a charge sensor, to which we turn next.

V. POPULATION SWITCHING WITH SENSOR

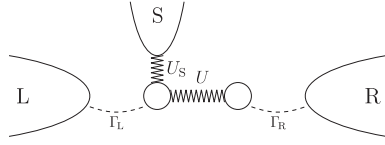


Figure 10: Cartoon of the Hamiltonian (57), describing an asymmetric SIAM with an additional sensor lead coupled electrostatically to the left dot.

In this section we study the effects of adding an electrostatically coupled charge sensor to the model of the previous section, as proposed by GBG.^{15,16} and analyse how this enhances the effects of AO. In particular, we show that by increasing the sensor coupling strength (U_S), the effective Kondo temperature (T_K^S) can be driven to zero, implying that population switching becomes abrupt. (A study of how additional leads increase the effects of AO for static quantities has recently been performed in similar context, involving a multi-lead IRLM.³²)

A. Width of switching regime

GBG proposed to extend the asymmetric SIAM studied above by introducing a third lead as “charge sensor” for the left dot (see Fig. 10). For simplicity, it is taken to have the same density of states as the other two leads, but in contrast to the latter, it couples to the left dot only electrostatically (*not* by tunnelling), with interaction strength U_S (with $\hat{c}_S \equiv \sum_e \hat{c}_{eS}$):

$$\hat{H} = \hat{H}_{\text{SIAM}} + \sum_e \varepsilon \hat{c}_{eS}^\dagger \hat{c}_{eS} + U_S (\hat{d}_L^\dagger \hat{d}_L - \frac{1}{2}) (\hat{c}_S^\dagger \hat{c}_S - \frac{1}{2}). \quad (57)$$

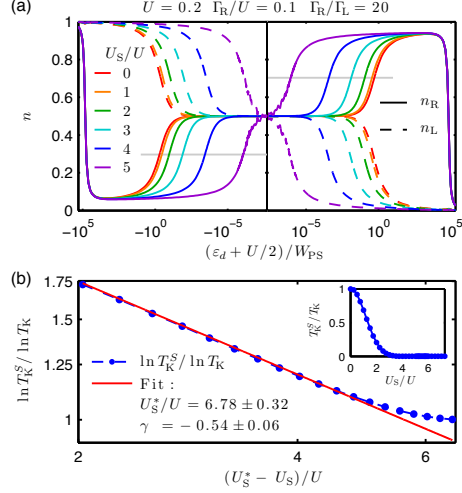


Figure 11: (Color online) Population switching for the charge sensor model of Eq. (57). (a) $n_R(\varepsilon_d)$ (solid lines) and $n_L(\varepsilon_d)$ (dashed lines) for several values of U_S/U , plotted versus $(\varepsilon_d + U/2)/W_{\text{PS}}$ in a pseudo-logarithmic fashion (“pseudo” in that the x-axis is plotted logarithmic with positive and negative values to the left and right of the switching point, respectively, represented by the vertical solid line). The horizontal light solid lines indicate the values of n_R which define the widths W_{PS}^S of the PS regimes. The noisy behaviour of the curves for $U_S = 5U$ at small values of ε_d indicates that our analysis cannot resolve smaller values for ε_d as we are reaching the limits of double precision numerical accuracy. (b) Inset: T_K^S/T_K as function of U_S/U , showing the rapid decrease of the Kondo temperature with increasing coupling. Main panel: $\ln T_K^S / \ln T_K$ versus $(U_S^* - U_S)/U$, plotted on a log-log scale (dashed line with dots), together with a linear fit using Eq. (59) (solid line).

A plot of n_L and n_R as functions of ε_d for this model looks essentially similar to Fig. 7(b), showing population switching at $\varepsilon_d = -U/2$. However, when the strength of the coupling U_S is increased, the width of the PS, say W_{PS}^S , is strongly reduced below the value W_{PS} it had for $U_S = 0$, as predicted by GBG. This is illustrated in Fig. 11(a), which shows n_R (solid lines) and n_L (dashed lines) as functions of $(\varepsilon_d + U/2)/W_{\text{PS}}$, using a logarithmic scale to zoom in on the immediate vicinity of the PS. In fact, as U_S approaches a critical value U_S^* , the width W_{PS}^S drops exponentially towards zero, until it becomes too small to be resolved within double precision numerical accuracy.

The behaviour of W_{PS}^S is mimicked by that of the Kondo temperature, calculated via the pseudospin susceptibility, $T_K^S \equiv 1/\chi_s$. We find that it decreases relative to its $U_S = 0$ value T_K , precisely in proportion to W_{PS}^S ,

such that

$$\frac{T_K^S}{T_K} = \frac{W_{PS}^S}{W_{PS}} \quad (58)$$

holds within our numerical accuracy.

The transition from a continuous to an abrupt PS as U_S crosses U_S^* has been predicted to be of the Kosterlitz-Thouless type.^{15,16} This implies that T_K^S is expected to approach zero according to

$$-\ln T_K^S \sim (U_S^* - U_S)^\gamma, \quad (59)$$

where $\gamma = -1/2$. To test whether our data is conform to this expectation, Fig. 11(b) shows $\ln(T_K^S)/\ln(T_K)$ vs. $(U_S^* - U)$ on a log-log plot. Indeed, we find a straight line for U_S not too close to U_S^* , consistent with Eq. (59). We extract the values $\gamma = -0.54 \pm 0.06$ and $U_S^*/U = 6.78 \pm 0.32$, by making linear fits over several somewhat different fitting ranges and taking the average and standard deviation of the fit parameters as final fitting results. The relatively large errors of about 10% are a consequence of the fact that it is not possible to obtain data for U_S closer to U_S^* , since this would drive T_K^S below the level of numerical noise.

We note that analytical calculations based on Refs. 15 and 16 [using the more accurate criterion, $J_z(U_S^*) = J_{xy}(U_S^*)$ in the notation of these papers] predict the critical interaction to be $U_S^*/U \sim 7.6$. The agreement of this prediction with the numerical result of 6.8 is quite respectable, given the inaccuracies in both the numerical and analytical calculations [for the latter, inaccuracies arise since the cutoff scheme employed in the analytical calculation is different from the one realized numerically. The cutoff appears explicitly in the arguments of the functions Q in Eqs. (6) to (10) of Ref. 15].

Though the above results unambiguously show that the width of PS decreases exponentially as U_S approaches a critical value U_S^* , an analysis based purely on W_{PS}^S can not access the critical point itself or the regime beyond. We therefore proceed now with a numerical calculation of the dynamics of the pseudospin-flip operator, for which we are not constrained to $U_S < U_S^*$.

B. AO in dynamics of pseudospin-flip operator

The reason for the U_S -dependence of W_{PS} and T_K^S is that the introduction of the sensor ($U_S \neq 0$) increases the influence of AO in the leads. As pointed out by GBG, the scaling dimension of \hat{Y} acquires an extra contribution $\frac{1}{2}\Delta_S^2$ due to the sensor lead:

$$\eta_Y^S = \frac{1}{2}(\Delta_L + 1)^2 + \frac{1}{2}(-\Delta_R - 1)^2 + \frac{1}{2}\Delta_S^2, \quad (60)$$

where Δ_S is given by Eq. (38), with U_S replacing U . By increasing U_S and thereby Δ_S^2 , it is thus possible to drive η_Y^S beyond 1. This will render the pseudospin-flip operators \hat{Y} and \hat{Y}^\dagger *irrelevant*, thus suppressing quantum

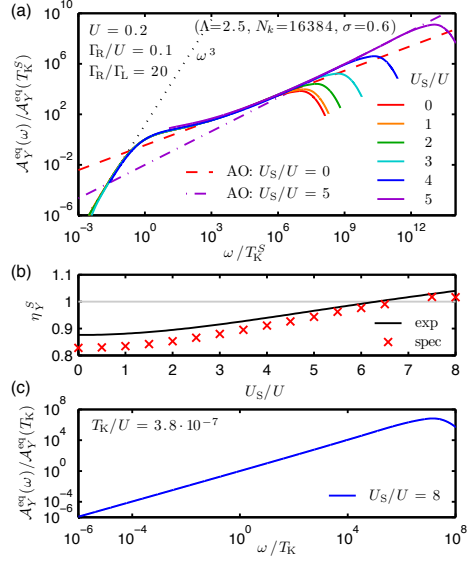


Figure 12: (Color online) (a) The pseudospin-flip spectral function $\mathcal{A}_Y^{\text{eq}}(\omega)$ [cf. Eq. (53)] for the PS model with charge sensor, for several values of U_S/U , calculated at $\varepsilon_d = -U/2$: plotting $\mathcal{A}_Y^{\text{eq}}(\omega)/\mathcal{A}_Y^{\text{eq}}(T_K^S)$ versus ω/T_K^S yields a scaling collapse. The general shape of the curves is similar to those shown in Fig. 8: for $\omega < T_K^S$ we find Fermi liquid behaviour, $\sim \omega^3$ (dotted line), while for $\omega > T_K^S$ each curve shows a nontrivial AO power-law, $\sim \omega^{-1+2\eta_Y^S}$ [cf. Eq. (54)], exemplified by the dashed and dash-dotted lines for $U_S/U = 0$ and 5, respectively. (b) Comparison of the values for η_Y^S expected from Eq. (60) (solid line), or extracted from the spectral function $\mathcal{A}_Y^{\text{eq}}(\omega)$ in the intermediate-frequency regime between T_K and the high frequency maximum (crosses). The relative errors are below 5%, where the errors decrease with increasing U_S for similar reasons as in Fig. 8. The light horizontal line indicates $\eta_Y^S = 1$. (We were unable to obtain reliable data for U_S around $7U$, presumably because this is too close to U_S^* .) (c) $\mathcal{A}_Y^{\text{eq}}(\omega)/\mathcal{A}_Y^{\text{eq}}(T_K)$ versus ω/T_K for $U_S/U = 8U$. The AO power-law behaviour $\omega^{-1+2\eta_Y^S}$ extends down to the smallest frequencies accessible, illustrating that the crossover scale T_K^S has become undetectably small.

fluctuations between the (0,1) and (1,0) configurations, and, hence, pushing T_K^S down to zero.

To check this scenario explicitly, we have studied the U_S -dependence of η_Y^S by extracting it from the spectral function $\mathcal{A}_Y^{\text{eq}}(\omega)$, calculated at the particle-hole symmetric point for several values of U_S . The general shape of $\mathcal{A}_Y^{\text{eq}}$, shown in Fig. 12(a), is similar to that of Fig. 8(a) for $U_S = 0$: For frequencies well below T_K^S , $\mathcal{A}_Y^{\text{eq}}(\omega)$ scales as ω^3 , while in the regime of intermediate frequencies,

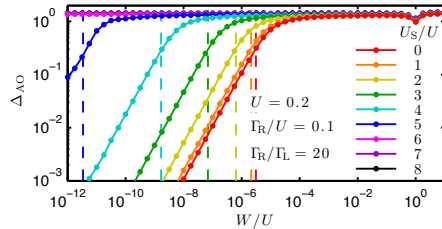


Figure 13: (Color online) AO for the PS model with charge sensing. The exponent Δ_{AO} [extracted from Eq. (1)] (solid lines with dots) is shown as function of quench size W/U [Eq. (55)], for several values of U_S/U , with fixed values of Γ_R and Γ_L . We see that T_K^S/b_0 (indicated by dashed vertical lines) is pushed to zero as U_S increases past $U_S^*/U \simeq 6.78$. Already for $U_S/U \geq 6$ the curves are essentially indistinguishable, in that they do not deviate from their constant value for all W/U -values accessible to our analysis. For $W \gg T_K^S/b_0$ the exponent Δ_{AO} saturates to a maximal value given by Eq. (61). The corresponding values of Δ_{ch} [from Eq. (7)] are not shown but agree with Δ_{AO} with relative errors of a few percent.

$T_K^S \lesssim \omega \lesssim \omega_{\text{he}}$ (cf. Sec. IV B), the spectrum shows AO power-law behaviour, $\sim \omega^{-1+2\eta_V^S}$. Indeed, Fig. 12(b) shows that the values for η_V^S extracted from the spectra (crosses) agree fairly well with those expected from Eq. (60). Moreover, for sufficiently large U_S/U , the exponents η_V^S increase past 1, confirming that the pseudospin-flip operators become irrelevant.

C. AO induced by quench of level positions

To further highlight the effect of AO on T_K^S , let us consider again the quench of level position [Eq. (55)] studied in Sec. IV C, and repeat the analysis presented there, but now for several different values of U_S/U . Figure 13 shows the results for the exponent Δ_{AO} . For large values of W the AO factor reaches its maximal value

$$\Delta_{\text{AO}}^{\text{max}} = \sqrt{(1)^2 + (1)^2 + \Delta_S^2}. \quad (61)$$

This is similar to Eq. (56) for the model without sensor, but includes the additional contribution Δ_S^2 [given by Eq. (38), with U_S replacing U] from the displaced charge induced in the sensor lead by the change in local occupancy of the left dot from $n_L = 0$ to 1.

The most important feature of Fig. 13 is the fact that the crossover scale T_K^S/b_0 (indicated by vertical dashed lines) is rapidly pushed to extremely small values as U_S/U is increased. Indeed, for $U_S = 8U$, which lies beyond the critical value of $U_S^*/U \simeq 6.78$ discussed above, Δ_{AO} is essentially pinned to its maximal value down to the smallest values of quench range W that we can access numerically. This is consistent with the fact that the cor-

responding spectral function $\mathcal{A}_V^{\text{eq}}(\omega)$ at $U_S = 8U$, shown in Fig. 12(c), shows nontrivial AO power laws down to the lowest frequencies accessible, with no trace of a Fermi-liquid ω^3 . This demonstrates very clearly, if somewhat indirectly, that the PS will be abrupt for $U_S > U_S^*$.

D. Summary for PS with sensor

Let us summarize the results of this section, by way of extending the list of salient points collected in Sec. IV D. (iv) The presence of a charge sensor reduces the crossover scale T_K^S , which reaches zero at a critical coupling U_S^* [Fig. 11]. (v) This reduction is due to the increased effect of AO in the leads, which increases the scaling dimension η_V^S [Fig. 12]; when the latter passes 1 (corresponding to $U_S = U_S^*$), the pseudospin-flip operators become irrelevant and T_K^S equals zero, rendering the PS abrupt. (vi) Correspondingly, for $U_S > U_S^*$, the spectrum $\mathcal{A}_V^{\text{eq}}(\omega)$ shows nontrivial AO power-law behaviour, $\omega^{-1+2\eta_V^S}$, all the way down to the smallest frequencies accessible [Fig. 12(c)], and a low-frequency regime showing Fermi-liquid exponents does not exist.

VI. CONCLUDING REMARKS

The goal of this paper was to elucidate the role of the Anderson orthogonality catastrophe in giving rise to anomalous scaling dimensions in dynamical correlation functions for quantum impurity models. To this end, we have studied several setups involving (interacting) quantum dots and (non-interacting) leads. The quantum dots and leads may be interconnected electrostatically, or also through tunnel-coupling. In our analysis we focussed on the asymptotic behaviour of various correlation functions $\mathcal{G}(t)$ and the corresponding spectral functions $\mathcal{A}(\omega)$ in the limit of long times or low frequencies, respectively. Their asymptotic behaviour could be understood via a generalized version of Hopfield's rule, whose validity was checked and confirmed through an extensive NRG analysis. As a particular application, we performed a detailed study of population switching, both without and with a third lead that acts as a charge sensor. We confirmed a previous prediction^{15,16} that when the charge sensor is sufficiently strongly coupled, population switching can turn into an abrupt quantum phase transition.

Aside from presenting a systematic discussion of the generalized Hopfield rule, which, hopefully, will be useful for practitioners in the fields, several general features have emerged from our analysis:

(1) In the context of a local quantum quench of type 1, where a change of parameters switches the Hamiltonian from \hat{H}_i to \hat{H}_f , each lead-dot electrostatic coupling gives rise to an AO factor in the ground state overlap $\langle G_i | G_f \rangle$, reflecting a change in the many-body configuration of the lead when the charging state of the dot is

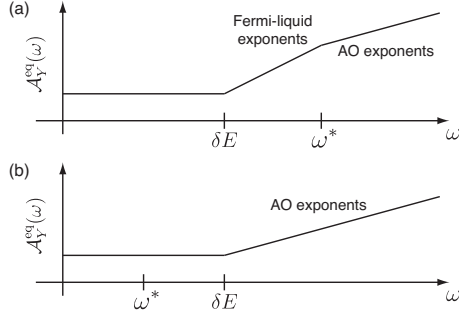


Figure 14: Schematic depiction of an equilibrium spectral function $\mathcal{A}_Y^{\text{eq}}(\omega)$ for the cases that the local charge relaxation rate ω^* is (a) larger or (b) smaller than the lead level spacing δE .

modified. This AO factor scales as $N_\mu^{-\frac{1}{2}\Delta_\mu^2}$, where N_μ is the number of electrons in lead μ and Δ_μ the change in the scattering phase, divided by π , in that lead. (AO factors from leads that are not interconnected by tunnelling, so that the total charge within each channel is conserved, are multiplicative [Eq. (27)].¹⁹)

(2) AO also arises for a type 2 quench, induced by an operator \hat{X}^\dagger that connects initial and final ground states $|G_i\rangle$ and $|G_f\rangle$ lying in dynamically disconnected sectors of Hilbert space. In particular, AO influences the corresponding quench spectral function $\mathcal{A}_X(\omega)$ which scales as $\mathcal{A}_X(\omega) \sim \omega^{-1+\Delta_X}$ [Eq. (23)]. For a Hamiltonian without tunnelling terms such as the LCM of Eq. (2), the spectral function for $\hat{X}^\dagger = \hat{d}^\dagger$ thus scales as $\mathcal{A}_d(\omega) \sim \omega^{-1+\Delta_d^2}$.

(3) When a type 2 quench has the form of a tunnelling operator, $\hat{Y}^\dagger = \hat{c}\hat{d}^\dagger$, the asymptotic power law is modified to become $\mathcal{A}_{dc^\dagger} \sim \omega^{-1+(\Delta_d+1)^2}$ [Eq. (35c)], implying a scaling dimension $\eta_{dc^\dagger}^0 = \frac{1}{2}(\Delta_d+1)^2$. For a particle-hole symmetric interaction term [as in Eq. (36)], we have $-1 \leq \Delta_d \leq 0$ [Eq. (38)], implying that $0 \leq \eta_{dc^\dagger}^0 \leq 1/2$, thus tunnelling between a dot and a single lead is always a relevant perturbation.

(4) The scaling exponent can be increased, and AO strengthened, by coupling the dot(s) to further leads. In particular, leads that couple to the dot only electrostatically (not via tunnelling) contribute AO exponents of the form $\frac{1}{2}\Delta_\mu^2$, and thus enhance AO more strongly than leads that are tunnel-coupled [cf. point (3)]. In this way, the scaling dimension of the tunnelling operator can be increased past 1 [cf. Eq. (60)], and tunnelling rendered irrelevant. In such a situation, population switching becomes a quantum phase transition, tuned by gate voltage.

(5) A particularly revealing way of demonstrating the effect of AO for population switching is to calculate the exponent Δ_{AO} for a type 1 quench in which the level position is abruptly changed from lying above to below

the PS point (see Figs. 9 and 13, which are analogous to Fig. 6(a) for the IRLM).

(6) In the presence of tunnelling terms of the form $(\hat{c}^\dagger \hat{d} + \hat{d}^\dagger \hat{c})$, operators such as $\hat{Y}^\dagger = \hat{d}^\dagger$, $\hat{c}\hat{d}^\dagger$ and $\hat{c}^\dagger \hat{d}$ do not induce a quench, since they do not cause a switch between disconnected sectors of Hilbert space. Thus, when such an operator acts on the ground state, the resulting state will relax back to the ground state over long time scales, say $t \gg 1/\omega^*$, where ω^* represents the local charge relaxation rate.

(7) The corresponding equilibrium spectral function $\mathcal{A}_Y^{\text{eq}}(\omega)$ thus typically shows trivial Fermi-liquid exponents [e.g. Eq. (39)] in the regime of very small frequencies, $\delta E \lesssim \omega \ll \omega^*$, where δE represents an infrared cutoff such as the level spacing in the lead. (Throughout this paper we took $\delta E \simeq 0$, since in NRG calculations δE can be made arbitrarily small by using sufficiently long Wilson chains.)

(8) In an intermediate frequency regime $\omega > \omega^*$, the equilibrium spectral function $\mathcal{A}_Y^{\text{eq}}(\omega)$ may nevertheless contain signatures of anomalous AO exponents, scaling as $\omega^{-1+2\eta_Y^0}$ [e.g. Eq. (41)], where η_Y^0 represents the scaling dimension of \hat{Y} calculated in the absence of tunnelling. Thus, such exponents may be extracted by focussing on this regime of intermediate frequencies [as done in Figs. 4, 8 and 12]. This is schematically indicated in Fig. 14(a).

(9) If AO can be made so strong that the scaling dimension η_Y^0 of the operator \hat{Y}^\dagger is larger than 1, the scale ω^* is pushed below δE (or, in the context of NRG, below the level of numerical noise). In this case, the regime of anomalous AO scaling $\omega^{-1+2\eta_Y^0}$ will extend all the way down to the smallest frequencies accessible [e.g. 12(c)], as schematically indicated in Fig. 14(b).

To conclude, we note that cases where AO dominates in the low frequency limit such that $\omega^* \simeq 0$, [as in point (9)], quantum fluctuations of the charge on the dot(s) are essentially completely frozen out. At zero temperature and in the absence of any extraneous decay mechanism, the system will remain localized in a particular local charge configuration. Thus, varying the gate voltage in such a situation may lead to hysteretic behaviour. It would be very interesting to experimentally search for such signatures of the freezing out of charge fluctuations by performing linear response measurements at the PS point.

Acknowledgments

We thank L. Borda, Y. Imry, Y. Oreg, G. Zaránd, R. Berkovits and A. Schiller for helpful discussions. This work received support from the DFG (SFB 631, De-730/3-2, De-730/4-2, SFB-TR12, WE4819/1-1), in part from the NSF under Grant No. PHY05-51164, from the Israel-Russia MOST grant, the Israel Science Foundation, and the EU grant under the STREP program GE-OMDISS. Financial support by the Excellence Cluster

“Nanosystems Initiative Munich (NIM)” is gratefully acknowledged. M.G. is supported by the Adams Foundation of the Israel Academy of Sciences and Humanities, the Simons Foundation, the Fulbright Foundation, and the BIKURA (FIRST) program of the Israel Science Foundation.

Appendix: Fermi-liquid spectral functions

In this appendix we study analytically the low energy ($\omega < \omega^*$) behaviour of the spectral functions of the IRLM (Sec. III B) and the PS setup (Sections IV B and V B).

Let us start from the noninteracting resonant level (Eq. (36) with $U = 0$). In that case an elementary calculation gives for the retarded dot Green function,⁴⁵

$$\mathcal{G}_d^R(\omega) = \frac{1}{\omega - \varepsilon_d - \frac{\Gamma}{\pi\rho}\mathcal{G}_c^{R,0}(\omega)} = \frac{1}{\omega - \varepsilon_d + i\Gamma}, \quad (\text{A.1})$$

where $\mathcal{G}_c^{R,0}$ is the retarded c Green function for $\Gamma = 0$, and we assumed the wide band limit (used just to simplify expressions, but actually not essential for any of the following arguments) $\mathcal{G}_c^{R,0}(\omega) = -i\pi\rho = -i\pi/2$ in units where $D = 1$. The imaginary part of the retarded Green function gives (up to a factor of $-1/\pi$) the well-known Lorentzian spectral function

$$\mathcal{A}_d^{\text{eq}}(\omega) = \frac{1}{\pi} \frac{\Gamma}{(\omega - \varepsilon_d)^2 + \Gamma^2}. \quad (\text{A.2})$$

Thus, at low energies ($\omega \ll \Gamma$) $\mathcal{A}_d^{\text{eq}}(\omega)$ becomes a constant, corresponding to $\eta_d^{\text{eq}} = 1/2$ [which reproduces Eq. (39a)]. This behaviour is easy to understand: In the absence of tunnelling $\mathcal{A}_c^{\text{eq},0}(\omega) = \rho$ is constant, reflecting the constant local density of states of the lead electrons near the end of the lead. In the presence of tunnelling, at low energy the dot level is well-hybridized with the lead, and assumes the role of the end of the lead, thus featuring the slowly-varying low-energy spectral function $\mathcal{A}_d^{\text{eq}}(\omega)$.

Based on similar arguments, one would expect that, in the presence of tunnelling, $\mathcal{A}_c^{\text{eq}}(\omega)$ is still constant at low-energies, since in that limit the small spatial separation between the dot and the end of the lead should be unimportant. However, commensurability at half filling (particle-hole symmetry) makes things bit more complicated. An explicit calculation gives:

$$\begin{aligned} \mathcal{G}_c^R(\omega) &= \mathcal{G}_c^{R,0}(\omega) + \mathcal{G}_c^{R,0}(\omega) \sqrt{\frac{\Gamma}{\pi\rho}} \mathcal{G}_d^R(\omega) \sqrt{\frac{\Gamma}{\pi\rho}} \mathcal{G}_c^{R,0}(\omega) \\ &= -i\pi\rho \frac{\omega - \varepsilon_d}{\omega - \varepsilon_d + i\Gamma}. \end{aligned} \quad (\text{A.3})$$

Thus, when ε_d is nonzero, we indeed get a constant low energy limit, i.e. $\eta_c^{\text{eq}} = 1/2$. However, when $\varepsilon_d = 0$ (the value used throughout this paper for the IRLM), $\mathcal{G}_c^R(\omega) \sim \omega$ while $\mathcal{A}_c^{\text{eq}}(\omega) \sim \omega^2$, corresponding to $\eta_c^{\text{eq}} =$

3/2. To understand this behaviour, let us examine a half infinite tight-binding chain with lattice spacing a and Hamiltonian $\hat{H}_{\text{TB}} = \sum_{n=1}^{\infty} (\hat{\Psi}_{n+1}^\dagger \hat{\Psi}_n + \text{h.c.})$. Taking the continuum limit in the standard way, we can expand the fast-varying annihilation operators Ψ_n in terms of slowly-varying (on the scale of the Fermi wavelength) right/left moving fields $\psi_{R/L}(x)$, with $x = na$:

$$\Psi_n = e^{ik_F na} \psi_R(na) + e^{-ik_F na} \psi_L(na), \quad (\text{A.4})$$

where k_F is the Fermi wavevector. From the boundary condition $\Psi_0 = 0$ one gets $\psi_L(0) = -\psi_R(0)$, so we can define the single slowly-varying field $\psi(x)$ by $\psi(x) = \psi_R(x)$ if $x > 0$ and $\psi(x) = -\psi_L(-x)$ if $x < 0$. Then:

$$\Psi_n = e^{ik_F na} \psi(na) - e^{-ik_F na} \psi(-na). \quad (\text{A.5})$$

At half filling, $k_F a = \pi/2$, we get at the site next to the boundary

$$\Psi_{n=2} = -\psi(2a) + \psi(-2a) \sim -4a\partial_x \psi(0), \quad (\text{A.6})$$

The same thing happens at the *first site* ($n = 1$) when we attach a dot, since at low energies the dot behaves as the new first site. The spatial derivative is equivalent to a time derivative, up to the Fermi velocity v_F . This extra time derivative is responsible for the vanishing of the spectral function $\mathcal{A}_c^{\text{eq}}(\omega)$ for $\omega \rightarrow 0$. Since we have derivative for both \hat{c} and \hat{c}^\dagger in the Green function, and each gives an extra factor of ω , we end up with $\mathcal{A}_c^{\text{eq}}(\omega) \sim \omega^2$. This behaviour depends on being at half filling (particle-hole symmetry), hence is modified when ε_d is not zero.

Now we can discuss the higher spectral functions, $\mathcal{A}_{dc^1}^{\text{eq}}(\omega)$, and $\mathcal{A}_d^{\text{eq}}(\omega)$. These are the imaginary parts of the corresponding retarded Green functions, up to a factor of $-1/\pi$. The retarded Green functions are in turn the analytical continuation of the temperature Green functions to the real frequency axis. And the temperature Green functions can be found in the noninteracting case using Wick's theorem.⁴⁵

Performing these calculations for $\mathcal{A}_{dc^1}^{\text{eq}}(\omega)$, one gets:

$$\begin{aligned} \mathcal{A}_{dc^1}^{\text{eq}}(\omega) &= \frac{\rho}{\pi} \Im \left[\ln \frac{\omega - \varepsilon_d + i\Gamma}{-\varepsilon_d + i\Gamma} \right. \\ &\quad \left. - \frac{\Gamma^2}{\omega(\omega + 2i\Gamma)} \ln \frac{\varepsilon_d^2 - (\omega + i\Gamma)^2}{\varepsilon_d^2 + \Gamma^2} \right]. \end{aligned} \quad (\text{A.7})$$

Concentrating on $\omega \ll \Gamma$ one finds $\eta_{dc^1}^{\text{eq}} = \eta_c^{\text{eq}} + \eta_d^{\text{eq}} = 1$ for $\varepsilon_d \neq 0$ and $\eta_{dc^1}^{\text{eq}} = \eta_c^{\text{eq}} + \eta_d^{\text{eq}} = 2$ for $\varepsilon_d = 0$ [the data in Fig. 4(c) corresponds to the latter case, which reproduces Eq. (39c)]. This simple summation of scaling dimensions is natural here, since there is only one possible different-time Wick-pairing, of each single-particle operator with its conjugate.

For $\mathcal{A}_d^{\text{eq}}(\omega)$, however, there are two different-time Wick-pairings, causing cancellations, and resulting in:

$$\mathcal{A}_d^{\text{eq}}(\omega) = \frac{\rho}{\pi} \Im \left[\frac{\omega - 2\varepsilon_d + 2i\Gamma}{\omega - 2\varepsilon_d} \ln \frac{\omega - \varepsilon_d + i\Gamma}{-\varepsilon_d + i\Gamma} \right]. \quad (\text{A.8})$$

Concentrating again on $\omega \ll \Gamma$ one finds now that $\eta_{dc}^{\text{eq}} = 2$ for *all* values of ε_d [which reproduces Eq. (39c)].³⁴ The reason is that in the low-energy continuum limit the product $\hat{d}\hat{c}$ becomes the product of annihilation operators at almost the same point. Hence, one should expand in the distance between \hat{d} and \hat{c} (lattice spacing). The leading term (with no spatial derivatives) vanishes by Pauli's principle; the next term involves a spatial derivative, leading to a factor of ω , similarly to the arguments above. Another factor of ω comes from the operator $\hat{c}^\dagger\hat{d}^\dagger$ appearing in the definition of $\mathcal{G}_{dc}^{\text{eq}}(\omega)$. Thus, at low energies we end up with $\mathcal{A}_{dc}^{\text{eq}}(\omega) \sim \omega^3$ even for $\varepsilon_d \neq 0$.

Although the above calculations were performed for the noninteracting case, the qualitative arguments explaining the low-energy behaviour are valid even when $U > 0$. Moreover, since the system flows to the same fixed point for all values of $U > 0$, the low energy power-laws are in any case *independent* of U . Our numerical results (Fig. 4) are in agreement with this picture.

Let us now turn to the low-energy behaviour of the PS setup in the case where PS is continuous. At low-energy the system is governed by Kondo physics, Eq. (49),^{41–44} where the L-R degree of freedom plays the role of a pseudo-spin. The equivalence to Kondo continues to hold even in the presence of a charge sensor, as shown by GBG.^{15,16} The operator $\hat{Y} = \hat{d}_R^\dagger \hat{d}_L \hat{c}_R \hat{c}_L^\dagger$ (which is relevant in the continuous-PS phase) is the pseudospin-flip local exchange term between the dot and the lead. Similarly, the IRLM is also equivalent to the Kondo model,^{11,31,32} with the role of spin replaced by the charging state of the dot. The pseudo-spin local exchange term is simply $\hat{d}\hat{c}^\dagger$. Hence, when the parameters are properly mapped, the spectral functions $\mathcal{A}_Y^{\text{eq}}(\omega)$ and $\mathcal{A}_{dc}^{\text{eq}}(\omega)$ are equivalent when the Kondo description applies (i.e. for $\omega \ll D$ for the IRLM, and $\omega \ll \omega_{\text{he}}$ for the PS setup). In particular, $\mathcal{A}_Y^{\text{eq}}(\omega)$ should exhibit an ω^3 behaviour at low energy, similarly to $\mathcal{A}_{dc}^{\text{eq}}(\omega)$ for $\varepsilon_d = 0$, as the NRG data shows [dotted line in Fig. 8(a) and Fig. 12(a)].

-
- ¹ P. W. Anderson, *Phys. Rev. Lett.* **18**, 1049 (1967).
² K. D. Schotte and U. Schotte, *Phys. Rev.* **185**, 509 (1969).
³ G. D. Mahan, *Phys. Rev.* **163**, 612 (1967).
⁴ J. J. Hopfield, *Comments Solid State Phys.* **2**, 40 (1969).
⁵ B. Roulet, J. Gavoret, and P. Nozières, *Phys. Rev.* **178**, 1072 (1969); P. Nozières, J. Gavoret, and B. Roulet, *Phys. Rev.* **178**, 1084 (1969); P. Nozières, and C. T. De Dominicis, *Phys. Rev.* **178**, 1097 (1969).
⁶ B. L. Altshuler and A. G. Aronov, *Pis'ma Zh. Eksp. Teor. Fiz.* **30**, 514 (1979).
⁷ A. O. Gogolin, *Phys. Rev. Lett.* **71**, 2995 (1993).
⁸ N. V. Prokof'ev, *Phys. Rev. B* **49**, 2148 (1994).
⁹ I. Affleck and A. W. W. Ludwig, *J. Phys. A* **27**, 5375 (1994).
¹⁰ A. Furusaki, *Phys. Rev. B* **56**, 9352 (1997).
¹¹ A. O. Gogolin, A. A. Nersisyan, and A. M. Tsvelik, *Bosonization and Strongly Correlated Systems* (Cambridge University Press, Cambridge, 2004).
¹² R. Helmes, M. Sindel, L. Borda, and J. von Delft, *Phys. Rev. B* **72**, 125301 (2005).
¹³ H. E. Türeci, M. Hanl, M. Claassen, A. Weichselbaum, T. Hecht, B. Braunecker, A. Govorov, L. Glazman, A. Imamoglu, and J. von Delft, *Phys. Rev. Lett.* **106**, 107402 (2011).
¹⁴ C. Latta, F. Haupt, M. Hanl, A. Weichselbaum, M. Claassen, W. Wuester, P. Fallahi, S. Faelt, L. Glazman, J. von Delft, H. E. Türeci, and A. Imamoglu, *Nature* **474**, 627 (2011).
¹⁵ M. Goldstein, R. Berkovits, and Y. Gefen, *Phys. Rev. Lett.* **104**, 226805 (2010).
¹⁶ M. Goldstein, Y. Gefen, and R. Berkovits, *Phys. Rev. B* **83**, 245112 (2011).
¹⁷ K. G. Wilson, *Rev. Mod. Phys.* **47**, 773 (1975).
¹⁸ R. Bulla, T. A. Costi, and T. Pruschke, *Rev. Mod. Phys.* **80**, 395 (2008).
¹⁹ A. Weichselbaum, W. Mündler, and J. von Delft, *Phys. Rev. B* **84**, 075137 (2011).
²⁰ J. Friedel, *Phil. Mag.* **43**, 153 (1952).
²¹ J. Friedel, *Can. J. Phys.* **34**, 1190 (1956).
²² D. C. Langreth, *Phys. Rev.* **150**, 516 (1966).
²³ A. C. Hewson, *The Kondo problem to heavy Fermions* (Cambridge University Press, Cambridge, 1993).
²⁴ Compare Ref. 20, p. 159; Ref. 21, Eq. (7); Ref. 22, Eq. (21); Ref. 23, Sec. 1.2.
²⁵ O. Gunnarsson and K. Schönhammer, *Phys. Rev. B* **28**, 4315 (1983).
²⁶ J. Cardy, *Scaling and Renormalization in Statistical Physics* (Cambridge University Press, Cambridge, 1996).
²⁷ F. B. Anders and A. Schiller, *Phys. Rev. Lett.* **95**, 196801 (2005).
²⁸ F. B. Anders and A. Schiller, *Phys. Rev. B* **74**, 245113 (2006).
²⁹ R. Peters, T. Pruschke and F. B. Anders, *Phys. Rev. B* **74**, 245114 (2006).
³⁰ A. Weichselbaum and J. von Delft, *Phys. Rev. Lett.* **99**, 076402 (2007).
³¹ P. Schlottmann, *Phys. Rev. B* **22**, 622 (1980).
³² L. Borda, A. Schiller, and A. Zawadowski, *Phys. Rev. B* **78**, 201301 (2008).
³³ M. Goldstein, Y. Weiss, and R. Berkovits, *Europhys. Lett.* **86**, 67012 (2009); *Physica E* **42**, 610 (2010).
³⁴ M. Goldstein and R. Berkovits, *Phys. Rev. B* **82**, 235315 (2010).
³⁵ G. Hackenbroich, W. D. Heiss, and H. A. Weidenmüller, *Phys. Rev. Lett.* **79**, 127 (1997).
³⁶ R. Baltin, Y. Gefen, G. Hackenbroich and H. A. Weidenmüller, *Eur. Phys. J. B* **10**, 119 (1999).
³⁷ P. G. Silvestrov and Y. Imry, *Phys. Rev. Lett.* **85**, 2565 (2000).
³⁸ P. G. Silvestrov and Y. Imry, *Phys. Rev. B* **65**, 035309 (2001).
³⁹ D. I. Golosov and Y. Gefen, *Phys. Rev. B* **74**, 205316 (2006).
⁴⁰ C. Karrasch, T. Hecht, A. Weichselbaum, Y. Oreg, J. von Delft, and V. Meden, *Phys. Rev. Lett.* **98**, 186802 (2007).
⁴¹ V. Kashcheyevs, A. Schiller, A. Aharony, and O. Entin-

- Wohlmann, *Phys. Rev. B* **75**, 115313 (2007).
- ⁴² H. W. Lee and S. Kim, *Phys. Rev. Lett.* **98**, 186805 (2007).
- ⁴³ P. G. Silvestrov and Y. Imry, *Phys. Rev. B* **75**, 115335 (2007).
- ⁴⁴ V. Kashcheyevs, C. Karrasch, T. Hecht, A. Weichselbaum, V. Meden, and A. Schiller, *Phys. Rev. Lett.* **102**, 136805 (2009).
- ⁴⁵ G. D. Mahan, *Many-Particle Physics* (Kluwer, New York, 2000).

Part III

Miscellaneous

Bibliography

- [1] S. R. White, *Density matrix formulation for quantum renormalization groups*, Phys. Rev. Lett. **69**, 2863 (1992). S. R. White, *Density-matrix algorithms for quantum renormalization groups*, Phys. Rev. B **48**, 10345 (1993).
- [2] K. G. Wilson, *The renormalization group: Critical phenomena and the Kondo problem*, Rev. Mod. Phys. **47**, 773 (1975).
- [3] S. A. Cheong and C. L. Henley, *Correlation density matrix: An unbiased analysis of exact diagonalizations*, Phys. Rev. B **79**, 212402 (2009).
- [4] S. A. Cheong and C. L. Henley, *Exact ground states and correlation functions of chain and ladder models of interacting hardcore bosons or spinless fermions*, Phys. Rev. B **80**, 165124 (2009).
- [5] R. Helmes, M. Sindel, L. Borda, and J. von Delft, *Absorption and emission in quantum dots: Fermi surface effects of Anderson excitons*, Phys. Rev. B **72**, 125301 (2005).
- [6] H. E. Türeci, M. Hanl, M. Claassen, A. Weichselbaum, T. Hecht, B. Braunecker, A. Govorov, L. Glazman, A. Imamoglu, and J. von Delft, *Many-Body Dynamics of Exciton Creation in a Quantum Dot by Optical Absorption: A Quantum Quench towards Kondo Correlations*, Phys. Rev. Lett. **106**, 107402 (2011).
- [7] C. Latta, F. Haupt, M. Hanl, A. Weichselbaum, M. Claassen, W. Wuester, P. Fallahi, S. Faelt, L. Glazman, J. von Delft, H. E. Türeci, and A. Imamoglu, *Quantum quench of Kondo correlations in optical absorption*, Nature **474**, 627 (2011).
- [8] G. Hackenbroich, W. D. Heiss, and H. A. Weidenmüller, *Deformation of Quantum Dots in the Coulomb Blockade Regime*, Phys. Rev. Lett. **79**, 127 (1997).
- [9] R. Baltin, Y. Gefen, G. Hackenbroich and H. A. Weidenmüller, *Correlations of conductance peaks and transmission phases in deformed quantum dots*, Eur. Phys. J. B **10**, 119 (1999).
- [10] P. G. Silvestrov and Y. Imry, *Towards an Explanation of the Mesoscopic Double-Slit Experiment: A New Model for Charging of a Quantum Dot*, Phys. Rev. Lett. **85**, 2565 (2000).

- [11] P. G. Silvestrov and Y. Imry, *Spin effects and transport in quantum dots with overlapping resonances*, Phys. Rev. B **65**, 035309 (2001).
- [12] D. I. Golosov and Y. Gefen, *Transmission through quantum dots: Focus on phase lapses*, Phys. Rev. B **74**, 205316 (2006).
- [13] C. Karrasch, T. Hecht, A. Weichselbaum, Y. Oreg, J. von Delft, and V. Meden, *Mesoscopic to Universal Crossover of the Transmission Phase of Multilevel Quantum Dots*, Phys. Rev. Lett. **98**, 186802 (2007).
- [14] M. Goldstein, R. Berkovits, and Y. Gefen, *Population Switching and Charge Sensing in Quantum Dots: A Case for a Quantum Phase Transition*, Phys. Rev. Lett. **104**, 226805 (2010).
- [15] M. Goldstein, Y. Gefen, and R. Berkovits, *Entanglement entropy and quantum phase transitions in quantum dots coupled to Luttinger liquid wires*, Phys. Rev. B **83**, 245112 (2011).
- [16] P. W. Anderson, *Infrared Catastrophe in Fermi Gases with Local Scattering Potentials*, Phys. Rev. Lett. **18**, 1049 (1967).
- [17] N. F. Mott and R. Peierls, *Discussion of the paper by de Boer and Verwey*, Proc. Phys. Soc. **49**, 72 (1937);
N. F. Mott, *The Basis of the Electron Theory of Metals, with Special Reference to the Transition Metals*, Proc. Phys. Soc. A **62**, 416 (1949).
- [18] J. Kondo, *Resistance Minimum in Dilute Magnetic Alloys*, Prog. Theor. Phys. **32**, 37 (1964).
- [19] W. J. de Haas, J. H. de Boer and G. J. van den Berg, *The electrical resistance of gold, copper, and lead at low temperatures*, Physica (Amsterdam) **1**, 1115 (1934).
- [20] T. A. Costi, L. Bergqvist, A. Weichselbaum, J. von Delft, T. Micklitz, A. Rosch, P. Mavropoulos, P. H. Dederichs, F. Mallet, L. Saminadayar, and C. Bäuerle, *Kondo Decoherence: Finding the Right Spin Model for Iron Impurities in Gold and Silver*, Phys. Rev. Lett. **102**, 056802 (2009).
- [21] U. Schollwöck, *The density-matrix renormalization group*, Rev. Mod. Phys. **77**, 259 (2005).
- [22] H. R. Krishna-murthy, J. W. Wilkins, and K. G. Wilson, *Renormalization-group approach to the Anderson model of dilute magnetic alloys. I. Static properties for the symmetric case*, Phys. Rev. B **21**, 1003 (1980);
H. R. Krishna-murthy, J. W. Wilkins, and K. G. Wilson, *Renormalization-group approach to the Anderson model of dilute magnetic alloys. II. Static properties for the asymmetric case*, Phys. Rev. B **21**, 1044 (1980).

-
- [23] R. Bulla, T. A. Costi, and T. Pruschke, *Numerical renormalization group method for quantum impurity systems*, Rev. Mod. Phys. **80**, 395 (2008).
- [24] J. Friedel, *The distribution of electrons round impurities in monovalent metals*, Phil. Mag. **43**, 153 (1952);
J. Friedel, *On some electrical and magnetic properties of metallic solid solutions* Can. J. Phys. **34**, 1190 (1956).
- [25] D. C. Langreth, *Friedel Sum Rule for Anderson's Model of Localized Impurity States*, Phys. Rev. **150**, 516 (1966).
- [26] A. C. Hewson, *The Kondo problem to heavy Fermions*, Cambridge University Press, Cambridge (1993).
- [27] G. D. Mahan, *Excitons in Metals: Infinite Hole Mass*, Phys. Rev. **163**, 612 (1967).
- [28] K. D. Schotte and U. Schotte, *Threshold Behavior of the X-Ray Spectra of Light Metals*, Phys. Rev. **185**, 509 (1969).
- [29] J. J. Hopfield, *Infrared Divergences, X-Ray Edges, and all that*, Comments Solid State Phys. **II**, 2 (1969).
- [30] B. Roulet, J. Gavoret, and P. Nozières, *Singularities in the X-Ray Absorption and Emission of Metals. I. First-Order Parquet Calculation*, Phys. Rev. **178**, 1072 (1969);
P. Nozières, J. Gavoret, and B. Roulet, *Singularities in the X-Ray Absorption and Emission of Metals. II. Self-Consistent Treatment of Divergences*, Phys. Rev. **178**, 1084 (1969);
P. Nozières, and C. T. De Dominicis, *Singularities in the X-Ray Absorption and Emission of Metals. III. One-Body Theory Exact Solution*, Phys. Rev. **178**, 1097 (1969).
- [31] I. Bloch, J. Dalibard and W. Zwerger, *Many-body physics with ultracold gases*, Rev. Mod. Phys. **80**, 885 (2008).
- [32] L. D. Landau, *The Theory of a Fermi Liquid*, Soviet Phys. JETP **3**, 920 (1957).
- [33] L. D. Landau, *On the Theory of the Fermi Liquid*, Soviet Phys. JETP **8**, 70 (1959).
- [34] A. A. Abrikosov, L. P. Gorkov, and I. E. Dzyaloshinski, *Methods of Quantum Field Theory in Statistical Mechanics*, Prentice-Hall, Inc., Englewood Cliffs, New Jersey (1963).
- [35] P. Nozières, *Theory of Interacting Fermi Systems*, W. A. Benjamin, Inc., Amsterdam, New York (1964).
- [36] N. Andrei and C. Destri, *Solution of the Multichannel Kondo Problem*, Phys. Rev. Lett. **52**, 364 (1984); A. M. Tvelick and P. B. Wiegmann, *Solution of the n-channel Kondo problem (scaling and integrability)*, Z. Phys. B **54**, 201 (1984).

- [37] Sin-itiro Tomonaga, *Remarks on Bloch's Method of Sound Waves applied to Many-Fermion Problems*, Prog. Theor. Phys. **5**, 544 (1950).
- [38] J. M. Luttinger, *An Exactly Soluble Model of a Many-Fermion System*, J. Math. Phys. **4**, 1154 (1963).
- [39] D. C. Mattis and E. H. Lieb, *Exact Solution of a Many-Fermion System and Its Associated Boson Field*, J. Math. Phys. **6**, 304 (1965).
- [40] F. D. M. Haldane, *'Luttinger liquid theory' of one-dimensional quantum fluids. I. Properties of the Luttinger model and their extension to the general 1D interacting spinless Fermi gas*, J. Phys. C **14**, 2585 (1981).
- [41] J. von Delft and H. Schoeller, *Bosonization for beginners – refermionization for experts*, Annalen der Physik **7**, 225 (1998).
- [42] T. A. Costi, A. C. Hewson, and V. Zlatic, *Transport coefficients of the Anderson model via the numerical renormalization group*, J. Phys.: Condens. Matter **6**, 2519 (1994).
- [43] D. Goldhaber-Gordon, H. Shtrikman, D. Mahalu, D. Abusch-Magder, U. Meirav and M. A. Kastner, *Kondo effect in a single-electron transistor*, Nature **391**, 156 (1998).
- [44] P. W. Anderson, *Localized Magnetic States in Metals*, Phys. Rev. **124**, 41 (1961).
- [45] J. R. Schrieffer and P. A. Wolff, *Relation between the Anderson and Kondo Hamiltonians*, Phys. Rev. **149**, 491 (1966).
- [46] H. Bethe, *Zur Theorie der Metalle. Eigenwerte und Eigenfunktionen der linearen Atomkette.*, Z. Phys. **71**, 205 (1931).
- [47] P. B. Wiegmann, *Towards an exact solution of the Anderson model*, Phys. Lett. A **80**, 163 (1981).
- [48] N. Kawakami and A. Okiji, *Exact expression of the ground-state energy for the symmetric anderson model*, Phys. Lett. A **86**, 483 (1981).
- [49] R. J. Warburton, C. Schäflein, D. Haft, F. Bickel, A. Lorke, K. Karrai, J. M. Garcia, W. Schoenfeld, and P. M. Petroff, *Optical emission from a charge-tunable quantum ring*, Nature (London) **405**, 926 (2000); K. Karrai, R. J. Warburton, C. Schulhauser, A. Högele, B. Urbaszek, E. J. McGhee, A. O. Govorov, J. M. Garcia, B. D. Gerardot, and P. M. Petroff, *Hybridization of electronic states in quantum dots through photon emission*, Nature (London) **427**, 135 (2004).
- [50] B. L. Altshuler and A. G. Aronov, *Pis'ma Zh. Eksp. Teor. Fiz.* **30**, 514 (1979).
- [51] A. O. Gogolin, *Local time-dependent perturbation in Luttinger liquid*, Phys. Rev. Lett. **71**, 2995 (1993).

-
- [52] N. V. Prokof'ev, *Fermi-edge singularity with backscattering in the Luttinger-liquid model*, Phys. Rev. B **49**, 2148 (1994).
- [53] I. Affleck and A. W. W. Ludwig, *The Fermi edge singularity and boundary condition changing operators*, J. Phys. A **27**, 5375 (1994).
- [54] A. Furusaki, Phys. Rev. B **56**, 9352 (1997).
- [55] R. Bulla, N.-H. Tong and M. Vojta, *Numerical Renormalization Group for Bosonic Systems and Application to the Sub-Ohmic Spin-Boson Model*, Phys. Rev. Lett. **91**, 170601 (2003).
- [56] R. Bulla, H.-J. Lee, N.-H. Tong and M. Vojta, *Numerical renormalization group for quantum impurities in a bosonic bath*, Phys. Rev. B **71**, 045122 (2005).
- [57] T. Hecht, *Numerical Renormalization Group studies of Correlation effects in Phase Coherent Transport through Quantum Dots*, Dissertation, Ludwig-Maximilians-Universität München, Fakultät für Physik, 2008.
- [58] R. Bulla, T. Pruschke, and A. C. Hewson, *Anderson impurity in pseudo-gap Fermi systems*, J. Phys.: Condens. Matter **9**, 10463 (1997).
- [59] M. Yoshida, M. A. Whitaker, and L.N. Oliveira, *Renormalization-group calculation of excitation properties for impurity models*, Phys. Rev. B **41**, 9403 (1990).
- [60] V. L. Campo, Jr., and L.N. Oliveira, *Alternative discretization in the numerical renormalization-group method*, Phys. Rev. B **72**, 104432 (2005).
- [61] R. Žitko and T. Pruschke, *Energy resolution and discretization artifacts in the numerical renormalization group*, Phys. Rev. B **79**, 085106 (2009).
- [62] A. Weichselbaum, F. Verstraete, U. Schollwöck, J. I. Cirac, and J. von Delft, *Variational matrix-product-state approach to quantum impurity models*, Phys. Rev. B **80**, 165117 (2009).
- [63] A. I. Tóth, C. P. Moca, Ö. Legeza and G. Zaránd, *Density matrix numerical renormalization group for non-Abelian symmetries*, Phys. Rev. B **78**, 245109 (2008).
- [64] A. Alex, M. Kalus, A. Huckleberry, and J. von Delft, *A numerical algorithm for the explicit calculation of $SU(N)$ and $SL(N,C)$ Clebsch-Gordan coefficients*, J. Math. Phys. **52**, 023507 (2011).
- [65] F. B. Anders and A. Schiller, *Real-Time Dynamics in Quantum-Impurity Systems: A Time-Dependent Numerical Renormalization-Group Approach*, Phys. Rev. Lett. **95**, 196801 (2005).

- [66] F. B. Anders and A. Schiller, *Spin precession and real-time dynamics in the Kondo model: Time-dependent numerical renormalization-group study*, Phys. Rev. B **74**, 245113 (2006).
- [67] A. Weichselbaum and J. von Delft *Sum-Rule Conserving Spectral Functions from the Numerical Renormalization Group*, Phys. Rev. Lett. **99**, 076402 (2007).
- [68] H. Bruus and K. Flensberg, *Many-Body Quantum Theory in Condensed Matter Physics*, Oxford University Press, Oxford (2004).
- [69] O. Sakai, Y. Shimizu, and T. Kasuya, *Single-Particle and Magnetic Excitation Spectra of Degenerate Anderson Model with Finite f - f Coulomb Interaction*, J. Phys. Soc. Jpn. **58**, 3666 (1989).
- [70] See EPAPS Document No. E-PRLTAO-99-025733 for appendices which give more details. For more information on EPAPS, see <http://www.aip.org/pubservs/epaps.html>.
- [71] R. Bulla, A. C. Hewson and T. Pruschke, *Numerical renormalization group calculations for the self-energy of the impurity Anderson model*, J. Phys.: Condens. Matter **10**, 8365 (1998).
- [72] I. Affleck, A. W. W. Ludwig, H.-B. Pang, and D. L. Cox, *Relevance of anisotropy in the multichannel Kondo effect: Comparison of conformal field theory and numerical renormalization-group results*, Phys. Rev. B **45**, 7918 (1992).
- [73] W. Hofstetter and G. Zarand, *Singlet-triplet transition in lateral quantum dots: A numerical renormalization group study*, Phys. Rev. B **69**, 235301 (2004).

List of Publications

The results presented in this thesis have been published in the following papers:

1. *Correlation density matrices for 1-dimensional quantum chains based on the density matrix renormalization group*
W. Munder, A. Weichselbaum, A. Holzner, J. von Delft, and C. L. Henley
New J. Phys. **12**, 075027 (2010)
2. *Anderson orthogonality and the numerical renormalization group*
A. Weichselbaum, W. Munder, and J. von Delft
Phys. Rev. B **84**, 075137 (2011)
3. *Anderson Orthogonality in the Dynamics After a Local Quantum Quench*
W. Munder, A. Weichselbaum, M. Goldstein, Y. Gefen and J. von Delft
submitted to arXiv:submit/0308004 [cond-mat.str-el] 29 Aug 2011
(submission to Phys. Rev. B intended)

Deutsche Zusammenfassung

In dieser Doktorarbeit werden zwei Felder aus dem Gebiet der stark korrelierten elektronischen Systeme behandelt: die spezifische Natur von Korrelationen zwischen Elektronen in einer Dimension und die Folgen eines Quanten-Quenches in Quanten-Störstellenmodellen. Ganz allgemein sind stark korrelierte Systeme dadurch charakterisiert, dass ihr physikalisches Verhalten durch eine Vielteilchentheorie beschrieben werden muss, d.h. Wechselwirkungen korrelieren alle Teilchen auf komplexe Weise. Die Herausforderung hierbei ist, dass der Hilbertraum in einer Vielteilchentheorie exponentiell groß ist in der Anzahl der Teilchen. Wenn also keine analytische Lösung verfügbar ist - was typischerweise der Fall ist - ist es notwendig das Problem solch großer Hilberträume irgendwie zu umgehen. Daher besteht die Verbindung zwischen den beiden Studien in dieser Arbeit aus ihrer numerischen Behandlung: sie machen Gebrauch von der Dichtematrix-Renormierungsgruppe (DMRG) [1] bzw. der numerischen Renormierungsgruppe (NRG) [2], die beide auf Matrixproduktzuständen basieren.

Das erste Projekt dieser Arbeit behandelt das Problem wie man auf numerische Weise die dominanten Korrelationen in Quanten-Gittermodellen finden kann, und zwar unvoreingenommen, also ohne Vorwissen über das aktuelle Modell. Ein nützliches Konzept dafür ist die Korrelations-Dichtematrix (CDM) [3], die alle Korrelationen zwischen zwei Gruppen von Gitterplätzen beinhaltet. Wir zeigen wie man aus der CDM einen Überblick über die relative Stärke der Korrelationen aus verschiedenen Symmetriesektoren extrahieren kann. Weiterhin wird gezeigt wie man detaillierte Informationen über die Operatoren gewinnt, die langreichweitige Korrelationen besitzen, wie die räumliche Abhängigkeit ihrer Korrelationsfunktionen. Wir demonstrieren dies mittels einer DMRG-Studie eines eindimensionalen, spinlosen, erweiterten Hubbard-Modells [4], wobei betont werden muss, dass die vorgeschlagene Analyse der CDM nicht auf eine Dimension beschränkt ist.

Das zweite Projekt dieser Arbeit ist motiviert durch zwei Phänomene aus dem Gebiet der Quanten-Störstellenmodelle, deren experimentelle und theoretische Behandlung immer noch andauert: optische Absorption im Zusammenhang mit einem Kondo-Exziton [5, 6, 7] und Besetzungsvertauschung in Quantenpunkten [8, 9, 10, 11, 12, 13, 14, 15]. Es stellt sich heraus, dass beide Phänomene auf den zahlreichen Aspekten der Anderson-Orthogonalität (AO) [16] beruhen. Diese beschreibt die Tatsache, dass die Reaktion des Fermisees auf einen Quanten-Quench (also einer abrupten Änderung einer Eigenschaft der Störstelle oder des Quantenpunktes) die Änderung aller Streuphasenverschiebungen aller Einteilchenwellenfunktionen ist, wodurch das System drastisch verändert wird. In diesem Zusammenhang zeigen wir dass NRG (eine äußerst genaue Methode für Quanten-Störstellenmodelle) für die Berechnung aller statischen und dynamischen Größen im Zusammenhang mit AO geeignet ist. Darauf aufbauend präsentieren wir eine ausführliche NRG-Studie der Besetzungsvertauschung in Quantenpunkten.

Acknowledgements

First of all I want to thank my advisor Jan von Delft for the guidance he gave me throughout my thesis. He always encourages the exploration of new ways, the will to keep on learning and not to be satisfied with the status quo. Even though he has to manage a chair with a lots of people he always found the time for discussions and questions. His personal habits but also the way he organizes his chair create a very fruitful ground for scientific work. At all times, it is possible to find someone for questions or discussions about physical or mathematical issues as well as problems with organisational stuff. His way of being a group leader stands exemplary for me. Due to his accurate guidance in several talks and posters for conferences, but also within our group meetings, I gained most of my presentational skills. He also gave me the opportunity to attend several conferences and schools around the world.

I am also very thankful to Andreas Weichselbaum who was always there for my questions. He supplied me with his NRG code as well as help with technical and physical problems. A good part of my knowledge about computers and programming comes from him.

Most of the studies presented in this thesis greatly benefited from the knowledge, experience and ideas of my collaborators, namely Christopher L. Henley, Moshe Goldstein and Yuval Gefen.

Thanks go to all the group members, but in particular to Markus Hanl, my “Bürobeziehung”, who was more than just an office mate. We had great discussions about physics and philosophy. My office was a nice place also due to my other office mates over the years: Wael Chibani, Alex Buchner, Arne Alex, Jad Halimeh and Barbara Englert. Special thanks go to Andreas Holzner, who was helping me in the first few weeks with my first steps in computational physics and Linux. I am grateful for the help of the team of the rbg, first of all Ralph Simmler, for keeping the computers up and running. I also want to thank all the other group members over the years who made my PhD a good time: Stefan Kehrein, Helmut Bross, Herbert Wagner, Alexandre Faribault, Oleg Yevtushenko, Florian Bauer, Cheng Guo, Alexander Hoffmann, Markus Heyl, Maximilian Treiber, Oliver Viehmann, Jan Heyder, Alois “Al” Dirnaichner, Philipp Snajberk, Nikolai Ufer, Annika Wöhner, Pablo Dominguez, Georg Heinrich, Florian Marquardt, Björn Kubala, Max Ludwig, Korbinian Paul, Hamed Saberi, Peter Fritsch, Ferdinand Helmer, Theresa Hecht, Benjamin Abel, Enrique Solano, Vitaly Golovach, Afif Siddiki, Piet Brouwer, Joern Kupferschmidt.

I thankfully acknowledge funding of the DFG through the Sonderforschungsbereich “Solid-State Quantum Information Processing: Physical Concepts and Material Aspects” (SFB 631) and the German Excellence Initiative via the “Nanosystems Initiative Munich” (NIM). Thanks also go to the Center for NanoScience (CeNS) and the Arnold Sommerfeld Center for Theoretical Physics (ASC) for providing a good working environment with excellent lectures and conferences.

Of course, also the A-Team needs to be mentioned here for excellent entertainment on Fridays (recently also often on other days), great food supplies in the Biergarten and the “weniger als drei Bier”-rate.

Last but not least I want to thank my parents Renate and Hacki Mnder for being always there and my wife Sandra for her love and her support. I do not know how I should have gone through the years of my thesis without her.